2012-07-03

The Synthesis and Structural Characterization of Metal Oxide Nanoparticles Having Catalytic Applications

Stacey Janel Smith
Brigham Young University - Provo

The Synthesis and Structural Characterization of Metal Oxide Nanoparticles Having Catalytic Applications

Stacey J. Smith

A dissertation submitted to the faculty of
Brigham Young University
in partial fulfillment of the requirements for the degree of

Doctor of Philosophy

Juliana Boerio-Goates, Chair
Branton J. Campbell
Brian F. Woodfield
Roger G. Harrison
Matthew Asplund
Karine Chesnel

Department of Chemistry and Biochemistry

Brigham Young University

August 2012

ABSTRACT

The Synthesis and Structural Characterization of Metal Oxide Nanoparticles
Having Catalytic Applications

Stacey J. Smith
Department of Chemistry and Biochemistry, BYU
Doctor of Philosophy

Nanotechnology is blossoming into one of the premiere technologies of this century, but the key to its progress lies in developing more efficient nanosynthesis methods. Variations in synthetic technique, however, can cause variations in size, structure, and surface characteristics, thereby altering the physical properties and functionality of the particles. Careful structural characterizations are thus essential for understanding the properties and appropriate applications for particles produced by new synthetic techniques.

In this work, a new 'solvent-deficient' method is presented for the synthesis of an unprecedentedly wide range of metal oxide nanomaterials including at least one metal oxide from each group in Groups 3-4, 6-15, and the Lanthanides. XRD, BET, and TEM structural characterizations as well as chemical purity analyses of the products are given. The intermediates associated with the method are also investigated, allowing the reaction parameters to be rationalized and culminating in a proposed mechanism for the reaction. Several of the reaction intermediates are themselves useful products, expanding the range of this already versatile method. Optimized synthesis parameters as well as structural characterizations are presented for one such intermediate product, the iron oxyhydroxide called ferrihydrite.

The Al_2O_3 nanoparticles produced by the new method show promise in catalyst support applications, and the synthesis and structural analysis (XRD, X-ray PDF, ^{27}Al NMR, TG/DTA-MS) of these nanoparticles is provided. The XRD, PDF, and NMR analyses reveal that the initial boehmite-like phase transforms to the catalytically useful γ-Al_2O_3 phase at unusually low temperatures (300-400°C), but boehmite-like local structure defects remain which heal slowly with increasing temperature up to 800°C. The 'pure' γ-Al_2O_3 may still contain randomized, non-cubic, local structure distortions, and it transforms directly to α-Al_2O_3 at ~1050°C. To rationalize the local structure and the absence of the δ- and θ-Al_2O_3 phases during the α-phase transition, relationships between the many Al_2O_3 phases are presented via innovative symmetry-mode analyses, revealing a potential quazi-topotactic mechanism for the γ-to-α transition.

To stabilize the γ-Al_2O_3 phase to higher temperatures for catalyst applications, 3 wt% of a lanthanum dopant was added via a new, 1-pot process based on the new solvent-deficient method. This process is described and X-ray PDF, TEM, ^{27}Al NMR, and EXAFS analyses of the La-doped γ-Al_2O_3 nanoparticles reveal that the dopant resides as isolated, adsorbed atoms on the γ-Al_2O_3 surface. The first coordination shell of the isolated La is increasingly La_2O_3-like as calcination temperature increases but changes drastically to be more $LaAlO_3$-like after the α-phase transition, which is delayed ~100°C by the La dopant. Combining the EXAFS, PDF, NMR, and symmetry-mode analyses, we provide new insight into the mechanism of stabilization provided by the La dopant.

Keywords: metal oxide nanoparticles, synthesis, solvent-deficient method, ferrihydrite, γ-Al_2O_3 nanoparticles, PDF, EXAFS, La-doped γ-Al_2O_3 nanoparticles

ACKNOWLEDGEMENTS

In my graduate experience, I have had the unique privilege of working with essentially three advisors. Though the impact that each has had on me both as a scientist and a person is immeasurable, I shall endeavor to put at least some of my feelings into words.

I may as well start at the beginning. Thank you, Brian, for hiring me as an ignorant, undergraduate freshman and catalyzing my journey as a scientist. Thank you for giving me hard tasks (both as an undergraduate and graduate student) and actually believing that I could do them; the independence you granted me combined with your high expectations of me pushed me to be more than I thought I could be. Thank you for all your guidance.

Thank you, Julie, for mentoring me from the time I started working in the lab as an undergraduate. Your support, encouragement, and counsel have meant more than you can possibly know. Thank you for guiding and directing me as a graduate student while at the same time giving me the freedom and the support to try new things. Thank you for your good example of a devoted scientist, teacher, and mother; you blazed the trail for female scientists at BYU.

Thank you, Branton, for opening up the world of structural analysis to me. Thank you for the countless hours devoted to tutoring me and for your inexhaustible patience with me as I learned everything I know about crystallography from you. Thank you for all the careful and constructive critiques of my work; you have helped me become a better scientist and a more effective writer. Thank you for going out of your way to integrate me into the crystallography community and make me feel welcome in it.

In addition to excellent advisors, I was fortunate to have good friends that also made good collaborators. Thank you, Kari, for introducing me to XAFS and for making beamtime at the APS a fun experience. Thank you, Samrat, for your MAS-NMR work; it was as invaluable to

my project as your friendship has been to me. Thank you, Baiyu, for getting our group into catalysis, for motivating my work on Al_2O_3 catalyst supports, and for collaborating with me both in coursework and lab work. Thank you, Betsy, for all the help you've given me over the years in and out of the lab; you've made classes, conferences, APS trips, and everyday life in the lab more enjoyable.

I guess if I wanted to start at the true beginning, I should really have started with my parents. Thank you, Mom and Dad, for instilling the value of education in me and for helping me develop a love of learning early in my life. Thank you for providing me opportunities to acquire knowledge, develop talents, and gain confidence; I owe everything I am to you and the start you gave me. Thank you for your good examples of honesty and hard work; you have taught me by example to be the best person I can be and to always do my best in everything that I do. Thank you for your constant love and support.

Lastly, but perhaps mostly, I need to thank my husband, Justin. Without your unwavering love, encouragement, optimism, and confidence in me, I would have fallen apart at the seams more times than I can count. You are my personal cheerleader—my external source of self confidence. I couldn't have done any of this without you.

Contents

Chapter 1

Introduction

Nanoparticles are materials that have crystallite dimensions less than 100 nm.[1] At such small dimensions, the properties of a material can change in interesting and useful ways. For example, bulk gold is quite inert and exhibits the familiar gold hue seen on most wedding rings, but gold nanoparticles can be bright red and are highly reactive, making excellent catalysts.[2-3] In addition to catalytic activity,[4-6] semiconductor band gap,[7] magnetic behavior,[8-9] melting point,[3,10] surface area, and surface energy[11-12] are size-dependent properties.

Nanotechnology is blossoming into one of the key technologies of this century[13] as these aberrant properties of nanoparticles find increased industrial application. Metal oxide nanoparticles in particular have numerous potential industrial applications. For example, the larger surface areas of SnO_2 and In_2O_3 nanoparticles increase these metal oxides' capacity for gas adsorption, thereby producing more sensitive and efficient gas sensors while simultaneously requiring less material.[14] The small diameters of metal oxide nanoparticles can also produce thinner and/or more efficient optical coatings (TiO_2, $BaTiO_3$ ZnO, Ga_2O_3),[15-17] gate dielectrics ($BaTiO_3$, $SrTiO_3$, Al_2O_3),[18] diodes (SnO_2, Sb_2O_3, ZnO, Al_2O_3, Ga_2O_3),[19] solar cells (TiO_2,),[17,20] batteries (Li metal oxides),[21] adsorbants (MgO, CaO, TiO_2, ZrO_2, Fe_2O_3, NiO, CuO, Al_2O_3, ZnO),[22-23] and ultrafiltration membranes (Zr, Ti, Sn, In, Ce, Zn, Al, Ni, Mg, Y, Fe, Co, Cr and Mn oxides, among others).[24] Even biotech industries are finding application for nano metal oxides in MRI imaging agents (Mn, Fe oxides),[25-26] dental implants (ZrO_2),[27] cosmetics (Al, Ce, Fe, Ti, Zn, Zr, oxides),[17,28] and hygiene products (ZnO).[3]

Nanoparticles seem to be particularly useful in the field of catalysis.[4-6] As Figure 1.1 indicates, nanoparticles have much more surface area per gram of material than larger, bulk-sized particles. Thus, when the metal oxides used in catalyst supports (such as Al_2O_3, ZrO_2, TiO_2, and CeO_2) are composed of nanoparticles, the enhanced surface area allows for greater catalyst dispersion, providing more efficient use of the typically expensive catalyst materials. Additionally, the drastic curvature of the nanoparticle surface results in higher surface energy which may translate to an increase in reactivity, or catalytic activity, of the support and thereby the catalyst.[29]

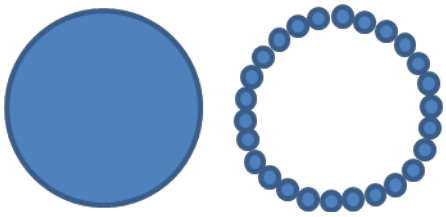

Figure 1.1 Illustration of the increase in surface area per gram of material in nanoparticles.

The key to developing and utilizing these burgeoning industrial nanotechnologies lies in being able to efficiently produce the nanomaterials they use. Hence, a wide range of synthetic techniques are being developed, and nanosynthesis is arising as an important and diverse discipline. Variations in synthetic technique, however, can cause variations in the size, structure, and surface characteristics of the nanoparticle products, thereby altering the physical properties and functionality of the particles.[4,6] Careful characterizations of nanoparticle size and structure are therefore essential for understanding the nanoparticles' properties and appropriate applications.

This study focuses on the development of a new and versatile method of synthesizing metal oxide nanoparticles and on the structural analysis of several of the nanoparticle products. For the sake of comparison with our new method, it is important to provide an overview of

existing nanosynthesis methods. Following this overview, we introduce the various structural analysis techniques we have applied in the study of our nanoparticles. Finally, a synopsis of the projects described in this dissertation is provided.

1.1 Nanosynthesis Techniques

Nanomaterials are generally synthesized via two approaches.[1] In the "top-down" approach, bulk-sized materials are broken down into nano-sized particles. "Bottom-up" approaches assemble nanometer-sized particles from the original atomic or molecular building blocks. Numerous and varied synthetic techniques using both bottom-up and top-down approaches have been developed for producing metal oxide nanoparticles. These methods can be generally grouped into three categories: solid-state (milling, sonication), solution-phase (molten salt, co-precipitation, sol-gel, microemulsion, solvothermal/hydrothermal, non-aqueous), and vapor-phase methods (spray pyrolysis, inert gas condensation, plasma or flame based methods).[3] The following sections briefly outline these techniques and summarize the advantages and disadvantages of each, which several excellent reviews reveal in greater detail.[3,9,17,30-34]

1.1.1 Solid-State Methods

Solid-state methods employ mechanical attrition to attain small particle sizes and are thus top-down approaches.[3,32] Generally, the compound is synthesized first (often being heated to achieve the desired crystal structure), and the relatively large particles produced are then milled or sonicated to grind or break them into finer particles. High-energy ball milling using stainless steel balls is a common practice though media-milling is gaining widespread use as well. In media-milling, uniformly-sized beads of hard ceramics such as ZrO_2 (the media) are mixed with the sample in a suspension which is then cycled repeatedly at high velocities through a mesh

screen. By sequentially decreasing the size of the media and mesh screens used in the milling process, smaller average particles sizes can be achieved.

Several modified versions of mechanical attrition have been developed. For example, instead of synthesizing the material prior to milling, milling can be used to induce the chemical reaction in the reagents through ball-powder collisions (either dry or in a liquid/solution environment), and then the desired particle size can be achieved through attrition. Milling temperature has also been tested as a means of altering particle size and characteristics. As alternatives to high velocity impact, torsion and friction have been explored as the driving forces of the attrition, though these have met with limited success in producing nanoparticles.

Traditionally, solid-state methods have had difficulty producing average particle sizes below 100nm. Innovations in media milling have more recently been able to achieve average particle sizes close to 30 nm by using media with very small sizes (200 μm). However, the milling process often introduces significant impurities in the materials. Additionally, the process results in a very wide distribution of particle sizes and lacks control over the shape and surface characteristics of the particles. Despite these challenges, the speed, cost-efficiency, and scalability of mechanical attrition make it the most widely used technique in industry for producing micron and sub-micron sized particles.

1.1.2 Solution-Phase Methods

Solution-phase methods, described in several excellent reviews,[3,9,17,31,34] are bottom-up approaches wherein nanoparticles are precipitated from a solution of chemical compounds. A wide variety of solution-phase techniques have been developed, but some of the most commonly used are the co-precipitation, microemulsion, sol-gel, and non-aqueous methods. These techniques are discussed in turn below. They provide perhaps the best means of producing

monodispersed, small particles (~5-50 nm) with tight size distributions and controllable morphologies. They are thus the most commonly used methods in academic research settings for synthesizing nanoparticles, but the lengthy and tedious procedures are often not easily scaled for industrial applications.

1.1.2.1 Co-precipitation

In co-precipitation, an aqueous solution of reagent(s) is formed, and a reaction is induced which will form either the oxide product or, more commonly, a somewhat amorphous precipitate (often a hydroxide, carbonate, oxalate, or chalcogenide) that can be thermally decomposed to form the oxide product. Several different types of reactions can be used, including chemical reduction, photoreduction, oxidation, and hydrolysis, but in the synthesis of nanoparticles, addition/exchange reactions of the form $xA^{y+}(aq) + yB^{x-}(aq) \rightleftarrows A_xB_y(s)$ are the most common.[31]

Merely inducing precipitation does not guarantee nanoparticle formation, however. To produce nanoparticles, the nucleation, growth, coarsening, and agglomeration processes that occur during precipitation must be controlled.[17,31] Precipitation begins when the product of the reagents' activities exceeds the equibilibrium constant of the precipitation reaction ($a_A a_B \geq K_{sp}$). The greater the degree of supersaturation, or ratio between these factors ($S = a_A a_B / K_{sp}$), the greater the driving force for, and rate of, precipitation. Once a threshold concentration of precipitate molecules are formed, they begin clustering, or nucleating. Rapid nucleation is desirable because the size distribution will theoretically be smaller if the particles nucleate and begin growing at the same time. Nucleation rate can be manipulated by controlling the factors that affect solubility such as temperature and concentration of reagents.

Clusters, or nucleation sites, that reach a critical radius, R^* (which is related to S and temperature, among other factors) will continue to grow while those with $R < R^*$ will dissolve. The growth rate is usually diffusion-limited, or limited by the rate at which new materials are supplied to the particle surface via mass transfer. In contrast to nucleation rate, slow growth rates are preferable in order to allow even distribution of materials to all particles and to allow the particles enough time to crystallize. Manipulating temperature, stirring/mixing, and the rate of reagent addition can provide some control over this.

Complicating the process, the growing particles are subject to Ostwald ripening, or coarsening, in which smaller particles are essentially consumed by the larger particles over time due to the increased solubility of smaller particles. Additionally, the small, forming particles tend to stick together, or agglomerate, to satisfy their high surface energies. Two approaches are generally used to stabilize the particles: (1) capping agents (including surfactants, polymers, or other organic species) are bound to the growing nanoparticles' surfaces to provide steric repulsion between particles, or (2) charged species (typically H^+ or OH^-) are chemisorbed on the nanoparticles' surfaces to provide electrostatic repulsion. In co-precipitation processes that require subsequent thermal treatment, some agglomeration is inevitable, but capping agents significantly reduce the extent of agglomeration if the heating conditions are kept as mild as possible.

For a few simple binary oxides, co-precipitation reactions can precipitate the oxide product directly. When capping agents are employed, nanoparticles can be produced with small sizes, small size distributions, controlled morphologies, low agglomeration, and good redispersability, but low crystallinity and impurities can be issues. For the majority of oxides, a calcination step is necessary, which step can increase the size, size distribution, and extent of

agglomeration of the product, even when capping agents are used. Additionally, capping agents block the nanoparticle surface (which can be problematic for certain applications), and removing them is often difficult or impossible to do without altering the particles. The great advantage of the co-precipitation method, though, is its versatility and adaptability; numerous variations can be employed to produce nanoparticles < 100 nm in size of a vast number of metal oxides and mixed metal oxides. The unique procedures necessary for each product can, however, also be a deterrent to industrial application.

1.1.2.2 Microemulsion

In the microemulsion technique, an amphiphilic surfactant and a hydrophilic co-surfactant are mixed with a nonpolar hydrocarbon solvent. The resulting mixture, though optically isotropic, is not the homogenous solution it appears to be; the surfactant forms spherical aggregates in which the ionic heads of the surfactant molecules are oriented towards the middle of the sphere where the polar co-surfactant molecules provide electronegative spacers between the surfactant heads. When water is added to the system, the spherical aggregates expand as the polar H_2O molecules position themselves in the hydrophilic center of the aggregates. In fact, the size of the aggregates can be controlled to a certain extent by fixing the ratio between surfactant and water. These spherical aggregates are commonly referred to as reverse micelles, and their solution is termed a 'microemulsion.'

The small reverse micelles undergo constant Brownian motion and collide frequently. In ~0.1% of the collisions, a short-lived (~100 ns) dimer will form, allowing the contents of the aqueous cores to be freely exchanged. Reverse micelles can thereby act as nanoreactors for any of the co-precipitation reactions discussed previously; collisions distribute reactants among the micellar cores whose uniform dimensions ensure that the forming particles will be nearly

uniform in size and shape. The microemulsion technique thus allows tight control over particle size, size distribution, and morphology while maintaining much of the versatility of the co-precipitation method. Additionally, the surfactant surrounding the aqueous solution acts somewhat like a capping agent and prevents agglomeration. It does not, however, prevent Ostwald ripening, and the added complexity of both the synthesis conditions and the final products limits the industrial utility of the method.

1.1.2.3 Sol-gel

In the sol-gel technique, a solution of a metal alkoxide precursor (or other compound with similar chemistry) is formed. Oxide- or hydroxide-bridged networks of the metal cations begin forming in the solution, and gelation occurs. The gel is aged for several days, allowing the polycondensation reactions to continue until the gel becomes a solid mass, contracts, and expels the solvent from the pores. The gel is dried either by thermal evaporation (xerogel) or supercritical solvent extraction (aerogel) using a four-step process of controlled heating and cooling. The gel is then calcined at high temperatures (often 400- 800°C) to crystallize the particles and/or remove surface-bound M-OH groups in order to stabilize the gel against rehydrating. An additional sintering step at even higher temperatures is sometimes performed to decompose remaining organic species and collapse the pore structure.

Varying the pH of the initial solution, the identity of the precursor, and the amount of water alters the gel network formed, thereby providing control over the particle size and morphology. However, the selection of precursors is limited to those that have alkoxide-like chemistry and will form a gel. Also, though the dried xerogel and aerogels are nanoparticulate, they are typically amorphous. The calcination step improves the crystallinity but leads to agglomeration and grain growth. Thus, the sol-gel method can produce uniform particles with

controlled morphology, but crystallinity and agglomeration are often issues. The agglomerates tend to have high surface areas and a useful, porous nature, however.

1.1.2.4 Non-aqueous methods

All of the solution-phase methods discussed previously involve reactions in an aqueous environment. Both co-precipitation and sol-gel techniques can also be performed in a non-aqueous environment.[3,9,31,33]

Several common reactant/solvent systems in non-aqueous sol-gel reactions are (1) metal halides in alcohols, (2) metal alkoxides, acetates, and acetylacetonates in alcohols, (3) metal alkoxides in keytones, and (4) metal acetylacetonates in benzylamine. In most of these cases, the organic solvent also serves as the reactant by providing the oxygen for the metal oxide bridges in the gel. As such, the solvent can have a sort of template effect, influencing the particle size and shape as well as the assembly behavior and corresponding network characteristics of the gel. The organic solvent can also stabilize the forming particles to a certain extent, resulting in less aggregation than in surfactant-free aqueous methods. The control over size and shape is not as tight as in surfactant-assisted processes, though, and the particles tend to exhibit broader size distributions, more agglomeration, and restricted redispersability. Nevertheless, surfactant-free non-aqueous sol-gel techniques have become valuable alternatives to aqueous surfactant-assisted methods, particularly for applications where the oxide surface should be accessible.

Though not as widespread as the non-aqueous sol-gel methods, organic solvents can be employed in precipitation reactions. For example, organic solvents can sometimes prove useful when precipitating two metals (such as Li and Co into $LiCoO_2$) whose stable pH ranges are too dissimilar to precipitate simultaneously from aqueous solution. Also, an organic solvent can allow the hydrolysis rate to be controlled, preventing the premature precipitation of

oxides/hydroxides, which can be a problem for high valence metals such as Ti^{4+} and Zr^{4+} in aqueous solutions. Rarely, an organic solvent can actually participate in the reaction, serving as an oxidizing agent, precipitating agent, or other such reactant. The organic solvent can also serve as a stabilizing agent, though it is still typically exchanged with a more effective capping agent such as oleic or myristic acid to ensure that growth is terminated.

1.1.3 Vapor-Phase Methods

In vapor-phase methods, a plasma, a flame, or thermal excitation is used to vaporize metal (or other precursor) atoms. These gas-phase atoms then react to form metal oxide molecules which cluster and eventually condense into nanoparticles upon cooling. Vapor-phase methods are thus bottom-up approaches. The variations of this process are discussed according to the vaporization method (thermal, plasma, or flame).

With thermal excitation, the air surrounding a metal (or other precursor) is evacuated and replaced with a very small amount of an inert gas. The metal is heated, and metal atoms effused from the source coalesce to form clusters as the atoms lose energy through collisions with the inert gas (metal oxide clusters will form if O_2 is also introduced into the chamber). The vapor-phase clusters will solidify into nanoparticles on cold fingers or surfaces. This 'inert gas condensation' process allows homogenous nucleation, resulting in nanoparticles with fairly tight size distributions, and mean sizes as small as 10 nm can be obtained. However, the slow production rates and high energy costs for evaporating the metals make this technique a fairly expensive procedure except for metals such as Mo that readily sublime.

Alternatively, a plasma can be used as the excitation source. In one variation, an arc induced in the inert gas (that is sometimes mixed with H_2) that surrounds the metal precursor creates a plasma that heats and vaporizes the metal atoms. In another version, the precursor

particles are aerosolized and then delivered into the plasma. Either way, the vaporized metal particles are carried downstream where a reactive gas is introduced to form the metal oxide particles which then condense, coalesce, and deposit as the stream cools. High production rates and particle diameters ~20 nm can be attained, but non-uniformities during the cooling conditions can cause significant size distributions in the particles.

Flame-based methods are well-suited for producing metal oxide nanomaterials; a hydrocarbon (or hydrogen)-oxygen flame is used to pyrolize precursor species which react quickly with oxygen in the surrounding atmosphere to form metal oxides that coalesce, condense, and deposit as they cool. Volatile organometallic precursors can be mixed with the fuel prior to flame treatment, or, with nonvolatile reagents such as nitrates and acetates, a solution of the reagents can be atomized and fed independently into the flame. This latter process can produce high surface area powders, but the pyrolysis conditions are difficult to control, and large particle sizes, wide size distributions, and aggregation are issues. Aggregation can be reduced by using low-pressure flame processes (wherein the surrounding atmosphere is rarefied to inhibit collisions), but these methods struggle to produce high quality nanoparticles at commercial rates.

Spray pyrolysis combines some aspects of both vapor and solution methods. A precursor solution is aerosolized and then delivered by a carrier gas to a heating zone. There, the solvent droplets evaporate while reactions occur inside each droplet to form a nanoparticle. Spray pyrolysis can produce large volumes of uniform, dense, spherical particles of a versatile range of products including multi-component nanoparticles, but the unavoidably large droplet sizes (μm range) limit the particle size to 100-1000 nm, even with reduced precursor concentrations.

1.1.4 Comparison

To summarize, solid-state methods are typically fast, inexpensive, and easily scaled to produce industrial quantities, but the particles produced are usually >100 nm in size and thus tend to have lower surface areas.[3] The milling or sonication process can also cause stress/strain on the crystal structure as well as introduce impurities.[32,35] Vapor-phase methods are highly successful in synthesizing nanoparticles with relatively small sizes and high purities, but the equipment and energy required to vaporize the reagents tend to be costly.[3,9] Solution-phase methods, particularly those which employ either surfactants or non-aqueous solvents, can produce uniform metal oxide nanoparticles with excellent control over size, size distribution, morphology, and dispersability. However, impurities are often an issue,[36-37] and for several applications (e.g. catalysis and gas sensing), the capping agents are an obstacle that must be removed in order to access the oxide surface.[13,36,38] Surfactant-free aqueous processes introduce fewer impurities and are readily scaled up for industrial production, but low crystallinity, larger size distributions, and agglomeration are often issues.[36-37]

In essence, no single technique is ideal in every way or for every application.[38] Perhaps as importantly, most methods are successful/applicable for only a small subset of nanomaterials. The variation in equipment and procedures necessary for the synthesis of the various useful nano metal oxides represents one of the challenges to widespread industrial application of these materials.

1.2 Structural Characterization Techniques

The physical properties of metal oxide nanoparticles are influenced by several structural aspects including the atomic arrangement, the size and shape (morphology) of each crystallite,

the morphology of agglomerated crystallites, and the available surface area of the particles and agglomerates.

One of the most important factors determining the properties of a material is the arrangement of its atoms, or its crystal structure. For example, when carbon atoms are organized in sheets, the resulting gray-colored graphite makes an excellent writing utensil because the stacked planes of carbon are easily separated and deposited on paper. In contrast, when carbon atoms are arranged in a covalent network, the resulting colorless diamond material is one of the hardest naturally-occurring substances. Similarly, when Al_2O_3 units are arranged in the roughly cubic γ-Al_2O_3 crystal structure, the resulting alumina tends to be mesoporous, have high surface area, and be catalytically active, making it a popular catalyst support material. In contrast, when the Al_2O_3 units are arranged in the rhombohedral α-Al_2O_3 crystal structure, the resulting alumina is neither porous nor catalytically active; instead, it is extremely hard and stable to high temperatures, so it is widely used as an abrasive and a refractory material.

After atomic structure, particle size most strongly influences a nanomaterial's physical properties. For example, a blue shift is often observed in the semiconductor band gap of metal oxide nanoparticles such as TiO_2; the smaller the size, the larger the band gap.[7] Similarly, in ferromagnetic or ferrimagnetic nanoparticles smaller than ~10 nm, the magnetic moments of entire crystallites rather than individual atoms will fluctuate with thermal energy and align themselves with external magnetic fields, resulting in superparamagnetic behavior, or paramagnetic behavior with an unusually large magnetic susceptibility.[8-9] Similarly, the cohesive energy of crystals decreases with crystallite size (probably due to the increased surface energy and strain of the extreme surface curvature), thereby decreasing the melting point of nanoparticles relative to larger particles.[3,10]

The effects of size on catalytic activity,[4-6] surface area, and surface energy[11-12] were already discussed; but another structural factor influencing surface area and catalytic utility is morphology. The morphology of the individual particles influences how they pack together in agglomerates, and this packing determines the surface area available for catalysts and other adsorbants. Spherical particles often have gaps between particles (or clumps of particles), allowing for more available surface area as well as a porous nature conducive to adsorption. Plate-like or rod-like particles, however, may align and stack in such a way that little surface area or pore structure is accessible.

Determining the structural characteristics of metal oxide nanoparticles is thus critical for determining their appropriate applications. Of the structural analysis techniques available, we have used a combination of X-ray diffraction (XRD), X-ray absorption fine structure (XAFS), magic-angle spinning (MAS) NMR, transmission electron microscopy (TEM), and gas adsorption (Brunauer-Emmett-Teller, or BET, analysis) to study atomic arrangement, particle size, particle and agglomerate morphology, and surface area. XRD, XAFS, and MAS-NMR are useful in studying atomic arrangement, and XRD can provide useful estimates of the average particle size. TEM can likewise provide information about atomic arrangement, but it is particularly apt at revealing the morphology and size of particles and agglomerates. The exposed surface area is most commonly measured through BET analysis. A basic outline of these techniques and the information they provide is given in the following sections, with greater detail provided for the somewhat less commonly familiar XRD(and PDF), XAFS, and BET techniques.

1.2.1 X-ray Diffraction (XRD)

One of the best tools for determining atomic structure is X-ray diffraction (XRD). X-rays are electromagnetic radiation with wavelengths between 0.01Å and 100Å. The oscillating

electric field of an X-ray can interact with the electron cloud of an atom, resulting in the light being elastically scattered. According to the Born approximation for weak scattering events, each atom in a crystal can be treated as an independent point source of spherical waves (Figure 1.2). These waves interfere with each other as they expand in space. When the distance between the scatterers is on the same order of magnitude as the wavelength of light, the interference will result in concerted constructive interference at specific angles, a phenomenon termed *diffraction*. Because the distance (or *d*-spacing) between atoms and atomic planes in a crystal is ~1-100 Å, crystals diffract X-rays.

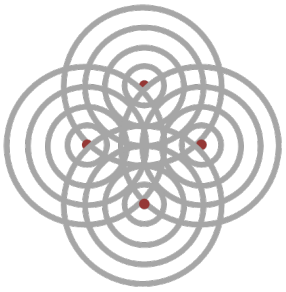

Figure 1.2 In the Born approximation for weakly scattered waves, each atom is viewed as an independent point source of spherical waves.

In 1913, William Henry Bragg and his son William Lawrence Bragg developed a simple way of understanding and predicting the angles at which diffraction will occur. In their model illustrated in Figure 1.3, the periodic array of atoms in a crystal is viewed as sets of parallel atomic planes (labeled by the Miller indices *hkl*)[i] that are separated by a distance *d*. When X-rays are reflected by these planes, Snell's law requires that the angle of reflection equal the angle of incidence, θ. Because waves penetrating deeper into the crystal (waves 2 and 3 in Figure 1.3) must travel farther, all the waves will be at different points in their phases upon reflection from the different planes. If the extra distance ($2*d\sin(\theta)$) travelled by the penetrating waves between points ABC is an integral multiple of the wavelength ($n\lambda$), then the reflected waves from all the

[i] The three Miller indices, *hkl*, relate to the planes' orientation with respect to the three axes (**a**, **b**, and **c**) of the unit cell, or smallest repeating unit, defined for the crystal. The intercepts of the *hkl* plane nearest the origin with the three unit cell axes can be calculated by **a**/h, **b**/k, and **c**/l.

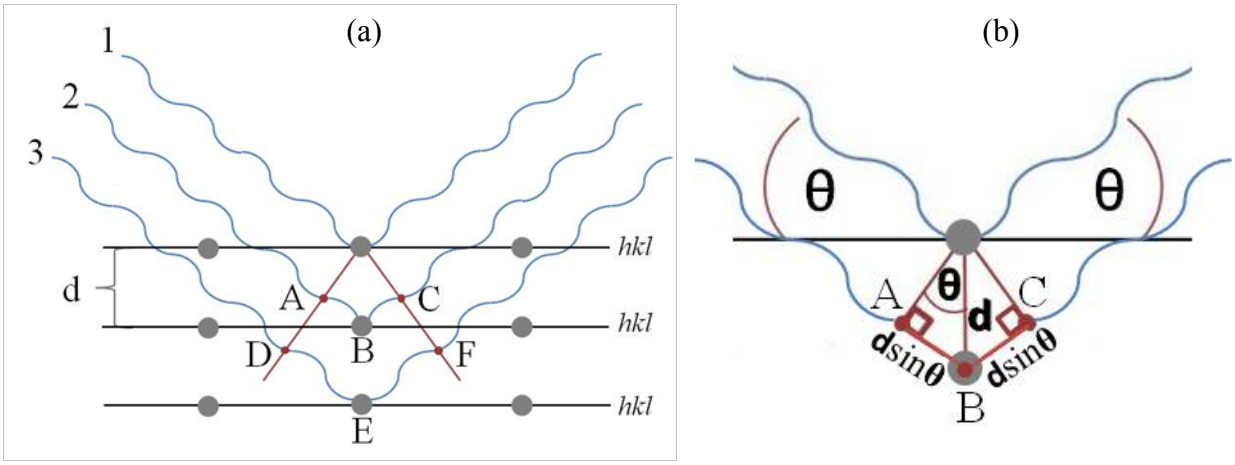

Figure 1.3 (a) Reflection of X-rays by crystallographic planes of atoms. (b) Geometrical relationships leading to Bragg's law.

subsequent planes will be in-phase with wave 1, resulting in constructive interference. The angles of constructive interference (diffraction) for each set of planes *hkl* can thus be determined using Bragg's Law:

$$2d_{hkl}\sin(\theta) = n\lambda \qquad \text{Eq. 1.1}$$

This two-dimensional view provides a valuable visual understanding of diffraction, but the most useful method of describing diffraction from crystals in all three dimensions was developed by P. P. Ewald.[39] In his construction, each set of planes (*hkl*) can be represented by the vector $\mathbf{d}_{hkl}$ defined to be the perpendicular distance from the origin of the unit cell to the nearest plane in the *hkl* family (Figure 1.4). A full three-dimensional plot of all the $\mathbf{d}_{hkl}$ vectors would be a dense sheaf of vectors projecting out of the origin in all directions, but noting that the vectors approach the origin as the reciprocal of the $\mathbf{d}_{hkl}$ value, (see Figure 1.5a), Ewald proposed that the reciprocal vector,

$$\mathbf{d}^*_{hkl} \equiv \frac{1}{\mathrm{d}_{hkl}} \qquad \text{Eq. 1.2}$$

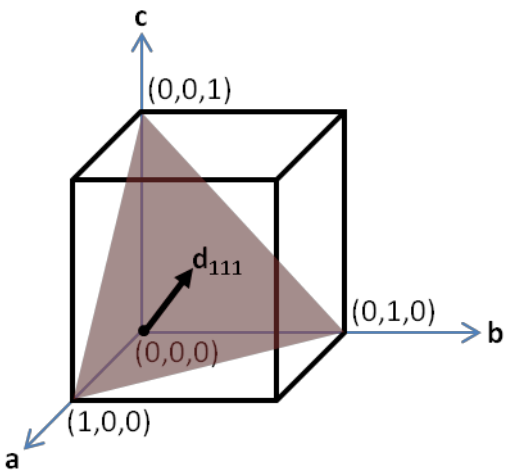

Figure 1.4 The vector $\mathbf{d}_{hkl}$, defined to be the perpendicular distance from the origin of the unit cell to the nearest plane in the *hkl* family.

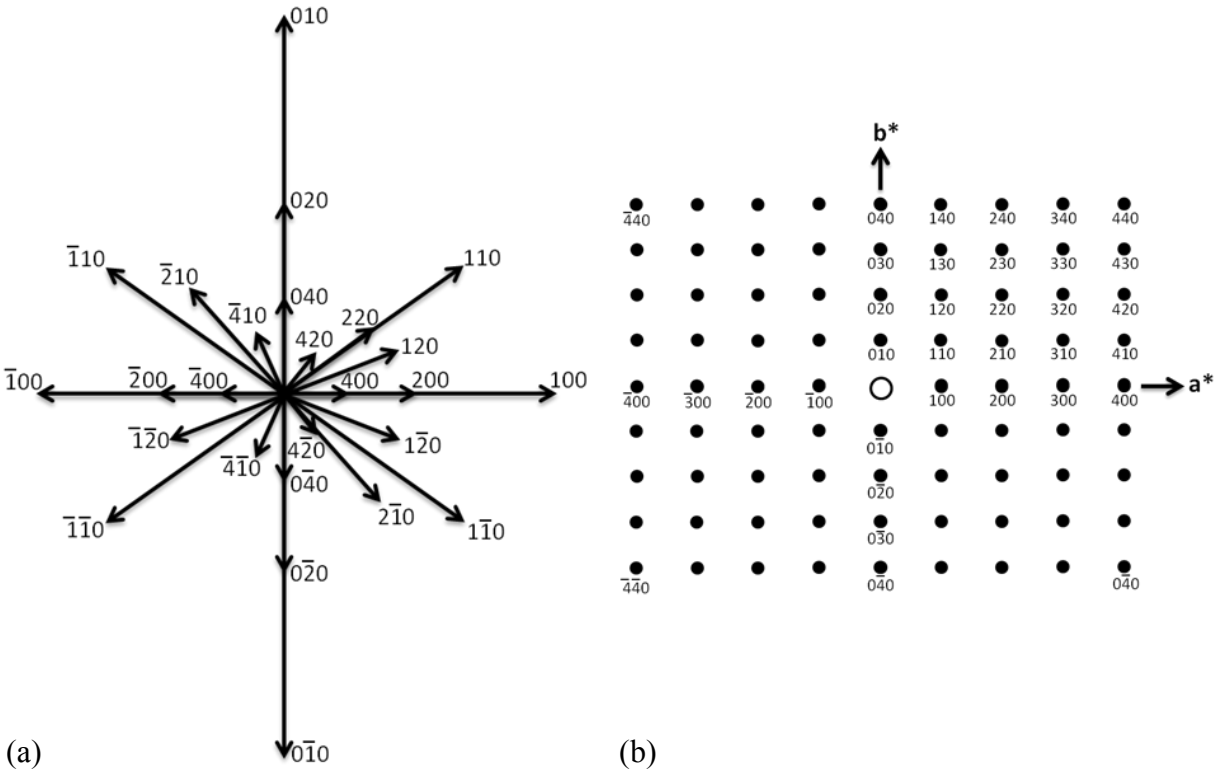

Figure 1.5 (a)Two-dimensional slice (the **ab**-plane) of the sphere of $\mathbf{d}_{hkl}$ vectors showing that the vectors approach the origin as 1/**d**. (b) Plot of the $\mathbf{1/d} = \mathbf{d}^*_{hkl}$ vectors (from the **ab**-plane) where the vectors are represented as points. Images adapted from Jenkins and Snyder (1996).[39]

be plotted instead. Such a plot, where the $\mathbf{d}^*_{hkl}$ vectors are represented by points, is given in Figure 1.5b. The points repeat at perfectly periodic intervals, forming a lattice called the reciprocal lattice. Just like the real lattice, the reciprocal lattice has repeating translation vectors (**a***, **b***, and **c***) which can be used to define the location of any $\mathbf{d}^*_{hkl}$ using its Miller indices as follows:

$$\mathbf{d}^*_{hkl} = h\mathbf{a}^* + k\mathbf{b}^* + l\mathbf{c}^* \qquad \text{Eq. 1.3}$$

The translation vectors **a***, **b***, and **c*** of the reciprocal lattice also form a unit cell whose shape is directly related to the shape and size of the real unit cell; for example, $\mathbf{d}^*_{100} = \mathbf{a}^*$ through Eq. 1.3, and because $\mathbf{d}_{100} = \mathbf{a}$ in an orthogonal unit cell, Eq. 1.2 gives the relationship $\mathbf{a}^* = 1/\mathbf{a}$. By extension, $\mathbf{b}^* = 1/\mathbf{b}$ and $\mathbf{c}^* = 1/\mathbf{c}$ in an orthogonal unit cell. Different relationships exist for non-orthogonal unit cells, but the symmetry of the reciprocal lattice can nonetheless reveal the symmetry of the real space lattice of any crystal.

Using the idea of the reciprocal lattice, Ewald constructed a means of geometrically visualizing the diffraction process in three dimensions. An imaginary sphere with radius 1/λ is centered on the real crystal such that the X-ray beam (with wavelength λ) enters the sphere on the left, passes through the crystal, and exits on the right (see Figure 1.6a). The origin of the reciprocal lattice is placed on the sphere's edge at the point of the beam's exit. Any rotation of the real crystal will rotate its reciprocal lattice since the two are directly related (Figure 1.6b). When the crystal is rotated so that one of the $\mathbf{d}^*_{hkl}$ vectors (points) touches the imaginary Ewald sphere, the geometrical relationships shown in Figure 1.6c reveal that the Bragg conditions are met for those *hkl* planes in the crystal, and constructive interference occurs. The diffracted beam will pass through the sphere at the point of the reciprocal lattice. A detector placed tangent to the sphere at that point in real space will record a spot of X-ray intensity. If the Ewald sphere is large

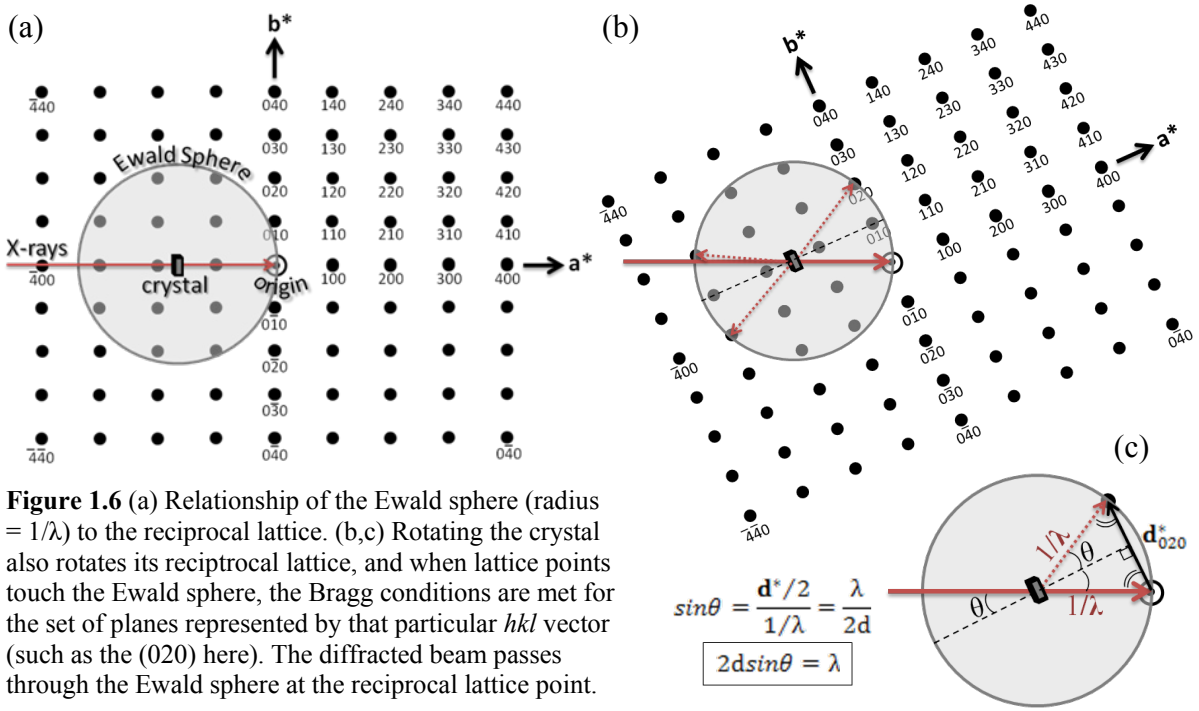

Figure 1.6 (a) Relationship of the Ewald sphere (radius = 1/λ) to the reciprocal lattice. (b,c) Rotating the crystal also rotates its reciptrocal lattice, and when lattice points touch the Ewald sphere, the Bragg conditions are met for the set of planes represented by that particular *hkl* vector (such as the (020) here). The diffracted beam passes through the Ewald sphere at the reciprocal lattice point.

enough (as it is in electron diffraction due to the very small wavelength of electrons), several of the reciprocal lattice points will touch the sphere simultaneously, and an image of that reciprocal lattice plane can be recorded, as shown in Figure 1.7. By identifying the vectors and measuring their spacing, the size and shape of the real space unit cell can be determined through the relationships discussed above.

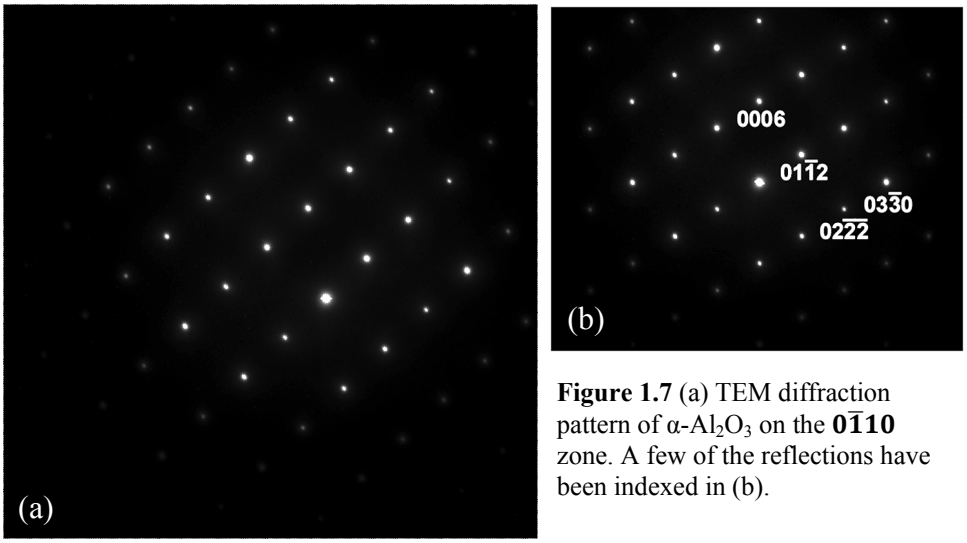

Figure 1.7 (a) TEM diffraction pattern of α-Al_2O_3 on the $\mathbf{0\bar{1}10}$ zone. A few of the reflections have been indexed in (b).

The larger wavelengths of X-rays create a much smaller Ewald sphere, however, so the diffraction spots recorded by a flat, two dimensional detector will not be from the same reciprocal lattice plane, as is evident in the images in Figure 1.8. In X-ray diffraction, the detector must be panned through three dimensional space in order to construct the reciprocal lattice and deduce the unit cell dimensions.

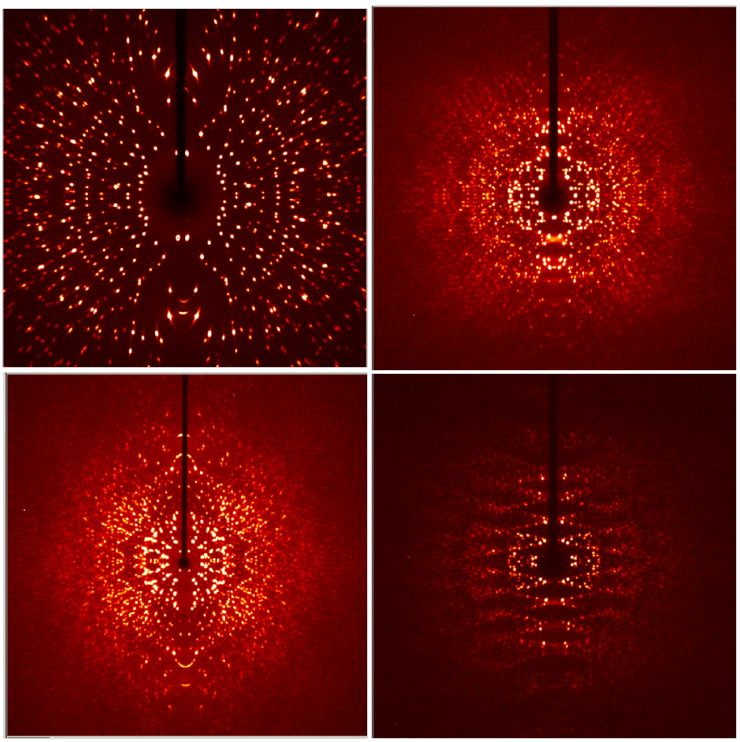

Figure 1.8 X-ray diffraction of citric acid at four different orientations. Because of the relatively small size of the Ewald sphere, the diffracted beams are not from a single lattice plane, and most are not perpendicular to the 2D detector and thus display streaking. Though unsuitable for actual analysis, these images reveal the symmetry of the crystal.

An important observation from Figure 1.8 is that the diffraction spots have different intensities. The variation in intensity can be used to deduce the identities and positions of the atoms inside the real space unit cell. To model/interpret the diffraction intensities, we return to the Born approximation in which each atom in the unit cell can be treated as a point source for a spherical wave that can be described by the wave equation $\varphi(\mathbf{r}) = \frac{e^{i\mathbf{k}\cdot\mathbf{r}}}{\mathbf{r}}$. Because $e^{i\mathbf{k}\cdot\mathbf{r}}$ is a vector in the complex Euler coordinate system (see Figure 1.10 later), the waves can be treated as vectors whose length and polar coordinate correspond to the amplitude and phase of the wave, respectively. The X-ray wave incident to the unit cell can thus be described as

$$\varphi_{init}(\mathbf{r}) = e^{i\mathbf{k}_{init}\mathbf{r}} \qquad \text{Eq. 1.4}$$

and the scattered wave can be described as

$$\varphi_{final}(\mathbf{r}) = Ae^{i\mathbf{k}_{final}\mathbf{r}} \qquad \text{Eq. 1.5}$$

where $\mathbf{k}_{init}$ and $\mathbf{k}_{final}$ are the initial and final wavevectors. A is the new amplitude of the scattered wave relative to that of the incident wave.

Because the scattering in diffraction is coherent/elastic, the initial and final wavevectors are equal in magnitude even though they differ in direction. Since $|\mathbf{k}_{final}| = |\mathbf{k}_{init}| = 2\pi/\lambda$, the wavevectors can be thought of as radii of the Ewald sphere as seen in Figure 1.9, and their difference,

$$\mathbf{Q} = \mathbf{k}_{init} - \mathbf{k}_{final} \qquad \text{Eq. 1.6}$$

is known as the scattering vector, $\mathbf{Q}$. As Figure 1.9 shows, when a particular $\mathbf{d}^*_{hkl}$ touches the Ewald sphere, $\mathbf{Q} = 2\pi\mathbf{d}^*_{hkl} = 2\pi(h\mathbf{a}^* + k\mathbf{b}^* + l\mathbf{c}^*)$ and $|\mathbf{Q}| = 2\pi/\mathrm{d}_{hkl}$, thus reciprocal space is often referred to as Q-space.

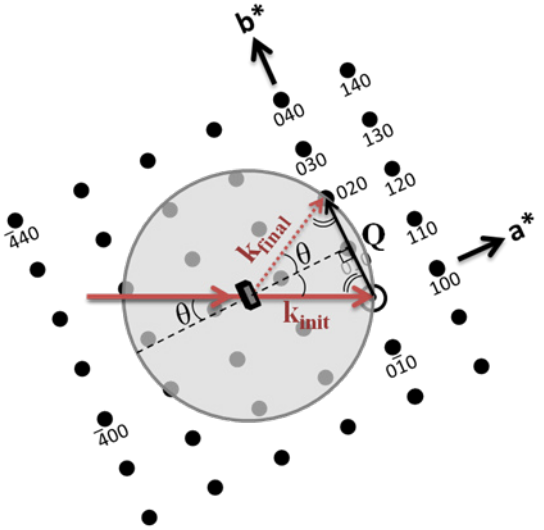

Figure 1.9 The initial and final wavevectors ($\mathbf{k}_{init}$ and $\mathbf{k}_{final}$) of a diffracted beam can be placed as radii of the Ewald sphere. With the (020) planes diffracting as shown here, the scattering vector $\mathbf{Q}$ (which is $\mathbf{k}_{initial} - \mathbf{k}_{final}$) clearly equals: $\mathbf{Q} = 2\pi(0\mathbf{a}^* + 2\mathbf{b}^* + 0\mathbf{c}^*) = 2\pi\mathbf{d}^*_{020} = 2\pi/\mathrm{d}_{020}$

The intensity of the scattered wave in Eq. 1.5 will be related to its flux density, which is proportional to the square of its vector's magnitude, or $|\varphi_{final}|^2$.[40] Because the magnitude of the vector is simply its length, the intensity of the scattered wave is proportional to the square of the amplitude, or $|A|^2$. The amplitude of the scattered wave depends on both the identities and relative positions of all the atoms in the unit cell. To arrive at an expression for A, let us first consider the scattering from one atom, i, whose position relative to the origin of the unit cell is

$$\mathbf{r}_i = x_i\mathbf{a} + y_i\mathbf{b} + z_i\mathbf{c} \qquad \text{Eq. 1.7}$$

The wave scattered by atom i at position $\mathbf{r}_i$ (in the direction of $\mathbf{k}_{final}$) can be described by

$$\varphi_{final}(\mathbf{r}_i) = A_i e^{i\mathbf{k}_{final}\mathbf{r}_i} \quad \text{Eq. 1.8}$$

This scattered wave can be related to the incident wave by a change in amplitude as follows:

$$\varphi_{final}(\mathbf{r}_i) = B_i \varphi_{init}(\mathbf{r}_i) \quad \text{Eq. 1.9}$$

$$A_i e^{i\mathbf{k}_{final}\mathbf{r}_i} = B_i e^{i\mathbf{k}_{init}\mathbf{r}_i} \quad \text{Eq. 1.10}$$

The amplitude of the scattered wave is thus

$$A_i = B_i e^{-i[(\mathbf{k}_{final}-\mathbf{k}_{init})\cdot\mathbf{r}_i]} \quad \text{Eq. 1.11}$$

$$A_i = B_i e^{i[\mathbf{Q}\cdot\mathbf{r}_i]} \quad \text{Eq. 1.12}$$

The change in amplitude from the incident wave, B_i, depends on the scattering strength of atom i; heavier elements have larger electron clouds and thus scatter X-rays more strongly, so B_i is proportional to atomic number. However, because the size of atoms (and not just their spacing in a crystal) is comparable to the wavelength of X-rays, scattering from different regions of the electron cloud on each atom gives rise to interference effects, and these effects change according to the angle of the diffraction (θ) and the wavelength of light (λ). Based on the distribution of electrons surrounding each element (calculated via quantum computational methods for approximating the wavefunctions of elements heavier than hydrogen), the scattering strength of all types of atoms can be calculated as a function of $(\sin\theta)/\lambda$. The resulting functions, which are called atomic scattering factors or sometimes form factors and which are designated as f_0, have been tabulated for each element. Substituting the atomic scattering factor (f_i) for B_i, Eq. 1.12 becomes

$$A_i = f_i e^{i[\mathbf{Q}\cdot\mathbf{r}_i]} \quad \text{Eq. 1.13}$$

The amplitude of the wave scattered by atom i is thus itself a vector in the complex coordinate system, with an amplitude (f_i) determined by the atom's scattering strength and with a phase ($i\mathbf{Q}\cdot\mathbf{r}_i$, typically denoted ϕ) determined by the atom's position. The amplitudes from

each atom in the unit cell can be represented by a vector equation such as that in Eq. 13. As Figure 1.10 then shows, the total amplitude, A, of the wave scattered from the entire unit cell can thus be represented as the vector sum of the individual scattering amplitude vectors from each atom in the unit cell, or

$$A = \sum_i f_i e^{i[\mathbf{Q}\cdot\mathbf{r}_i]} = F(\mathbf{Q}) \qquad \text{Eq. 1.14}$$

This expression for the amplitude of the scattered wave is usually designated $F(\mathbf{Q})$. Substituting the values of $\mathbf{Q}$ and $\mathbf{r}_i$ (defined above) into $F(\mathbf{Q})$

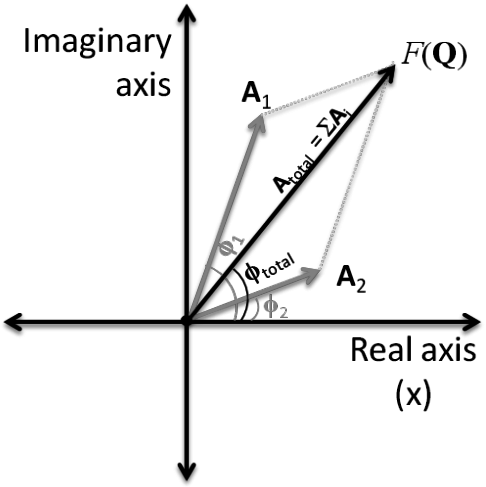

Figure 1.10 The amplitude, $\mathbf{A}_i = f_i e^{-i\phi}$, of the scattered waves from each atom, i, in the unit cell can be represented as a complex vector with phase $\phi_i = i\mathbf{Q}\cdot\mathbf{r}_i$ and amplitude f_i. The sum of these vectors equals $F(\mathbf{Q})$, the scattering factor.

$$F(\mathbf{Q}) = \sum_i f_i e^{i[2\pi(h\mathbf{a}^*+k\mathbf{b}^*+l\mathbf{c}^*)\cdot(x_i\mathbf{a}+y_i\mathbf{b}+z_i\mathbf{c})]} \qquad \text{Eq. 1.15}$$

which for an orthogonal system, will simplify to

$$F(\mathbf{Q}) = \sum_i f_i e^{i[2\pi(hx_i+ky_i+lz_i)]} \qquad \text{Eq. 1.16}$$

we see that $F(\mathbf{Q})$—the amplitude of the diffracted wave from each unit cell—can be calculated for any set of *hkl* planes using only the positions (x_i, y_i, z_i) and identities (f_i) of the atoms in the unit cell. To obtain the amplitude of the diffracted wave for the entire crystal, we sum $F(\mathbf{Q})$ from each unit cell j (whose origin is related to the origin of the crystal by the vector $\mathbf{U}_j$) as follows:

$$\sum_j \sum_i f_i e^{i[\mathbf{Q}\cdot(\mathbf{r}_i+\mathbf{U}_j)]} = \sum_j e^{i[\mathbf{Q}\cdot\mathbf{U}_j]} \sum_i f_i e^{i[\mathbf{Q}\cdot\mathbf{r}_i]} = L(\mathbf{Q})F(\mathbf{Q}) \qquad \text{Eq. 1.17}$$

The amplitude of the diffracted wave from the entire crystal is thus the product of $F(\mathbf{Q})$ with $L(\mathbf{Q})$, a sum describing a discrete lattice of points with identical amplitudes. This is the physical origin of the reciprocal lattice. The $F(\mathbf{Q})$ factor modulates this lattice by an envelope, giving the points in the reciprocal lattice different amplitudes. Because the value of $F(\mathbf{Q})$ is determined solely by the unit cell's structure, $F(\mathbf{Q})$ is referred to as the structure factor.

The measured intensity of a diffracted X-ray wave (each spot in Figure 1.8) is thus equal to the square of the wave's amplitude, $|F(\mathbf{Q})|^2$. As the previous paragraph implies, it is relatively simple to calculate $|F(\mathbf{Q})|^2$ for a known structure and compare it to experimental values. However, it is *not* trivial to deduce the $F(\mathbf{Q})$ for an unknown structure from experimental $|F(\mathbf{Q})|^2$ values. As Figure 1.10 illustrates, $F(\mathbf{Q})$ is itself a vector in the complex coordinate system, and this means that only its magnitude, $|F(\mathbf{Q})|$, is recorded in the intensity of the diffracted beam; the phase of the $F(\mathbf{Q})$ vectors (diffraction spots) in Figure 1.8 is lost, without which the real space lattice cannot be constructed. This is the infamous 'phase problem' of crystallography. Over the years, however, a suite of clever tricks (direct methods, Patterson methods, etc.) have been developed to infer the phases of the reflections. With the help of modern computers, the process of detecting/constructing the reciprocal lattice, assigning phases to each reflection, and solving the real space structure has become tenable for even highly complex structures such as proteins.

Crystallographic analysis of a well-ordered crystal roughly 100-500 μm in size (termed a 'single crystal') can thereby reveal the location of each atom in the crystal structure—invaluable information for explaining or predicting a material's properties. Unfortunately, many (if not most) materials cannot be grown as single crystals; rather, they exist as powders, which are mixtures of a myriad of small crystallites oriented in all possible directions. By definition, nanoparticles are too small to be single crystals and are thus inevitably powders. When a powder is placed in an X-ray beam, diffraction still only occurs at the characteristic Bragg angles (θ) of the *hkl* planes, but because the crystallites (and their reciprocal lattices) are oriented in all directions, the $\mathbf{d}^*_{hkl}$ vectors (reciprocal lattice points) touching the Ewald sphere are oriented in all directions, creating an annulus as Figure 1.11a shows.[39] The diffracted beams from the

various crystallites project outward through this annulus, and as the myriad diffraction spots blur together, this creates a cone of diffracted intensity at each of the Bragg angles (Figure 1.11b).

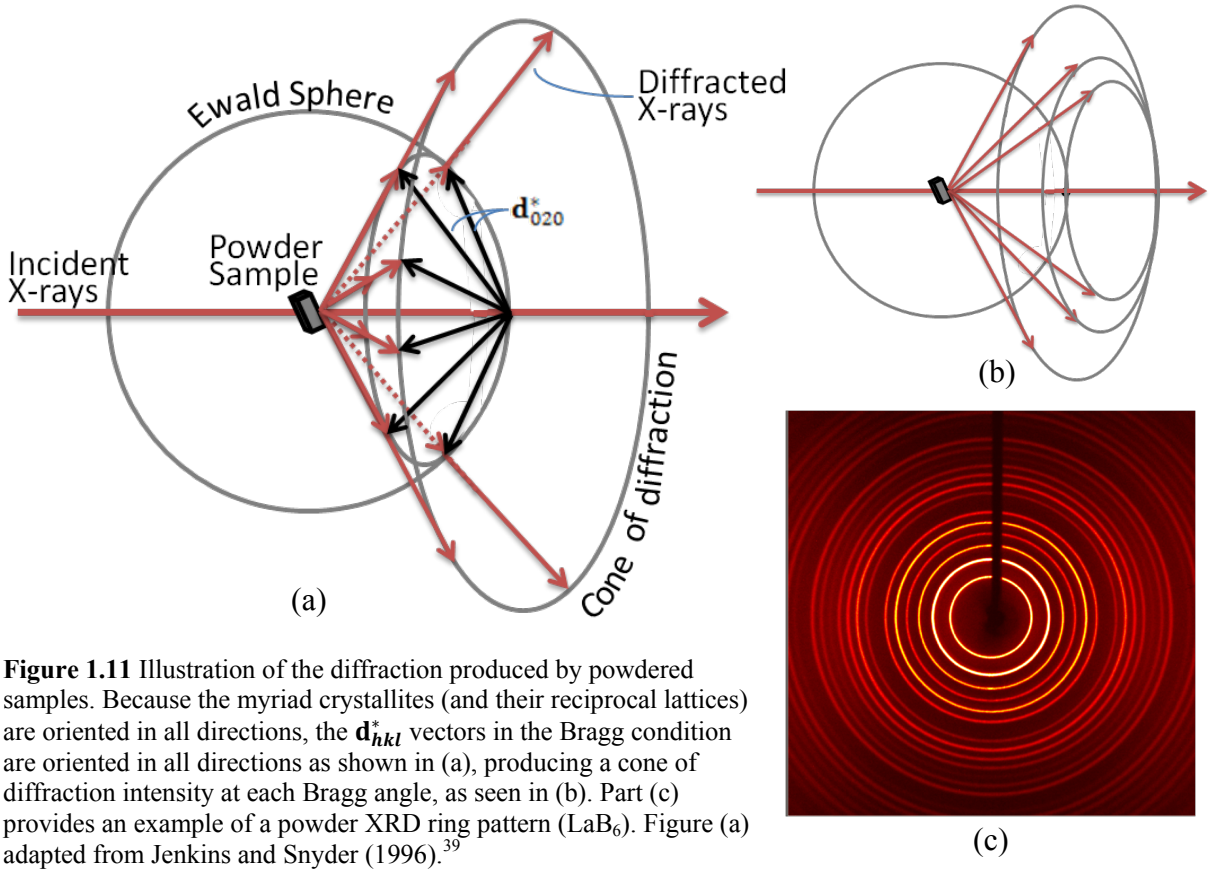

Figure 1.11 Illustration of the diffraction produced by powdered samples. Because the myriad crystallites (and their reciprocal lattices) are oriented in all directions, the $\mathbf{d}^*_{hkl}$ vectors in the Bragg condition are oriented in all directions as shown in (a), producing a cone of diffraction intensity at each Bragg angle, as seen in (b). Part (c) provides an example of a powder XRD ring pattern (LaB_6). Figure (a) adapted from Jenkins and Snyder (1996).[39]

The diffraction pattern of a powder is thus a set of concentric cones which appear as rings on a two dimensional detector, as Figure 1.11c shows. The intensity of each ring can be integrated and plotted as a function of the scattering angle θ (or, more often, 2θ), giving a two-dimensional diffraction pattern (see Figure 1.12). The powder XRD pattern for every compound is unique. Thus, somewhat like a fingerprint, a material can be identified by matching its powder XRD pattern to that of a known material. Large databases of powder XRD patterns now exist for this purpose.

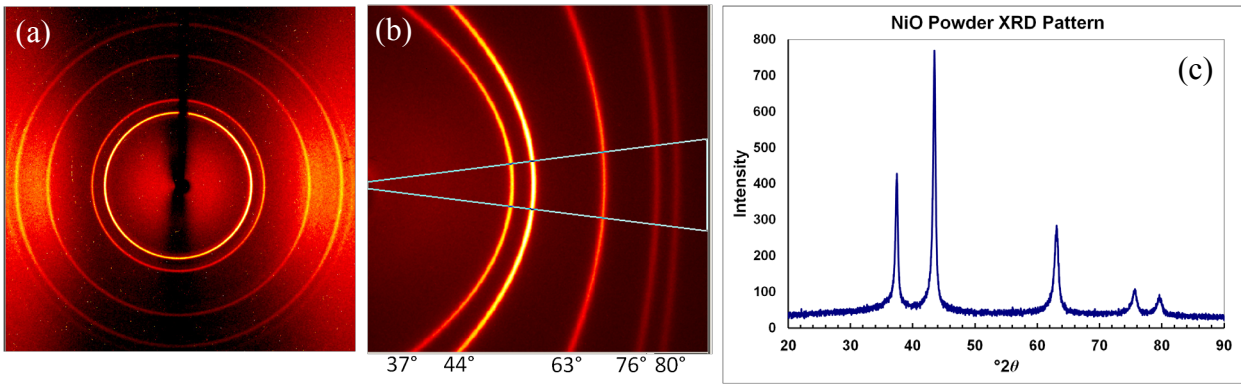

Figure 1.12 (a) Powder XRD ring pattern for 24nm NiO nanoparticles. A slice of the rings can be integrated as shown in (b) to give the 2-dimensional XRD pattern shown in (c).

Quantitative analysis of powder XRD patterns is also possible. Rietveld refinement, developed by Hugo Rietveld in 1969,[41] can glean from powder patterns nearly the same comprehensive structural parameters attainable from single crystal analysis. However, the method is not easily applied to unknown materials because the crystal structure must be known or at least closely approximated in the beginning; using a good, initial structural model, the angles and intensities of the Bragg reflections are calculated via the Bragg equation and the structure factor. Gaussian and/or Lorenztian functions are used to model peak broadening originating from both the instrument and the sample. The thermal motion of the atoms (which also broadens the peak shape) is modeled using elliptical equations centered at the location of each atom. Using these and other parameters, the XRD pattern of the model structure is calculated and compared with the experimental data. A process of least-squares refinement is then used to optimize the model's structural parameters against the experimental data until the patterns match reasonably well.

Unfortunately, Rietveld refinement is not particularly well suited for nanomaterials. The small sizes of the crystallite affects the powder XRD pattern in ways that are (currently) not well-accounted for in Rietveld refinement. To understand the size effect, it is useful to examine the interference effects of the one-dimensional lattice illustrated in Figure 1.13.[42] In Figure

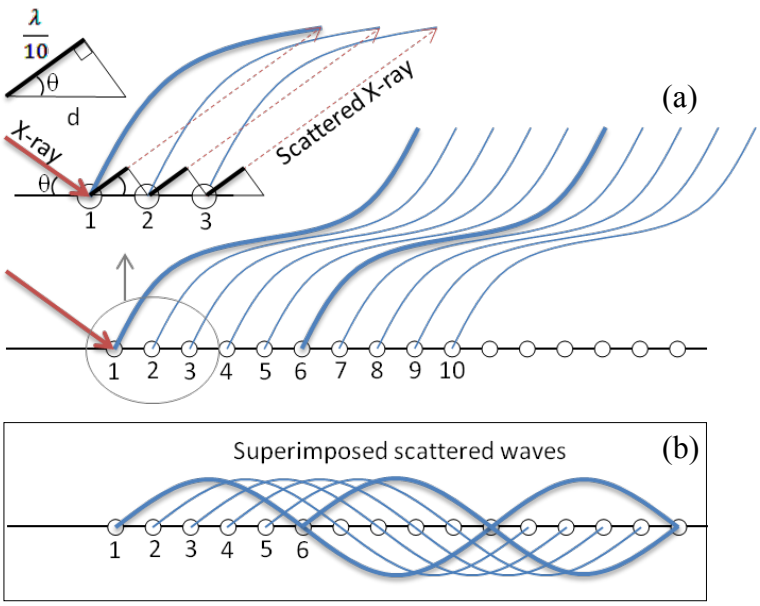

Figure 1.13 Illustration of the scattered X-ray waves from a one-dimensional lattice with spacing *d*. (a) Here, the θ angle is such that the path difference between adjacent scattered waves is λ/10, causing waves 1 and 6, 2 and 7, 3 and 8, 4 and 9, and 5 and 10 to destructively interfere. The scattered waves are superimposed in (b) to make the destructive interference between waves 1 and 6 more apparent. Figure adapted from Massa (2004).[42]

1.13a, the angle of the incident light is off the Bragg angle enough that a phase difference of λ/10 exists between waves scattered by neighboring points. The phase differences become more obvious if the waves are superimposed, as they are in Figure 1.13b. As can be seen from the figure, the slight phase difference between the waves from points 1 and 2 would cause the intensity of the resultant wave to be only slightly reduced, but as further points are considered, the phase difference increases until at point 6 it reaches a value of λ/2. Waves 1 and 6 are thus completely out of phase and completely destructively interfere, as do waves 2 and 7, 3 and 8, 4 and 9, and 5 and 10. Ten lattice points are therefore required to cause complete destructive interference when a λ/10 phase difference exists between neighboring scatterers. Similarly, 100 lattice points would be required where the phase difference is λ/100. More and more lattice points are thus required for complete destructive interference to occur as the Bragg angle approaches.

For large crystallites with vast numbers of unit cells in every direction, constructive interference essentially only occurs at the precisely defined Bragg angles, producing sharp peaks in the diffraction patterns. However, nanoparticles may only have a few unit cells in each direction, so the destructive interference is incomplete at angles near the Bragg angles. The

smaller the crystallites, the larger the range of angles surrounding the Bragg angles at which intensity is observed as Figure 1.14 shows.

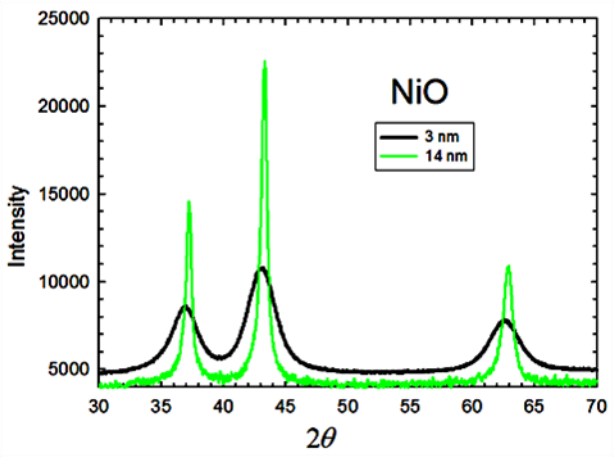

Figure 1.14 XRD patterns for NiO nanoparticles 3nm (black) and 14 nm (green) in diameter which illustrate the extreme size-related peak broadening effects seen in nanoparticles.

Nanoparticle XRD patterns thus have very broad peaks. The breadth provides too much 'wiggle room' for the unit cell, atom position, and other parameters during Rietveld refinement, often resulting in ambiguous or non-unique refinements unless substantial constraints/restraints are applied (somewhat defeating the purpose of the refinement). The broad peaks can also lead to unreasonable values for parameters such as thermal ellipsoids that influence the decrease in intensity as Q increases (at higher 2θ values).

A positive consequence of the peak broadening in nanoparticles is that the average crystallite size and shape[ii] can be estimated by applying the Scherrer formula,[43]

$$d = \frac{0.9\lambda}{w \cdot \cos(\theta)} \qquad \text{Eq. 1.18}$$

to each peak where d is the crystallite diameter, λ is the wavelength of the incident X-rays, w is the peak width at half of the maximum height (in radians), and θ is the angle of that particular reflection. The simple Scherrer formula provides fast and reasonably accurate (5-10%) size estimates as the crystallite size approaches a few (or a few tens) of nanometers where the size-related peak broadening effects dominate the instrumental broadening effects, as Figure 1.15 illustrates.

[ii] The size calculated from each peak reveals the coherence length in the particular crystal direction responsible for that diffraction intensity. Thus, applying the Scherrer formula to each peak can give an idea of the crystal length in each direction thereby revealing the shape. If the particles are spherical, the size calculated from each peak will be roughly the same and can be averaged to obtain the average diameter of the particles.

X-ray synchrotron and neutron radiation facilities have spurred the development of other tools for analyzing powder diffraction data, opening new possibilities for quantitatively determining the crystal structure of nanomaterials. One such technique, called pair distribution function analysis, is gaining popularity for nanostructure studies.[44] A number of helpful reviews are available;[40,44-59] a brief summary of PDF theory and its application is given below.

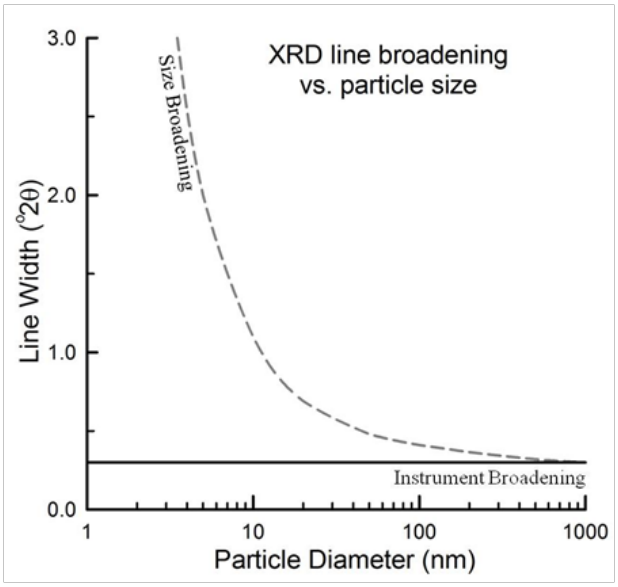

Figure 1.15 Comparison of instrumental and particle size line broadening effects as a function of particle size.[39]

1.2.1.1 PDF Analysis

Another way to think about a crystal structure is as a large number of atoms situated at positions $\mathbf{r}_m$ with respect to some origin. Mathematically, this amounts to a set of delta functions $\delta(\mathbf{r}-\mathbf{r}_m)$. The scattering density, $\rho(\mathbf{r})$, of the crystal is then

$$\rho(\mathbf{r}) = \sum_m f_m \delta(\mathbf{r}-\mathbf{r}_m) \qquad \text{Eq. 1.19}$$

where $\mathbf{r}_m$ and f_m are the position and scattering strength of atom m. The structure factor can then be written in terms of $\rho(\mathbf{r})$ as

$$F(\mathbf{Q}) = \sum_m f_m e^{i\mathbf{Q}\cdot\mathbf{r}} = \int e^{i\mathbf{Q}\cdot\mathbf{r}} \rho(\mathbf{r})\, d \qquad \text{Eq. 1.20}$$

and the observed intensity, $|F(\mathbf{Q})|^2$, can also be written in terms of $\rho(\mathbf{r})$ as

$$S(\mathbf{Q}) = \frac{1}{N}|F(\mathbf{Q})|^2 = \frac{1}{N}\iint \rho(\mathbf{r})\rho(\mathbf{r}')\, e^{i\mathbf{Q}\cdot(\mathbf{r}-\mathbf{r}')} d\mathbf{r} d\mathbf{r}' \qquad \text{Eq. 1.21}$$

where $S(\mathbf{Q})$ is often referred to as the structure function.[40]

As Eq. 1.20 shows, the structure factor, $F(\mathbf{Q})$, is the Fourier transform (from real space, $\mathbf{r}$, to reciprocal space, $\mathbf{Q}$) of the real-space scattering density. As Eq. 1.21 shows, the observed intensity, $S(\mathbf{Q})$ or structure function, is also a Fourier transform. To better understand its functional relationship to real space, we can Fourier transform $S(\mathbf{Q})$ into a real space function, $P(\mathbf{R})$, as follows[40]

$$P(\mathbf{R}) = \frac{1}{(2\pi)^3}\int S(\mathbf{Q})e^{i\mathbf{Q}\cdot\mathbf{R}}d\mathbf{Q} \qquad \text{Eq. 1.22}$$

$$= \frac{1}{8\pi^3 N}\iiint \rho(\mathbf{r})\rho(\mathbf{r}')e^{i\mathbf{Q}\cdot(\mathbf{r}-\mathbf{r}'+\mathbf{R})}d\mathbf{r}d\mathbf{r}'d\mathbf{Q} \qquad \text{Eq. 1.23}$$

Because $\int e^{i\mathbf{Q}\cdot(\mathbf{r}-\mathbf{r}'+\mathbf{R})}d\mathbf{Q}$ is equivalent to the delta function $\delta(\mathbf{r}-\mathbf{r}'+\mathbf{R})$, this equals

$$= \frac{1}{N}\iint \rho(\mathbf{r})\rho(\mathbf{r}')\delta(\mathbf{r}-\mathbf{r}'+\mathbf{R})d\mathbf{r}d\mathbf{r}' \qquad \text{Eq. 1.24}$$

$$= \frac{1}{N}\int \rho(\mathbf{r})\rho(\mathbf{r}+\mathbf{R})d\mathbf{r} \qquad \text{Eq. 1.25}$$

$$= \rho_0 g(\mathbf{R}) \qquad \text{Eq. 1.26}$$

where N is the number of atoms in the system, ρ_0 is the average density of atoms in the system, and $g(\mathbf{R})$ is the *atomic pair distribution function*, whose statistical mechanical definition is

$$g(\mathbf{R}) = \frac{1}{N_a N_b}\sum_{\gamma=1}^{N_a}\sum_{\mu=1}^{N_b}\delta\left(r - R_{\gamma\mu}\right), \qquad \text{Eq. 1.27}$$

a function that describes the distribution (or frequency of occurrence) of interatomic distances, $R_{\gamma\mu} = |\mathbf{r}_\gamma - \mathbf{r}_\mu|$, between all pairs of atoms ν and μ in a material consisting of N atoms. The function $g(\mathbf{R})$ is somewhat like a probability function in that it gives the likelihood that any randomly chosen pair of atoms in the sample will be separated by a distance R.

The Fourier transform of the observed intensity, $S(\mathbf{Q})$, in a diffraction experiment is thus directly related to $g(\mathbf{R})$, the pair distribution function. This relationship suggests an alternate way of analyzing XRD data; the two-dimensional powder diffraction pattern can be Fourier transformed into the real space pair distribution function (PDF) which can then be compared to

the PDF of a refinable structural model. But first, because both $S(\mathbf{Q})$ and $g(\mathbf{R})$ are isotropic for powders, angular variables can be integrated out of the expression for $\rho_0 g(\mathbf{R})$:

$$\rho_0 g(R) = \frac{1}{8\pi^3} \iiint S(Q) e^{iQR\cos\theta} d\cos\theta \, d\phi Q^2 dQ \qquad \text{Eq. 1.28}$$

$$= \frac{1}{4\pi^2} \int_0^{\infty} \int_0^{\pi} S(Q) e^{iQR\cos\theta} d\cos\theta \, Q^2 dQ \qquad \text{Eq. 1.29}$$

$$= \frac{1}{2\pi^2} \int_0^{\infty} S(Q) \frac{\sin(QR)}{QR} Q^2 dQ \qquad \text{Eq. 1.30}$$

In practice, the integral must be terminated at a finite value[iii] of Q as follows

$$= \frac{1}{2\pi^2 R} \int_0^{Q_{max}} S(Q) \sin(QR) \, Q \, dQ \qquad \text{Eq. 1.31}$$

but because $S(Q)$ approaches unity at large Q values, this integral oscillates wildly as a function of Q_{max}. To avoid this issue, unity can be subtracted from $S(Q)$, giving the standard expression (with R replaced by r) for the *reduced* atomic pair distribution function, $G(r)$,

$$G(r) = 4\pi r \rho_0 [g(r) - 1] = \frac{2}{\pi} \int_0^{Q_{max}} [S(Q) - 1] \sin(Qr) \, Q \, dQ. \qquad \text{Eq. 1.32}$$

$G(r)$ is the function commonly referred to as the experimental PDF. The functions $\rho(r)$, $g(r)$, and $G(r)$ for an amorphous material are shown in Figure 1.16 a-c. As the figures show, the practice of subtracting unity simply subtracts the contribution of the average continuum from $g(r)$ so that $G(r)$ oscillates about 0 instead of 1; all of the information in $g(r)$ is retained in $G(r)$, and they can be interpreted in precisely the same manner. As Figure 1.16d illustrates, at low r, the interatomic distances are on the order of bond lengths, and the distances with high probability (the peaks) represent actual bonds; at higher r, the peaks simply represent common interatomic distances. The total area under each peak is determined both by the concentration of that interatomic distance in the sample and by the scattering factors of the atoms involved. The width

[iii] Due to the Fourier transform relationship between the scattering data and $G(r)$, scattering data should be collected in as far a range of reciprocal, or Q, space (or to as high a value of 2θ) as possible; short Q ranges in reciprocal space result in low resolution in real space after the transform.

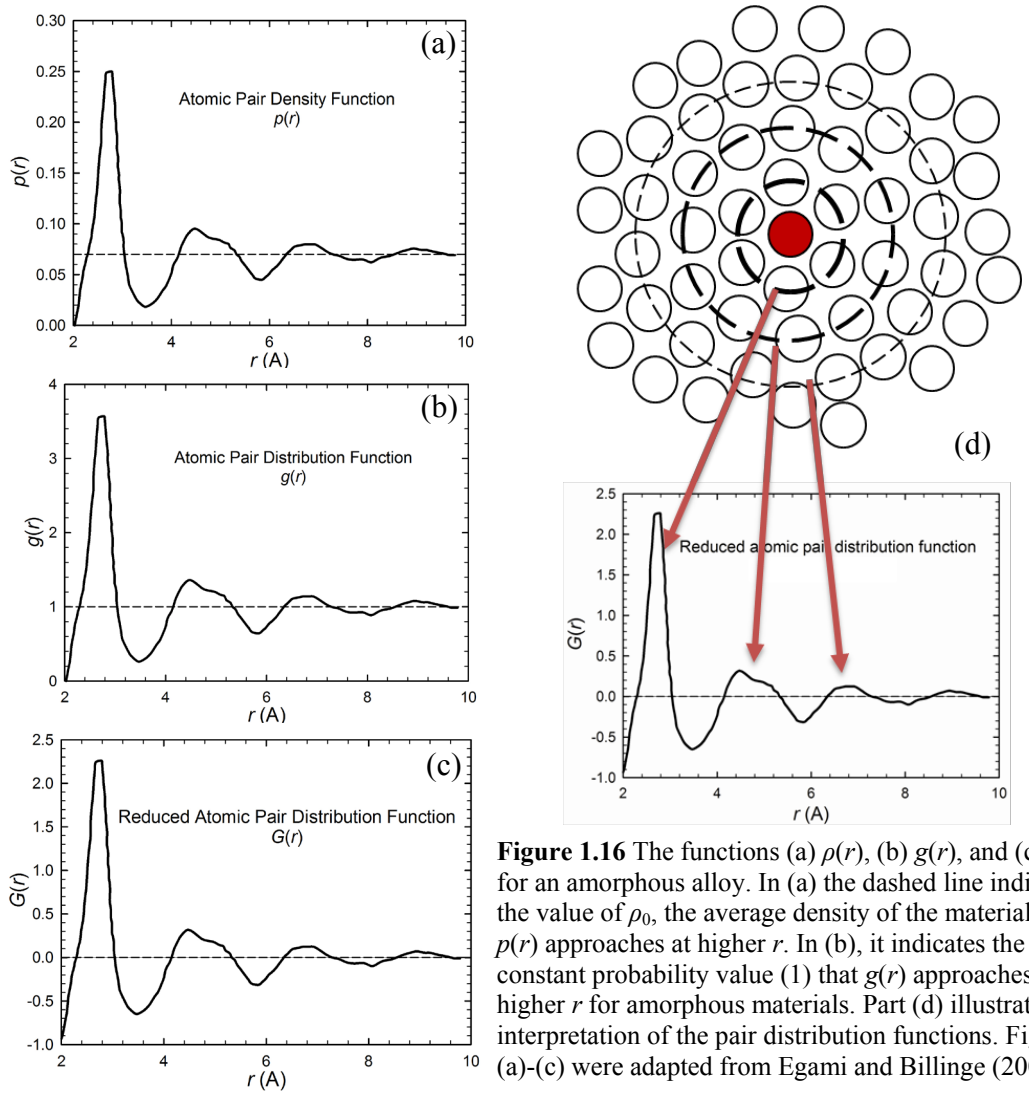

Figure 1.16 The functions (a) $\rho(r)$, (b) $g(r)$, and (c) $G(r)$ for an amorphous alloy. In (a) the dashed line indicates the value of ρ_0, the average density of the material, which $p(r)$ approaches at higher r. In (b), it indicates the constant probability value (1) that $g(r)$ approaches at higher r for amorphous materials. Part (d) illustrates the interpretation of the pair distribution functions. Figures (a)-(c) were adapted from Egami and Billinge (2003).[40]

of each peak indicates the degree of variation in the bond length due to either thermal vibration or inherent structural disorder.

Because $G(r)$ and $g(r)$ describe interatomic distances in the range ~1-30 Å, these functions are said to reveal the 'local structure,' or the structure of the material on the order of bond lengths. This range is ideal for nanoparticles. In fact, because the maximum r value at which peaks still occur in the PDF loosely corresponds to the coherence length (the length through which an ordered structure exists), the PDF provides an indication of the crystallite size for nanoparticles which are only a few nanometers in diameter, as Figure 1.17 illustrates.

The Fourier relationship between $S(Q)$ and the PDF has been known for most of the last century; X-ray scattering amplitudes were being related to structural parameters as early as 1915,[60] and in 1927, Zernire and Prins[61] demonstrated the relationship between the scattering of X-rays by liquids and the (isotropically averaged) atomic pair distribution function. In 1930, Debye and Menke[62] further developed the approach as they applied it to study the structure of liquid mercury. However, the technique was not widely used until the last two decades primarily for two reasons: 1) the complex computations required made PDF analysis a rather long, tedious, and formidable process until modern computers were developed, and 2) laboratory X-ray instrumentation can probe only very short Q ranges, providing poor resolution in the real space PDF; as Figure 1.18 shows,[63] the ~8 $Å^{-1}$ range of Q values attainable by common laboratory Cu radiation (λ = 1.54 Å) is insufficient to resolve the

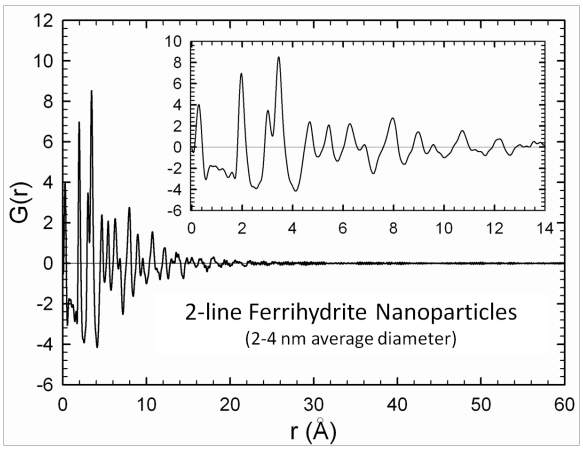

Figure 1.17 PDF of 2-line ferrihydrite nanoparticles. The damping of the PDF beyond 20Å confirms the 2-4 nm average diameter of the nanoparticles.

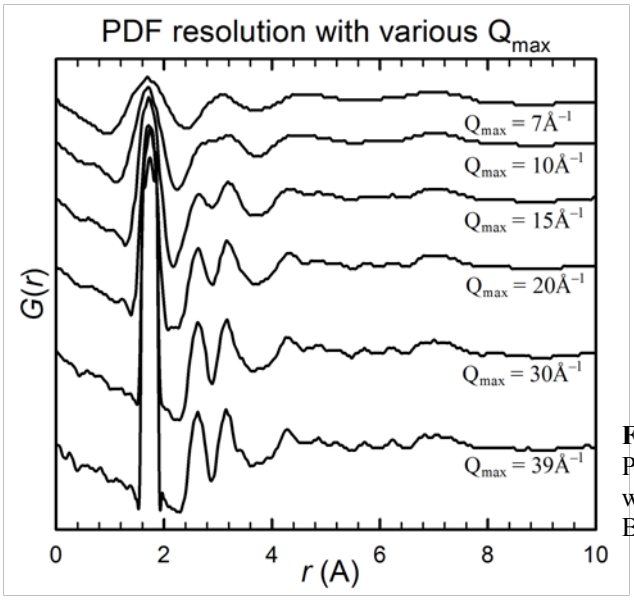

Figure 1.18 The effect of Q_{max} on the PDF, $G(r)$, of an As_4O_6 molecule. Figure was adapted from that presented by Benmore (2009).[63]

Table 1.1 Q_{max} values for common X-ray radiation sources.

X-ray Source	Q_{max}
Cu (λ = 1.54Å)	8 Å
Mo (λ = 0.71Å)	17 Å
Ag (λ = 0.56Å)	24 Å
Synchrotron ()	30-40 Å

peaks, and large artifact "wiggles" are difficult to distinguish from the real data. This made PDF analysis very complicated, unreliable, and therefore unpopular for many decades. Only since the advent of X-ray sources with higher Q ranges than Cu (see Table 1.1) and the development of powerful computers has PDF analysis become practical and widely applicable.

As with XRD patterns, the PDF can be quantitatively analyzed to reveal the atomic structure of a material. 'PDF analysis' consists of four conceptually simple steps: 1) a plausible structural model of the sample is concocted, 2) the PDF for this model is calculated, 3) the calculated and experimental PDFs are compared, and 4) the model is adjusted so that its PDF better reproduces the experimental PDF. These steps are repeated until the PDF of the model matches that of the experimental data within a reasonable margin of error.

In practice, there are two main approaches for accomplishing these steps. One approach involves big-box models of entire nanoparticles whose PDFs are optimized by moving atom positions via Monte Carlo simulations. The more common approach involves small-box models and the use of least squares refinement programs such as PDFfit2 (formerly PDFFIT).[53,64] As in Rietveld refinement; an initial structural model is generated, and the parameters of the structural model (such as unit cell constants, atomic coordinates, site occupancies, and thermal factors, to name a few) are adjusted in an iterative process so that a reliability factor, *R*, given by

$$R = \sqrt{\left\{ \sum_{i=1}^{N} [G_{\exp}(r_i) - G_{calc}(r_i)]^2 \Big/ \sum_{i=1}^{N} [G_{\exp}(r_i)]^2 \right\}} \qquad \text{Eq. 1.33}$$

in PDF analyses, is minimized.[65] *R*-values of 10% are excellent for PDF refinements;[66] good refinements can have *R*-values as high as 20-30%.[40]

Because of the similarity of these steps to the Rietveld procedure, PDF analysis is often referred to as 'real-space Rietveld.' However, there are other key differences besides the fact that PDF refinements are performed in real space instead of reciprocal space. First, because the entire

XRD pattern is Fourier transformed, PDF analysis utilizes both Bragg and diffuse scattering data instead of only the Bragg reflections used in Rietveld analyses. This is why PDF analyses are called 'total scattering analyses' and is why they are advantageous in studying the broad/diffuse nanoparticle XRD patterns. Also unlike Rietveld analyses, PDF analyses can refine structural models without the use of long-range symmetry constraints, making the technique applicable for amorphous as well as crystalline materials.

Being somewhat younger than Rietveld analysis, the software available for PDF analysis is not as sophisticated; constraints and restraints cannot be applied to keep the parameters physically reasonable, and bond distances and angles of the refined structures are not as readily checked. Thus, one must be very careful to avoid unphysical refinements.

Because of the uniquely wide range of local structure (1-30 nm) probed, PDF analysis can be used to obtain quantitative atomic structure information for the entire nanoparticle (or a large fraction of it) and not just a few coordination shells of a specific element, as will be the case for the XAFS and NMR methods. PDF analysis is also highly useful for studying local structure in amorphous materials as well as bulk materials; PDF analysis of bulk materials can reveal distortions in the local structure that are undetectable in the average, long-range structure probed by Rietveld analysis.

1.2.2 X-ray absorption Fine Structure (XAFS) Spectroscopy

X-ray Absorption Fine Structure, or XAFS, spectroscopy harnesses the X-ray photoelectric effect and the wave nature of the electron to glean information about the formal oxidation state and local coordination environment of one particular type of atom in a sample.[67-69] Numerous books and reviews on the theory and equations are available;[68-77] this section provides a brief summary.

X-ray radiation has energy of the same order of magnitude as the binding energy of core electrons (1s, 2s, 2p, etc.). When the energy of an incident X-ray photon exactly matches the binding energy (E_0) of a particular core electron, the photon can be absorbed, enabling the electron to transition to a higher-energy, unfilled orbital of appropriate symmetry (see Table 1.2). This causes a dramatic increase in X-ray absorption (and a corresponding decrease in the X-ray transmission) at each binding energy, creating what are called absorption edges (Figure 1.19). Because of the unique nuclear structure of each element, the binding energies and corresponding X-ray absorption edges are element-specific. The chart below details the initial and final states of the most commonly probed transitions, or edges, in XAFS spectroscopy.

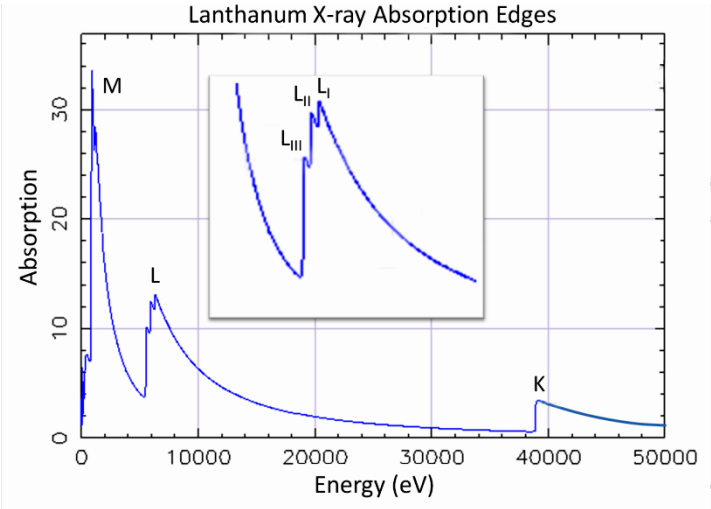

Figure 1.19 Absorption edges (K, L, M) of an isolated atom of lanthanum. The insert highlights the L_I, L_{II}, and L_{III} edges.

Table 1.2 Initial and final states of the most commonly probed transitions in XAFS analyses as required by the selection rules for discrete transitions [$\Delta J = 0, \pm 1$ (except $0 \leftrightarrow 0$) and $\Delta M = 0, \pm 1$ (except $0 \leftrightarrow 0$ when $\Delta J = 0$)].

Edge	Initial State	Final State
K edge	1*s* orbital (n=1, l=0, m=0)	*p* orbital
L_1 edge	2*s* orbital (n=2, l=0, m=0)	*p* orbital
L_2 edge	2*p* orbital (n=2, l=1) (j=½)	*d* orbital (or *s*)
L_3 edge	2*p* orbital (n=2, l=1) (j=3/2)	*d* orbital (or *s*)

As the energy (E) of the incident X-ray beam exceeds the binding energy (E_0), the excess energy is transferred to the electron in the form of kinetic energy:

$$(E - E_0) = \frac{1}{2}mv^2 = \frac{p^2}{2m} = \frac{\hbar^2 k^2}{2m} \qquad \text{Eq. 1.34}$$

Due to the dual wave/particle nature of matter, the ejected photoelectron can be treated as though it propagates from the absorbing atom as a spherical wave whose wavelength is given by the de Broglie relation[76]

$$\lambda = \frac{2\pi}{k} = \frac{2\pi}{\sqrt{\frac{2m}{\hbar^2}(E-E_0)}} \qquad \text{Eq. 1.35}$$

The electron densities of the neighboring atoms can scatter this photoelectron wave. Based on both the photoelectron's wavelength and the distances to the neighboring atoms (i.e. the local structure), the backscattered wave will interfere constructively or destructively with the outgoing wave, thereby enhancing or reducing the total amplitude of the final wavefunction of the photoelectron. Because the probability of absorption is determined by the matrix element between the initial and final state wavefunctions of the photoelectron as follows,

$$| < \psi_f | \hat{\epsilon} \cdot \vec{r} e^{i\vec{k}\vec{r}} | \psi_i > |^2 \qquad \text{Eq. 1.36}$$

the absorption probability is also modified. Thus, as the energy of the X-rays (and thus the photoelectron) increases beyond E_0, the local structure of the absorbing atom causes modulations/oscillations in the absorption (transmission) signal.

At energies near the absorption edge (within ~50 eV of E_0), multiple scattering events contribute significantly to the photoelectron's final state wavefunction. At higher energies, scattering of the photoelectron becomes progressively weaker, and the dominant contribution comes from single-scattering events.[52,60] An XAFS spectrum is therefore broken into two regions typically referred to as the XANES and EXAFS regions, as Figure 1.20 illustrates.[69] The EXAFS, or Extended X-ray Absorption Fine Structure, region refers to the part of the spectrum roughly 50-800 eV beyond the absorption edge. The XANES, or X-ray Absorption Near Edge Structure, region refers to the part of the spectrum lying between the absorption threshold and the onset of the EXAFS region. The point of separation between the XANES and EXAFS regions

varies between systems and is somewhat artificial, but the enhanced multiple scattering contribution in the XANES region does, in actuality, probe different structural information. The following overviews of EXAFS and XANES analyses describe the information each can provide about the absorbing atom and its local structure.

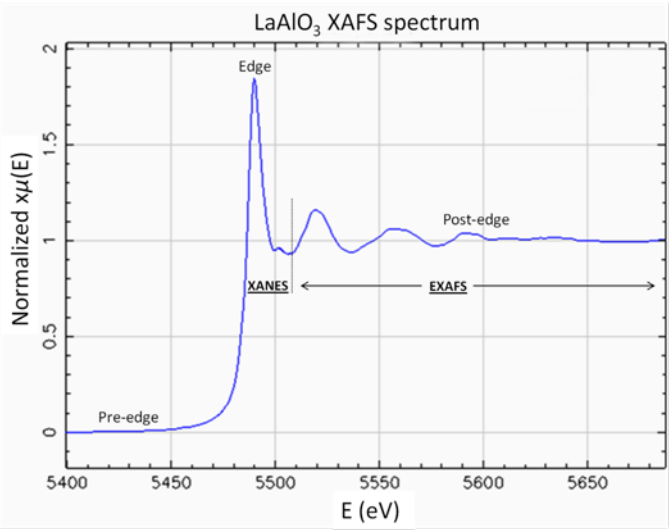

Figure 1.20 XAFS spectrum of $LaAlO_3$ with the XANES and EXAFS regions highlighted.

1.2.2.1 EXAFS

The extended fine structure in X-ray absorption spectra was recognized over 80 years ago.[78-79] The extent of its structural content, however, was not fully recognized until the mid 1970's through the work of Stern, Lytle, and Sayers,[80-82] and only through the availability of synchrotron radiation and the work of Eisenberger[83] and Kincaid[84] did EXAFS analysis become a practical tool for structural analysis.[76] There are many rigorous, quantum mechanical derivations of the theory available,[70,73,77,80-82,85-86] but the following brief heuristic derivation[70] will use the qualitative picture above to directly motivate the expression for EXAFS.

The absorption of X-rays is determined by the matrix element in Eq. 1.36 between the initial and final states of the electron. At the high energies of the EXAFS region, the final state of the photoelectron lies in the continuum of states and can thus be approximated by a plane wave that is only weakly scattered by the surrounding atoms.[70] Because the matrix element is nonzero only near the center of the absorbing atom where the core state wavefunction is nonzero, it is only necessary to determine how the surrounding atoms modify the photoelectron wave at the

center of the absorbing atom to determine an expression for the EXAFS signal. From the absorbing atom, the spherical outgoing wave is proportional to

$$\frac{e^{ikr}}{r} \qquad \text{Eq. 1.37}$$

The wave scattered by a neighboring atom at a distance of r_i is proportional to

$$\frac{e^{ik|r-r_i|}}{|r-r_i|} \qquad \text{Eq. 1.38}$$

The amplitude of the backscattered wave at r_i is thus proportional to a product of the outgoing and scattered waves

$$T_i(2k)\frac{e^{ikr_i}}{r_i}\frac{e^{ik|r-r_i|}}{|r-r_i|} \qquad \text{Eq. 1.39}$$

where $T_i(2k)$ is the backward scattering amplitude characteristic of the backscatterer at r_i. At the origin ($r = 0$), the backscattered wave has an amplitude proportional to

$$T_i(2k)\frac{e^{i2kr_i}}{r_i^2} \qquad \text{Eq. 1.40}$$

The $2kr_i$ factor is the phase shift introduced as the wave (with wave number $k = 2\pi/\lambda$) travels the distance to the neighboring atom and back to the origin again ($2r_i$). An additional phase shift of $[\delta_i(k) - (\pi/2)]$ is also necessary because the photoelectron is moving out of and into the varying potential of the absorbing atom and is also sensing the varying potential of the backscattered atom. The complex expression for the backscattered wave at the origin thus becomes

$$T_i(2k)\frac{e^{i[2kr_i+\delta_i(k)-\frac{\pi}{2}]}}{r_i^2} \qquad \text{Eq. 1.41}$$

As this backscattered wave interferes with the outgoing wave, the absorption is modulated. This modulation is, by definition, the EXAFS. Denoting the EXAFS by $\chi_i(k)$, the real part of Eq. 1.41 is

$$\chi_i(k) = K\frac{T_i(2k)}{r_i^2}\sin[2kr_i + \delta_i(k)] \qquad \text{Eq. 1.42}$$

where K is a proportionality constant. By defining

$$KT_i(2k) = \frac{m}{2\pi\hbar^2 k^2} t_i(2k) \qquad \text{Eq. 1.43}$$

the expression for $\chi_i(k)$, the EXAFS, then becomes

$$\chi_i(k) = \frac{m}{2\pi\hbar^2} t_i(2k) \frac{\sin[2kr_i + \delta_i(k)]}{(kr_i)^2} \qquad \text{Eq. 1.44}$$

Because of the high photoelectron energies in the EXAFS region, the dominant contribution to the final state wavefunction comes from paths in which the electron is scattered only once by surrounding atoms, or from single-scattering paths.[70] Thus, through a 'single-scattering' approximation, a total EXAFS equation [$\chi(k)$] which includes the effects of all the neighboring scatterers can be obtained by adding the effects of each scatterer, i, as follows

$$\chi(k) = \sum_i \frac{m}{2\pi\hbar^2} \frac{t_i(2k)}{(kr_i)^2} \sin[2kr_i + \delta_i(k)] \qquad \text{Eq. 1.45}$$

Next, the finite lifetime of the excited photoelectron should be taken into account. This can be done by adding a mean free path term, $e^{-2r/\lambda}$, that represents the probability that the photoelectron can travel to the backscattering atom and back to the origin without either the wave being further scattered by other surrounding atoms or the hole in the absorbing atom being filled. Adding this lifetime contribution to $\chi(k)$ we get

$$\chi(k) = \frac{m}{2\pi\hbar^2 k^2} \sum_i \frac{t_i(2k)}{r_i^2} e^{-2r_i/\lambda} \sin[2kr_i + \delta_i(k)] \qquad \text{Eq. 1.46}$$

This sum is over all the neighboring atoms at a distance r_i from the absorbing atom. It is useful to group atoms having similar distances and atomic numbers into "shells" by dividing the sum over like atoms that have roughly the same average distance, R_i. Then we can sum over these coordination shells instead of summing over all the atoms. However, because of thermal vibrations and structural disorder, the atoms in any coordination shell will not be at exactly the same distance from the absorbing atom, meaning that the contribution of each atom in the shell

to the interference will not be precisely in phase. Assuming this disorder is small and has a Gaussian distribution centered at R_i, each atom in the shell has a probability of deviating from the average by

$$\frac{1}{\sqrt{2\pi\sigma_i^2}} e^{-(r_i-R_i)^2/2\sigma_i^2} \quad \text{Eq. 1.47}$$

The dephasing produced by N_i atoms of type i in the shell thereby produces a factor of

$$N_i e^{-2k^2\sigma_i^2} \quad \text{Eq. 1.48}$$

where σ_i is the rms deviation from the average distance R_i. The EXAFS equation then becomes

$$\chi(k) = \frac{m}{2\pi\hbar^2 k^2} \sum_i N_i \frac{t_i(2k)}{{R_i}^2} \mathrm{e}^{-2\mathrm{R_i}/\lambda} \mathrm{e}^{-2\mathrm{k}^2\sigma_\mathrm{i}^2} \sin[2kR_i + \delta_i(k)] \quad \text{Eq. 1.49}$$

Finally, an amplitude loss factor should be included due to the many-body relaxation effect that occurs in response to the formation of the core-hole in the absorbing atom. Incorporating corrections for many-body effects, the EXAFS formula becomes

$$\chi(k) = S_0^2 \sum_i N_i \frac{|f_i(k)|}{k{R_i}^2} \mathrm{e}^{-2\mathrm{R_i}/\lambda} \mathrm{e}^{-2\mathrm{k}^2\sigma_\mathrm{i}^2} \sin[2kR_i + \delta_i(k)] \quad \text{Eq. 1.50}$$

where $f_i(k) = |f_i(k)|\, e^{i\varphi(k)}$ is the backscattering amplitude and S_0^2 is the amplitude loss factor. S_0^2 is often approximated by a constant, but it is actually weakly energy dependent.

Eq. 1.50 has become the standard EXAFS equation for much of the work done since the 1970's.[86] The EXAFS equation is thus essentially a sum of damped sine waves in which the various beats are a result of the correlations between atomic pairs. Though this pair correlation function is not the true PDF, EXAFS analysis can be thought of to some extent as being like the PDF analysis of a single type of atom in the sample; the EXAFS data, which is collected in energy space, can be Fourier transformed into k-space to obtain the experimental $\chi(k)$, and then, if a model of the absorbing atom's local structure can be generated, the $\chi(k)$ of the model can be calculated using Eq. 1.50, compared to the experimental $\chi(k)$, and refined.

In practice, the XAFS spectrum is collected as a transmission signal vs. energy. The intensity of the transmitted X-ray beam (I_T) is related to the absorption coefficient $\mu(E)$ through the Beer-Lambert Law[67-68,76,87]

$$\frac{I_T}{I_0} = e^{-\mu(E)x} \qquad \text{Eq. 1.51}$$

where I_0 is the intensity of the incident beam and x is a combination of the sample length and concentration.[iv] By normalizing to the 'background' absorption, μ_0, the EXAFS is then given by[76]

$$\chi(E) = \frac{\mu(E) - \mu_0(E)}{\mu_0(E)} \qquad \text{Eq. 1.52}$$

This $\chi(E)$ is Fourier transformed into $\chi(k)$.

In more recent years, it has become apparent that multiple scattering cannot be ignored, even in the EXAFS region. Much work has been done in the last two decades to include multiple scattering into the EXAFS equations[85-86,88] and analysis programs.[89-91]

Whether using a single-scattering approximation or incorporating multiple scattering theory, the main difficulty in EXAFS modeling lies in approximating the non-structural components such as the phase shifts, $\delta(k)$, and backscattering amplitudes, $f(k)$. Both depend on the chemical states of the absorbing and neighboring atoms, and both have a dependence on R_i when the small-atom approximation (in the more rigorous quantum mechanical derivation) breaks down. Additionally, multiple scattering effects and variations of the mean free path, λ, affect the transferability of $f(k)$ to further-out shells.

[iv] In addition to the transmission signal, a fluorescence signal can also be recorded; the ejected electron leaves behind a hole in the core electron configuration, and an electron from a nearby, higher-energy level can relax into the hole and release its extra energy via either a photon (X-ray fluorescence) or another ejected electron (Auger effect). For materials with a reasonable fluorescence yield, the ratio of the fluorescence signal to I_0 can also be used to recover $\mu(E)$. Whether transmission or fluorescence is preferable depends greatly on the nature of the sample.

To ameliorate these difficulties, it is common practice to use standards to obtain estimates for the phases and amplitudes. Ideally, the standard would have the same number and type of backscattering atoms in the same chemical state and with the same distance from the absorbing atom as that of the 'unknown' sample. This way, the scattering phases and amplitudes can be extracted directly and used to model the spectrum of the unknown material, thereby producing quantitative local structure information including the number of nearest neighbors, N_i, in each shell and their distance, r_i, from the absorbing atom. When standards are not available, but a local structure model can be generated, software such as IFEFFIT,[89-90] can be used to obtain the phases and amplitudes via *ab initio* multiple scattering calculations on the cluster of atoms.

In practice, such modeling is feasible mainly for relatively simple systems (e.g. metals or isolated molecules) where all of the absorbing atoms have the same local environment. When a mixture of known local structures is expected, the unknown spectrum can be fit using a linear combination of various standards representing each anticipated environment. Linear combination fitting is particularly useful for complex systems (such as the oxides in this study) where modeling is difficult, even with the use of appropriate standards.

1.2.2.2 XANES

In the XANES part of the spectrum, the final states of the excited photoelectron are below the continuum of states.[v] Here, the photoelectron energy is low enough that the wave interacts more strongly with the surrounding atoms and is thus more strongly affected by multiple scattering events, many-body interactions, and distortions by the varying Coulomb fields of the atoms.[76] The photoelectron is also more strongly influenced by changes in band

[v] For example, the XANES states in metals are mainly the unoccupied part of the *d* band just above the Fermi level as well as the less tightly bound *s* or *p* states. The XANES states in isolated molecules are typically the unoccupied bound states and the low-lying continuum states.[70]

structure; different chemical environments (oxidation states, coordination species) create different charge distributions surrounding the absorbing atom, and this can alter the core electron binding energies enough to produce shifts or unique features in near the absorption edge.[70] If de-convoluted, the enhanced multiple scattering could confer not only the number and radial distance of neighboring atoms but also their relative geometric arrangement, bond angles, bonding and anti-bonding orbital orientations, etc. Likewise, the sensitivity to band structure could relate a wealth of electronic structure information.

A full theoretical description of the XANES region, however, requires incorporating all of these effects and solving the many-electron Shrödinger equation to construct the initial and final states of the photoelectron. Because this is not feasible, an extension of the single-scattering EXAFS theory that includes multiple scattering components is sometimes used to model the XANES region.[70] However, due to the complexity of such models, only qualitative or semi-quantitative analyses of the XANES region are usually pursued.

Qualitative analyses typically include matching the XANES spectrum to the spectra of other, known materials. Thus, similar to the XRD pattern, the XANES spectrum is somewhat like a fingerprint and can be used to identify the oxidation state and sometimes the coordination environment of the atom. For example, the different oxidation states of platinum (Pt vs. Pt^{2+}, seen in Figure 1.21a) shift the absorption edge energy and alter the edge's appearance; the absorption edge peak of the oxide is substantially higher than that of the metal, as is common for all metals/oxides. Similarly, different coordination environments can produce significantly different features in the absorption edge; as Figure 1.21b shows, the Ti^{4+} atoms in anatase, rutile, and a fresnoite-like 5-coordinated environment manifest substantially different features. If the different oxidation states and/or coordination environments can be identified, and appropriate

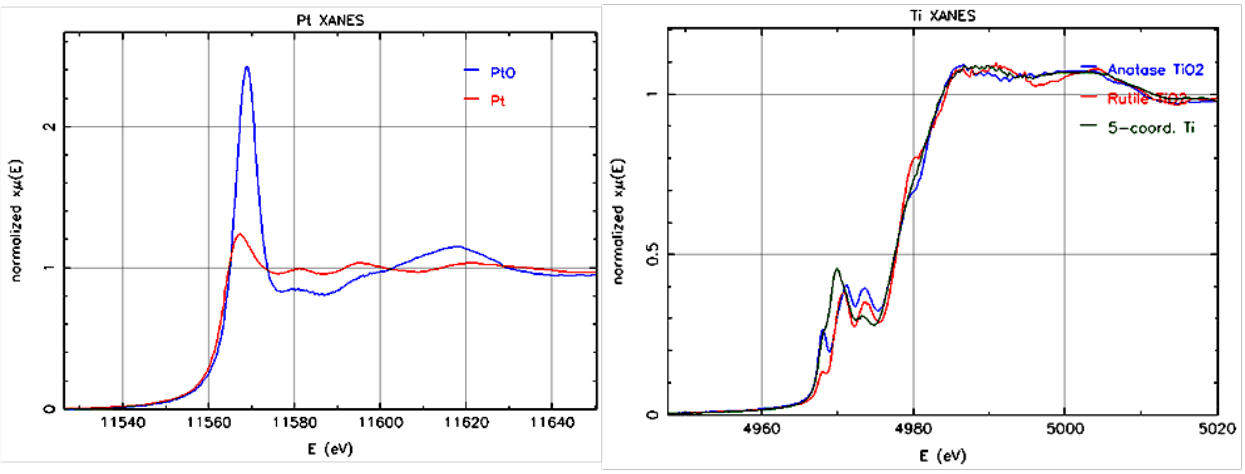

Figure 1.21 (a) XANES spectrum for Pt and PtO. The Pt^{2+} oxidation state results in a shift of +2.5eV in the absorption edge energy and a markedly higher absorption peak. (b) XANES spectrum Ti in three coordination environments: the anatase TiO_2 (blue) and rutile TiO_2 (red) crystal structures and a fresnoite-like 5-coordinated environment. The different coordination environments manifest significantly different pre-edge features.

standard spectra obtained for each environment, linear combination fitting can be used to quantify the various oxidation states and/or coordination environments, as in EXAFS analyses.

1.2.3 Transmission Electron Microscopy (TEM)

Like the typical visible-light microscope, a transmission electron microscope (TEM) produces a magnified image of a specimen. Instead of visible light, however, a narrow beam of electrons is used to illuminate the sample. As diagrammed in Figure 1.22,[92] electrons are emitted from an electron 'gun' at the top of the evacuated column of the TEM via thermionic, Schottky, or field emission processes. The beam is accelerated through a voltage typically ranging from 100-500 kV before passing through a system of apertures and lenses. Electromagnetic rings act as lenses for the charged electrons instead of the glass lenses used in visible-light microscopes. The pre-sample 'condenser' lens(es) (1) ensure that the beam is aligned and has uniform current density and (2) permit variation of the beam size and focal point. The intensity distribution of the beam after it passes through the sample is then imaged onto a fluorescent screen through another system of between 3 and 8 lenses including at least an objective, an intermediate, and a projector

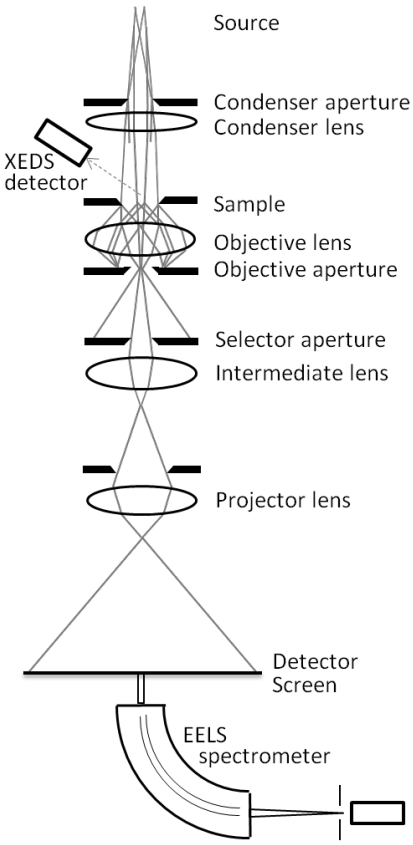

Figure 1.22 Diagram of a transmission electron microscope.

Table 1.3 Relativistic wavelength of the electron as a function of accelerating voltage.

Voltage (kV)	Wavelength (nm)
100	0.00370
200	0.00251
300	0.00197
400	0.00164

lens. The image can be recorded using either direct exposure (a photographic emulsion or an image plate) or a digital CCD camera coupled to a fluorescent screen via a fiber-optic plate.

Due to the very small wavelength of electrons accelerated at 100-400 kV (see Table 1.3) calculated using the de Broglie equation (including relativistic effects),[93] TEM instruments can image with substantially greater resolution (0.1 nm versus 300 nm) and at much higher magnification (1,000,000x versus 2000x) than light microscopes.[94] Electrons interact very strongly with matter both by elastic and inelastic scattering processes, though, so the sample must be very thin (1-100 nm) to transmit a detectable portion of the electron beam.[92-93] These size ranges are ideal for nanoparticles, though, and the various TEM analysis techniques utilizing the elastic and inelastic processes can provide a wealth of structural information.

Utilizing primarily the elastically scattered electrons, both an image and a diffraction pattern of the illuminated sample can be collected. This is accomplished by changing how the beam is focused after it passes through the sample; as parts *a* and *c* of Figure 1.23 illustrates, the strength of either the objective or intermediate lens is decreased (thereby increasing the focal length) in order to project the diffraction pattern instead of the image onto the detector screen.

There are also two ways in which the beam can be focused prior to reaching the sample. Figure 1.22 andFigure 1.23 show the conventional transmission mode in which the electron beam is collimated by the condenser lens(es) so that it is roughly parallel when it strikes the sample. This illuminates the entire desired area of the sample at once. Alternatively, the electron beam can be focused to a small point (0.2-5 nm) and used to scan the desired area of the sample point-by-point in a raster. This mode is referred to as scanning transmission electron microscopy (STEM).[95-97] As a result of the small probes now attainable, STEM mode can reach significantly higher resolution (< 1nm) than the standard TEM mode.

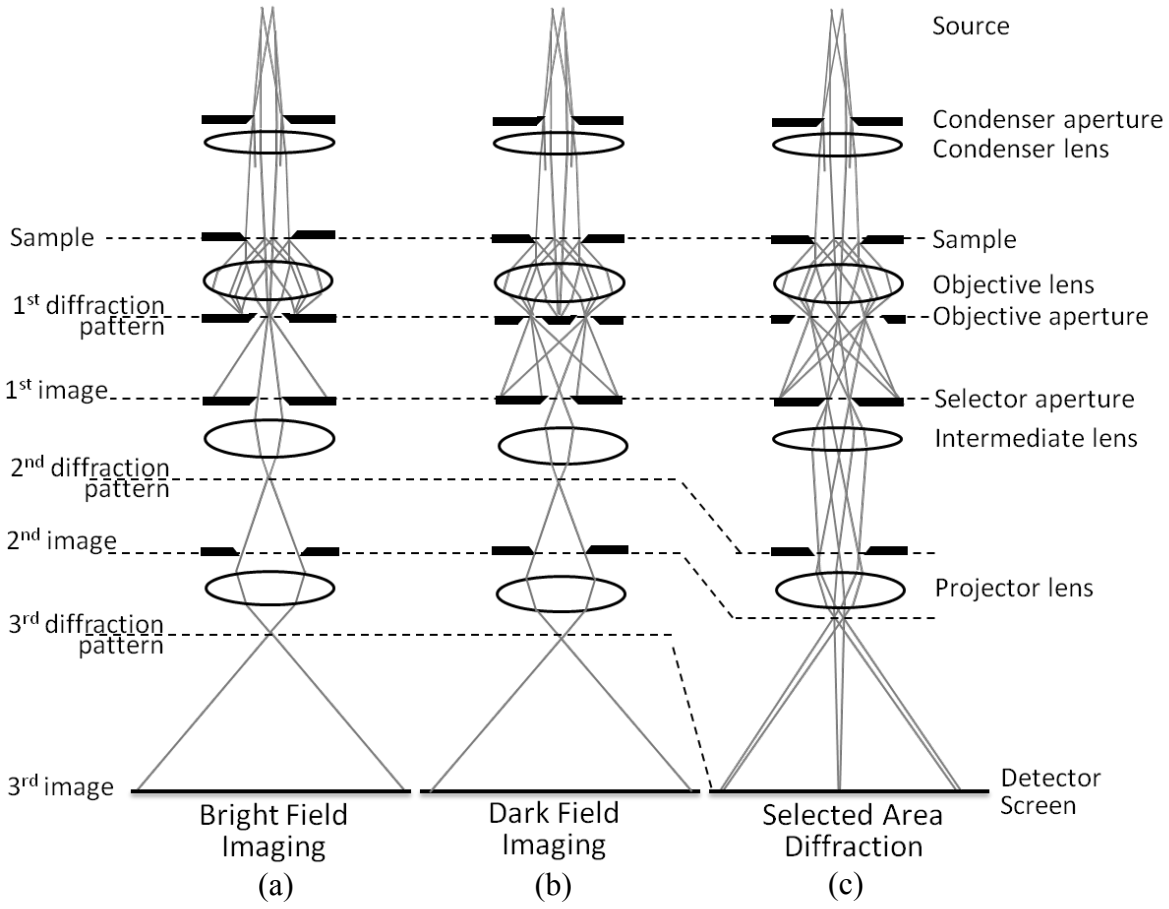

Figure 1.23 Ray diagrams for the (a) bright field, (b) dark field, and (c) selected area electron diffraction (SAED) modes of TEM imaging, adapted from Reimer 2008.[92] To the left, the relative levels of the intermediate diffraction patterns and images produced by the various lenses to illustrate the lower lens strengths used to project the diffraction pattern onto the detector in SAED mode. The TEM components are listed to the right.

In both transmission and STEM mode images, the primary source of contrast is 'mass/thickness' contrast (an example of which is given in Figure 1.24) that occurs because areas or particles with larger atomic numbers or greater thicknesses transmit fewer electrons. Several techniques have been developed to enhance contrast in the images to allow for easier interpretation. As diagrammed in Figure 1.23a, 'bright field' contrast (seen in Figure 1.25a) can be produced by constricting the objective aperture so that it blocks the scattered/diffracted electrons and transmits only the primary beam. This causes the particles that scatter/diffract weakly (due to orientation and/or composition) to be much brighter than those that scatter/diffract strongly. Somewhat conversely, 'dark field' contrast (seen in Figure 1.25b) can be obtained by shifting the objective aperture so that one (or more) of the diffracted beams pass through the aperture while the primary beam is blocked (Figure 1.23b). This causes the particles which scatter/diffract strongly to be very bright

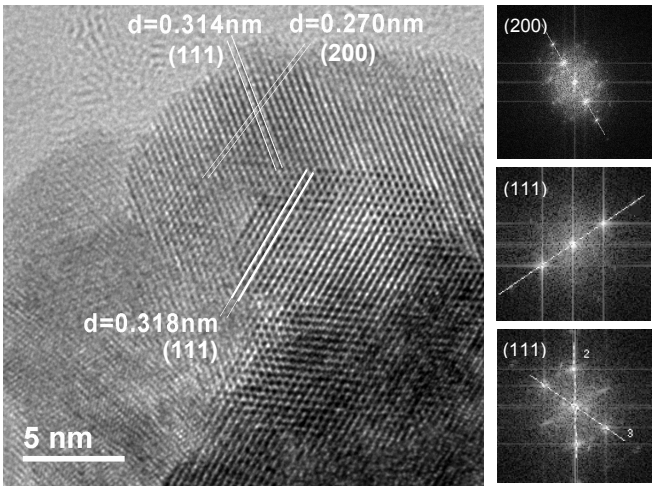

Figure 1.24 Standard high resolution TEM image (using mass-thickness contrast) of CeO_2 nanoparticles showing the Fresnel lattice fringes. The Fourier transforms of several portions of the image (shown to the right) were used to measure the fringe spacings and assign the crystal plane indices.

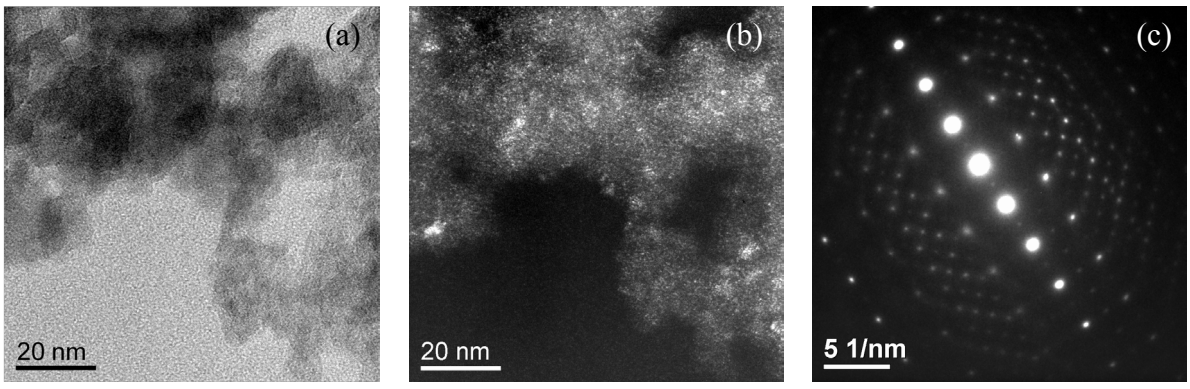

Figure 1.25 Bright field (a) and dark field (b) images of La-doped γ-Al_2O_3 nanoparticle agglomerates impregnated with Pt. (c) A selected area electron diffraction (SAED) pattern from several large PrO_2 crystallites.

while all others are very dim—the opposite of the contrast obtained by bright field imaging as Figure 1.25a-b illustrates. In combination, bright field and dark field modes provide complimentary information about the particle orientation and composition.

Figure 1.25c illustrates a selected area diffraction (SAED) pattern obtained using the diffraction mode diagrammed in Figure 1.23c. As with X-ray diffraction patterns, a sample can be identified and its lattice parameters determined from its electron diffraction pattern if the microscope's diffraction length is regularly calibrated. However, using the typical SAED mode, relatively large areas (0.1-1 μm) of the specimen are necessarily sampled due to the selection errors (stray peaks from unselected areas) caused by spherical aberrations in the objective lens. Thus, as Figure 1.25c illustrates, the diffraction patterns often contain contributions from multiple, if not many, particles. The electron diffraction of smaller areas (2-10 nm) can be collected without the selection errors of the SAED patterns by converging the beam into a small probe (similar to STEM mode). The analysis of the data obtained using this convergent beam electron diffraction (CBED) method can be rather complex, but it holds much promise for the study of nanoparticles. Currently, however, X-ray diffraction experiments (when possible) are still more convenient and optimized for obtaining accurate crystallographic parameters.

Using any of these modes, images of the nanoparticles can be obtained which allow particle size and morphology as well as agglomerate size and morphology to be directly viewed, measured, and interpreted. Also, when high enough magnifications are used, the rows and columns of atoms in a crystal become visible as seen in Figure 1.24, revealing the crystallinity and size of the particles. The distances between these Fresnel 'atomic fringes' can be measured and matched to the characteristic *d*-spacings of the crystal planes, enabling both the material and its crystal direction to be positively identified.

Aside from producing crystallographic information and atomic-resolution images, the TEM can be used for elemental analysis. Still using the coherent scattering processes, different types of atoms can be qualitatively distinguished by using an annular detector to collect the electrons scattered at very high angles. There, the intensity of the scattering approaches a Z^2 dependence (the square of the atomic number), providing more contrast between different types of atoms than can be obtained otherwise. Using STEM mode with this 'Z-contrast' technique, an atomic resolution compositional map can be generated for particles that are in zone-axis orientations (as long as the probe size is smaller than the distance between atomic columns).[95,98]

Other more quantitative elemental analysis techniques utilize the inelastic scattering of the electron beam. Much like X-rays, the electron beam in the TEM is a type of ionizing radiation that is capable of removing core electrons (as discussed in the XAFS section) by transferring energy to individual atoms in the sample. The ejected electron leaves behind a hole in the core electron configuration, and an electron from a nearby, higher-energy level can relax into the hole, dispelling its extra energy via one of several routes including releasing a photon (X-ray fluorescence), ejecting another nearby electron (Auger effect), or undergoing various non-radiative processes[73]

For atoms with a large fluorescence yield, the energies of the X-ray fluorescence can be detected using an energy dispersive spectrometer (EDS).[99] The resulting X-ray energy dispersive spectrum (XEDS) shows the characteristic emission lines for every element in the sample. The signals tend to be somewhat low because of the small sample sizes in the TEM and because of the small solid angle of the detector inside the TEM which catches a limited fraction of the isotropically emitted X-rays (see Figure 1.22). Thus, alternatively, the electron energy loss spectrum (EELS) can be collected by detecting the inelastically scattered electrons (which are

forward-scattered at small angles and are thus more concentrated) using a magnetic prism spectrometer behind the final imaging plate (see Figure 1.22). As with XANES and EXAFS, the energy-loss near-edge structure (ELNES, within ~50 eV of each edge) contains information about the bonding and band structure of that atom, and the extended energy-loss fine structure (EXELFS, continuing to a few hundred eV beyond each edge) contains information about the coordination of neighboring atoms.[92,95]

EELS data are not used for modeling as in XAFS analyses, however, because the electrons exciting the core transitions interact much more strongly with the sample than X-rays, making the EELS data even more complicated by multiple scattering and other effects. Instead, the EELS and XEDS signals are more widely used as fingerprints to identify (and sometimes quantify) the elements in a particular area of the sample. Combined with the small probe sizes of STEM mode, XEDS and EELS are capable of mapping the elements in a desired region of the sample to very high resolution (~1 nm). This has exciting implications for nanoparticle analyses; if STEM-mode XEDS or EELS are performed on an isolated nanoparticle that is several nm in diameter, the distribution of the atoms across the particle should allow one to distinguish a dopant located on the surface from one located within the bulk structure of the particle.[vi] If performed on nanoparticles in agglomerates, however, the presence of the dopant can be confirmed, but it cannot be assigned to a specific particle, much less to a surface or bulk location.

1.2.4 Solid State NMR

Like the EXAFS technique, Nuclear Magnetic Resonance (NMR) spectroscopy can provide information about the immediate environment (coordination number, bond type, etc.) of

[vi] If a dopant atom is located on the surface of a nanoparticle, the dopant concentration determined by STEM-mode XEDS or EELS will theoretically spike on the edges. If the dopant is distributed inside the lattice, the dopant distribution should be reasonably continuous throughout the particle.

a particular type of atom in a sample. Unlike EXAFS, the NMR technique is limited to those atoms that have a nonzero nuclear spin ($I \neq 0$) which produces a nonzero magnetic moment (μ) via the relationship $\mu = \gamma I$, where γ is the magnetogyric ratio (a constant for a given type of nucleus). Generally, atoms that have an odd number of protons and neutrons are NMR active. Most elements have at least one NMR active isotope, but the natural abundance of these isotopes varies widely.

To briefly describe an NMR experiment in terms of the magnetic moment,[100-101] a large magnetic field, $\mathbf{B}_0$, is applied to the sample. This exerts a torque on the nuclear magnetic moments which move to align themselves with the field. As a result, the moments precess about the fixed $\mathbf{B}_0$ direction at a constant rate, $\omega_0 = -\gamma\mathbf{B}_0$, called the Larmor frequency, which is generally in the radiofrequency range. A separate radiofrequency (rf) wave is then applied to the sample as a pulse (or series of pulses in multidimensional experiments). The magnetic field component of this pulse oscillates perpendicular to $\mathbf{B}_0$ with a frequency ω_{rf} that is close to being (or is) resonant with ω_0. This changes the strength and direction of the magnetic field felt by the nuclei, causing the magnetic moments to 'flip' and precess around the new field, $\mathbf{B}_1$, with a new resonance, or 'nutation,' frequency of $\omega_1 = -\gamma\mathbf{B}_1$. These oscillating moments induce a current in a nearby detector that oscillates according to the resonance frequencies of the nuclei. When the rf pulse is ceased, the moments relax back into the original configuration, and the induced current decays. The decaying current can be Fourier transformed into the frequency domain to reveal the resonant frequencies of the nuclei relative to that of a standard. The signals from many pulses can thereby be collected and averaged to obtain a better signal-to-noise ratio.

Described quantum mechanically, the large magnetic field results in Zeeman splitting of the previously degenerate magnetic energy levels of the nuclei in the sample. The energy

difference between the levels is on the order of the energy of radio waves. Transitions are induced by radio frequency irradiation, and the absorbed energy recorded in the NMR signal reveals the energy, or resonance frequency, of the transition(s) in each nucleus in the sample.[102]

Due to several factors, not all of the nuclei in the sample have the same resonance frequencies. First, the electrons surrounding each nucleus (and the nuclei of surrounding atoms) produce a secondary field that alters the magnetic field felt by the nucleus. This 'shielding' interaction changes the energy level spacing, thereby perturbing the resonance frequency of the nucleus, shifting it by an amount called the chemical shift. It is this chemical shift that enables NMR to probe the local structure. Next, the closely-spaced collection of nuclear magnetic moments in the sample can interact with each other, though the strength of this 'dipole-dipole coupling' decreases rapidly ($1/r^3$) with increasing internuclear distance, r. Dipolar coupling can be both homogeneous and heterogeneous. Finally, the distribution of charge in nuclei with spins greater than ½ gives rise to a nuclear electric quadrupole moment (see Figure 1.26) that interacts with electric field gradients from nearby electrons and other nuclei. This 'quadrupole coupling' can split the energy levels to a greater extent than other interactions.

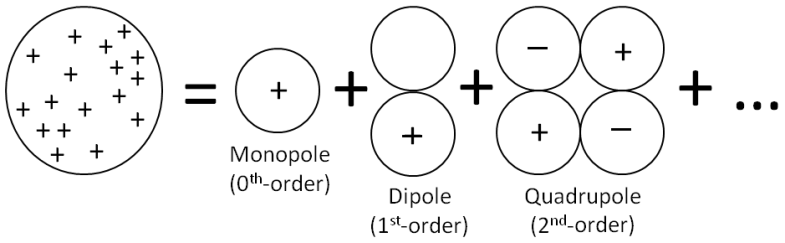

Figure 1.26 Charge distribution in a nucleus represented as the expansion of a series of multipoles (Duer (2004)).[100] The total nuclear charge is the 0th order term (monopole), the 1st -order term (the electric dipole) is always zero for nuclei, and the 2nd-order term is the electric quaudrupole moment, which is nonzero for nuclei such as Al with spins greater than ½.

These nuclear spin interactions (chemical shielding, dipole-dipole coupling, and quadrupole coupling) all depend on the orientation of the nuclei. In solution, the isotropic tumbling of the molecules is rapid enough to average the orientation dependence to zero on the

NMR timescale, but in solid samples (such as nanoparticles), the orientations of the nuclei are fixed. All the different orientations give rise to different spectral frequencies, resulting in a set of very broad lines in the NMR spectra of powder samples.

To achieve a similar effect as the isotropic tumbling in liquids, solid samples can be spun very rapidly at a so-called 'magic angle (see Figure 1.27). This is because the orientation dependence of anisotropic effects is of the form

$$3\cos^2\theta - 1 \qquad \text{Eq. 1.53}$$

where θ is the angle of the particular spin interaction tensor (chemical shielding, for example) to the applied field $\mathbf{B}_0$ (see Figure 1.27). In powder samples, θ takes on all possible values due to the randomly oriented crystallites. If the powder is spun on an axis inclined at an angle θ_R to the applied field as Figure 1.27 shows, θ varies with time. The average orientation dependence then becomes

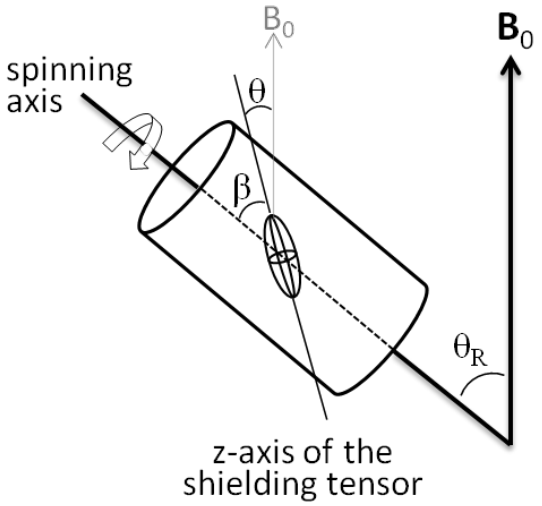

Figure 1.27 Diagram of a magic angle spinning (MAS) experiment based on that reported by Duer (2004).[100] The sample is spun in a cylindrical rotor at an angle $\theta_R = 54.74°$ to the applied field $\mathbf{B}_0$ to remove chemical shift anisotropy and dipolar coupling. θ and β (the angles that the shielding tensor's z-axis forms with $\mathbf{B}_0$ and with the spinning axis, respectively) take on all possible values in a powder due to the randomized but fixed molecular orientations.

$$\langle 3\cos^2\theta - 1\rangle = \frac{1}{2}(3\cos^2\theta_R - 1)(3\cos^2\beta - 1) \qquad \text{Eq. 1.54}$$

where β is the angle formed between the spinning (θ_R) axis and the z-axis of the shielding tensor, as Figure 1.27 diagrams. Like θ, β takes on all possible values in a powder, but θ_R can be controlled; if it is set to 54.74° then $(3\cos^2\theta_R - 1) = 0$, making $\langle 3\cos^2\theta - 1\rangle = 0$ as well.

The anisotropy of any interaction can thus theoretically be removed by spinning at an angle of 54.74°. However, the spinning rate must be 3-4 times faster than the largest interaction

anisotropy in order for this 'magic-angle spinning' technique, or MAS, to completely remove the anisostropy and reduce the powder pattern to narrow, single lines centered at each isotropic chemical shift value (like that observed in solution). With the 30-50 kHz spinning rates currently possible, the chemical shift anisotropy can be completely removed as can the effects of homonuclear dipolar coupling (but only with very high spinning rates—when high enough spin speeds are not possible, special pulse sequences can assist in removing these anisotropies). In the case of heteronuclear dipolar coupling, other techniques such as continuous rf irradiation at the resonance frequency of the unwanted nuclei can be used along with MAS and pulse sequences to help remove the anisotropy effects.

For quadrupolar nuclei such as ^{27}Al, however, the sample cannot be spun fast enough for MAS to remove the anisotropy. Spinning quadrupolar nuclei inevitably produces a set of 'spinning sidebands' that radiate out from the isotropic chemical shift line (Figure 1.28), the spacing of which sidebands depends on the spinning rate. MAS does greatly narrow the sidebands, though, enabling the true chemical shift of each type of nuclei to be discerned. This way, the resonant peaks corresponding to the different types of nuclei in the sample can be analyzed just as in typical 1D, solution-phase NMR patterns; the number of peaks indicates the number of different nuclei (different environments). The characteristic shift values and splitting of the peaks indicates the extent of the shielding from nearest neighbors and can reveal the number and type of each nuclei's nearest neighbors. The relative

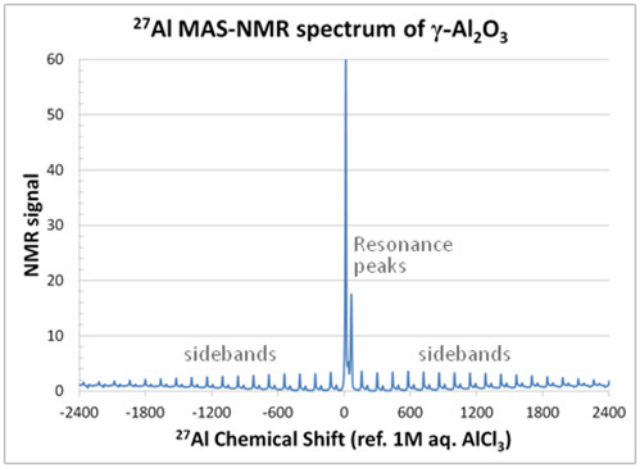

Figure 1.28 MAS NMR spectrum of the ^{27}Al nuclei in γ-Al_2O_3, illustrating the spinning sidebands produced by quadrupolar nuclei in MAS NMR.

concentration of each nuclei can also be determined by quantifying the area under each peak.

MAS NMR has become the standard technique for removing anisotropic effects and increasing resolution enough to obtain sensible NMR spectra for materials in the solid-state, and it can be readily applied to nanoparticle samples to deduce the local structure information just mentioned (e.g. the number of unique nuclear environments, their concentration, and the identity and number of their nearest neighbors). In addition to traditional NMR analyses, however, pulse sequencing and other advanced techniques are being developed which can essentially switch the various interaction anisotropies on and off. Though difficult to analyze, these anisotropies could give quantitative information on molecular structure, conformation, and dynamics. Solid-state NMR will thus be an increasingly valuable tool in the local structure analysis of nanoparticles.

1.2.5 Gas Adsorption Measurements: BET Analysis

Over 100 years ago, it became apparent that the adsorption of gas molecules by solid surfaces at a constant temperature produces characteristic profiles, or adsorption isotherms. Though the adsorption profiles of each material are unique, the strikingly similar shapes of the isotherms allow them to be generally categorized as one of the six types (I, II, III, IV, V, and VI) shown in Figure 1.29, following the notation originally proposed by Brunauer, Deming, Deming, and Teller.[103-105] Through various mathematical models of the adsorption process that have been developed over the last century, these adsorption isotherms can provide valuable information about the adsorbent's surface structure, surface area, and sometimes pore size in the case of porous materials.

Because porosity strongly influences the shape of the adsorption isotherm, a system has been adopted over the years (and is now sanctioned by the IUPAC) for categorizing pores according to their size; pores that have diameters ≤ 2 nm as micropores, 2-50 nm as mesopores,

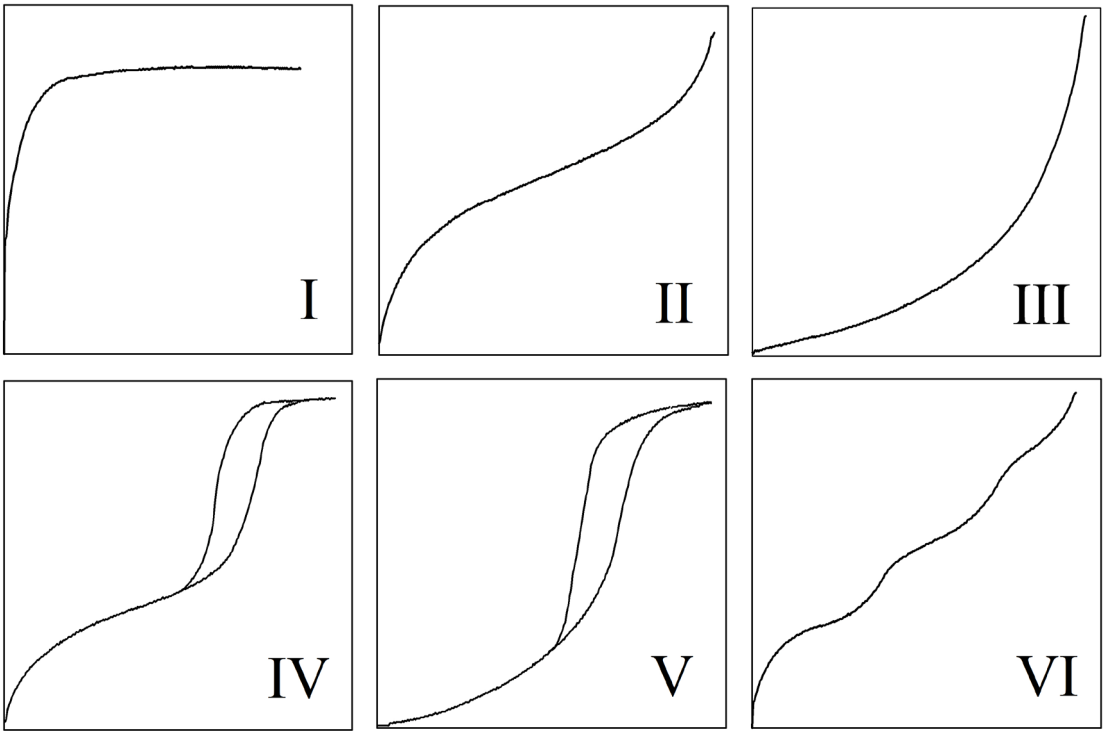

Figure 1.29 The six types of adsorption isotherms, as presented by Lercher 1999.[104]

and ≥ 50 nm as macropores.[105-108] Using these designations, the six types of isotherms can be described as follows. Type I isotherms are produced by physisorption in microporous materials that have relatively small external surface areas. Type II isotherms represent multilayer physisorption on the flat surfaces of nonporous materials. Types III and V isotherms are indicative of weak gas-solid interactions such as that of water adsorption on gold. Type IV isotherms are characteristic of mesoporous adsorbents (such as silica gels and other porous oxides) on which multilayer adsorption is followed by capillary condensation inside the mesopores. Type VI isotherms are a result of stepwise adsorption on nonporous adsorbents with energetically uniform surfaces.

The conventional method of measuring the adsorption isotherm is a point-by-point procedure. Prior to the measurements, the sample is 'de-gassed,' or is mildly heated under vacuum or flowing gas to remove any adsorbed species. The sample container is then evacuated,

and the system is cooled to the desired temperature (77 K for N_2 measurements), which temperature is maintained throughout the measurements. Successive amounts of the adsorptive or adsobate (such as N_2) are introduced to the sample, and the system is allowed sufficient time to equilibrate so that p can be measured at each stage, producing a series of points that make up the adsorption isotherm.[109]

Several excellent reviews are available which detail the history and theories behind the characterization of porous materials through adsorption.[104-105,109-114] Brief summaries are given below of the use of gas adsorption to characterize surface area and pore size with special attention given to the Type IV isotherms that are most applicable to this work. Because nitrogen (at 77 K) is the adsorptive gas most widely used for the characterization of porous materials and particularly Type IV materials,[105] these summaries also center on the use of N_2 as the adsorptive.

1.2.5.1 Surface Area

In 1916, Langmuir derived his celebrated isotherm equation for adsorption of a unimolecular layer, or monolayer, of gas (or solvent).[115] His interpretation of the Type I isotherm was that the plateau of the adsorption isotherm represented completion of the monolayer[vii] and thus provided a measure of the monolayer capacity, n_m.[109] It then followed that the surface area (A) of the adsorbent could be estimated as follows if the average area (a_m) occupied by each adsorbed molecule was known[105,110]

$$A = n_m a_m L \qquad \text{Eq. 1.55}$$

Little use was made of this idea, however, until 1938 when Brunauer, Emmett, and Teller (BET) proposed that the other isotherms could be explained by the adsorption of multiple layers,

[vii] It has since been found that the plateau of a Type I isotherm corresponds to the completion of pore filling in microporous materials, not to the formation of a single monolayer.[108]

or multilayers.[116] As in the Langmuir theory, the surface of the adsorbent in the BET theory is viewed as an array of equivalent sites to which gas molecules (the adsorbate or adsorptive) adsorb in a random manner. The same assumptions are made that no lateral interactions occur between adsorbed molecules in this layer (or that the gas-solid interactions are much stronger than the gas-gas interactions) and that the probability that a site will be occupied is independent of the occupancy of neighboring sites. The molecules of this 'ideal localized monolayer' from the Langmuir theory then act as the adsorption sites for a second layer, which in turn act as the adsorption sites for a third layer, and so on. The layers above the first layer are assumed to have liquid-like properties; for example, the nitrogen molecules adsorbed at 77 K are assumed to be in a close-packed 'liquid' state.[109]

Through these assumptions, BET derived an equation to describe the multimolecular adsorption of gases seen in isotherms[116]

$$\frac{n}{n_m} = \frac{Cx}{(1-x)(1-x+Cx)} \qquad \text{Eq. 1.56}$$

where n is the moles of gas adsorbed at the equilibrium pressure p, n_m are the moles of gas required to form a complete monolayer, x is the relative pressure (p/p^0) of the adsorbent where p^0 is the vapor pressure of the liquid adsorbate, and C was assumed to be a constant unique to each material (though further work has revealed that C can vary with the surface coverage).[113] BET transformed this equation into the following linear function

$$\frac{x}{n(1-x)} = \frac{C-1}{n_m C}x + \frac{1}{n_m C} \qquad \text{Eq. 1.57}$$

proposing that a plot of $x/[n(1-x)]$ vs. x should yield a straight line whose slope and intercept can be used to deduce the values of C and n_m and thereby estimate the surface area.[viii]

[viii] In practice, the linear region of the isotherm is quite limited and varies depending on the nature of the adsorbent and adsorbate as well as on the operational temperature. Types III and V do not exhibit a truly linear region.

With these equations, BET provided an interpretation of Type II isotherms. Interpretations of Type III, IV, and V isotherms were published two years later,[103] justifying the use of the BET equations for analyzing all types of isotherms. According to their theories, the S-shapes of Type II isotherms are the result of multi-layer adsorption on flat surfaces such as a non-porous powder. When a non-porous powder is compressed (or when nanoparticles form agglomerates), the interstices between the particles form a mesopore system, and a Type IV isotherm is observed.[110] The shape of the Type IV isotherm is thus identical to the Type II isotherm until an abrupt upward departure occurs which is interpreted to be the onset of capillary condensation (the pore-filling process) inside the mesopores. The plateau at higher p/p^0 is taken to mean that mesopore filling is complete.[105] By this interpretation, the well-established BET procedure for analyzing Type II isotherms can be applied to type IV isotherms to obtain the monolayer capacity, n_m, and thereby obtain an estimate of surface area.

Though the BET theory is based on a somewhat over-simplified picture of multilayer adsorption, it remains today the standard procedure for determining surface area. DFT and empirical methods have been developed but remain less widely used.[109,114]

1.2.5.2 Pore Size

For well over 60 years, gas adsorption has been used to analyze not just surface area but also pore size. First pioneered in 1932 by Foster[117] then further developed by Shull[118] in 1948 and Barrett *et al*. in 1951,[119] the procedure developed by Barret, Joiner, and Halenda—the BJH method—remains the most popular method for pore size analysis, particularly the analysis of mesopore size distribution in Type IV isotherms.[105]

In the BJH method, or 'classical' method, a corrected form of the Kelvin equation is used to evaluate the pore width from the pore filling pressure, p, as follows

$$RTln\left(\frac{p}{p^0}\right) = -\frac{2\gamma V_L}{r_m} \quad \text{Eq. 1.58}$$

where γ is the surface tension and V_L is the molar volume of the liquid adsorbate, and r_m is the mean radius of curvature for the meniscus of the capillary condensate inside the mesopores.[109-110] In the Type IV isotherm, capillary condensation is assumed to begin with the abrupt upward deviation from the Type II-like isotherm and is complete when the p/p^0 ratio reaches a plateau, thus the Kelvin equation is only applied to points on the hysteresis loop of Type IV isotherms. It has been debated whether the adsorption or desorption branch of the loop is more appropriate for these analyses, but recent opinions favor the estimates from the adsorption branch.[110]

Because multilayer adsorption has already occurred when capillary condensation begins, the walls of the pores are already lined with an adsorbed film of thickness t. The r_m in Eq. 1.58 hus corresponds to an inner 'core' rather than the pore itself.[110] To convert r_m to a measurement of the pore volume, assumptions must be made about t, and a model of the pore structure is necessary. For this model to be tractable, it is necessarily assumed that the pores are rigid and all have the same simple shape; the two most widely-used shapes are that of a cylinder (where the pore radius, r_p, is given by $r_p = r_m + t$) or a parallel-sided slit (where the pore width, d_p, is given by $d_p = r_m + 2t$).[109-110] Based on the model chosen, the meniscus curvature is assumed to be either hemispherical (for cylinders) or hemicylindrical (for slits) in the calculation of pore volume.

Due to the oversimplifications in the theoretical models and thus the inherent flaws in both the BJH and BET analyses, N_2 adsorption should not be expected to provide more than a semi-quantitative estimate of surface area and pore size. Yet these methods are held to be reasonably reliable in the case of Type IV, or mesoporous, materials.[105,109] Hence, we have employed the classical BET and BJH methods to obtain surface area and pore size statistics for the mesoporous oxide materials investigated in this work. Because these methods are so widely

used, the values obtained are highly useful in product control, product comparison, and patent specifications.[109]

1.3 Overview of the Dissertation

In the next chapter, a new method is presented for the synthesis of an unprecedentedly wide range of metal oxide nanomaterials along with characterizations of the products. Chapter 3 investigates the reaction parameters and intermediates associated with this method, culminating in a proposed mechanism for the reaction. These studies of the reaction intermediates led to the discovery of additional potential products using this method, and Chapter 4 relates the synthesis and structural characterization of one such unexpected oxyhydroxide product, ferrihydrite.

The new synthesis method produces Al_2O_3 nanoparticles that show promise in catalyst support applications, thus Chapter 5 details the synthesis and structural analysis of these nanoparticles. To understand and explain some surprising results in these analyses, we studied the symmetry relationships between the many phases of Al_2O_3, and these symmetry-mode analyses are presented in Chapter 6.

The structural analyses in Chapter 5 indicated that the transition from the catalytically favorable γ-Al_2O_3 phase to the less-desirable α-phase occurs at atypically low temperatures. A lanthanum dopant was added to the Al_2O_3 nanoparticles to stabilize the γ-Al_2O_3 phase, and Chapter 7 describes this new, 1-pot process for producing La-doped γ-Al_2O_3 nanoparticles which is based on the new synthetic method in Chapter 2. Chapter 7 also provides structural analyses of the Al_2O_3 in the La-doped γ-Al_2O_3 nanoparticles. Chapter 8, on the other hand, provides structural analyses of the La dopant. In Chapter 9, the results from Chapters 5-8 are combined to form a new hypothesis about the La dopant's role in stabilizing the γ-Al_2O_3 phase.

References

1. Siegel, R. W.; Hu, E.; Roco, M. C.; Editors, *WTEC Panel on: Nanostructure Science and Technology - R&D Status and Trends in Nanoparticles, Nanostructured Materials, and Nanodevices*. 1999; p 15 of 342.
2. Schaffer, B.; Riegler, K.; Kothleitner, G.; Grogger, W.; Hofer, F., Monochromated, spatially resolved electron energy-loss spectroscopic measurements of gold nanoparticles in the plasmon range. *Micron* **2009,** *40* (2), 269-273.
3. Skandan, G.; Singhal, A., Perspectives on the science and technology of nanoparticle synthesis. *Nanomater. Handb.* **2006**, 13-27.
4. Almquist, C. B.; Biswas, P., Role of Synthesis Method and Particle Size of Nanostructured TiO2 on Its Photoactivity. *J. Catal.* **2002,** *212* (2), 145-156.
5. Anpo, M.; Shima, T.; Kodama, S.; Kubokawa, Y., Photocatalytic hydrogenation of propyne with water on small-particle titania: size quantization effects and reaction intermediates. *J. Phys. Chem.* **1987,** *91* (16), 4305-10.
6. Bell, A. T., The Impact of Nanoscience on Heterogeneous Catalysis. *Science (Washington, DC, U. S.)* **2003,** *299* (5613), 1688-1691.
7. Reddy, K. M.; Manorama, S. V.; Reddy, A. R., Bandgap studies on anatase titanium dioxide nanoparticles. *Materials Chemistry and Physics* **2003,** *78* (1), 239-245.
8. Theerdhala, S.; Vitta, S.; Bahadur, D., Magnetic nanoparticles through sonochemistry. *Mater. Technol. (London, U. K.)* **2008,** *23* (2), 88-93.
9. Pinna, N.; Niederberger, M., Surfactant-free nonaqueous synthesis of metal oxide nanostructures. *Angew. Chem., Int. Ed.* **2008,** *47* (29), 5292-5304.
10. Qi, W. H.; Wang, M. P., Size effect on the cohesive energy of nanoparticle. *Journal of Materials Science Letters* **2002,** *21* (22), 1743-1745.
11. Navrotsky, A., Energetics of oxide nanoparticles. *Int. J. Quantum Chem.* **2009,** *109* (12), 2647-2657.
12. Nanda, K. K.; Maisels, A.; Kruis, F. E.; Fissan, H.; Stappert, S., Higher surface energy of free nanoparticles. *Physical Review Letters* **2003,** *91* (10), 106102/1-106102/4.
13. Zhou, R. S.; Snyder, R. L., Structures and transformation mechanisms of the η, γ, and θ transition aluminas. *Acta Crystallogr., Sect. B: Struct. Sci.* **1991,** *B47* (5), 617-30.
14. Pinna, N.; Neri, G.; Antonietti, M.; Niederberger, M., Gas sensors: Nonaqueous synthesis of nanocrystalline semiconducting metal oxides for gas sensing. *Angew. Chem., Int. Ed.* **2004,** *43* (33), 4345-4349.
15. Arney, D. S.; Wood, T. E. Nanosize metal oxide particles for producing transparent metal oxide colloids and ceramers. 98-US15843 2000006495, 19980730, 2000.
16. Hirai, H.; Fujimoto, H.; Nakamura, S. Light-emitting element and method of producing the same. 2003-375094 2003160260, 20030228, 2003.
17. Oskam, G., Metal oxide nanoparticles: synthesis, characterization and application. *Journal of Sol-Gel Science and Technology* **2006,** *37* (3), 161-164.
18. Philseok, K.; Kippelen, B.; Perry, J.; Marder, S.; Jones, S.; Haddock, J. N.; Zhang, X.; Domercq, B.; Hotchkiss, P. Printable thin-film transistors with high dielectric constant gate insulators and methods for producing same. 2007-US23835 2008060534, 20071113, 2008.

19. Verbakel, F.; Meskers, S. C. J.; de Leeuw, D. M.; Janssen, R. A. J., Resistive Switching in Organic Memories with a Spin-Coated Metal Oxide Nanoparticle Layer. *J. Phys. Chem. C* **2008,** *112* (14), 5254-5257.
20. Kim, K.-K.; Park, N.-G.; Kim, D.-Y.; Kim, J.-K. Fabrication of oxide electrodes for dye-sensitized solar cells. 2006-KR5346 2008050931, 20061208, 2008.
21. Kumar, S.; Horne, C. R. Electrodes and batteries formed from lithium metal oxide nanoparticles. 2001-US40979 2001099215, 20010614, 2001.
22. Klabunde, K. J. Nanometer sized metal oxide particles for ambient temperature adsorption of toxic chemicals. 97-US14647, 9807493, 19970820., 1998.
23. Hua, M.; Zhang, S.; Pan, B.; Zhang, W.; Lv, L.; Zhang, Q., Heavy metal removal from water/ by nanosized metal oxides: A review. *Journal of Hazardous Materials* **2012,** *211-212*, 317-331.
24. Pintault, B.; Guenadou, D.; Bianchi, L.; Belleville, P.; Valle, K.; Boscher, C.; Toulc'hoat, J. Manufacture of membranes consisting of a nanoporous nanoparticle layer on a substrate. 2007-EP54076 2007122256, 20070425, 2007.
25. Cheon, J.-W.; Jun, Y.-W.; Lee, J.-H.; Suh, J.-W.; Suh, J.-S.; Ko, S.-J.; Huh, Y.-M.; Song, H.-T. Magnetic resonance imaging contrast agents containing water-soluble nanoparticles of manganese oxide or manganese metal oxide. 2006-KR5160 2007064175, 20061201, 2007.
26. Gupta, A. K.; Gupta, M., Synthesis and surface engineering of iron oxide nanoparticles for biomedical applications. *Biomaterials* **2005,** *26* (18), 3995-4021.
27. Furman, B. R.; Rawls, H. R.; Norling, B. K.; Wellinghoff, S. T.; Dixon, H. Mechanically strong and transparent or translucent composites made using zirconium oxide nanoparticles. 2000-US13708 2000069392, 20000519, 2000.
28. Rieger, J.; Kissel, J.; Andre, V.; Bouillo, N. Preparation of surface-modified metal oxide nanoparticles for use in cosmetics. 2006-EP62732 2006128874, 20060530, 2006.
29. Carrettin, S.; Concepcion, P.; Corma, A.; Lopez Nieto, J. M.; Puntes, V. F., Gold Catalysts: Nanocrystalline CeO2 increases the activity of Au for CO oxidation by two orders of magnitude. *Angew. Chem., Int. Ed.* **2004,** *43* (19), 2538-2540.
30. Pradhan, S. K.; Deng, Z. T.; Tang, F.; Wang, C.; Ren, Y.; Moeck, P.; Petkov, V., Three-dimensional structure of CdX (X = Se,Te) nanocrystals by total x-ray diffraction. *J. Appl. Phys.* **2007,** *102* (4), 044304/1-044304/6.
31. Cushing, B. L.; Kolesnichenko, V. L.; O'Connor, C. J., Recent Advances in the Liquid-Phase Syntheses of Inorganic Nanoparticles. *Chem. Rev. (Washington, DC, U. S.)* **2004,** *104* (9), 3893-3946.
32. Koch, C. C., Top-down synthesis of nanostructured materials. Mechanical and thermal processing methods. *Rev. Adv. Mater. Sci.* **2003,** *5* (2), 91-99.
33. Niederberger, M.; Garnweitner, G., Organic reaction pathways in the nonaqueous synthesis of metal oxide nanoparticles. *Chemistry--A European Journal* **2006,** *12* (28), 7282-7302.
34. Kuiry, S. C.; Seal, S., Synthesis of nanomaterials using microemulsion process. *Encyclopedia of Nanoscience and Nanotechnology* **2004,** *10*, 369-379.
35. Drofenik, M.; Lisjak, D.; Makovec, D., The synthesis and properties of magnetic nanoparticles. *Mater. Sci. Forum* **2005,** *494*, 129-136.
36. Saalfeld, H., Corundum structure. *Naturwissenschaften* **1961,** *48*, 24.

37. Bezjak, A.; Jelenic, I., The crystal structures of boehmite and bayerite. *Symp. Bauxites, Oxydes Hydroxydes Alum., [C. R.]* **1964,** (1), 105-12.
38. Ewing, F. J., Crystal structure of diaspore. *J. Chem. Phys.* **1935,** *3*, 203-7.
39. Jenkins, R.; Snyder, R. L., *Introduction to X-ray Powder Diffractometry*. John Wiley & Sons, Inc.: New York, NY, 1996.
40. Egami, T. B., S. J. L., *Underneath the Bragg Peaks: Structural Analysis of Complex Materials*. First ed.; Pergamon: Kidlington, Oxford, UK, 2003; Vol. 7, p 404.
41. Rietveld, H. M., A Profile Refinement Method for Nuclear and Magnetic Structures. *J. Appl. Crystallogr.* **1969,** *2*, 65-71.
42. Massa, W., *Crystal Structure Determination*. 2nd ed.; Springer: Verlag, Germany, 2004.
43. Patterson, A. L., The Scherrer formula for x-ray particle-size determination. *Physical Review* **1939,** *56*, 978-82.
44. Billinge, S. J. L.; Kanatzidis, M. G., Beyond crystallography: the study of disorder, nanocrystallinity and crystallographically challenged materials with pair distribution functions. *Chem. Commun. (Cambridge, U. K.)* **2004,** (7), 749-760.
45. Assmus, W.; Bruehne, S., Rudiments of crystallography. *Springer Handb. Condens. Matter Mater. Data* **2005**, 27-41.
46. Billinge, S., Local structure from total scattering and atomic pair distribution function (PDF) analysis. *Powder Diffr.* **2008**, 464-493.
47. Billinge, S. J. L., Real-space Rietveld: full profile structural refinement of the atomic pair distribution function. *Local Struct. Diffr., [Proc. Conf.]* **1998**, 137-156.
48. Billinge, S. J. L., Strain, nano-phase separation, multi-scale structures and function of advanced. *Los Alamos Natl. Lab., Prepr. Arch., Condens. Matter* **2002**, 1-17, arXiv:cond-mat/0210559.
49. Billinge, S. J. L., Strain, nano-phase separation, multiscale structures and function of advanced materials. *Intrinsic Multiscale Struct. Dyn. Complex Electron. Oxides, Proc. Workshop* **2003**, 25-40.
50. Billinge, S. J. L., The atomic pair distribution function: Past and present. *Z. Kristallogr.* **2004,** *219* (3), 117-121.
51. Billinge, S. J. L., Nanoscale structural order from the atomic pair distribution function (PDF): There's plenty of room in the middle. *J. Solid State Chem.* **2008,** *181* (7), 1695-1700.
52. Egami, T.; Poon, S. J., Atomic structure of quasicrystals. *Mater. Sci. Eng.* **1988,** *99*, 323-9.
53. Farrow, C. L.; Juhas, P.; Liu, J. W.; Bryndin, D.; Bozin, E. S.; Bloch, J.; Proffen, T.; Billinge, S. J. L., PDFfit2 and PDFgui: computer programs for studying nanostructure in crystals. *J. Phys.: Condens. Matter* **2007,** *19* (33), 335219/1-335219/7.
54. Fitch, A. N., Applications of high-resolution powder X-ray diffraction. *Diffus. Defect Data, Pt. B* **2007,** *130* (Applied Crystallography XX), 7-14.
55. Kodama, K., Local structural analysis on crystalline materials by using atomic pair distribution function (PDF). *Seramikkusu* **2008,** *43* (11), 909-916.
56. Petkov, V.; Billinge, S. J. L.; Heising, J.; Kanatzidis, M. G.; Shastri, S. D.; Kycia, S., High real-space resolution structure of materials by high-energy x-ray diffraction. *Mater. Res. Soc. Symp. Proc.* **2000,** *590* (Applications of Synchrotron Radiation Techniques to Materials Science V), 151-156.

57. Proffen, T., Analysis of disordered materials using total scattering and the atomic pair distribution function. *Rev. Mineral. Geochem.* **2006,** *63* (Neutron Scattering in Earth Sciences), 255-274.
58. Proffen, T.; Billinge, S. J. L.; Egami, T.; Louca, D., Structural analysis of complex materials using the atomic pair distribution function - a practical guide. *Z. Kristallogr.* **2003,** *218* (2), 132-143.
59. Proffen, T.; Page, K. L., Obtaining structural information from the atomic pair distribution function. *Z. Kristallogr.* **2004,** *219* (3), 130-135.
60. Debye, P., Dispersion of R.ovrddot.ontgen rays. *Annalen der Physik (Berlin, Germany)* **1915,** *46*, 809-23.
61. Zernire, F.; Prins, J. A., The bending of x-rays in liquids as an effect of molecular arrangement. *Zeitschrift fuer Physik* **1927,** *41*, 184-94.
62. Debye, P.; Menke, H., The determination of the inner structure of liquids by x-ray means. *Physikalische Zeitschrift* **1930,** *31*, 797-8.
63. Benmore, C., Pair Distribution Function Analysis. In *National School of Neutron and X-ray Scattering*, Oakridge National Laboratory, 2009.
64. Proffen, T.; Billinge, S. J. L., PDFFIT, a program for full profile structural refinement of the atomic pair distribution function. *J. Appl. Crystallogr.* **1999,** *32* (3), 572-575.
65. Petkov, V.; Gateshki, M.; Niederberger, M.; Ren, Y., Atomic-Scale Structure of Nanocrystalline BaxSr1-xTiO3 (x = 1, 0.5, 0) by X-ray Diffraction and the Atomic Pair Distribution Function Technique. *Chem. Mater.* **2006,** *18* (3), 814-821.
66. Bruehne, S.; Gottlieb, S.; Assmus, W.; Alig, E.; Schmidt, M. U., Atomic Structure Analysis of Nanocrystalline Boehmite AlO(OH). *Cryst. Growth Des.* **2008,** *8* (2), 489-493.
67. Bunker, G., XAFS Introduction. In *XAFS Tutorial Documents*, http://gbxafs.iit.edu/training/tutorials.html: 2009.
68. Bunker, G., *Introduction to XAFS: A Practical Guide to X-ray Absorption Fine Structure Spectroscopy*. Cambridge University Press: Cambridge, UK, 2010; p 260.
69. Nelson, R. C.; Miller, J. T., An introduction to X-ray absorption spectroscopy and its in situ application to organometallic compounds and homogeneous catalysts. *Catalysis Science & Technology* **2012,** *2* (3), 461-470.
70. Koningsberger, D. C.; Prins, R., *Chemical Analysis, Vol. 91: X-ray Absorption: Principles, Applications, Techniques of EXAFS SEXAFS, and XANES*. 1988; p 673 pp.
71. Lee, P. A.; Citrin, P. H.; Eisenberger, P.; Kincaid, B. M., Extended x-ray absorption fine structure - its strengths and limitations as a structural tool. *Reviews of Modern Physics* **1981,** *53* (4, Pt. 1), 769-806.
72. Meitzner, G., Experimental aspects of x-ray absorption spectroscopy. *Catalysis Today* **1998,** *39* (4), 281-291.
73. Teo, B. K.; Joy, D. C., *EXAFS (extended X-ray absorption fine structure) spectroscopy: techniques and applications*. Plenum Press: New York, 1981.
74. de Groot, F. M. F.; Knop-Gericke, A.; Ressler, T.; van Bokhoven, J. A., *In-Situ Spectroscopy of Catalysts*. American Scientific Publishers: 2004; p 107-174.
75. Faraci, G., Nanocluster characterization by EXAFS spectroscopy. *Encyclopedia of Nanoscience and Nanotechnology* **2004,** *6*, 197-214.
76. Teo, B. K., *EXAFS: Basic Principles and Data Analysis*. Springer-Verlag: Berlin, Germany, 1986; p 349.

77. Lytle, F. W.; Sayers, D. E.; Stern, E. A., The history and modern practice of EXAFS spectroscopy. *Adv. X-Ray Spectrosc.* **1982**, 267-86.
78. Kronig, R. d. L., The theory of fine structure in the x-ray absorption spectra. *Zeitschrift fuer Physik* **1931,** *70*, 317-23.
79. Kronig, R. d. L., Theory of fine structure of x-ray absorption spectra. III. *Zeitschrift fuer Physik* **1932,** *75*, 468-75.
80. Sayers, D. E.; Stern, E. A.; Lytle, F. W., Application of EXAFS [extended x-ray absorption fine structure] to amorphous structure studies. *Transactions of the American Crystallographic Association* **1974,** *10*, 45-60.
81. Stern, E. A., Theory of the extended x-ray-absorption fine structure. *Physical Review B: Solid State* **1974,** *10* (8), 3027-37.
82. Stern, E. A.; Sayers, D. E.; Lytle, F. W., Extended x-ray-absorption fine-structure technique. III. Determination of physical parameters. *Physical Review B: Solid State* **1975,** *11* (12), 4836-46.
83. Eisenberger, P.; Kincaid, B. M., Synchrotron radiation studies of x-ray absorption spectra of ions in aqueous solutions. *Chemical Physics Letters* **1975,** *36* (1), 134-6.
84. Kincaid, B. M.; Eisenberger, P., Synchrotron radiation studies of the K-edge photoabsorption spectra of krypton, bromine, and germanium tetrachloride. Comparison of theory and experiment. *Physical Review Letters* **1975,** *34* (22), 1361-4.
85. Lee, P. A.; Pendry, J. B., Theory of the extended x-ray absorption fine structure. *Physical Review B: Solid State* **1975,** *11* (8), 2795-811.
86. Rehr, J. J.; Albers, R. C., Theoretical approaches to x-ray absorption fine structure. *Reviews of Modern Physics* **2000,** *72* (3), 621-654.
87. Miller, J. T., EXAFS fitting. Workshop, Ed. Argonne, IL, 2010.
88. Ravel, B., A practical introduction to multiple scattering theory. *Journal of Alloys and Compounds* **2005,** *401* (1-2), 118-126.
89. Newville, M., IFEFFIT: interactive XAFS analysis and FEFF fitting. *Journal of Synchrotron Radiation* **2001,** *8* (2), 322-324.
90. Newville, M., EXAFS analysis using FEFF and FEFFIT. *Journal of Synchrotron Radiation* **2001,** *8* (2), 96-100.
91. Ravel, B.; Newville, M., ATHENA, ARTEMIS, HEPHAESTUS: data analysis for x-ray absorption spectroscopy using IFEFFIT. *Journal of Synchrotron Radiation* **2005,** *12* (4), 537-541.
92. Reimer, L.; Kohl, H., *Transmission Electron Microscopy: Physics of Image Formation and Microanalysis, Fifth Edition*. Springer Science: New York, NY, 2008; Vol. 36, p 584 pp.
93. Williams, D. B.; Carter, C. B., *Transmission Electron Microscopy: A Textbook for Materials Science*. Second ed.; Springer: New York, NY, 2009.
94. Lentzen, M., Aberration-corrected high-resolution transmission electron microscopy. *Schriften des Forschungszentrums Juelich, Reihe Materie und Material* **2007,** *34* (Probing the Nanoworld: Microscopies, Scattering and Spectroscopies of the Solid State), C1/1-C1/14.
95. Browning, N. D.; James, E. M.; Kishida, K.; Arslan, I.; Buban, J. P.; Zaborac, J. A.; Pennycook, S. J.; Xin, Y.; Duscher, G., Scanning transmission electron microscopy. An experimental tool for atomic scale interface science. *Reviews on Advanced Materials Science* **2000,** *1* (1), 1-26.

96. Cowley, J. M., Electron nanodiffraction and STEM imaging of nanoparticles and nanotubes. *Advances in Metal and Semiconductor Clusters* **1998,** *4* (Cluster Materials), 67-113.
97. Nellist, P. D., Scanning transmission electron microscopy. *Science of Microscopy* **2007,** *1*, 65-132.
98. Rice, S. B.; Bradley, S. A., Imaging supported metal catalysts: the case for annular dark-field microscopy. *Catalysis Today* **1994,** *21* (1), 71-82.
99. Peacor, D. R., Analytical electron microscopy: x-ray analysis. *Reviews in Mineralogy* **1992,** *27* (Miner. React. At. Scale: Transm. Electron Microsc.), 113-40.
100. Duer, M. J., *Introduction to Solid-State NMR Spectroscopy*. Blackwell Publishing Ltd: Malden, MA, 2004; p 349.
101. Duer, M. J., *Solid-State NMR Spectroscopy: Principles and Applications*. Blackwell Science: Malden, MA, 2002; p 563.
102. Bakhmutov, V. I., *Solid-State NMR in Materials Science: Priciples and Applications*. CRC Press: Boca Raton, FL, 2012.
103. Brunauer, S.; Deming, L. S.; Deming, W. E.; Teller, E., A theory of the van der Waals adsorption of gases. *Journal of the American Chemical Society* **1940,** *62*, 1723-32.
104. Lercher, J. A., Adsorption methods for the assessment of the specific surface area, the pore size distribution and the active sites of heterogeneous catalysts. *Studies in Surface Science and Catalysis* **1999,** *123* (Catalysis: An Integrated Approach (2nd Edition)), 543-566.
105. Sing, K. S. W., Adsorption methods for the characterization of porous materials. *Advances in Colloid and Interface Science* **1998,** *76-77*, 3-11.
106. Dubinin, M. M., Porous structure and adsorption properties of active carbons. *Chemistry and Physics of Carbon* **1966,** *2*, 51-120.
107. Gregg, S. J.; Sing, K. S. W., *Adsorption, Surface Area and Porosity. 2nd Ed*. 1982; p 303.
108. Sing, K. S. W.; Everett, D. H.; Haul, R. A. W.; Moscou, L.; Pierotti, R. A.; Rouquerol, J.; Siemieniewska, T., Reporting physisorption data for gas/solid systems with special reference to the determination of surface area and porosity (Recommendations 1984). *Pure and Applied Chemistry* **1985,** *57* (4), 603-19.
109. Sing, K., The use of nitrogen adsorption for the characterization of porous materials. *Colloids and Surfaces, A: Physicochemical and Engineering Aspects* **2001,** *187-188*, 3-9.
110. Gregg, S. J., Adsorption of gases - tool for the study of the texture of solids. *Studies in Surface Science and Catalysis* **1982,** *10* (Adsorpt. Gas-Solid Liq.-Solid Interface), 153-64.
111. Llewellyn, P. L.; Maurin, G., Gas adsorption in zeolites and related materials. *Studies in Surface Science and Catalysis* **2007,** *168* (Introduction to Zeolite Molecular Science and Practice), 555-610.
112. Rouquerol, F.; Rouquerol, J.; Sing, K. S. W., The experimental approach [to adsorption]. *Handbook of Porous Solids* **2002,** *1*, 236-275.
113. Salvador, F.; Sanchez-Jimenez, C.; Sanchez-Montero, M. J.; Salvador, A., A review of the application of the BET equation to experimental data. The C parameter. *Studies in Surface Science and Catalysis* **2002,** *144* (Characterization of Porous Solids VI), 379-386.
114. Sing, K. S. W.; Williams, R. T., Empirical procedures for the analysis of physisorption isotherms. *Adsorption Science & Technology* **2005,** *23* (10), 839-853.

115. Langmuir, I., Constitution and fundamental properties of solids and liquids. I. Solids. *Journal of the American Chemical Society* **1916,** *38*, 2221-95.
116. Brunauer, S.; Emmett, P. H.; Teller, E., Adsorption of gases in multimolecular layers. *Journal of the American Chemical Society* **1938,** *60*, 309-19.
117. Foster, A. G., Sorption of condensable vapors by porous solids. I. Applicability of the capillary theory. *Transactions of the Faraday Society* **1932,** *28*, 645-57.
118. Shull, C. G.; Elkin, P. B.; Roess, L. C., Physical studies of gel microstructure. *Journal of the American Chemical Society* **1948,** *70*, 1410-14.
119. Barrett, E. P.; Joyner, L. G.; Halenda, P. P., The determination of pore volume and area distributions in porous substances. I. Computations from nitrogen isotherms. *Journal of the American Chemical Society* **1951,** *73*, 373-80.

Chapter 2

Solvent-Deficiency: A General Method for Making Metal Oxide Nanomaterials

2.1 Introduction

Applications for high surface area metal oxide nanomaterials are numerous and varied,[1] including such technologies as catalysis,[2-4] gas sensing,[5] optical coatings,[1,6-7] gate dielectrics,[8] diodes,[9] solar cells,[1,10] batteries,[11] and ultrafiltration membranes.[12] Even biotech industries are finding application for nano metal oxides in MRI imaging agents,[13-14] dental implants,[15] cosmetics,[1,16] and hygiene products.[17] Because most of these applications require particles below 100 nm in size[2,7,12,14,18-20] with many requiring sizes below 20 nm,[3-4,6,21-23] the key to developing and utilizing these burgeoning industrial nanotechnologies lies in being able to efficiently produce the nanomaterials they use.

This chapter reports a novel synthetic technique capable of efficiently producing a vast array of relatively high surface area metal oxide nanomaterials.[24] Originally developed to obtain a high purity CoO nanoparticle sample for heat capacity studies, the synthetic method has since been successfully applied in the synthesis of 23 different binary metal oxide nanomaterials. Among the products are at least one binary metal oxide nanomaterial from every transition metal group (Groups 3-4 and 6-12) and semi-metal group (Groups 13-15) in the periodic table as well as several from the lanthanide group. The method itself is similar to co-precipitation[18,25] but is unique in that H_2O in traditional solvent quantities is not added, and this "solvent-deficient"

environment appears to be crucial for enabling the formation of nanomaterials without the use of the capping agents typically required by co-precipitation.[20] In the following sections, the methodology of the solvent-deficient technique is outlined along with XRD, TEM, BET, and chemical purity characterizations of the many binary metal oxide products.

2.2 Experimental Methods

2.2.1 Overview of the Method

The solvent-deficient method consists of two primary steps with a third intermediate step (in gray) incorporated for some samples:

$$MX_y \bullet xH_2O + yNH_4HCO_3(s) \xrightarrow{\text{Grind}} \text{Precursor}(s) \xrightarrow{\text{Rinse}} \text{Rinsed Precursor}(s) \xrightarrow{\text{Heat}} \text{nano } M_aO_b(s) \qquad \text{Eq. 2.1}$$

In the first step, a hydrated metal salt ($MX_y \bullet xH_2O$, where X = NO_3^- or Cl^- and x = 6-9) is ground with bicarbonate (usually NH_4HCO_3 but $NaHCO_3$ can also be used) using a mortar and pestle. The moles of bicarbonate, y, should equal the moles of anion from the metal salt, as Eq. 2.1 indicates. We have noticed that if the metal salt is anhydrous or has < 6 moles of water per mole of salt, enough water must be added as the reagents are mixed to mimic the 6-9 moles of hydration present in most metal salts. For chloride metal salt reagents which have very exothermic reactions with water in which HCl gas is released, the water should be added slowly or dropwise while the reagents are ground together under a ventilated hood. This amount of water (6-9 moles per mole of metal salt reagent) is so minimal compared to the hundreds of moles of H_2O typically present in aqueous methods such as co-precipitation (for example, over 550 moles H_2O per mole of metal salt are in a 0.1 M solution), that the water cannot be considered a true solvent. Yet, because the process is not without some semblance of a solvent, we have named the method "solvent-deficient."

(a) (b) (c) (d) (e) (f)

Figure 2.1 First step (grinding) in the solvent-deficient synthetic method.

As Figure 2.1a-d shows, even though no true solvent is added, when the (typically solid) reagents are ground together, the mixture liquefies and bubbles vigorously, producing faint popping noises. The reagents should be ground until this bubbling/popping subsides (see Figure 2.1e), which can require 5-30 min of grinding. The grinding time decreases with increasing levels of hydration; hexahydrates require 20-30 minutes of grinding whereas nonahydrates require 5-15 minutes. We therefore typically add just enough water to make the metal salt a nona-hydrate, as this makes the reaction proceed more easily and quickly. Interestingly, the reaction is quite endothermic; the mortar becomes quite cool to the touch as grinding proceeds.

The grinding reaction produces a slurry/paste of solid precipitate particles (Figure 2.1e) which we call the precursor. For several materials (see Table 2.1), the precursor slurry should then be rinsed using a polar solvent; we typically use distilled H_2O and a vacuum filter flask to wash the precursor 2-5 times, though various alcohols have also been used as the rinsing agent. The precursor (either rinsed or untreated) can be dried in air at 50-100°C for several hours to form a powder (Figure 2.1f) that can be stored indefinitely, but in general, we do not dry the precursor before the final calcination step. Only a few precursors benefit from a drying step (see Table 2.1).

In the final calcination step, which is either the second or third step depending on whether or not rinsing is performed, the precursor (in the slurry, rinsed, or dried form) is transferred to a crucible and calcined at relatively low temperatures (220-550°C) in air (unless otherwise

specified) for 1-3 hours to produce the desired nanomaterial (see Table 2.1). For each material, a heating rate of 5°C/min is generally used to reach the calcination temperature. If large quantities (≥ 5 g) of nanomaterial are being calcined, the effluent gases should be directed through either a filtration system or a hood.

Table 2.1 Summary of synthetic parameters for each nanomaterial. Included are the metal salt reagent(s) used, the ratio of the metal salt to the bicarbonate (BC) reagent, whether or not a rinsing step was included and why (P = to increase purity, O = to maintain a particular metal oxidation state, and S = to produce a smaller crystallite size), calcination temperature, calcination time, calcination atmosphere, and the average yield of the given product.

Group	**Metal Salt Reagents**	**Reagent Mole Ratios** (Salt:BC)	**Rinsing (R) Drying (D) Steps**	**Calc. Temp.** (°C)	**Calc. Time** (hrs)	**Calc. Atm.**	**% Yield**	**Product**
			Transition metal oxides					
3	$Y(NO_3)_3•6H_2O$	1:3	-	475	1	air	>100%	Y_2O_3
4	$TiCl_4$	1:4	D,R^P	400	3	air	61%	$TiO_2^{anatase}$
4	$ZrCl_4$	1:4	R^P	350	2	air	78%	ZrO_2
6	$MoCl_5$	1:5	$R^{P,O}$	350	1	air*	70%	MoO_3
7	$MnCl_2•4H_2O$	1:2	$R^{P,O}$	500	2	air*	63%	α-Mn_2O_3
8	$Fe(NO_3)_3•9H_2O$	1:3	R^S	350	1	air	>100%	Fe_2O_3
8	$FeCl_3 + FeCl_2$	1:1.5:11	R^P	550	3.5	inert		Fe_3O_4
9	$Co(NO_3)_2•6H_2O$	1:2	$R^{O,S}$	300	1	inert	98%	CoO
9	$Co(NO_3)_2•6H_2O$	1:2	R^S	300	2	air*	93%	Co_3O_4
10	$Ni(NO_3)_2•6H_2O$	1:2	R^S	300	2	air	86%	NiO
10	$Pd(Cl)_2•xH_2O$	1:2[+]	D,R^P,D	375	1	air		PdO
11	$Cu(NO_3)_2•6H_2O$	1:2[+]	R^S	250	1	air	>100%	CuO
11	$AgNO_3$	1:1[+]	R^P	220	1	air*	99%	Ag_2O
12	$Zn(NO_3)_2•6H_2O$	1:2[+]	$R^{P,S}$	250	1	air	>100%	ZnO^{white}
	$Zn(NO_3)_2•6H_2O$	1:2	-	300	2	air	84%	ZnO^{pink}
			Semi-metal oxides					
13	$Al(NO_3)_3•9H_2O$	1:3	-	700	2	air	>100%	γ-Al_2O_3
13	$Al(NO_3)_3•9H_2O$	1:3	-	1100	2	air	97%	α-Al_2O_3
13	$In(NO_3)_3•xH_2O$	1:3	-	300	2	air	83%	In_2O_3
14	$SnCl_4$	1:4	$R^{P,O}$	340	1	air*	85%	SnO_2
15	$Bi(NO_3)_3•5H_2O$	1:3	R^O	400	2	air	97%	Bi_2O_3
			Lanthanide metal oxides					
	$Ce(NO_3)_4•6H_2O$	1:4	-	300	2	air*	>100%	CeO_2
	$Pr(NO_3)_3•6H_2O$	1:3	-	550	3	air*	97%	PrO_2
	$Nd(NO_3)_3•6H_2O$	1:3	-	550	3	air	>100%	Nd_2O_3

[+] $NaHCO_3$ should be used instead of NH_4HCO_3 to avoid NH_3 complexation

* Denotes precursors that may produce different oxides if calcined in a different environment

Yields >100% are attributed to adsorbed H_2O. Fe_3O_4 and Ag_2O were synthesized once; the yield was not tracked

These steps form the basis of the method. Table 2.1 provides a list of the specific reaction parameters used for each material produced thus far. Most of these syntheses have been performed numerous times, though the given yields and characterizations are for a single, representative batch of each sample using roughly 10-20 grams of metal salt reagent.

2.2.2 Characterization Methods

All nanomaterials produced and their crystallographic phases/phase-purities were identified using powder X-ray diffraction (XRD). A PANalytical X'Pert Pro diffractometer with a Cu source and a Ge monochromator tuned to the Cu-$K_{\alpha 1}$ wavelength (λ = 1.5406 Å) was used to scan each nanomaterial from 10-90°2θ with a step size of 0.016° at rates between 0.7 to 3.0 s/step. Each pattern was matched to a standard pattern in the ICDD (International Center for Diffraction Data) database. Crystallite sizes were estimated using the Scherrer formula for size-related peak broadening.[26] Transmission electron microscope (TEM) images were used to visually confirm the average size and to estimate the size distribution of the particles. Approximately 20-30 images of each product were used to make these estimates.

TEM images of each nanomaterial were recorded using either a FEI Philips Technai F30 operating at 300 kV or a FEI Philips Technai F20 Analytical STEM operating at 200 kV. Specimens were prepared by dispersing the nanoparticles in ethanol and placing a drop of the dilute solution on a formvar/carbon film supported by a 200 mesh Cu or Ni grid (Ted-Pella Inc.). The solvent was allowed to evaporate, and images were recorded in standard high resolution mode. The images were used to assess the crystallinity, size, and morphology of both the particles and agglomerates. The *d*-spacings of the visible lattice fringes were measured and compared with those of the standard crystal structures from the XRD analyses to confirm the crystal structure and to assign crystal plane indices in the images.

Chemical purity was assessed for a representative subgroup of samples including at least 1 sample from each group in the periodic table from which a metal oxide nanomaterial has been produced (Groups 3, 4, 6, 7, 8, 9, 10 ,11, 12, 13, 14, and 15 as well as the Lanthanides). Impurity contents were quantified by Galbraith Laboratories through combustion analyses (to determine the C, H, and N content) and through nonaqueous, ion-exchange chromatography (to determine the Cl^- content, where applicable).

Agglomerate sizes of the same subgroup of samples were analyzed using a Nanosight LM20 microscope. Using a small drop of a very dilute aqueous suspension, particle agglomerates were directly visualized and tracked via light scattering analysis. Agglomerate size statistics were generated based on the Brownian motion of between 500-1500 tracks. Multiple (2-3) analyses were averaged for those samples with lower tracking numbers than this. The d50 and d90 sizes (*i.e.* the sizes under which 50% and 90% of the particles fall) are reported here. The agglomerates of a few samples (Al_2O_3, CeO_2) were milled using a Netzsch MiniCer mill to investigate the feasibility of breaking apart the nanoparticle agglomerates. For the milling, the nanomaterials were suspended in distilled water, forming a 30% solution by mass.

Brunauer-Emmett-Teller (BET) specific surface areas of several of the samples were determined from N_2 adsorption at 77 K using a Micromeritics TriStar II instrument. For the experiments, roughly 200 mg of each sample were degassed at 200°C for 24 hours and then allowed to cool to room temperature prior to the analysis.

2.3 Results and Discussion

The XRD pattern and TEM images of each nanomaterial are given in Figure 2.2. The XRD patterns confirm the identity of each material and indicate that the products are generally

phase-pure.[ix] The high-magnification TEM images in Figure 2.2 highlight the crystallinity of the nanoparticles; the atomic planes are clearly visible and extend to the edges of the crystallites. Thus, low-crystallinity is not a problem exhibited by the solvent-deficient method, in contrast to many other aqueous solution methods. Additionally, the good agreement between the measured and expected *d*-spacings of the crystal planes (Figure 2.2) indicates that the particles exhibit little or no stress/strain in the crystal structure.

The TEM images also reveal the morphologies of the crystallites produced by the solvent-deficient method and enable direct observation of their size and size distribution. The crystallites have roughly spherical morphologies with the exception of the Y_2O_3 particles which are rod-like. The visible diameters of the roughly spherical crystallites confirm the calculations of the particle sizes from XRD data and allow the size distribution to be estimated. The resulting size and size distribution estimates (Table 2.2) reveal that all of the products have average crystallite diameters well below 100 nm with about 75% having average diameters below 20 nm. Thus, the products of the solvent deficient method satisfy the stringent size requirements for most applications of metal oxide nanomaterials.

Figure 2.2 XRD patterns and TEM images (one of higher and one of lower magnification) of the metal oxide nanomaterials synthesized using the solvent-deficient method. The legend of each XRD pattern gives the reference number of the ICDD pattern (red) matched to each product (black). The lower magnification TEM image below each XRD pattern illustrates the agglomerated nature of the products. The individual crystallites are more clearly visible in the high magnification TEM images, and the atomic fringes visible in these images were measured to compare the *d*-spacings to the expected values from the standard XRD patterns. For each highlighted and numbered lattice fringe, the crystal plane index, measured *d*-spacing, and expected *d*-spacing (in parentheses) are listed below the image. Products are organized according to group: (a) Groups 3 and 4, (b) Groups 6, 7, and 8, (c) Groups 9 and 10, (d) Groups 11 and 12, (e) Groups 13 and 14, (f) Group 15 and the Lanthanides. No lattice fringes were clearly visible in the selected images of PdO and Ag_2O due to the particle orientations, and the MoO_3 and Nd_2O_3 sustained too much beam damage for the lattice fringes to be effectively imaged, thus *d*-spacing and index assignments are not given for these products.

[ix] Nd_2O_3 may contain a very small amount of the hexagonal phase in addition to the main, cubic phase.

(a)

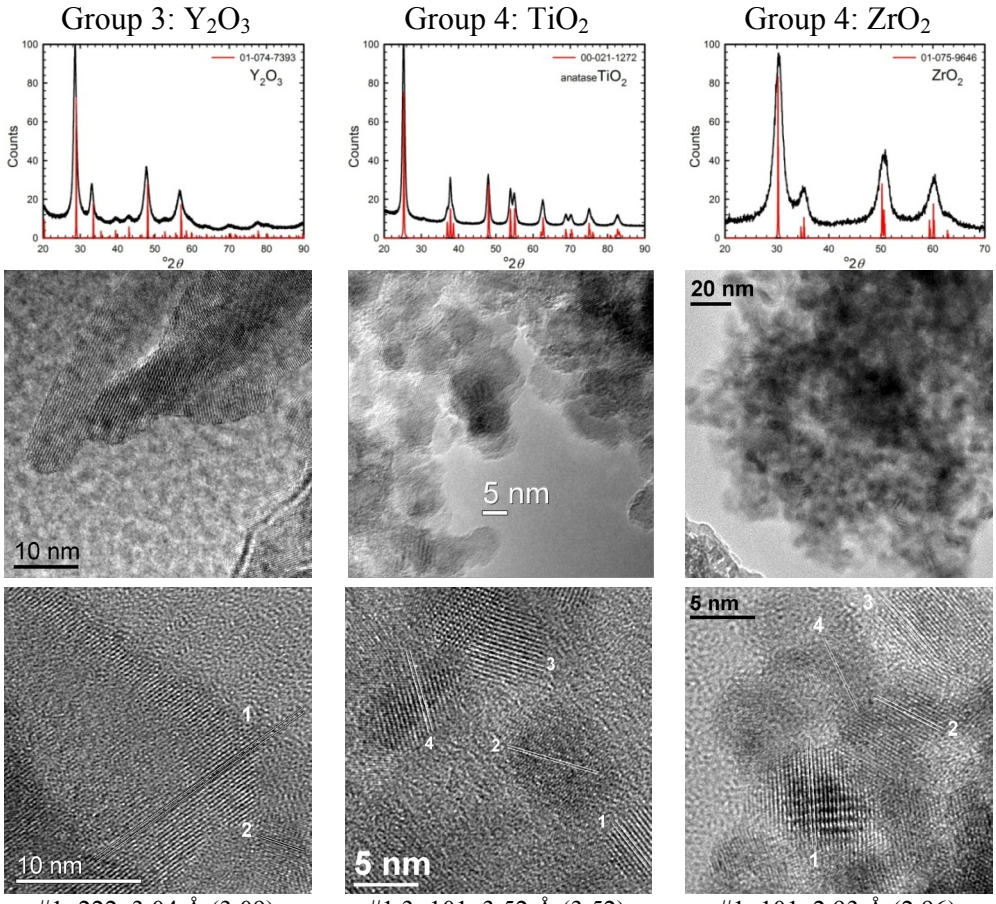

#1: 222, 3.04 Å (3.09)
#2: 440, 1.88 Å (1.89)

#1,3: 101, 3.52 Å (3.52)
#2: 004, 2.38 Å (2.38)
#4: 101, 3.51 Å (3.52)

#1: 101, 2.93 Å (2.96)
#2,3: 101, 2.92 Å (2.96)
#4: 112, 1.82 Å (1.82)

(b)

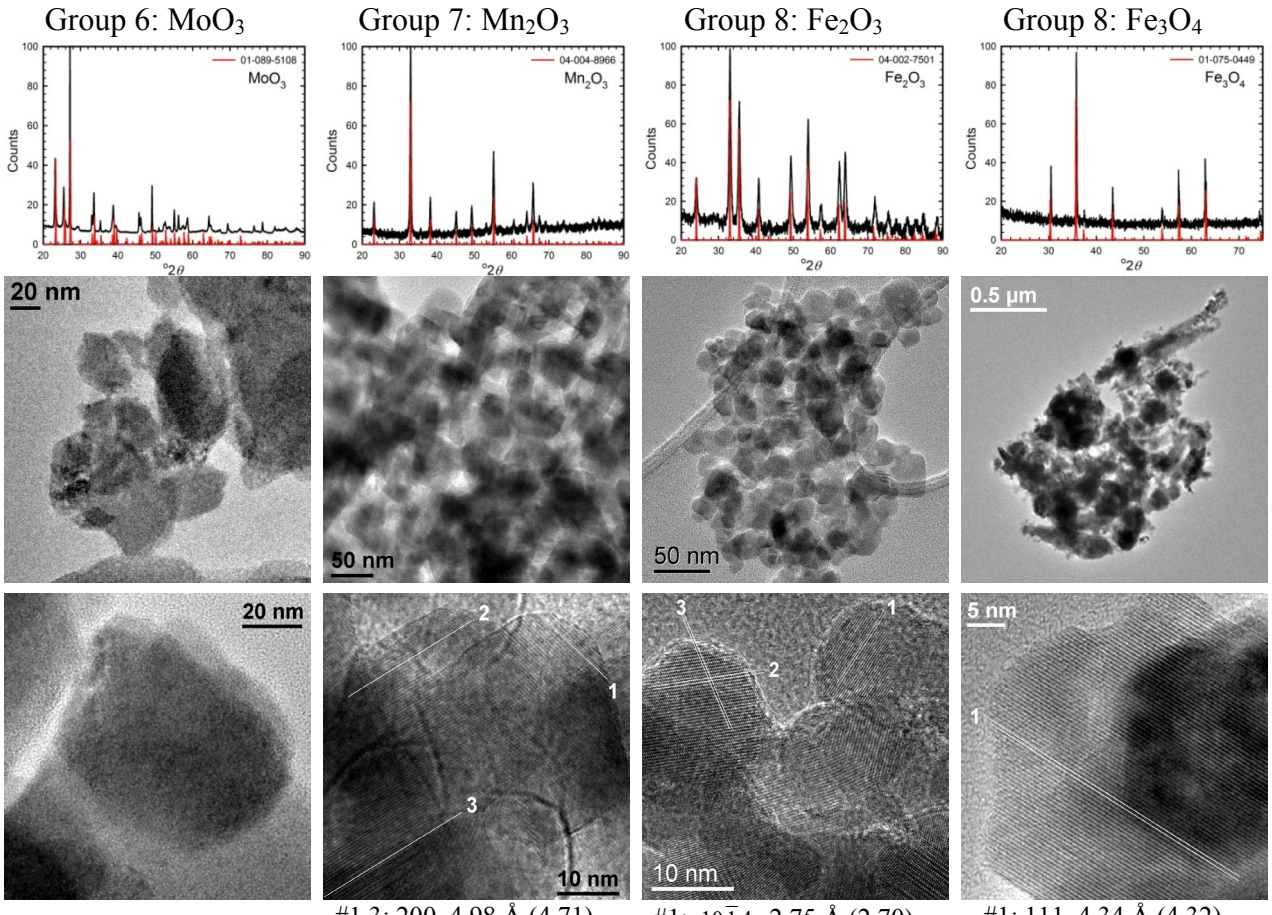

#1,3: 200, 4.98 Å (4.71)
#2: 222, 2.77 Å (2.72)

#1: $10\bar{1}4$, 2.75 Å (2.70)
#2: $01\bar{1}2$, 3.72 Å (3.68)
#3: $11\bar{2}3$, 2.22 Å (2.21)

#1: 111, 4.34 Å (4.32)

(c)

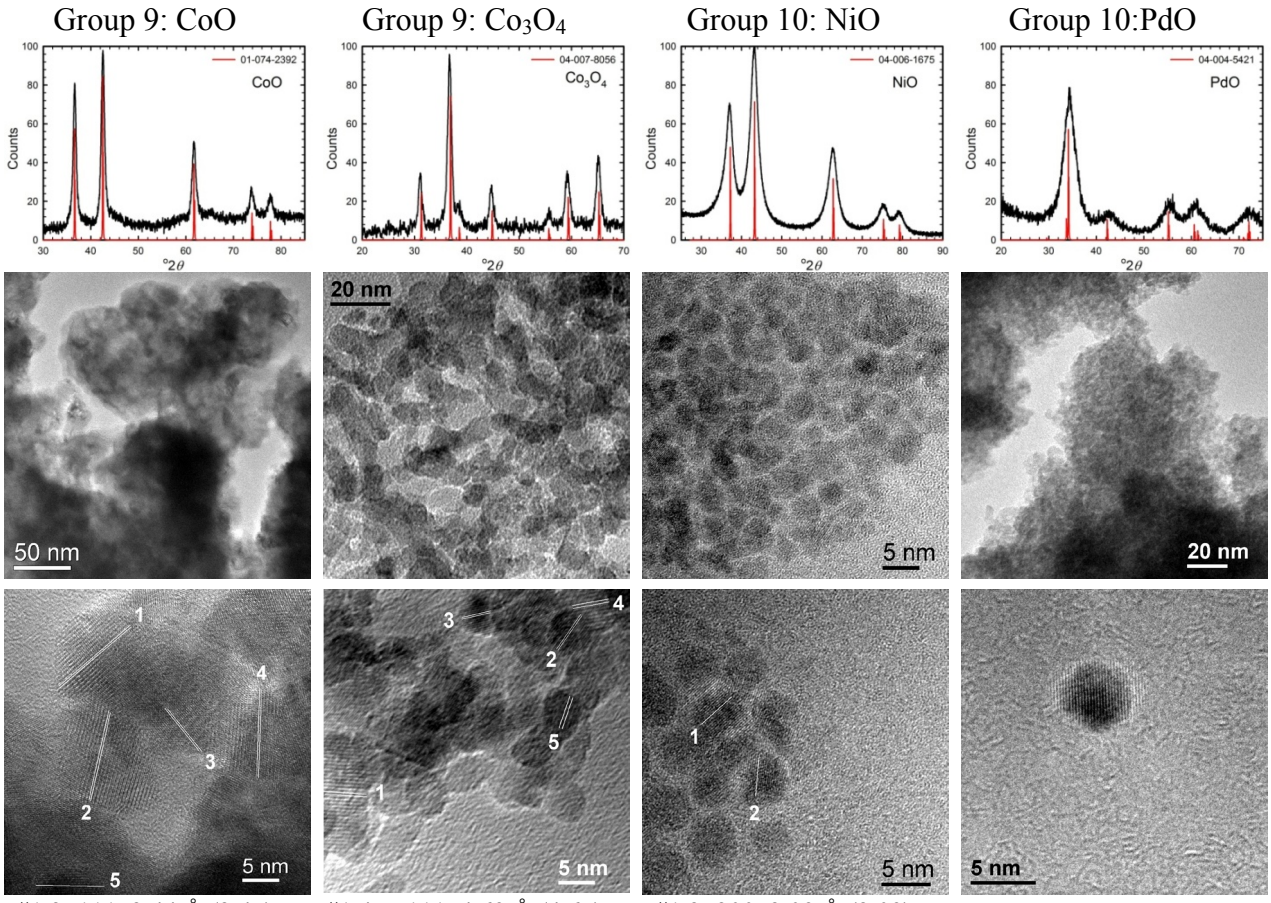

#1,3: 111, 2.44 Å (2.45)
#2,4: 111, 2.45 Å (2.45)
#5: 111, 2.13 Å (2.13)

#1,4.5: 111, 4.69 Å (4.67)
#2,3: 200. 2.91 Å (2.86)

#1,2: 200. 2.09 Å (2.09)

(d)

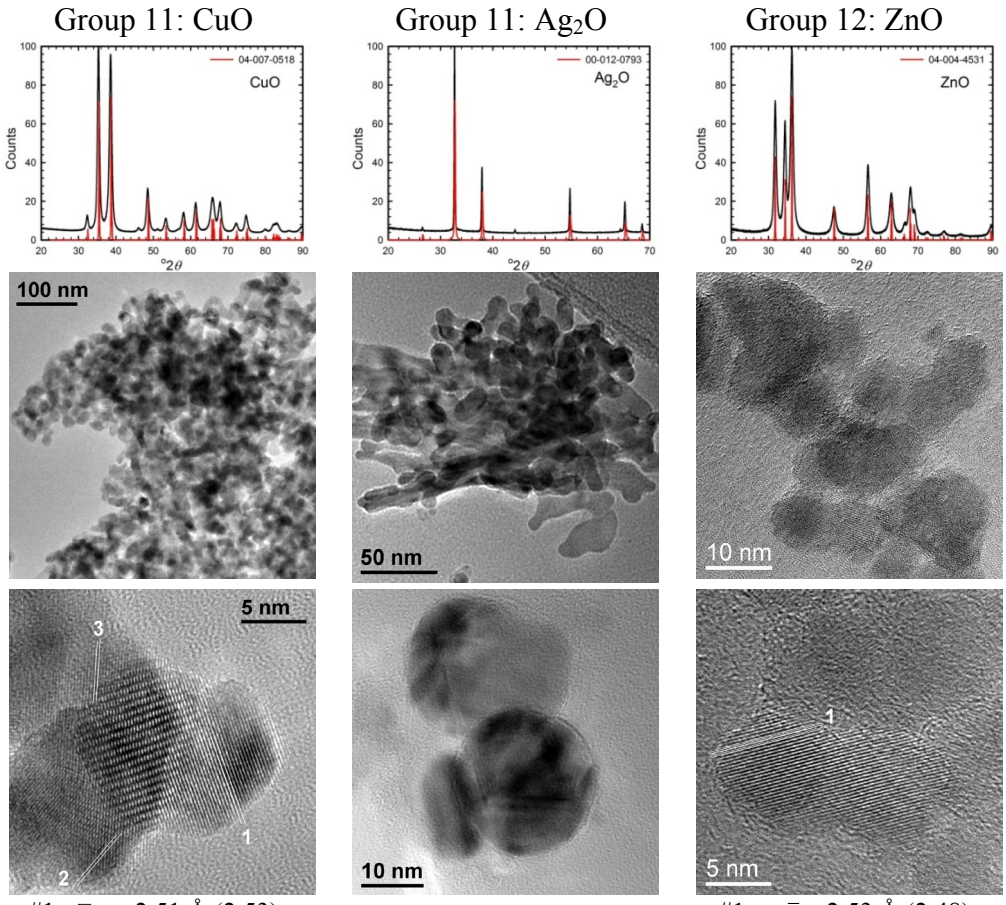

#1: $\bar{1}11$, 2.51 Å (2.53)
#2: 111, 2.34 Å (2.33)
#3: 111, 2.33 Å (2.33)

#1: $10\bar{1}1$, 2.53 Å (2.48)

(e)

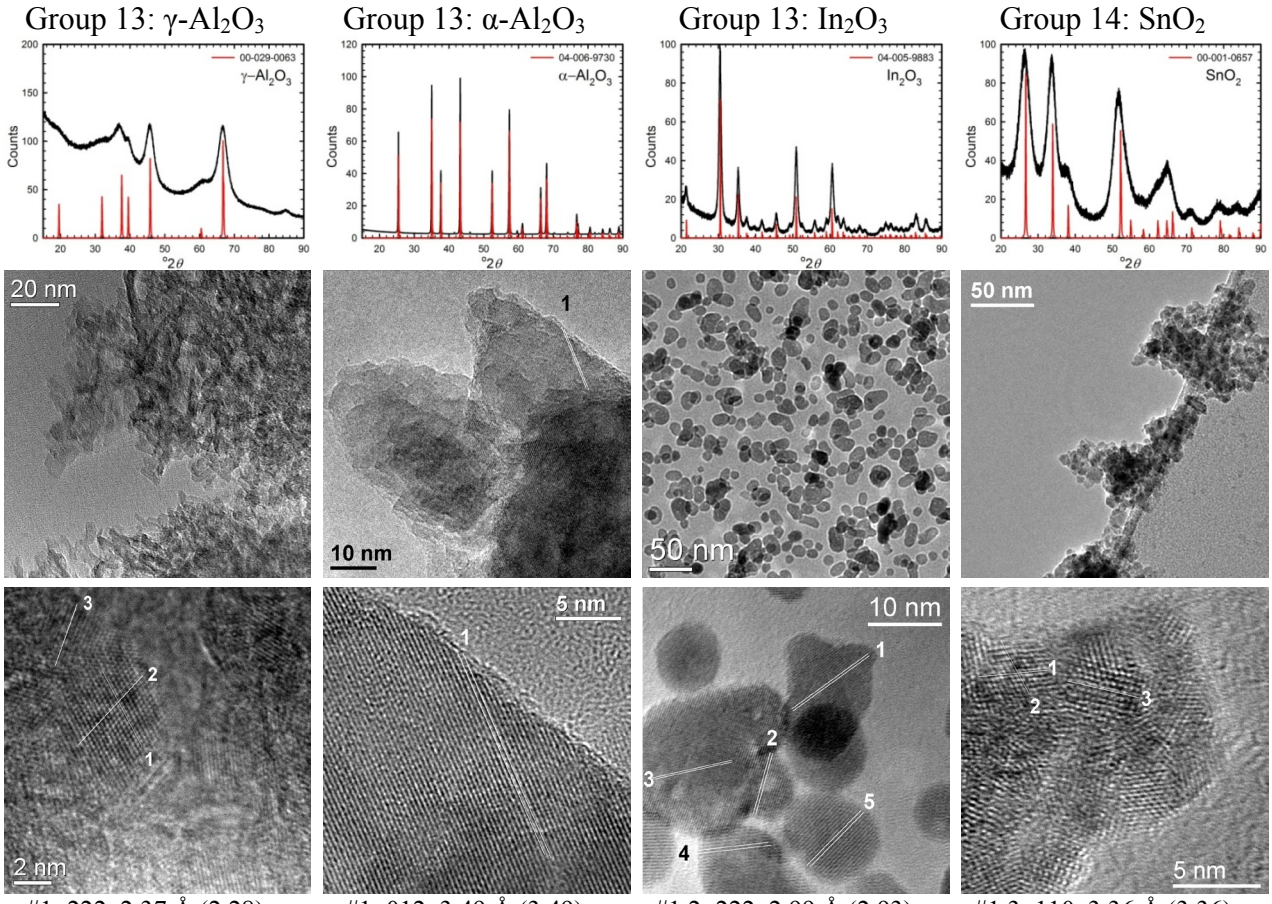

#1: 222, 2.37 Å (2.28)
#2: $\bar{2}22$, 2.37 Å (2.28)
#3: 400, 2.05 Å (1.98)

#1: 012, 3.49 Å (3.49)

#1,2: 222, 2.99 Å (2.93)
#3: 400, 2.57 Å (2.54)
#4,5: 211, 4.21 Å (4.14)

#1,3: 110, 3.36 Å (3.36)
#2: $_{101}$, 2.66 Å (2.65)

(f)

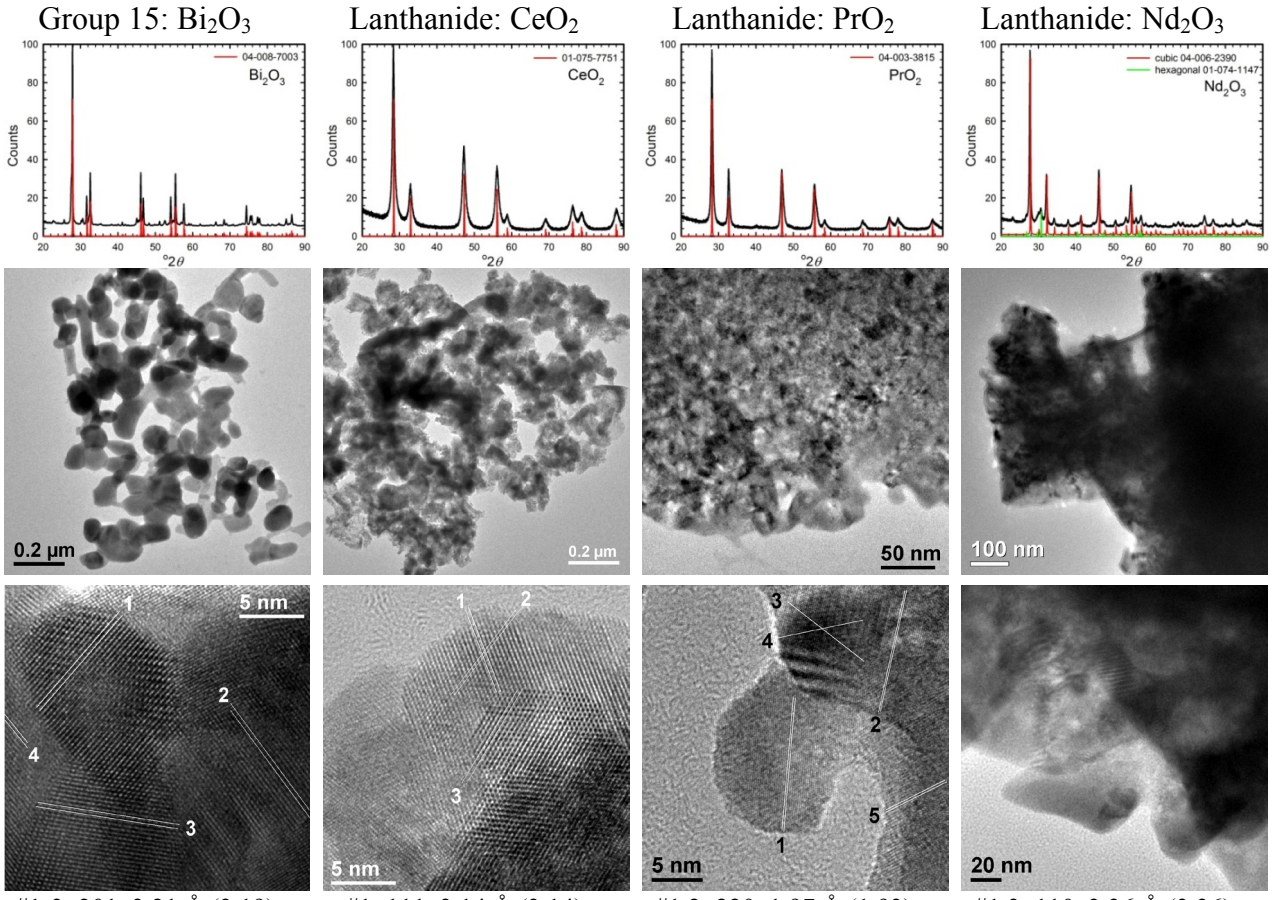

#1-3: 201, 3.21 Å (3.19)
#4: 002: 2.82 Å (2.81)

#1: 111, 3.14 Å (3.14)
#2: 200, 2.70 Å (2.72)
#3: 111, 3.16 Å (3.14)

#1,2: 220, 1.97 Å (1.93)
#3: 311, 1.69 Å (1.65)
#4: $\bar{3}11$, 1.69 Å (1.65)

#1,3: 110, 3.36 Å (3.36)
#2: 101, 2.66 Å (2.65)

Table 2.2 Summary of the size, surface area, and purity characterizations for the nanomaterial products.

Group	Product	Crystallite Size (nm)	Agglomerate Size (nm) (d50, d90)	Surface Area (m^2/g)	Pore Diam. (nm)	Impurity Contents			
						%C	*%H*	*%N*	*Cl⁻*
			Transition Metal Oxides						
3	Y_2O_3 (rods)	8(±1) x40(±10)	81, 302	3	97	0.70	1.10	0.68	-
4	$TiO_2^{anatase}$	8 (±2)	71, 104	80	7	<0.5	<0.5	<0.5	80ppm
4	ZrO_2	7 (±3)	73, 206	43	4				
6	MoO_3	25 (±15)	70, 98	2	26	<0.5	<0.5	<0.5	41ppm
7	α-Mn_2O_3	25 (±5)	55, 85	29	42	<0.5	<0.5	<0.5	
8	Fe_2O_3	8 (±3)	72, 169	178	4	<0.5	<0.5	<0.5	-
8	Fe_3O_4	50 (±20)	52, 67	5	10				
9	CoO	12 (±4)	86, 325	21	4	<0.5	<0.5	<0.5	-
9	Co_3O_4	10 (±4)	44, 76	22	10				
10	NiO	4 (±1)	67, 94	129	4	1.73	1.02	<0.5	-
10	PdO	3 (±1)							
11	CuO	15 (±5)	62, 89	40	41	<0.5	<0.5	<0.5	-
11	Ag_2O	42 (±20)	37, 60						
12	ZnO^{white}	8 (±5)	65, 79	52	34	<0.5	<0.5	<0.5	-
12	ZnO^{pink}	60(±25)	52, 110	1	0				
			Semi-metal Oxides						
13	γ-Al_2O_3	4 (±1)	73, 102	267	4	<0.5	1.57	<0.5	-
13	α-Al_2O_3	38 (±8)	61, 121	7	42				
13	In_2O_3	12 (±5)	71, 102	57	7				
14	SnO_2	4 (±1)	69, 187	145	3	<0.5	1.51	<0.5	0.2%
15	Bi_2O_3	30 (±20)	65, 91	11	90	<0.5	<0.5	<0.5	-
			Lanthanides						
	CeO_2	13 (±3)	57, 80	31	71	<0.5	<0.5	1.22	-
	PrO_2	18 (±7)	45, 121	4	7				
	Nd_2O_3	18 (±7)	47, 92	10	10				

Purity characterizations were not performed for all samples due to the high costs of these analyses, but the given analyses demonstrate the consistently low impurity content. PdO and Ag_2O were not synthesized in sufficient quantities to perform the necessary BET experiments for surface areas and pore size estimates.

As Table 2.2 indicates, the absolute size distribution of the crystallites increases as the average crystallite size increases, but the relative percent of the size distribution is roughly between 20-45% for nearly all samples. These size distributions are similar to those produced by other aqueous methods and are small compared to those obtained by mechanical processing methods, but they are larger than those attainable using solution or vapor phase methods that employ capping agents. The lack of capping agents combined with the rapid crystallite formation

and inequitable distribution of reagent materials in the solvent-deficient environment are the most likely causes of the somewhat irregular particle morphologies and crystallite size distributions.

In turn, the absence of capping agents in the solvent-deficient method results in excellent chemical purity. The C, H, and N impurity contents (Table 2.2) were immeasurable (less than 0.5%) for most samples. For the few samples which displayed measurable quantities of these impurities, the amounts were small (1-2%) and are thus likely to be adsorbed species. Small chloride impurities (< 100 ppm) were present in the samples made from chloride metal salt reagents, but the MoO_3 precursor that was subjected to one more rinsing cycle (3 cycles) than the TiO_2 precursor (2 cycles) displayed half the chloride content. Also, subsequent studies in which we followed the chloride content of the rinse water via ICP analysis have indicated that the chloride content is essentially undetectable after 5 cycles of rinsing with 100 mL H_2O per gram of material.[x] Thus, for chloride samples, we anticipate that 5 rinsing cycles will effectively eliminate the chloride impurity.

Another result of the absence of capping agents can be seen in Figure 2.2; the individual crystallites visible in the high-magnification TEM images stick together to form the agglomerates seen in the lower-magnification images. The sizes and morphologies of these agglomerates vary considerably; as Table 2.2 indicates, the agglomerate sizes can range from roughly 50 nm to over 300 nm in size. Fortuitously, these agglomerates are mesoporous with high surface areas (Table 2.2) and so are promising candidates for applications such as catalysis and gas sensing that require high surface area metal oxides.

[x] The combustion and chloride analyses were not repeated due to their high costs.

For applications in which aggregation is not advantageous, the agglomerates can be broken apart relatively easily using a mill, as indicated by the preliminary Netzsch milling results given in Figure 2.3. This milling procedure probably introduces the same types of impurities as the milling in solid-state nanosynthesis methods, but the resulting average particle sizes and size distributions are smaller than those attainable by mechanical processing alone.

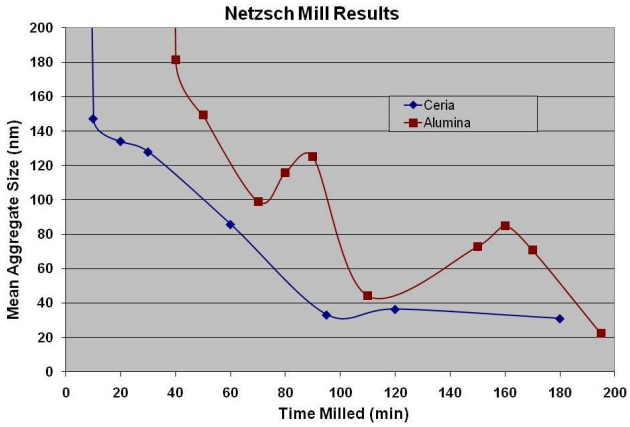

Figure 2.3 Average agglomerate size of Al_2O_3 (alumina) and CeO_2 (ceria) nanomaterials as a function of milling time in aqueous solution.

A few other notable characteristics of the method can be seen in Table 2.1. First, the reagents and equipment involved are common and relatively inexpensive materials, making the process itself fairly inexpensive. Next, the total time for the reaction ranges between 2-5 hours, so the method is quite rapid. The yield for the reaction is also quite high, being between roughly 60-80% for chloride and 80-100%[xi] for nitrate precursors. Encouragingly, the yield remains high when the reaction is scaled-up to produce large quantities; in single, 3-hour batches, over 100 g of Al_2O_3, Fe_2O_3, and ZnO nanomaterials have been produced with the same high yields.

[xi] A few of the samples consistently record yields greater than 100%. We have noted that the masses of these samples tend to increase when left open to the atmosphere, and this, combined with the immeasurable contents of other impurities, leads us to attribute the excess mass to adsorbed H_2O. This adsorption is unavoidable, as it helps to assuage the high surface energies of the small particles.

We anticipate that the consistently lower yields of the chloride precursor reactions is due to incomplete conversion of the reagents into the precursor compounds, This allows some of the metal cations to be rinsed away in the inevitable rinsing steps. The chloride precursor reactions are thus chemically-limited, but for nitrate precursors, more conscientious/efficient material transfer increases the yields for the majority of materials to >90%, and so the yield appears to be primarily process-limited. A few nitrates are chemically-limited, however; for example, when NH_4HCO_3 is used in the synthesis of CuO, significant quantities of Cu^{2+} are rinsed away as the deep blue ammine complex. Thus, $NaHCO_3$ can be used instead of NH_4HCO_3 to increase the yield for those metals (see Table 1) which form non-labile, soluble ammine or nitrate complexes, but this means that the same 5-step rinsing process used for chloride samples must be used to remove the Na^+ impurity. To avoid the Na^+ and Cl^- impurity and yield issues, we thus use nitrates and NH_4HCO_3 (which leaves no measurable impurities after calcination) whenever possible.

2.4 Conclusions

We thereby conclude that the solvent-deficient method is an efficient, general methodology for producing metal oxide nanomaterials for an unprecedentedly vast range of metal oxides. Using only 2-3 simple steps, the method as produced at least one metal oxide nanomaterial from nearly every transition metal and semi-metal group in the periodic table (Groups 3-4 and 6-15) as well as several from the lanthanide group. The “solvent-deficient” environment of the method results in increased crystallinity of the products over other aqueous methods. The products are chemically pure and phase pure with crystallites generally 3-30 nm in average size which aggregate without capping agents, often forming high surface area, mesoporous agglomerates 50-300 nm in size. The high yields of the reaction combined with the

low costs, scalability, versatility, speed, and ease of the method make it a promising candidate for application in the industrial production of high surface area metal oxide nanomaterials.

References

1. Oskam, G., Metal oxide nanoparticles: synthesis, characterization and application. *Journal of Sol-Gel Science and Technology* **2006,** *37* (3), 161-164.
2. Almquist, C. B.; Biswas, P., Role of Synthesis Method and Particle Size of Nanostructured TiO2 on Its Photoactivity. *J. Catal.* **2002,** *212* (2), 145-156.
3. Anpo, M.; Shima, T.; Kodama, S.; Kubokawa, Y., Photocatalytic hydrogenation of propyne with water on small-particle titania: size quantization effects and reaction intermediates. *J. Phys. Chem.* **1987,** *91* (16), 4305-10.
4. Bell, A. T., The Impact of Nanoscience on Heterogeneous Catalysis. *Science (Washington, DC, U. S.)* **2003,** *299* (5613), 1688-1691.
5. Pinna, N.; Neri, G.; Antonietti, M.; Niederberger, M., Gas sensors: Nonaqueous synthesis of nanocrystalline semiconducting metal oxides for gas sensing. *Angew. Chem., Int. Ed.* **2004,** *43* (33), 4345-4349.
6. Arney, D. S.; Wood, T. E. Nanosize metal oxide particles for producing transparent metal oxide colloids and ceramers. 98-US15843 2000006495, 19980730, 2000.
7. Hirai, H.; Fujimoto, H.; Nakamura, S. Light-emitting element and method of producing the same. 2003-375094 2003160260, 20030228, 2003.
8. Philseok, K.; Kippelen, B.; Perry, J.; Marder, S.; Jones, S.; Haddock, J. N.; Zhang, X.; Domercq, B.; Hotchkiss, P. Printable thin-film transistors with high dielectric constant gate insulators and methods for producing same. 2007-US23835 2008060534, 20071113, 2008.
9. Verbakel, F.; Meskers, S. C. J.; de Leeuw, D. M.; Janssen, R. A. J., Resistive Switching in Organic Memories with a Spin-Coated Metal Oxide Nanoparticle Layer. *J. Phys. Chem. C* **2008,** *112* (14), 5254-5257.
10. Kim, K.-K.; Park, N.-G.; Kim, D.-Y.; Kim, J.-K. Fabrication of oxide electrodes for dye-sensitized solar cells. 2006-KR5346 2008050931, 20061208, 2008.
11. Kumar, S.; Horne, C. R. Electrodes and batteries formed from lithium metal oxide nanoparticles. 2001-US40979 2001099215, 20010614, 2001.
12. Pintault, B.; Guenadou, D.; Bianchi, L.; Belleville, P.; Valle, K.; Boscher, C.; Toulc'hoat, J. Manufacture of membranes consisting of a nanoporous nanoparticle layer on a substrate. 2007-EP54076 2007122256, 20070425, 2007.
13. Cheon, J.-W.; Jun, Y.-W.; Lee, J.-H.; Suh, J.-W.; Suh, J.-S.; Ko, S.-J.; Huh, Y.-M.; Song, H.-T. Magnetic resonance imaging contrast agents containing water-soluble nanoparticles of manganese oxide or manganese metal oxide. 2006-KR5160 2007064175, 20061201, 2007.
14. Gupta, A. K.; Gupta, M., Synthesis and surface engineering of iron oxide nanoparticles for biomedical applications. *Biomaterials* **2005,** *26* (18), 3995-4021.

15. Furman, B. R.; Rawls, H. R.; Norling, B. K.; Wellinghoff, S. T.; Dixon, H. Mechanically strong and transparent or translucent composites made using zirconium oxide nanoparticles. 2000-US13708 2000069392, 20000519, 2000.
16. Rieger, J.; Kissel, J.; Andre, V.; Bouillo, N. Preparation of surface-modified metal oxide nanoparticles for use in cosmetics. 2006-EP62732 2006128874, 20060530, 2006.
17. Skandan, G.; Singhal, A., Perspectives on the science and technology of nanoparticle synthesis. *Nanomater. Handb.* **2006**, 13-27.
18. Drofenik, M.; Lisjak, D.; Makovec, D., The synthesis and properties of magnetic nanoparticles. *Mater. Sci. Forum* **2005,** *494*, 129-136.
19. Michel, F. M. E., L.; Antao, S. M.; Lee, P. L.; Chupas, P. J.; Liu, G.; Strongin, D. R.; Schoonen, M. A. A.; Phillips, B. L.; Parise, J. B., The Structure of Ferrihydrite, a Nanocrystalline Material. *Science (Washington, DC, U. S.)* **2007,** *316*, 1726-1729.
20. Cushing, B. L.; Kolesnichenko, V. L.; O'Connor, C. J., Recent Advances in the Liquid-Phase Syntheses of Inorganic Nanoparticles. *Chem. Rev. (Washington, DC, U. S.)* **2004,** *104* (9), 3893-3946.
21. Capek, I., Iron oxide nanoparticle dispersions. *Colloids Interface Sci. Ser.* **2007,** *3* (Colloid Stability and Application in Pharmacy), 1-60.
22. Morones, J. R.; Elechiguerra, J. L.; Camacho, A.; Holt, K.; Kouri, J. B.; Ramirez, J. T.; Yacaman, M. J., The bactericidal effect of silver nanoparticles. *Nanotechnology* **2005,** *16* (10), 2346-2353.
23. Valden, M.; Lai, X.; Goodman, D. W., Onset of catalytic activity of gold clusters on titania with the appearance of nonmetallic properties. *Science (Washington, D. C.)* **1998,** *281* (5383), 1647-1650.
24. Woodfield, B. F.; Liu, S.; Boerio-Goates, J.; Liu, Q.; Smith, S. J. Preparation of uniform nanoparticles of ultra-high purity metal oxides, mixed metal oxides, metals, and metal alloys. 2007-US4279, 2007098111, 20070216., 2007.
25. Lu, A. H.; Salabas, E. L.; Schueth, F., Magnetic nanoparticles: synthesis, protection, functionalization, and application. *Angew. Chem., Int. Ed.* **2007,** *46* (8), 1222-1244.
26. Patterson, A. L., The Scherrer formula for x-ray particle-size determination. *Physical Review* **1939,** *56*, 978-82.

Chapter 3

Mechanism Behind the Solvent-Deficient Synthetic Method

3.1 Introduction

In the previous chapter, a new method was introduced for synthesizing metal oxide nanoparticles. Briefly described, this "solvent-deficient" method consists of 2-3 simple steps. First, a hydrated nitrate or chloride metal salt is ground with ammonium bicarbonate, causing the solid reagents to liquefy and bubble vigorously. The reagents are ground until the bubbling ceases (~10-30 min) and a slurry/paste containing a solid precipitate, or the precursor, has formed. For some samples, the precursor is then rinsed. Finally, the precursor is calcined (~220-550°C) in air (unless otherwise specified) for 1-3 hours.

This single, simple method has produced over 20 different metal oxide nanomaterials including at least one oxide from nearly every transition metal and semi-metal group in the periodic table (Groups 3-4 and 6-15) as well as several oxides from the lanthanide group. With this wide range of products, the solvent-deficient method is one of the most versatile synthetic methods for making metal oxide nanoparticles, and the range of products continues to grow as the method is optimized for new materials.

As Table 2.1 shows, the method has several variable parameters which, to various extents, must be optimized for each nanomaterial: (1) hydration level of the metal salt reagent, (2) ratios of the metal salt and bicarbonate reagents, (3) grinding time, (4) inclusion of a rinsing

step, (5) calcination temperature, (6) calcination time, and (7) atmosphere during calcination. To rationalize the variations required in the synthetic parameters and to discover how these slight adaptations enable the method to succeed for so many materials, we have sought to understand the reactions occurring during the several steps of the method. This chapter discusses the X-ray diffraction (XRD), mass spectrometry (MS), and thermogravimetric/differential-thermal analysis (TGA/DTA) experiments performed to understand the mechanism behind the solvent-deficient method. By elucidating the fundamental reactions taking place, we hope to make it easier to anticipate and optimize the synthetic parameters when applying the solvent-deficient method to new materials.

3.2 Experimental Methods

To identify the reaction occurring during the first step of the reaction (grinding), the gases released by the bubbles evolved during grinding were identified using a Jeol JMS-SX102A electron impact (EI) mass spectrometer. In this experiment, $Fe(NO_3)_3 \cdot 6H_2O(s)$ and $NH_4HCO_3(s)$ in the typical 1:3 mole ratio were mixed in an air-tight reaction vessel filled with nitrogen. Vigorous stirring was maintained (to mimic grinding) using a mechanical stirrer. Nitrogen gas was flowed through the reaction vessel, carrying the gases released from the bubbling through a tube into the spectrometer. We intended to carry out this same experiment for various nanomaterials but were unable to replicate the setup with a different instrument after the Jeol system failed beyond repair. However, we expect that the gases evolved during the Fe reaction should be sufficiently representative.

The compositions of the precursor materials formed by the grinding reaction were identified using X-ray diffraction (XRD). A PANalytical X'Pert Pro diffractometer with a Cu source and a Ge monochromator tuned to the Cu-$K_{\alpha 1}$ wavelength ($\lambda = 1.540598$ Å). was used to

scan each precursor material from 10-90°2θ using a step size of 0.016° at scan rates between 0.7 to 3.0 s/step. For these analyses, precursors were produced using the procedures suggested by Table 2.1 and then split into either two or three portions: the first portion was simply dried; the second portion was dried, rinsed, and then dried again; and the occasional third portion was rinsed before being dried. Samples were dried by heating them in air in a drying oven at 80-100°C for typically ~24 hours. Samples were rinsed by washing the precipitate 3-5 times on a filter flask with enough distilled water to cover the solid. The XRD patterns of all portions were matched to standard patterns in the ICDD (International Center for Diffraction Data) database to identify the compound(s) in each precursor.

To better understand the calcination reaction, the gases released during calcination of each precursor were identified using tandem TG/DTA-MS analyses. The thermogravimetric and differential-temperature analyses (TG/DTA) were performed using a Netzsch STA 409PC instrument. The mass spectrometry (MS) data were collected in tandem with the TG/DTA measurements by attaching a miniature quadrupole MS unit built in-house[1] to the out-gas line of the Netzsch TG/DTA instrument. For these experiments, roughly 30 mg of each precursor material were heated in an alumina crucible to either 300°C (for most un-rinsed precursors made with nitrate metal salts), 350°C (for un-rinsed precursors made with chloride metal salts), or 650°C (for rinsed precursors and some un-rinsed nitrate precursors) at a rate of 5°C/min under He gas flow. The precursors heated to 300°C and 350°C were held at these temperatures for a minimum of 2 hours.

3.3 Results and Discussion

3.3.1 Grinding Reaction

Rationalizing the metal salt hydration, reagent ratios, and grinding time

In the first step of the process, a hydrated metal salt is ground with bicarbonate (NH_4HCO_3 or $NaHCO_3$) using a mortar and pestle. As Figure 2.1a-c illustrates, a bubbling liquid is formed as the solid reagents are ground together even though no solvent is added. This reaction occurs more quickly and is more vigorous for more hydrated metal salts. In fact, if the metal salt is anhydrous or has ≤ 5 moles of hydration per mole of salt, a few drops of water must be added to initiate the reaction.

The hydration level of the metal salt therefore plays a key role in the first step of the process. To understand this role and the proper amount of metal salt hydration, we studied the reactions occurring during grinding. Using mass spectrometry, we found that the bubbles evolved from the reactions consist solely of CO_2 gas (Figure 3.1). Bicarbonate is known to liberate CO_2 when dissolved in acidic solutions:

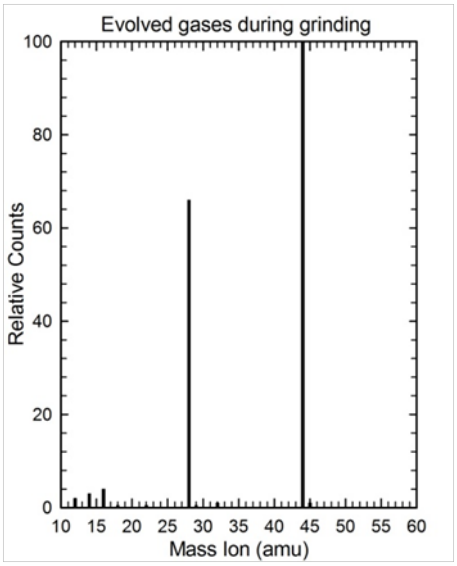

Figure 3.1 Mass spectrometry analysis of the gases released by the bubbling during the grinding reaction. Other than the N_2 carrier gas at 28 amu and its corresponding atomic N peak 14 amu, the only gas observed during the grinding reaction had a mass of 44 amu. This gas was most likely CO_2 because mass ions of 12 and 16 (atomic C and O) were also present in the appropriate 1:2 ratio.

$$HCO_3^- + H^+(aq) \rightarrow H_2O(l) + CO_2(g) \qquad \text{Eq. 3.1}$$

We therefore infer that the waters of hydration are acting as a solvent; the grinding action must free enough of the waters of hydration to enable the soluble metal salt and NH_4HCO_3 to begin dissociating. The metal cations acidify the solution, causing the bicarbonate to decompose into CO_2 gas according to Eq. 3.1. The decomposition of the

bicarbonate to form additional H_2O begins a chain reaction of dissociation and decomposition, producing the bubbles seen in the rapidly-forming liquid.

Greater levels of hydration on the metal salt enable the reaction to begin more easily and proceed more rapidly. We have found that six moles of hydration seems to be the minimum hydration level that will provide enough of a solvent for the reaction to begin. Because the reaction proceeds much faster and easier (5-15 vs. 20-30 minutes of grinding) if 9 moles of hydration are present per mole of metal salt, we typically add enough water to make the hydration level of the salt equal to that of a nona-hydrated salt.[xii] Because this amount of "solvent" is considerably less than that used in aqueous solution methods, we refer to the process as "solvent-deficient."

In the given reaction mixture, it seems likely that the metal cations form hydroxides:

$$M^{x+}(aq) + xH_2O \rightarrow M(OH)_x + xH^+(aq) \qquad \text{Eq. 3.2}$$

Because most metal hydroxides are insoluble, we originally hypothesized that the precipitate rapidly formed during the grinding reaction (evidenced by the brown coloration of the mixture in Figure 2.1) was a metal hydroxide. To verify the precipitation reaction(s) occurring, we used XRD to identify each material's precipitate, which we call the "precursor."

As Figure 3.2 shows, when the precursor slurry is dried (without being rinsed), all precursors contain an ammonium salt; NH_4NO_3 is formed if a nitrate metal salt is used, and NH_4Cl is formed if a chloride metal salt is used:

$$NO_3^-(aq) + NH_4^+(aq) \rightarrow NH_4NO_3(s) \qquad \text{Eq. 3.3}$$

$$Cl^-(aq) + NH_4^+(aq) \rightarrow NH_4Cl(s) \qquad \text{Eq. 3.4}$$

[xii] Adding water can influence the morphologies and corresponding surface areas of the agglomerates, however, so depending on the application it may or may not be desirable to add water to salts containing at least 6 moles of hydration.

Because these ammonium salts are highly soluble, however, we presume that they solidify as the slurry dries and are not part of the original (and often colorful) insoluble precipitate observed. The diffraction signal of the metal-containing precipitate are masked by the strong diffraction signals of the ammonium salts, however, so to identify the metal-containing precipitates, we had to isolate them by rinsing away the NH_4NO_3 and NH_4Cl. Table 3.1 lists the compound(s) identified in each precursor (for the actual XRD patterns/analyses see Appendix A.1).

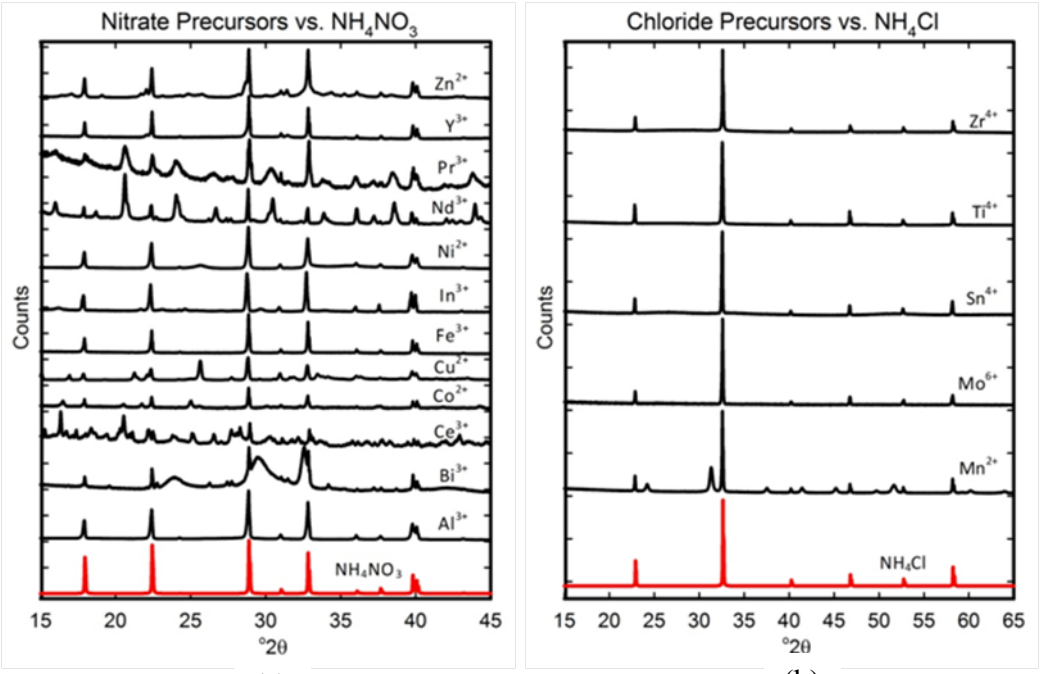

Figure 3.2 XRD patterns of dried precursors made from nitrate (a) and chloride (b) salts.

As Table 3.1 shows, most precursors contain a metal hydroxide of some sort: a simple hydroxide (Co^{2+}, Ni^{2+}) , an oxyhydroxide (Al^{3+}, Fe^{3+}), a hydroxide nitrate (Co^{2+}, Ni^{2+}, Cu^{2+}, Ce^{4+}), or a hydroxide carbonate (Y^{3+}, Zn^{2+}, In^{3+}, Ce^{4+}, Nd^{3+}, Pr^{3+}). However, a few precursors formed carbonates (Mn^{2+}, Ag^{+}, Bi^{3+}, Nd^{3+}), and several others formed what appears to be nearly amorphous hydrated oxides (Y^{3+}, Ti^{4+}, Zr^{4+}, Mo^{5+}, Sn^{4+}). A number of precursors contained mixtures of several of these compounds (Y^{3+}, Co^{2+}, Ni^{2+}, Cu^{2+}, Zn^{2+}, Bi^{3+}, Ce^{4+}, Nd^{3+}). Based on the precipitates formed, we infer that while the metal cation is gaining hydroxide ligands and

enabling the chain reaction of reactant dissocation, those metal cations that have an affinity for nitrate or carbonate also gain ligands of these anions via simple acid/base replacement reactions.

Table 3.1 Precursor components identified by matching the XRD patterns of the dried and rinsed/dried precursors to standard patterns in the ICDD database. The compounds appearing in gray text for the dried precursors are soluble and were rinsed out (in the dried/rinsed/dried samples) to better identify the insoluble compounds in black.

Group	Metal reagent	Dried Precursor	Rinsed/Dried Precursor
		Transition metal precursors	
3	Y^{3+} (nitrate)	NH_4NO_3 + †Y_2O_3·xH_2O + Y(OH)(CO3)	
4	Ti^{4+} (chloride)	NH_4Cl + †TiO_2·xH_2O(anatase)	
4	Zr^{4+} (chloride)	NH_4Cl + †ZrO_2·xH_2O	
6	Mo^{5+} (chloride)	NH_4Cl + †$HMoO_3$•H_2O	
7	Mn^{2+} (chloride)	NH_4Cl + $Mn(CO_3)$	
8	Fe^{3+} (nitrate)	NH_4NO_3 + FeOOH•0.4H_2O	
9	Co^{2+} (nitrate)	NH_4NO_3 + $Co(OH)_2$ + $Co_2(OH)_3(NO_3)$ + $Co(OH)(NO_3)$•H_2O	†$Co(OH)_2$
10	Ni^{2+} (nitrate)	NH_4NO_3 + $Ni(OH)_2$ + $Ni_3(OH)_4(NO_3)_2$	†$Ni(OH)_2$
11	Cu^{2+} (nitrate)	NH_4NO_3 + $Cu_2(OH)_3(NO_3)$ + $Cu(NO_3)_2(NH_3)_4$	$Cu_2(OH)_3(NO_3)$
11	Ag^{+} (nitrate)	$NaNO_3$ + Ag_2CO_3	
12	Zn^{2+} (nitrate)	NH_4NO_3 + $Zn_5(OH)_6(CO_3)_2$ + $Zn(OH)(NO_3)$•NH_3 +$Zn(OH)(NO_3)$•H_2O + $(NH_4)Zn(CO_3)(NO_3)$•NH_3	$Zn_5(OH)_6(CO_3)_2$ +$Zn_4(OH)_6CO_3$•H_2O
		Semi-metal precursors	
13	Al^{3+} (nitrate)	NH_4NO_3 + AlOOH	
13	In^{3+} (nitrate)	NH_4NO_3 + ‡In hydroxide-carbonate	
14	Sn^{4+} (chloride)	NH_4Cl + †SnO_2·xH_2O	
15	Bi^{3+} (nitrate)	NH_4NO_3 + $Bi_2O_2CO_3$ + Bi_2O_3•CO_2 and/or $Bi(OH)_3$	
		Lanathanide metal precursors	
	Ce^{3+} (nitrate)	NH_4NO_3 + $Ce(OH)(CO_3)$ + $Ce_2(CO_3)_6$•6H_2O + $(NH_4)_3Ce_2(NO_3)_9$ + $(NH_4)_2Ce(NO_3)_5(H_2O)_2$•2$H_2O$	$Ce(CO_3)(OH)$+CeO_2
	Pr^{3+} (nitrate)	NH_4NO_3 + $Pr(OH)(CO_3)$	
	Nd^{3+} (nitrate)	NH_4NO_3 + $Nd(OH)(CO_3)$ + $Nd_2(CO_3)_3$•2.5H_2O	

‡MS data suggest the In^{3+} precursors is a carbonate or hydroxide-carbonate, but no standard patterns of these were available. †These compounds are nearly amorphous

Then, as the excess water evaporates during either drying or calcination, the ammonium salt crystallizes. Because the reactions merely involve acid-base chemistry, other bases can be used such as $NaHCO_3$ and even hydroxide bases in cases where hydroxides and not carbonates form. In fact, $NaHCO_3$ *must* be used with the noble metals and with cations having an affinity for

NH_3 such as Zn to avoid ammine complexes. However, we use NH_4HCO_3 when possible because it leaves no Na^+ impurities after calcination.

The precursor identities reveal the rationale behind setting the reagent ratios. Using a 1:1 mole ratio between the ammonium cation (from the NH_4HCO_3) and the metal salt anion (NO_3^- or Cl^-) will enable the NH_4NO_3 or NH_4Cl salt to form at the conclusion of the grinding reaction while simultaneously ensuring that the appropriate ratios of metal cation to hydroxide (and/or carbonate) anion are present for a metal hydroxide (and/or carbonate) to form.

The metal-containing precipitates ('precursor' compounds) form rapidly and appear to form completely by the time bubbling has ceased, as illustrated in Figure 2.1. These precipitates are nanoparticles for most materials, as the broad XRD peaks in the patterns of the metal precursor compounds indicate (see Appendix A.1). Based on the well-studied mechanisms of nanoparticle nucleation, growth, and aging from other aqueous precipitation methods,[2-3] we attribute the nano size of the precursor crystallites and the rapidity of their formation to the solvent-deficient environment; the scarcity of solvent ensures that as soon as the reagents dissociate the ions are in a supersaturated environment, allowing nucleation to begin essentially immediately. The solvent deficiency then inhibits migration/mixing of the reagent materials, making growth of the hydroxide/carbonate nanoparticles so extremely diffusion-limited that growth is choked almost as soon as nucleation begins, allowing nanoparticles to form instead of bulk-sized particles.

The size of the precursor particles seems to provide the lower limit for the size of the product crystallites, thus the solvent deficient environment appears to play a key role in the method's success in making nanomaterials. Again, nine moles of hydration seems to provide

enough solvent to allow the reaction to proceed easily while still maintaining the solvent deficient environment.

Because the growth of the precursor nanoparticles therefore only requires as much time as it takes for the reagents to dissociate, we base the grinding time solely on the time it takes for bubbling (the evidence of bicarbonate decomposition) to cease. After this initial nucleation and growth, the hydroxide and/or carbonate precursor crystallites can undergo two well-known aging processes—Ostwald ripening and aggregation[2]—to assuage their high surface energies.[4] Because surfactants are not employed, aggregation is inevitable, but we have found that Ostwald ripening (coarsening) is greatly minimized if the precursors are not dried prior to calcination. Thus, to obtain smaller crystallite sizes, we generally calcine the wet (rinsed or unrinsed) precursors directly.[xiii]

During aggregation, the solvent-deficient environment again produces some interesting and fortuitous results. Because the agglomerates begin to form before the excess water evaporates and the ammonium salts crystallize, the spectator ions/molecules (H_2O, NH_4^+, NO_3^- /Cl^-) seem to provide a spatial buffer or possibly even a sort of template around which the agglomerates form, causing the agglomerates to be mesoporous after these ions are removed via calcination and/or rinsing. (Preliminary results showing that the pores have an unusually narrow size distribution and that the average size varies with the size of the spectator ions encourage this hypothesis. This work will be published elsewhere.) The mesoporous character combined with the high surface areas of the agglomerates (reported in the previous chapter) make the products promising candidates for several catalyst or gas-sensing applications.

[xiii] In a very few cases, we have noticed that drying before calcining and/or rinsing allows a more advantageous agglomerate pore structure to form. The order/inclusion of rinsing and drying steps may thus need to be explored for each material for different applications.

3.3.2 Calcination Reaction

Rationalizing calcination temperature and time

To produce the desired nano metal oxide, the nano-crystallite precursors in Table 3.1 produced by the grinding reaction must be calcined to decompose the ammonium salt and dehydrate/decompose the metal compound. The decomposition reactions of both NH_4NO_3 and NH_4Cl are well-known; above ~160°C, NH_4NO_3 liquefies and can decompose (non-explosively) via two, well-studied routes:[5]

$$NH_4NO_3(l) \xrightarrow{\geq 160°C} NH_3(g) + HNO_3(g) \quad \text{Eq. 3.5}$$

$$NH_4NO_3(l) \xrightarrow{\sim 250°C} N_2O(g) + H_2O(g) \quad \text{Eq. 3.6}$$

Above ~338°C, NH_4Cl sublimes:

$$NH_4Cl(s) \xrightarrow{\sim 338°C} NH_3(g) + H_2O(g) \quad \text{Eq. 3.7}$$

The decompositions of the metal compounds in the precursors (hydroxides, oxyhydroxides, hydroxide-nitrates, hydroxide-carbonates, and carbonates) are also predictable; precursors containing hydroxide ligands should dehydrate (evolve H_2O), precursors containing carbonate ligands should decarbonate (evolve CO_2), and the few precursors containing nitrates could evolve various NO_x gases.

To verify the reactions occurring and determine the temperatures/times required, the gaseous byproducts evolved during the calcination of each precursor were identified using mass spectrometry (MS) data collected in tandem with TG/DTA data. Figure 3.3 provides representative TG/DTA-MS data sets (TG/DTA-MS analyses for each sample are given in Appendix A.2).

As Figure 3.3 (a) illustrates, precursors containing an ammonium nitrate salt evolve large amounts of N_2O (44 amu) and H_2O (18 amu) at temperatures between 240-310°C, confirming

the NH_4NO_3 decomposition route given in Eq. 3.6. The evolution of a small amount of NH_3 (17 amu) is also observed,[xiv,6] but the HNO_3 predicted by Eq. 3.5 is never detected. Instead, substantial amounts of NO (30 amu) and even small amounts of NO_2 (46 amu) are observed, suggesting that any HNO_3 formed reacts with NH_3 (or other species) in several side reactions to form NO_x gases and/or additional N_2O and H_2O gases.

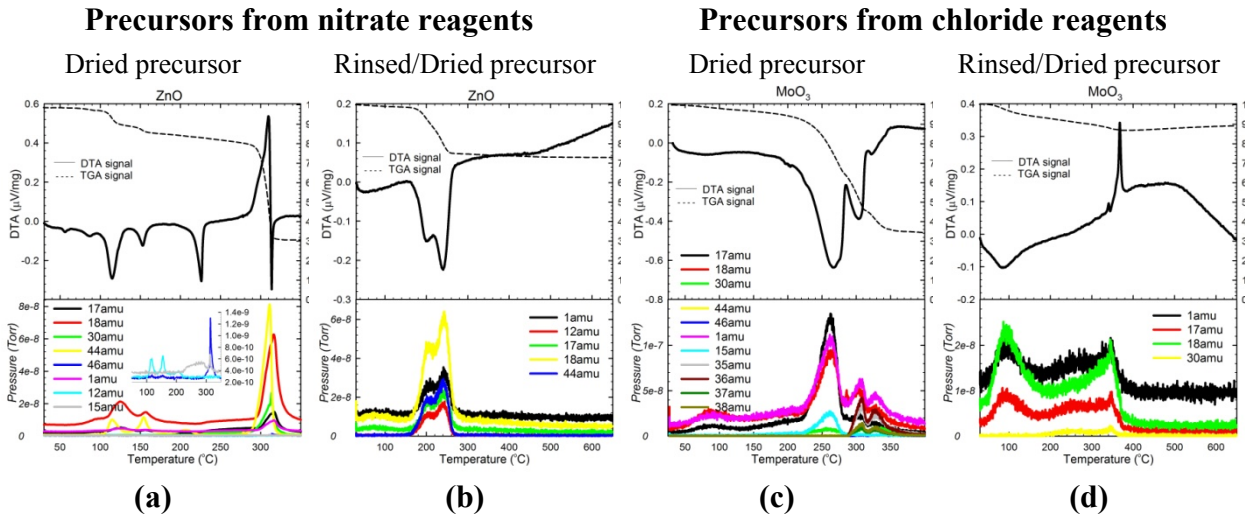

Figure 3.3 TG/DTA-MS data for both un-rinsed (a, c) and rinsed (b, d) precursors made from nitrate (ZnO) and chloride (MoO_3) metal salt reagents.

Similarly, Figure 3.3 (c) illustrates the NH_3 (17 amu) and HCl (35, 36, 37, 38 amu) mass ions[xv] observed at temperatures between 290-330°C in the calcinations of most chloride precursors, confirming that the decomposition reaction in Eq. 3.7 occurs to a certain extent. As in

[xiv] Due to the limited resolution of the miniature MS unit, NH_3 and OH fragments from H_2O (both 17 amu) could not be resolved. However, electron impacts can cause NH_3 to fragment into NH_2^+ (16 amu) and even small amounts (100:4.5 ratio) of NH^+ (15 amu) (see Olesik 1984, ref #6). Thus, the 15 amu byproduct exhibited by most nitrate precursors was interpreted as evidence of NH_3 evolution.

[xv] Again, the 15 amu byproduct was interpreted as evidence of NH_3 evolution. The four mass ions observed for HCl are a result of the 3:1 ratio of the ^{35}Cl and ^{37}Cl isotopes; mass ions of 36 and 38 amu are observed in a ratio of 3:1 for $H^{35}Cl$ and for $H^{37}Cl$, respectively, and additional mass ions of 35 amu and 37 amu (also in a ratio of 3:1) are observed due to the loss of the H during fragmentation of the HCl.

the nitrate precursors, the NH_3 (17 amu) seems to participate in side reactions to form NO (30 amu). Despite these side reactions which diminish the NH_3 quantity, the HCl mass ions often appear in much smaller quantities than would be expected based on the NH_3 quantity, and in fact, no HCl is observed for the Ti^{4+} and Mn^{2+} precursors (see Appendix A.2). Thus, for most chloride precursors, the majority of the Cl^- is not evolved as gaseous HCl but rather seems to remain as a Cl^- impurity in the oxide.

Somewhat surprisingly, the NH_4NO_3 and NH_4Cl decomposition temperatures varied significantly (between 240-310°C and 290-330°C, respectively) depending on the precursor involved. Based on previous studies,[7] the differing acidities of the metal cations/compounds in the precursors may cause these variations in the salt decomposition temperature, implying some level of complexation between the salt and the metal precursor compound(s).

To isolate and study the decomposition reactions of the metal-containing precursor compounds, TG/DTA-MS data were recorded for the rinsed precursors. As (b) and (d) in Figure 3.3 display, calcining the metal-containing precursor compounds evolves H_2O and CO_2 byproducts, confirming the dehydration/decarbonation reactions anticipated for these metal hydroxide/carbonate compounds.

Calcination temperatures must be chosen to enable decomposition of both the metal compound and the ammonium salt (if it has not been rinsed away). Because the dehydration/decarbonation reactions of the metal compounds often occur at temperatures below the ammonium salt decomposition ($\leq$ 300°C), calcination temperatures of 300°C and 350°C are usually sufficient for precursors containing NH_4NO_3 and NH_4Cl, respectively. For rinsed precursors, the calcination temperature can be determined solely by the dehydration/decarbonation temperature of the metal compound. The time generally required to

decompose the NH_4NO_3 or NH_4Cl components is 1-2 hours, as revealed by the TGA data. However, some oxides require up to 3 hours and temperatures >350°C to fully form or crystallize; these are generally the lanthanides and heavier metals/semi-metals (see Table 2.1). The minimum calcination time and temperature should be used to avoid unnecessary Ostwald ripening. Also, because of the small quantities of noxious gases (NO_x, NH_3, HCl) produced during the decompositions of NH_4NO_3 and NH_4Cl, the gaseous byproducts from all un-rinsed precursors should be directed either through a ventilated hood or an aqueous filtration system.

3.3.3 Effects of Rinsing

Rationalizing the addition of a rinsing step and control of the calcination atmosphere

Studying the calcination reactions for both the rinsed and un-rinsed precursors revealed some beneficial effects of rinsing the precursor. The first effect is that it prevents certain contaminants in the products. As previously mentioned, significant Cl^- impurities remain in the oxide products if the NH_4Cl is not removed prior to calcination. Thus, all precursors made from chloride metal salts (Mn^{2+}, Mo^{5+}, Ti^{4+}, Sn^{4+}, Zr^{4+}) must be rinsed to prevent Cl^- contamination. Also, the noble metal precursors such as Ag^+ and Pd^{2+} (for which $NaHCO_3$ must be used instead of NH_4HCO_3) require rinsing to remove the $NaNO_3$ salt formed. Unlike NH_4Cl and $NaNO_3$, the NH_4NO_3 in nitrate precursors only leaves noticeable impurities in one case; ZnO nanoparticles are a salmon/pink color indicative of nitrogen incorporation unless the Zn precursor is rinsed prior to calcination.[8] This may actually be useful for certain applications, however.

Besides purity, a second effect of rinsing the precursor is that smaller crystallite sizes are obtained for many materials. For some samples (Figure 3.4), the complexation previously mentioned between the metal precursor compound(s) and the ammonium salt results in a large exothermic release of energy (> 0.4 μV/mg) during calcination that enables grain growth. These

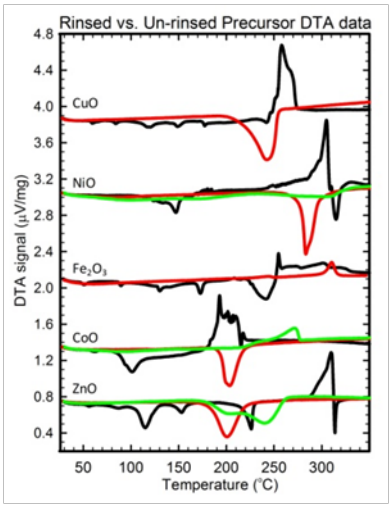

Figure 3.4 DTA data for the dried (black), rinsed/dried (green), and dried/rinsed/dried (red) precursors of oxides whose crystallite size is minimized if the precursor is rinsed prior to drying and/or calcination.

exothermic events are uncharacteristic of either the endothermic salt decompositions or the endothermic/weakly exothermic metal compound decompositions. As Figure 3.4shows, rinsing the NH_4NO_3 out of these precursors (Fe^{3+}, Co^{2+}, Ni^{2+}, Cu^{2+}, Zn^{2+}) prior to their calcination eliminates these large exothermic releases, allowing crystallite sizes < 20 nm to be obtained.

Rinsing the Co^{2+}, Ni^{2+}, and Zn^{2+} precursors has another size-decreasing effect. As Table 3.1 indicates, these precursors (un-rinsed) typically contain a metal hydroxide-nitrate compound. The hydroxide-nitrate compounds limit the crystallite size of CoO, NiO, and ZnO to be > 10 nm.[xvi] However, rinsing prior to drying/calcining prevents these nitrate compounds from forming (see Table 3.1), implying that the nitrate ligand only substitutes for one of the hydroxide ligands as the H_2O solvent evaporates. By rinsing the wet precursor and removing the nitrate ions before this substitution, the crystallite size of these materials tends to be < 10 nm.

The third reason for inserting a rinsing step is that it prevents uncontrolled oxidation/reduction of the metal cation during calcination. As the MS results indicate, numerous oxidizing and/or reducing agents (HNO_3, N_2O, NO, NO_2, NH_3) are released during the decompositions of un-rinsed precursors. As a result, mixed-oxidation state oxides can form for

[xvi] The reason for this increased size effect is uncertain, but it may be related to the increased crystallite size of the nitrate compounds compared to the pure hydroxides. Alternatively, the hydroxide-nitrate mode of decomposition may allow more Ostwald ripening.

cations with multiple stable oxidation states (such as Bi^{3+}, Co^{2+}, Fe^{2+}, Mn^{2+}, Mo^{5+}, Sn^{4+}). Rinsing allows the formation of phase pure oxides for these multi-valence metal cations.

For all of these reasons, we have added a rinsing step for many materials, as Table 2.1 reveals. In addition to rinsing, we have found it important to control the atmosphere during calcination for certain materials to maintain the metal oxidation state. Specifically, the CoO and Fe_3O_4 precursors need to be calcined in an inert atmosphere to prevent these multi-valence cations from being oxidized by O_2 in the air to form Co_3O_4 and Fe_2O_3.

We have only begun to explore using calcination atmosphere as a variable, but it may open a pathway to producing many more nanomaterials than those listed in Table 2.1. For example, some preliminary work has shown that nano-metals can be formed from the Pd^{2+}, Pt^{2+}, Cu^{2+}, Ni^{2+}, and Co^{2+} precursors if they are calcined in a highly reducing atmosphere such as H_2. We also hypothesize that calcining the Pr(III) and Mn(II) precursors in an inert environment might produce Pr_2O_3 and MnO instead of the oxidized PrO_2 and Mn_2O_3 produced by calcination in air. Similarly, Co_2O_3, AgO, and either MnO_2 or Mn_5O_8 might be formed if the Co(II), Ag(I), and Mn(II) precursors were calcined in an oxidizing environment, and conversely, SnO or Ce_2O_3 might be formed if the Sn(IV) and Ce(IV) precursors were calcined in a slightly reducing atmosphere. In essence, we predict that controlling the calcination atmosphere will add another valuable dimension of versatility to the solvent-deficient method.

3.4 Conclusion

In summary, we have identified the mechanism behind the versatile, solvent deficient method of producing metal oxide nanomaterials. In the first step of the reaction in which bicarbonate is ground together with a hydrated metal salt, the grinding action must free enough of the waters of hydration to enable the soluble metal salt and NH_4HCO_3 to begin dissociating.

The metal cations acidify the solution, causing the bicarbonate to decompose into CO_2 gas. The decomposition of the bicarbonate to form additional H_2O begins a chain reaction of dissociation and decomposition, producing the bubbles seen in the rapidly-forming liquid. Rapid acid/base replacement reactions result in the formation of a metal hydroxide, oxyhydroxide, hydroxide-nitrate, hydroxide-carbonate, carbonate, or amorphous oxide/hydroxide (depending on the metal cation used). An ammonium salt forms as the slurry dries or is calcined, and the resulting complex containing the salt and the metal compound are what is known as the precursor.

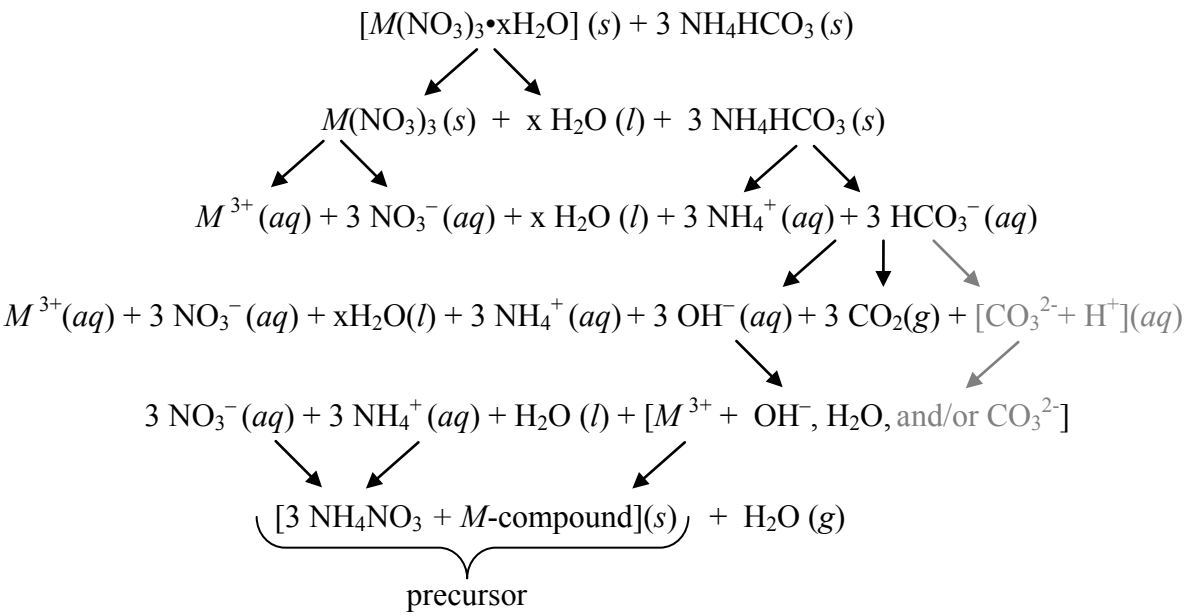

Scheme 3.1 Reaction summary of the first step of the solvent-deficient method (the grinding reaction) when a hydrated, trivalent nitrate metal salt is used as the reagent. For chloride salt reagents, simply replace NO_3^- with Cl^-. The particular metal compound (*M*-compound) formed varies with each metal but is generally $M(OH)_3$, $MOOH$, M_2O_3, $M(OH)(NO_3)$, $M(OH)(CO_3)$, or $M_2(CO_3)_3$ (with appropriate stoichiometries for the valency of the metal). The portions in gray text only occur for metals that form carbonate compounds.

In the second step, this "precursor" is calcined to dehydrate/decompose both the metal compound and the ammonium salt (if it has not already been rinsed away) to form the metal oxide nanomaterial (see Scheme 3.2). The minimum calcination time and temperatures are used to avoid unnecessary Ostwald ripening of the oxide nanoparticles.

$$\text{Metal Precursor Compound}(s) \xrightarrow{\Delta} \text{Metal Oxide}(s) + \text{H}_2\text{O}(g) + \text{CO}_2(g) + \text{NO}_x(g)$$
$$+$$
$$\text{NH}_4\text{NO}_3(s) \xrightarrow{\Delta} \text{H}_2\text{O}(g) + \text{N}_2\text{O}(g) + \text{NH}_3(g) + \text{NO}_x(g)$$
$$\text{or}$$
$$\text{NH}_4\text{Cl}(s) \xrightarrow{\Delta} \text{NH}_3(g) + \text{NO}_x(g) + [\text{H}^+ + \text{Cl}^-]_{\text{adsorbed}} + \text{HCl}(g)$$

Scheme 3.2 Reactions of the calcination step of the solvent-deficient method. Though written separately, the first reaction occurs in tandem with either the second or third reaction (depending on whether a nitrate or chloride salt reagent was used, respectively). Synergistic interactions bewteen the components and/or reactions cause variations between different precursors in the temperature of the reactions, the side-reactions and byproducts formed (particularly the NO_x gases), and the endothermic/exothermic nature of the step. The darker the hue of the product, the more common and concentrated its occurance.

Unexpectedly, these mechanistic investigations revealed an even more versatile range of products for the solvent-deficient method than previously expected. By rinsing away the soluble NH_4NO_3 or NH_4Cl and drying the remaining precipitate, the insoluble hydroxide, oxyhydroxide, hydroxide-carbonate, hydroxide-nitrate, or carbonate precursor compounds in Table 3.1 can be isolated. Additionally, by controlling the calcination atmosphere, the method may be able to access products with metal oxidation states other than those in Table 2.2, including nano metals.

Through these mechanistic studies, we can surmise reasons for the wide range of success of the method. As Scheme 3.1 illustrates, the dissociation of the reagents upon grinding must be so highly entropically favorable that even though the grinding process is endothermic, it is still thermodynamically favorable and occurs for nearly all metal salts. Once the reagents are dissociated, the metal cation forms the most kinetically and/or thermodynamically favorable compound, which for most metals is the metal hydroxide or carbonate (or a combination thereof) instead of the original metal salt. The combination of increasing entropy and favorable replacement reactions make the grinding process thermodynamically favorable for nearly all metals. The solvent deficient environment in which the precursors are formed imparts the rapidity of reaction and extreme diffusion-limited growth necessary to form nanoparticles instead

of bulk particles. During calcination, the precursor crystallites retain their nano-size as the hydroxide and carbonate species decompose to form the metal oxide products, and minimal Ostwald ripening occurs if minimal heating temperatures and times are employed.

This insight into the mechanism of the method will hopefully enable the technique to be applied more readily to new materials. Though the synthetic parameters must still be optimized for each material individually, their values can be more accurately predicted instead of determined solely by trial and error. A comprehensive study of how the physical properties of the products are altered by varying each synthetic parameter is beyond the scope of this work, but this study has highlighted some general trends that will guide the optimization process.

References

1. Jambor, J. L.; Dutrizac, J. E., Occurrence and Constitution of Natural and Synthetic Ferrihydrite, a Widespread Iron Oxyhydroxide. *Chem. Rev. (Washington, D. C.)* **1998,** *98* (7), 2549-2585.
2. Oskam, G., Metal oxide nanoparticles: synthesis, characterization and application. *Journal of Sol-Gel Science and Technology* **2006,** *37* (3), 161-164.
3. Cushing, B. L.; Kolesnichenko, V. L.; O'Connor, C. J., Recent Advances in the Liquid-Phase Syntheses of Inorganic Nanoparticles. *Chem. Rev. (Washington, DC, U. S.)* **2004,** *104* (9), 3893-3946.
4. Navrotsky, A., Energetics of oxide nanoparticles. *Int. J. Quantum Chem.* **2009,** *109* (12), 2647-2657.
5. Feick, G.; Hainer, R. M., A temperature-limiting mechanism in the thermal decomposition of ammonium nitrate. *Nature (London, U. K.)* **1954,** *173*, 1188-9.
6. Olesik, S. V.; Taylor, J. W., Unimolecular fragmentation pathways of methanol, ammonia, and water neutral clusters. *International Journal of mass spectrometry and ion processes* **1984,** *57* (3), 315-327.
7. Vuori, A. O., Kemira, Impact of impurities and pH on ammonium nitrate stability. In *2002 IFA Technical Conference*, Chennai, India, 2002.
8. Norman, V. J., The Non-Stoichiometry of Pink Zinc Oxide. *Aust. J. Chem.* **1975,** *28*, 229-235.

Chapter 4

Novel Synthesis and Structural Analysis of Ferrihydrite

4.1 Introduction

Ferrihydrite is a poorly crystalline Fe(III) oxyhydroxide mineral naturally found in near-surface soils and sediments as the precursor to hematite, often in areas contaminated by acid mine drainage.[1-4] It has a number of useful properties. The high surface area and reactivity of ferrihydrite enable it to sequester various species through adsorption, coprecipitation, and redox reactions.[5] It is a particularly effective sorbent for heavy metals[6] and arsenate[7] and is thus manufactured for use in wastewater treatment,[8] direct coal liquefaction,[9] and metallurgical processing.[9-10] Its adsorptive nature is also being explored for use in removal of volatile organic compounds from the air.[11] Electronically, ferrihydrite displays quantum dot behavior because its band gap varies from 1.3 to 2.5 eV as particle size varies from 2 to 8 nm.[12] It is also thought to be the structure formed in the iron core of ferritin, an iron storage protein ubiquitously found in animals, plants, and microbes.[4,13-14]

Naturally occurring ferrihydrite is both impure and difficult to isolate;[15] thus its applications and interesting properties have spurred the development of new synthetic techniques.[8,11,16-18] All are essentially variations on the hydrolysis of an iron salt. For example, a common synthetic route involves the titration (at numerous different rates) of an aqueous Fe(III) solution with a base at a controlled temperature (often either 25°C or 65-85°C) to either achieve

a neutral pH (usually 6.5-7.5) or maintain a specific acidic pH (roughly 2.65) until either a precipitate forms or the solution is quenched to cooler temperatures to induce precipitation. Virtually all reported synthetic processes require careful control over temperature, pH, concentration, and the rate of change in these variables, and all require subsequent washing/dialysis and drying steps to remove residual electrolytes.

In this paper, we report a new method for synthesizing ferrihydrite which does not require careful control over temperature, pH, concentration, or the rate of change in these variables, and is therefore the simplest method reported thus far. The distinctive feature of the synthesis is the solvent-deficient environment[19-21] in which the particles form which results in unusually low water content in the ferrihydrite. XRD, TEM, BET and chemical purity characterizations of our ferrihydrite product are presented, along with synchrotron X-ray pair-distribution function (PDF) data that has been analyzed using the structural model recently proposed by Michel *et al*.[1] These analyses suggest that ferrihydrite has a consistent, repeatable structure independent of variation in synthetic method, water content of the sample, or particle size of the crystallites, and this structure can be adequately described by the proposed hexagonal model.

4.2 Experimental Methods

4.2.1 Synthesis

The ferrihydrite synthesis was derived from the solvent-deficient method reported in the previous chapters[19-21] with the primary alteration being that drying and rinsing steps were employed in lieu of the calcination step used to produce the metal oxide materials. Our ferrihydrite synthesis thus has 4 simple steps: (1) grinding, (2) drying, (3) rinsing, and (4) drying.

First, $Fe(NO_3)_3 \cdot 9H_2O(s)$ and $NH_4HCO_3(s)$ in a 1:3 mole ratio are ground together using a mortar and pestle. The grinding action dislodges the waters of hydration from the metal salt, providing sufficient solvent for the reagents to begin dissociating. The metal cations acidify the solution, causing the bicarbonate to decompose into CO_2 gas and H_2O. The decomposition of the bicarbonate to form additional H_2O begins a chain reaction of dissociation and decomposition that produces visible bubbles in the rapidly-forming liquid. Grinding continues until bubbling ceases and a dark brown precipitate has formed.

The resulting slurry is then dried in air between 80-100°C. The dried precipitate is rinsed to remove the NH_4NO_3 salt that forms as the precursor is dried. Only 2-3 washings on vacuum filter using distilled water are necessary; we have found that the ferrihydrite can transform to goethite if it is allowed to sit in water for extended periods of time or if the precipitate is rinsed before being dried. The reddish-brown precipitate is then dried again in air as before.

For the characterizations discussed in this chapter, a ferrihydrite sample was produced by grinding 20.252 g of $Fe(NO_3)_3 \cdot 9H_2O(s)$ with 11.913 g of $NH_4HCO_3(s)$ for roughly 15 min using a mortar and pestle. The resulting slurry was dried in air at 100°C for 24 hours before being rinsed using three 50 mL portions of distilled water. The remaining precipitate was then dried in air at 100°C for 24 hours. The elemental nitrogen and hydrogen content in the ferrihydrite were determined via combustion analysis by Galbraith Laboratories in order to gauge the effectiveness of rinsing away the NH_4NO_3 impurity. This hydrogen analysis was then also used to estimate the water content of the ferrihydrite sample.

4.2.2 Structural Characterization Methods

A laboratory x-ray powder diffraction (XRD) pattern of the ferrihydrite sample was collected over a 10-90° 2θ range in 0.016° steps at a rate of 3 s/step using a PANalytical X'Pert

Pro diffractometer with a Cu source, a Ge 111 Johanssen-type monochromator tuned to the Cu-$K_{\alpha 1}$ wavelength (λ = 1.540598 Å), and an X'Celerator position-sensitive detector.

High resolution transmission electron microscope (HRTEM) images were recorded using a FEI Philips Technai F30 TEM operating at 300 kV. Specimens were prepared by dispersing the particles in ethanol, placing a drop of the very dilute solution on a formvar/carbon film supported by a 200 mesh Ni grid (Ted-Pella Inc.), and allowing the ethanol to evaporate. Mass/thickness contrast images were recorded in standard high-resolution mode.

Brunauer-Emmett-Teller (BET) specific surface area and pore size were determined from N_2 adsorption at 77 K using a Micromeritics TriStar II instrument. For these measurements, 0.2149 g of ferrihydrite were degassed at 200°C for 22 hours and then allowed to cool to room temperature prior to data collection.

High energy x-ray total scattering data for PDF (pair distribution function) analysis were collected under ambient conditions at the 11-ID-B beamline at the Advanced Photon Source (APS) at Argonne National Laboratory. Approximately 10 mg of ferrihydrite powder were loaded into a 0.0395 inch inner-diameter polyimide capillary that was sealed with epoxy at both ends. Using 90.4868 keV (λ = 0.1370 Å) incident-energy x-rays, a 2-D image of the diffraction data were collected out to a maximum value of Q = 39 Å^{-1} with a 2048 × 2048 pixel Perkin Elmer (PE) amorphous-silicon area detector of square dimension 410 cm. The Fit2D[22] and PDFgetX2[23] software packages were used to integrate the 2D ring patterns and extract the experimental PDF pattern, $G(r)$.[24] Structural model refinements against the PDF data were performed with the PDFgui software[25] in the range from r = 1.6 to r = 20.00 Å.

The Fhyd6 structure reported by Michel *et al.*[1] was used as the initial model in the PDF refinement. The unit cell parameters, atom positions, isotropic-displacement parameters, and

occupancies of the second and third Fe atoms (Fe2 and Fe3) were refined. A number of PDF-specific parameters were also refined, including the data scale factor, the *Qdamp* resolution-damping parameter, and the *sratio* parameter (with *rcut* set to 4.0 Å), which was added to model the sharpening of nearest-neighbor peaks due to correlated atomic motion. The Qdamp parameter was used to account for both instrument resolution and finite particle size effects (instead of refining a separate spherical shape factor to account for the size effects) in order to make the parameters comparable to those reported by Michel *et al*.

4.3 Results

XRD patterns reported for ferrihydrite typically display either two or six broad and poorly defined reflections, which is the source of the common practice of designating the compound as either 2-line or 6-line ferrihydrite. As evidenced by the two very broad diffraction peaks in Figure 4.1, the solvent deficient synthetic method produces 2-line ferrihydrite. The distinction between 2-line and 6-line ferrihydrite is somewhat artificial, however. Structurally, the two are quite similar, as Carta *et al*. recently demonstrated using XANES/EXAFS.[26] The primary difference lies in the size of their coherent scattering domains[27] or crystallite sizes; the broad peaks of 2-line ferrihydrite actually resolve smoothly into the slightly sharper reflections of 6-line ferrihydrite as the rate of hydrolysis is slowed and crystallinity increases.[28-29] We have found that our synthetic method cannot be slowed or extended sufficiently to produce the more

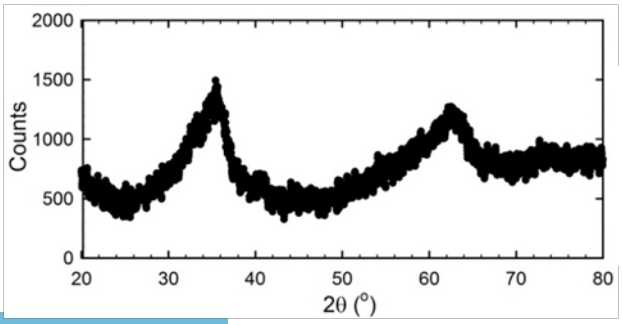

Figure 4.1 XRD pattern of the 2-line ferrihydrite synthesized via the solvent deficient method.

crystalline 6-line ferrihydrite; only 2-line ferrihydrite can be produced due to the rapid reaction rate and poor mass transport of the reagents in the solvent efficient environment.

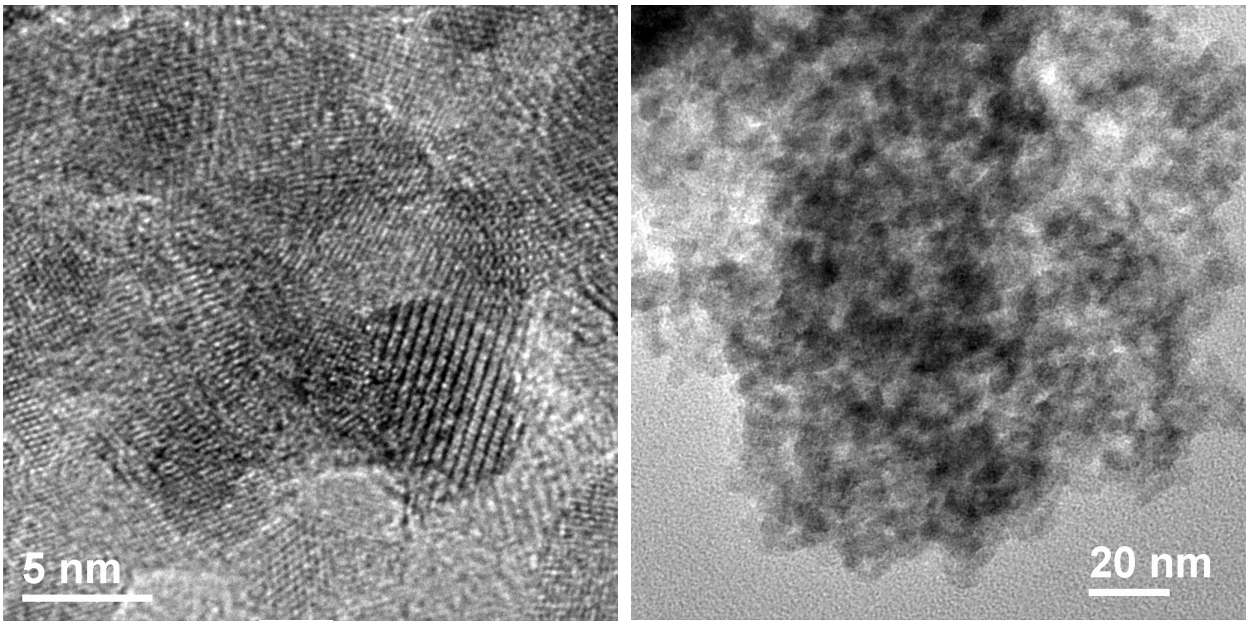

(a) (b)

Figure 4.2 TEM images of ferrihydrite synthesized via the solvent deficient method.

The small crystallites sizes (approximately 2-6 nm) of the 2-line ferrihydrite particles are shown in the TEM images of Figure 4.2a, which also reveal the roughly spherical morphology of the particles. These small particles aggregate to satisfy the high surface energies characteristic of nanoparticles,[29] forming the agglomerates illustrated in Figure 4.2b whose BET surface area is 248 m^2/g and whose pores are 3.4 nm in diameter and 0.26 cm^3/g in volume. Considering this large surface area, the ferrihydrite exhibits surprisingly low adsorbed water content. Because the undetectable (<0.5 mass%) nitrogen content implies that the sample does not contain any residual NH_4NO_3, the hydrogen content (1.09 mass%) from the Galbraith analyses can be attributed solely to either hydroxide anions or excess water. Assuming the chemical formula $Fe_{10}O_{14}(OH)_2 \cdot xH_2O$ for ferrihydrite suggested by Michel *et al.*,[1] the value of x for this sample is

3.8 (or else $x \approx 0$ for the commonly used chemical formula $FeOOH \cdot xH_2O$). Compared to precipitation methods, which typically report $x \approx 8$ ($x \approx 0.4$ for $FeOOH \cdot xH_2O$), the ferrihydrite synthesized via the solvent-deficient method has less than half the typical water content. We presume that this is a result of the oxyhydroxide's limited access to water in the solvent-deficient synthetic environment. Presuming it enables the ferrihydrite to be a more effective sorbent, however, this low water content could be highly advantageous. Combined with the excellent chemical purity, high surface area, and naturally mesoporous nature of the agglomerates, the ferrihydrite produced by our solvent-deficient method is an attractive candidate for adsorption applications.

The TEM images in Figure 4.2 also display conspicuous lattice fringes which confirm the crystalline nature of the particles despite their small size and poorly defined diffraction pattern. Notwithstanding the obvious crystallinity of the particles and the considerable attention ferrihydrite has received, studies and discussions continue to debate both its structure and its chemical formula.[1,14-15,30-35] No single chemical formula has been accepted because of the variable water content commonly observed in ferrihyrite,[4] and a definitive structural model is evasive because the nanocrystallinity (2-8 nm) of ferrihydrite stymies traditional crystallographic analyses which rely on long-range order.

Even so, several structural models have been proposed for ferrihydrite over the years. Chukrov *et al*.[35] and Towe and Bradley[14] both proposed defective hematite structures. Drits *et al.* proposed a multi-component model consisting of defective and defect-free ferrihydrite phases mixed with ultradisperse hematite.[34] More recently, Michel *et al*. employed the PDF method of analyzing total scattering data to propose a single-phase hexagonal structure with $P6_3mc$ symmetry and average unit cell dimensions of a = ~5.95 Å and c = ~9.06 Å (Figure 4.3a) that

successfully reproduced the X-ray PDFs of three different samples of ferrihydrite (2 nm, 3 nm, and 6 nm in size).[1] The basic unit of their structure is similar to a δ-Keggin cluster[36] and consists of a central tetrahedrally coordinated Fe atom sharing each of its corners with three edge-sharing Fe octrahedra (Figure 4.3b). Since then, XANES/EXAFS studies by both Carta *et al.*[15] and Maillot *et al.*[31] have supported the 20:80 ratio of tetrahedrally and octrahedrally coordinated Fe atoms in ferrihydrite suggested by Michel *et al.*'s model.

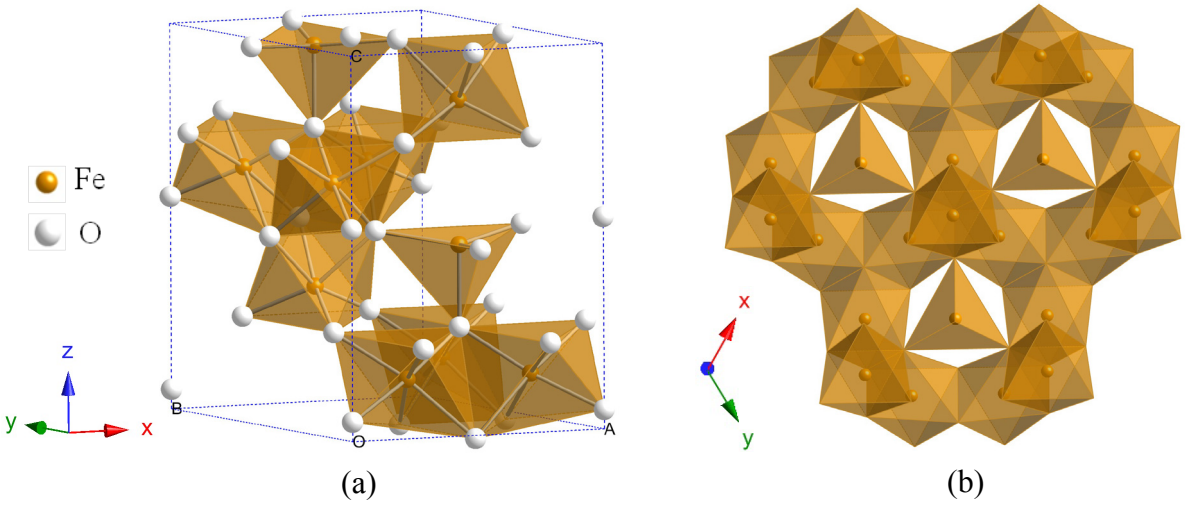

Figure 4.3 (a) Unit cell and (b) basic structural motif of the ferrihydrite structure proposed by Michel *et al.*

To determine the structural similarities or differences between the less-hydrated ferrihydrite synthesized via our solvent-deficient method and ferrihydrite reported elsewhere, we collected PDF data on our ferrihydrite sample and used Michel *et al.*'s structure as a starting model for a refinement. The refinement results, which appear in Table 4.1 and Figure 4.4, indicate that the structural parameters of our ferrihydrite sample generally fall within the ranges of those reported for Michel *et al.*'s three samples. The small discrepancies between our experimental and the calculated PDF peak heights, particularly those at 3.0, 4.6, 6.8, 8.9, and 10.7 Å, were also present in the previous study, wherein they were rationalized by noting their

similarity to stacking-fault induced misfits in studies of Al_2O_3.[29] The PDF data and refined models of the four samples are thus essentially identical despite the materials having been synthesized by four different methods and despite the differences in particle size and water content.[xvii]

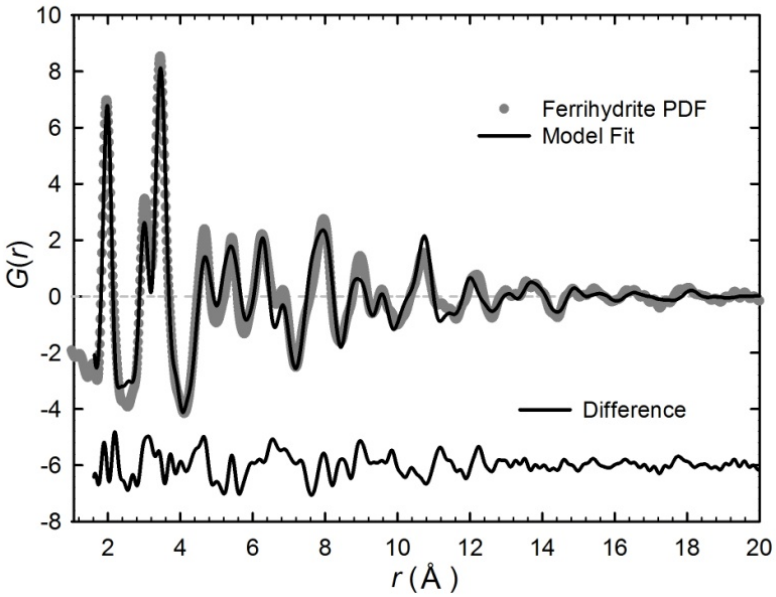

Figure 4.4 Experimental PDF, or *G(r)*, of the ferrihydrite (gray) with the refined fit of the model (black). The difference plot is shown below.

Table 4.1 Ferrihydrite structural parameters obtained from PDF refinements. Shown in comparison are the parameters of Michel *et al.*'s three samples (Fhyd 2, 3, and 6). To conserve space, only the range of values is given for the atomic coordinates and occupancies of the three samples.

	a	***c***	***Qdamp***	**R_w (%)**	***sratio***			
This work	**5.949**	**8.992**	**0.157**	**24.0**	**0.521**			
Fhyd2	5.958	8.965	0.217	26.2	0.336			
Fhyd3	5.953	9.096	0.157	24.9	0.406			
Fhyd6	5.928	9.126	0.137	26.7	0.400			
	This work				***Michel's work***			
Atom	***x***	***y***	***z***	***Occ***	***x***	***y***	***z***	***Occ***
Fe1 (6c)	0.16986	0.8302	0.6361	1.0	0.1688-95	0.8304-12	0.6356-0.6365	1.0
Fe2 (2b)	1/3	2/3	0.3359	0.94	1/3	2/3	0.3347-0.3414	0.90-97
Fe3 (2b)	1/3	2/3	0.9605	0.87	1/3	2/3	0.9538-0.9600	0.85-96
O1 (2a)	0	0	0.0503	1.0	0	0	0.0147-0.0460	1.0
O2 (2b)	1/3	2/3	0.7470	1.0	1/3	2/3	0.7353-0.7651	1.0
O3 (6c)	0.1650	0.8350	0.2487	1.0	0.1670-97	0.8302-29	0.2457-0.2547	1.0
O4 (6c)	0.5263	0.4737	0.9861	1.0	0.5227-58	0.4742-73	0.9778-0.0053	1.0

[xvii] The water contents of the other three samples were not reported, but we presume they are similar to those reported by other precipitation methods.

4.4 Conclusion

We conclude that our simple, solvent-deficient synthetic method produces chemically pure ferrihydrite crystallites 2-6 nm in size whose agglomerates are good candidates for adsorption applications due to their high surface areas, mesoporous nature, and unusually low water content. The ferrihydrite product is also virtually identical in structure to that produced by other synthetic methods which require very careful control over temperature, pH, concentration, and the changes in these variables. This result implies that the ferrihydrite material has a consistent, repeatable structure independent of variation in synthetic method, water content of the sample, or particle size of the crystallites, which structure is adequately described by the hexagonal model proposed by Michel *et al.*

References

1. Michel, F. M. E., L.; Antao, S. M.; Lee, P. L.; Chupas, P. J.; Liu, G.; Strongin, D. R.; Schoonen, M. A. A.; Phillips, B. L.; Parise, J. B., The Structure of Ferrihydrite, a Nanocrystalline Material. *Science (Washington, DC, U. S.)* **2007,** *316*, 1726-1729.
2. Rancourt, D. G.; Fortin, D.; Pichler, T.; Thibault, P.-J.; Lamarche, G.; Morris, R. V.; Mercier, P. H. J., Mineralogy of a natural As-rich hydrous ferric oxide coprecipitate formed by mixing of hydrothermal fluid and seawater: implications regarding surface complexation and color banding in ferrihydrite deposits. *Am. Mineral.* **2001,** *86* (7-8), 834-851.
3. Schwertmann, U.; Carlson, L.; Murad, E., Properties of iron oxides in two Finnish lakes in relation to the environment of their formation. *Clays Clay Miner.* **1987,** *35* (4), 297-304.
4. Jambor, J. L.; Dutrizac, J. E., Occurrence and Constitution of Natural and Synthetic Ferrihydrite, a Widespread Iron Oxyhydroxide. *Chem. Rev. (Washington, D. C.)* **1998,** *98* (7), 2549-2585.
5. Fortin, D.; Langley, S., Formation and occurrence of biogenic iron-rich minerals. *Earth-Science Reviews* **2005,** *72* (1-2), 1-19.
6. Ford, R. G.; Bertsch, P. M.; Farley, K. J., Changes in Transition and Heavy Metal Partitioning during Hydrous Iron Oxide Aging. *Environmental Science and Technology* **1997,** *31* (7), 2028-2033.
7. Raven, K. P.; Jain, A.; Loeppert, R. H., Arsenite and Arsenate Adsorption on Ferrihydrite: Kinetics, Equilibrium, and Adsorption Envelopes. *Environmental Science and Technology* **1998,** *32* (3), 344-349.

8. Li, Z.; Zhang, T.; Li, K., One-step synthesis of mesoporous two-line ferrihydrite for effective elimination of arsenic contaminants from natural water. *Dalton Transactions* **2011,** *40* (9), 2062-2066.
9. Huffman, G. P.; Ganguly, B.; Zhao, J.; Rao, K. R. P. M.; Shah, N.; Feng, Z.; Huggins, F. E.; Taghiei, M. M.; Lu, F.; et al., Structure and dispersion of iron-based catalysts for direct coal liquefaction. *Energy Fuels* **1993,** *7* (2), 285-96.
10. Riveros, P. A.; Dutrizac, J. E.; Spencer, P., Arsenic disposal practices in the metallurgical industry. *Can. Metall. Q.* **2001,** *40* (4), 395-420.
11. Mathew, T.; Suzuki, K.; Nagai, Y.; Nonaka, T.; Ikuta, Y.; Takahashi, N.; Suzuki, N.; Shinjoh, H., Mesoporous 2-Line Ferrihydrite by a Solution-Phase Cooperative Assembly Process for Removal of Organic Contaminants in Air. *Chemistry--A European Journal* **2011,** *17* (4), 1092-1095, S1092/1-S1092/9.
12. Liu, G.; Debnath, S.; Paul, K. W.; Han, W.; Hausner, D. B.; Hosein, H.-A.; Michel, F. M.; Parise, J. B.; Sparks, D. L.; Strongin, D. R., Characterization and Surface Reactivity of Ferrihydrite Nanoparticles Assembled in Ferritin. *Langmuir* **2006,** *22* (22), 9313-9321.
13. Lewin, A.; Moore, G. R.; Le Brun, N. E., Formation of protein-coated iron minerals. *Dalton Transactions* **2005,** (22), 3597-3610.
14. Towe, K. M.; Bradley, W. F., Mineralogical constitution of colloidal "hydrous ferric oxides". *Journal of Colloid and Interface Science* **1967,** *24* (3), 384-92.
15. Carta, D.; Casula, M. F.; Corrias, A.; Falqui, A.; Navarra, G.; Pinna, G., Structural and magnetic characterization of synthetic ferrihydrite nanoparticles. *Materials Chemistry and Physics* **2009,** *113* (1), 349-355.
16. Anschutz, A. J.; Penn, R. L., Reduction of crystalline iron(III) oxyhydroxides using hydroquinone: influence of phase and particle size. *Geochemical Transactions* **2005,** *6* (3), 60-66.
17. Schwertmann, U. F., J.; Kyek, A., Formation and properties of a continuous crystallinity series of synthetic ferrihydrites (2- to 6-line) and their relation to FeOOH forms. *Clays Clay Miner.* **2004,** *52* (2), 221-226.
18. Dyer, L.; Fawell, P. D.; Newman, O. M. G.; Richmond, W. R., Synthesis and characterisation of ferrihydrite/silica co-precipitates. *Journal of Colloid and Interface Science* **2010,** *348* (1), 65-70.
19. Woodfield, B. F.; Liu, S.; Boerio-Goates, J.; Liu, Q.; Smith, S. J. Preparation of uniform nanoparticles of ultra-high purity metal oxides, mixed metal oxides, metals, and metal alloys. 2007-US4279, 2007098111, 20070216., 2007.
20. Smith, S. J.; Liu, S.; Liu, Q.; Olsen, R. E.; Boerio-Goates, J.; Woodfield, B. F., Mechanism behind the "solvent-deficient" synthetic method. *Chem. Mater.* **2012**, Submitted.
21. Smith, S. J.; Liu, S.; Liu, Q.; Olsen, R. E.; Rytting, M.; Selck, D. A.; Simmons, C. L.; Boerio-Goates, J.; Woodfield, B. F., Synthesis of metal oxide nanoparticles via a robust “solvent-deficient” method. *Chem. Mater.* **2012**, Submitted.
22. "Fit2D" V. 9.129 Reference Manual V. 3.1.
23. Qiu, X.; Thompson, J. W.; Billinge, S. J. L., PDFgetX2: a GUI-driven program to obtain the pair distribution function from X-ray powder diffraction data. *J. Appl. Crystallogr.* **2004,** *37* (4), 678.
24. Egami, T. B., S. J. L., *Underneath the Bragg Peaks: Structural Analysis of Complex Materials*. First ed.; Pergamon: Kidlington, Oxford, UK, 2003; Vol. 7, p 404.

25. Farrow, C. L.; Juhas, P.; Liu, J. W.; Bryndin, D.; Bozin, E. S.; Bloch, J.; Proffen, T.; Billinge, S. J. L., PDFfit2 and PDFgui: computer programs for studying nanostructure in crystals. *J. Phys.: Condens. Matter* **2007,** *19* (33), 335219/1-335219/7.
26. Digne, M.; Sautet, P.; Raybaud, P.; Toulhoat, H.; Artacho, E., Structure and Stability of Aluminum Hydroxides: A Theoretical Study. *J. Phys. Chem. B* **2002,** *106* (20), 5155-5162.
27. Levin, I.; Brandon, D., Metastable alumina polymorphs: crystal structures and transition sequences. *J. Am. Ceram. Soc.* **1998,** *81* (8), 1995-2012.
28. Wefers, K. M., Chanakya, "Oxides and Hydroxides of Aluminum". *Tech. Pap. - Alcoa Res. Lab.* **1987,** *19*.
29. Paglia, G.; Bozin, E. S.; Billinge, S. J. L., Fine-Scale Nanostructure in gamma -Al2O3. *Chem. Mater.* **2006,** *18* (14), 3242-3248.
30. Jansen, E.; Kyek, A.; Schafer, W.; Schwertmann, U., The structure of six-line ferrihydrite. *Appl. Phys. A: Mater. Sci. Process.* **2002,** *74* (Suppl., Pt. 2), S1004-S1006.
31. Maillot, F.; Morin, G.; Wang, Y.; Bonnin, D.; Ildefonse, P.; Chaneac, C.; Calas, G., New insight into the structure of nanocrystalline ferrihydrite: EXAFS evidence for tetrahedrally coordinated iron(III). *Geochimica et Cosmochimica Acta* **2011,** *75* (10), 2708-2720.
32. Kukkadapu, R. K. Z., J. M.; Fredrickson, J. K.; Smith, S. C.; Dohnalkova, A. C.; Russell, C. K., Transformation of 2-line ferrihydrite to 6-line ferrihydrite under oxic and anoxic conditions. *Am. Mineral.* **2003,** *88*, 1903-1914.
33. Schwertmann, U.; Friedl, J.; Stanjek, H., From Fe(III) ions to ferrihydrite and then to hematite. *Journal of Colloid and Interface Science* **1999,** *209* (1), 215-223.
34. Drits, V. A.; Sakharov, B. A.; Salyn, A. L.; Manceau, A., Structural model for ferrihydrite. *Clay Miner.* **1993,** *28* (2), 185-207.
35. Chukhrov, F. V.; Zvyagin, B. B.; Gorshkov, A. I.; Ermilova, L. P.; Balashova, V. V., Ferrihydrite. *Izvestiya Akademii Nauk SSSR, Seriya Geologicheskaya* **1973,** (4), 23-33.
36. Casey, W. H., Large Aqueous Aluminum Hydroxide Molecules. *Chem. Rev. (Washington, DC, U. S.)* **2006,** *106* (1), 1-16.

Chapter 5

Synthesis and Structural Characterization of Al_2O_3 Nanoparticles for Use as Catalyst Supports

5.1 Introduction

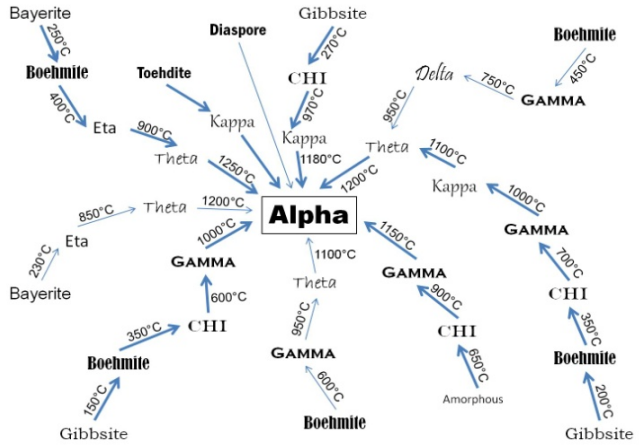

Figure 5.1 Illustration of a few of the many reported phase transition pathways of the Al_2O_3 system.

The Al_2O_3 (alumina) phase diagram is notoriously complex (Figure 5.1), having at least 15 reported structural phases (Figure 5.2).[1-12] The alumina system contains four hydroxide and three oxyhydroxide phases which can, upon heating, transform to one or more of the seven metastable "transitional" Al_2O_3 phases before reaching the thermodynamically stable alpha phase. Adding to the complexity, slight changes in the synthetic conditions, impurities, initial crystallite size, and/or hydrothermal history of the sample alter the phases and transformation temperatures observed.[10,13-17] Hence, a plethora of transition pathways have been reported (Figure 5.1).[4,9,18-22] Figure 5.3 shows the most commonly reported sequences.[4,10,14,22]

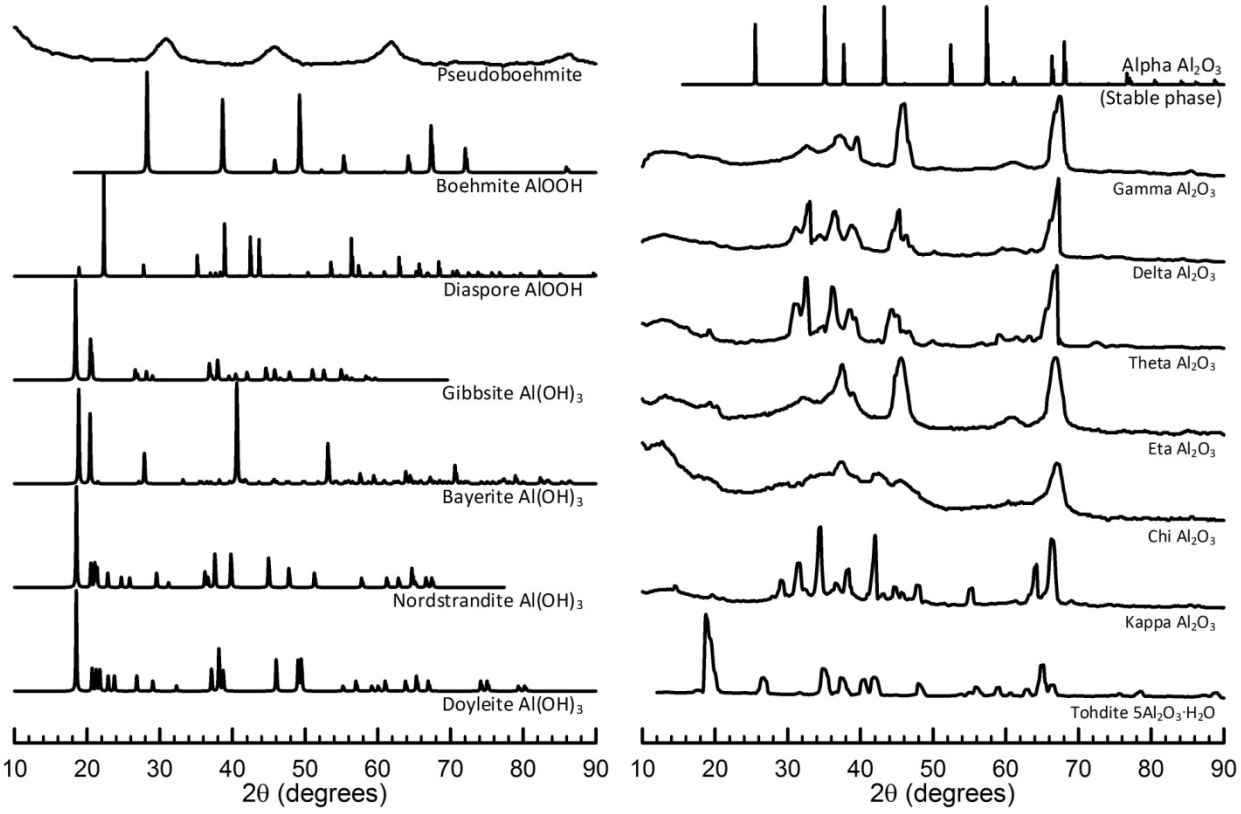

Figure 5.2 XRD patterns of the 15 reported structural phases of the Al_2O_3 system. Part (a) shows the hydroxide and oxyhydroxide phases of the alumina family, namely pseudoboehmite, boehmite (00-001-0774), diaspore (01-070-2138), gibbsite (00-012-0460), bayerite (00-020-0011), nordstrandite (00-018-0031), and doyleite (00-038-0376) where the numbers in parentheses are the reference numbers of the data in the ICDD database. Part (b) shows the thermodynamically stable alpha phase with the gamma, delta, theta, eta, chi, kappa, and tohdite transitional Al_2O_3 phases whose XRD patterns were obtained from the work of Wefers and Misra (ref.10).

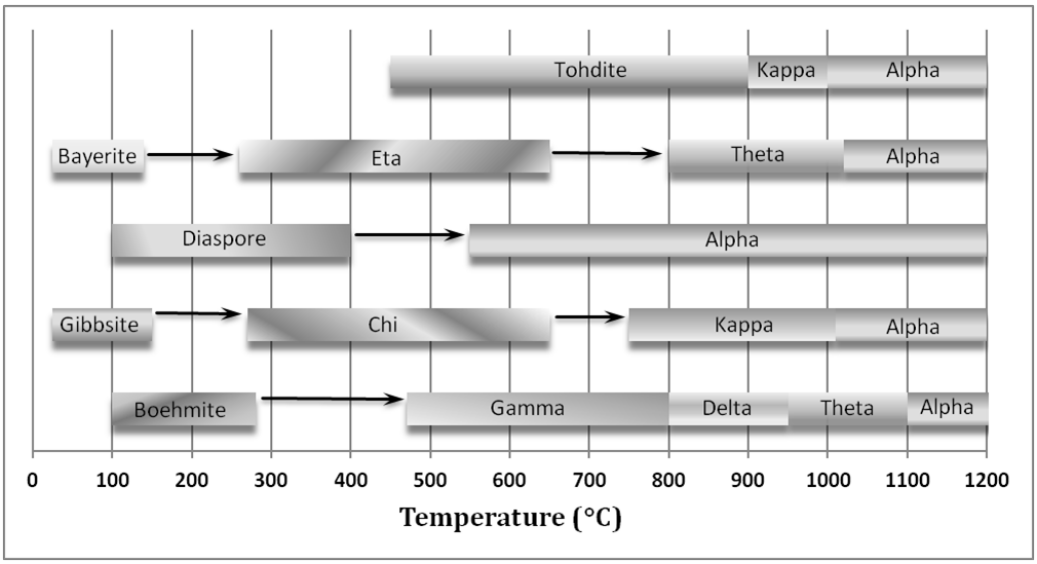

Figure 5.3 Most commonly reported phase transformation pathways of the Al_2O_3 system.

The phase transformations of alumina have been widely studied because alumina is a technologically and industrially important material, and the different phases have different uses. For example, the oxyhydroxide boehmite phase and the hydroxides gibbsite and bayerite are used in antacids,[23] as adjuvants in some vaccines,[24] and as the feedstock for the manufacture of many other aluminum compounds including aluminum metal. The hard, high-temperature alpha Al_2O_3 phase (α-Al_2O_3 or corundum) is widely used as a refractory material, as a pigment in paints and sunscreens, and as an abrasive material in sandpapers, cutting tools, and even toothpastes. The metastable transitional Al_2O_3 phases (chi (χ), eta (η), kappa (κ), gamma (γ), delta (δ), theta (θ)) are porous and can be dehydrated and "activated" for use as adsorbents or desiccants. The most widely used of these transitional phases is the γ phase; its porous nature, intrinsically high surface area, and catalytic activity[25] make it a popular catalyst support for a variety of processes including hydrocarbon processing,[26-27] the dehydration of alcohols,[28-29] automotive exhaust gas processing (as in catalytic converters),[30-31] and the Fischer Tropsch process of oxidizing CO into hydrocarbons for use as fuel.[32-34]

In many of these applications, particularly those of the α and γ phases, alumina nanoparticles are gaining interest and attention. For example, α-Al_2O_3 nanoparticles produce finer grades of sandpapers and allow for thinner layers of paints and sunscreens. Also, γ-Al_2O_3 nanoparticles produce catalyst supports with much more surface area per unit mass than bulk particles, thereby producing catalysts with higher dispersion and efficiency.

The expanding number of industrial applications for alumina nanoparticles is prompting the development of new and more efficient synthetic methods. A promising new method is the solvent-deficient process discussed in the previous chapters. Because potential applications are phase-specific, in this chapter we investigate the structure and properties of the Al_2O_3 produced

by the solvent-deficient method as a function of synthetic calcination temperature. TEM and BET analyses of the particle size, morphology, surface area, and pore size suggest that the new Al_2O_3 product is a favorable candidate for adsorption and catalyst support applications. XRD analyses show that the method produces the metastable γ-Al_2O_3 phase favored in these applications, and pair distribution function (PDF) analyses of the alumina calcined through a range of temperatures reveal the temperatures at which this important phase is formed. Thermogravimetric/differential-thermal (TG/DTA) and ^{27}Al MAS-NMR analyses support the PDF analyses. These investigations have led us to adopt a defect-riddled view of γ-Al_2O_3 which may be able to account for many of the unique properties of the γ-phase.

5.2 Experimental Methods

5.2.1 Sample preparation

Alumina nanoparticles were synthesized using the proprietary solvent-deficient method.[35-36] One large batch of the precursor material was prepared by using a mortar and pestle to grind 275.94g of $Al(NO_3)_3 \bullet 9H_2O$ (reagent grade purity, VWR) with 174.45g NH_4HCO_3 (reagent grade purity, VWR) for 15-20 minutes, forming a solid precursor in slurry form. The precursor slurry was then dried for 12 hours in air at 100°C using a Thermo Scientific Lindberg Blue M oven. The dried precursor was split into 23 portions, roughly 8.1 g each. Using the Thermo Scientific oven, one sample was calcined at each 50°C increment between 100°C and 1200°C by heating it in air at a rate of 5°C/min to its set temperature and then holding this temperature for 2 hours before being allowed to cool to room temperature. Throughout the text of the discussion, each sample will be referred to by its calcination temperature; for example, 'the 300°C alumina' refers to the sample in which the alumina precursor was calcined at 300°C

for 2 hours. Creating this suite of samples enabled us to study the phases produced through the entire range of synthetic temperatures while still being able to perform ambient temperature diffraction experiments.

In addition to our own suite of Al_2O_3 nanoparticles, we collected PDF data on commercial samples of alumina. This included two samples of boehmite (Sasol and SkySpring Inc.), one sample of α-Al_2O_3 (Alfa Aesar), and four samples of γ-Al_2O_3 including two samples from Sasol (one pure γ-Al_2O_3 sample and one mixture of the γ-, δ-, and θ-phases) and two samples from Alfa Aesar (one labeled as a catalyst support and one simply labeled as having 99.99% purity).

5.2.2 Data Collection

Preliminary powder X-ray diffraction (XRD) data were collected using a A PANalytical X'Pert Pro diffractometer with a Cu source and a Ge monochromator tuned to the Cu-$K_{\alpha 1}$ wavelength (λ = 1.540598 Å). Scans were performed between 10-90°2θ at a rate of 400 s/step with a step size of 0.016°2θ.

XRD data for the PDF analyses were collected at the 11 ID-B beamline[37] of the Advanced Photon Source (APS) at Argonne National Laboratory using synchrotron radiation of energy 58.2636 keV (λ = 0.2128 Å). For each sample, 10 mg of powder were loaded into a 0.0395 inch inner-diameter Kapton capillary, and 2-D images of the diffraction data were collected out to a maximum value of $Q = 29.5$ Å^{-1} in reciprocal space under ambient conditions using a Perkin Elmer area detector. The Fit2D software package[38] was used to integrate the 2D ring patterns and obtain 1D powder diffraction patterns. The PDFgetX2 software package[39] was used to extract $G(r)$, the experimental PDF,[40] using a maximum momentum transfer of $Q = 24.5$ Å^{-1} in the Fourier transform. PDF refinements were performed using the PDFgui program.[41]

Transmission electron microscope (TEM) images of the alumina nanoparticles were recorded using a FEI Philips Technai F20 Analytical STEM operating at 200 kV. Specimens were prepared by dispersing the alumina in ethanol, placing a drop of the very dilute solution on a formvar/carbon film supported by a 200 mesh Ni grid (Ted-Pella Inc.), and allowing the ethanol to evaporate. Images were recorded in standard high resolution mode.

Thermogravimetric and differential-thermal analyses (TG/DTA) were performed using a Netzsch STA 409PC. Mass spectrometry (MS) measurements were collected in tandem with the TG/DTA measurements using a quadrupole MS unit built in-house.[42] To characterize the water loss and thermal behavior of the Al_2O_3 during calcination between 300 and 1200°C, three TG/DTA-MS measurements were recorded in which 30-40 mg of the 300°C alumina were loaded into an alumina crucible and heated at a rate of either 5°/min from 25°C to 1100°C or 3°/min from 25°C to 1300°C under a flowing He atmosphere.

^{27}Al magic angle spinning (MAS) NMR experiments were conducted for the alumina samples calcined at 350, 500, 700, 900 1000, and 1100°C. The data were collected on a 800 MHz (18.8 T) Varian dual solids/liquids NMR spectrometer operating at a ^{27}Al frequency of 104.16 MHz. The samples were spun in 1.6mm zirconia rotors at 35 kHz MAS to avoid overlap between the central transition and the first order spinning sidebands. 2048 scans were collected using a 310 ns (pi/12) pulse for non-selective excitation along with a 1s recycle delay.[43] All spectra were collected under identical conditions and externally referenced to a 1M aluminum chloride solution. The ratios of tetrahedral to octahedral coordination environments were quantified by fitting under their respective resonances.

The BET specific surface area and BJH pore size of each Al_2O_3 sample were determined from N_2 adsorption at 77 K using a Micromeritics TriStar II instrument. For these measurements,

roughly 200-300 mg of each sample were degassed at 200°C for ~24 hours to remove adsorbed moisture. The samples were allowed to cool in air to room temperature prior to data collection.

5.3 Results and Discussion

5.3.1 Physical properties characterization

The TEM images in Figure 5.4a-c illustrate the 3-5 nm diameters of the roughly spherical Al_2O_3 crystallites produced by our new synthetic method at calcination temperatures between 300-950°C. Only these few representative images are shown because the particle size and morphology remain essentially constant in this temperature range. Beyond this temperature, the crystallites sinter to form particles ≥ 60 nm in size (Figure 5.4d), but between 300-950°C the crystallites simply aggregate to satisfy the characteristically high surface energies of small nanoparticles,[44] forming the agglomerates seen in (Figure 5.4f). These agglomerates are mesoporous and have high surface areas (Table 5.1), though the surface area and pore volume decrease steadily with increasing temperature (Figure 5.5) as is ubiquitously reported for Al_2O_3. Above roughly 950°C, a rapid drop in surface area occurs, consistent with the TEM observation that the particles are sintering.

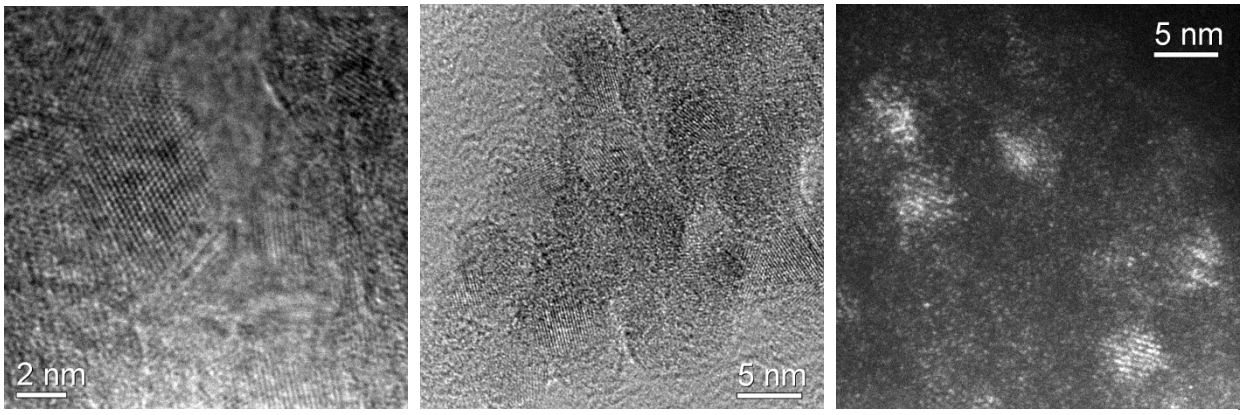

(a) (b) (c)

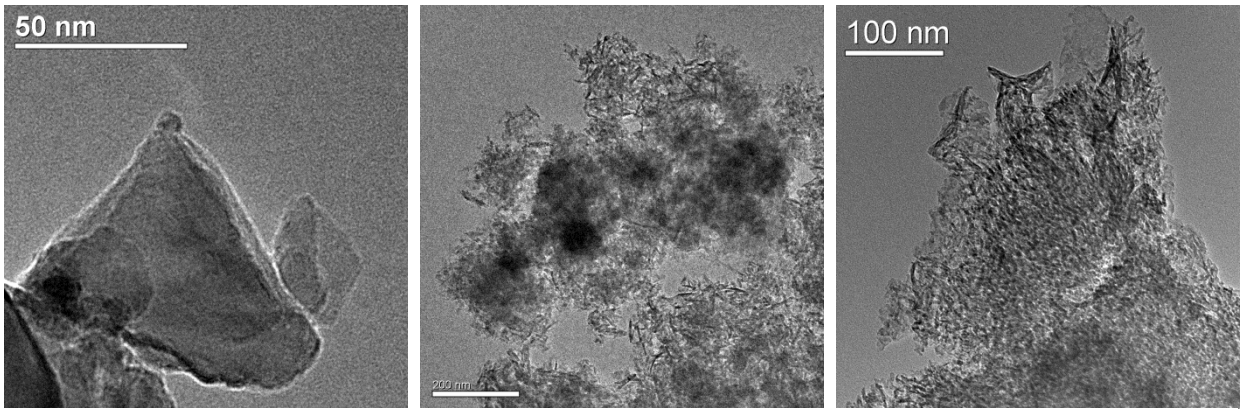

(d) (e) (f)

Figure 5.4 (a,b,c) High magnification TEM images using mass contrast (a, b) and dark field (c) contrast , highlighting the 3-5 nm size of the roughly spherical Al_2O_3 crystallites synthesized by the solvent-deficient method using calcination temperatures of 300-950°C (the images shown are from the 700°C sample). (d) Image of the large, sintered Al_2O_3 particles produced above 1000°C (the image shown is from the 1100°C sample). (e,f) Low magnification images showing the agglomerated nature of both (e) commercially-obtained γ-Al_2O_3 (Alpha Aesar) and (f) Al_2O_3 synthesized using the solvent-deficient method (the image shown is the 700°C sample).

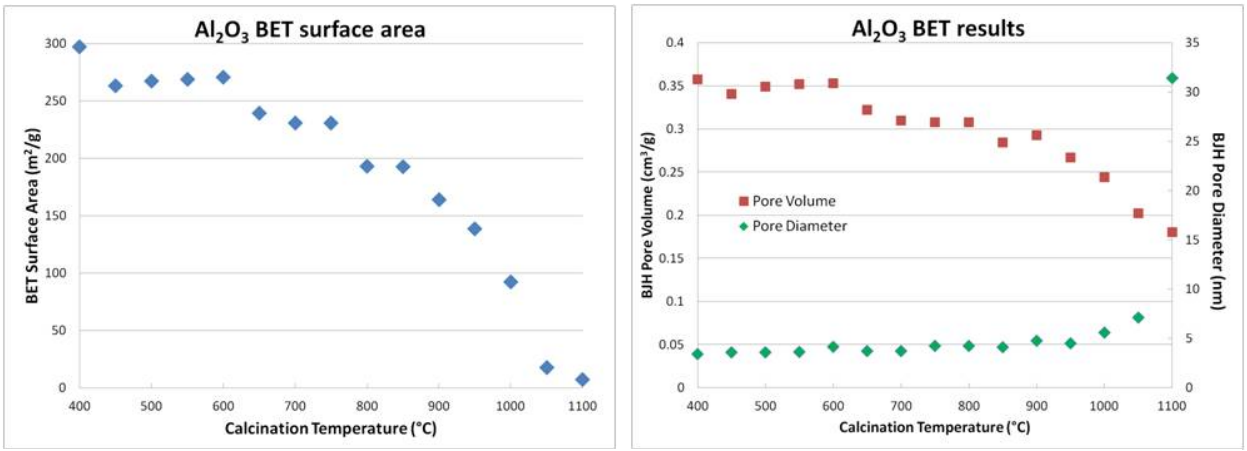

(a) (b)

Figure 5.5 BET (a) surface area and (b) pore volume/diameter as synthetic calcination temperature increases.

As Figure 5.4e-f show, commercial samples exhibit the same agglomerated morphology as our Al_2O_3 calcined between 300-1000°C. However, the Al_2O_3 agglomerates formed via the solvent-deficient process have a significantly higher average surface area (Table 5.1) than most commercial samples that have been calcined at comparable temperatures, which we attribute to the smaller crystallite sizes of the particles within the agglomerates. Because higher surface area

allows for greater catalyst dispersion which correlates to increased efficiency, our alumina is a promising candidate for adsorption and catalyst applications. Additionally, the distribution in pore size (Figure 5.6) for the Al_2O_3 synthesized via the solvent-deficient method is roughly half that of commercial materials, which would enable more uniform catalyst sites to form on our alumina.

Table 5.1 Surface area, pore size, and crystallite size of Al_2O_3 synthesized via the solvent-deficient method compared to commercially available products.

	BET surface area (m^2/g)	Crystallite size (nm)	Pore Diameter (nm)
BYU alumina	**250**	**3-5**	**1.85**
Davison Mi-286	170-230	22	
Grace Mi-286	300-350	22	5.0
Sasol Puralox	147	30	6.0
Sasol Catalox	191		4.0

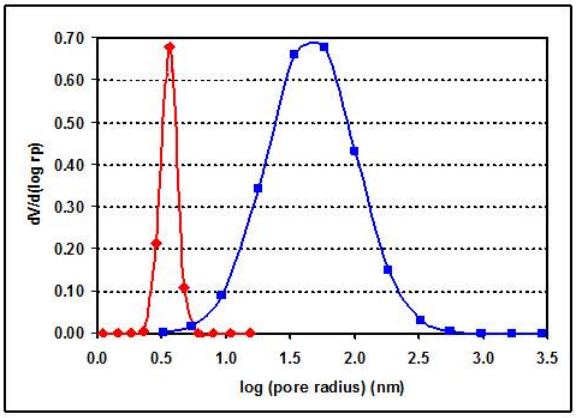

Figure 5.6 Distribution of the BET pore size for Al_2O_3 obtained commercially (Sasol Pural, blue) and synthesized from the solvent-deficient method (red).

These TEM and BET analyses thereby suggest that the physical properties of our Al_2O_3 are as good or possibly better than those of commercially available materials for adsorption and catalyst support applications. Most of these applications are specific to the γ-Al_2O_3 phase, however, so to truly gauge the industrial viability of our Al_2O_3 we found it necessary to carefully determine the phase progression realized by this new solvent-deficient synthetic method.

5.3.2 Phase Identification

A mixture of techniques such as FTIR, TG/DTA (thermogravimetric/differential thermal analysis), TEM, and/or NMR are sometimes employed to analyze the structural evolution of Al_2O_3, but most studies rely primarily on X-ray diffraction (XRD).[20,45-54] As Figure 5.2 illustrates, the unique XRD pattern of each Al_2O_3 phase identifies the structure much like a fingerprint. Accordingly, we collected XRD data for alumina calcined every 50°C from 100-1200°C to identify the phases produced by the solvent-deficient method as a function of temperature. As Figure 5.7 shows, at 100°C, the dried and rinsed precursor strongly resembles boehmite (Figure 5.7a). By 1100°C, the alumina clearly matches α-Al_2O_3 (Figure 5.7c).

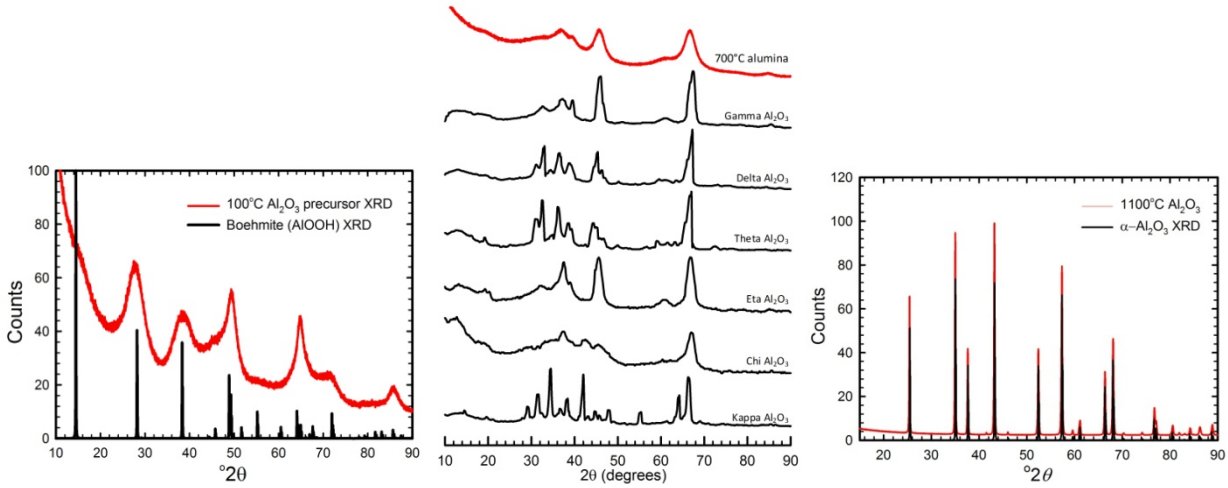

(a) (b) (c)

Figure 5.7 Normalized XRD patterns of (a) the alumina precursor rinsed and dried at 100°C matched to the boehmite AlOOH phase (ICDD #01-074-2899), (b) the 700°C Al_2O_3 compared to the transitional Al_2O_3phases (patterns from Wefers and Misra, ref 10), and (c) the 1100°C Al_2O_3 matched to the α-Al_2O_3 phase (ICDD #04-006-9730).

With boehmite as the initial phase, there are at least three routes through which the thermodynamically stable α-Al_2O_3 phase can form, according to the excellent review by Wefers and Misra.[10] Poorly crystalline boehmite has been reported to transform to η- then θ-Al_2O_3 on its way to α-Al_2O_3 (boehmite→η→θ→α), whereas well-crystallized boehmite is thought to transform to γ- then θ-Al_2O_3 before reaching α-Al_2O_3 (boehmite→γ→θ→α).[10] A third pathway

involving a δ-Al_2O_3 phase (boehmite→γ→δ→θ→α) is also commonly reported,[5,55] though no crystal structure has been determined for δ-Al_2O_3. Similarly, χ-Al_2O_3 (an unsolved crystal structure) is sometimes reported to precede or coincide with γ-Al_2O_3,[20,56] though it is more commonly reported in the gibbsite→χ→κ→α transition pathway.[8,19] Still other studies involving extremely small boehmite crystallites found that both the δ- and θ-Al_2O_3 phases were completely absent from the boehmite→γ→δ→θ→α pathway, resulting in the greatly simplified boehmite→γ→α pathway in which the γ→α transition occurs at significantly lower temperatures (~1050°C) than α-Al_2O_3 is typically formed (1100-1200°C).[18,57] Unfortunately, as Figure 5.7b shows, in the crucial temperature range between 300-1000°C, the small crystallite sizes (3-5 nm) of our alumina result in extremely broad diffraction peaks which make it difficult or impossible to distinguish between the various transitional phases (γ, δ, θ, η, χ, κ) whose diffraction patterns are already very similar.

To differentiate between the several transitional phases, we attempted Rietveld refinement, a more quantitative method of analysis that has been performed in a few other studies of alumina nanoparticles.[17-18,58] These other studies were performed on nanoparticles significantly larger (>20 nm) than ours (3-5 nm), however, and we found that the extremely broad nanoparticle diffraction peaks of our alumina nanoparticles push the method beyond its natural limits, resulting in ambiguous and sometimes unphysical refinements.

Recently, another quantitative method called pair-distribution function (PDF) analysis has developed into a powerful tool for probing "local structure"[59-60] and is being increasingly applied to the study of nanoparticle structures.[58,61-66] In this method, the entire XRD pattern is Fourier transformed into a real-space pair distribution function (PDF) that depicts the distribution of all interatomic distances in a material.[40,67-69] Oscillatory and diffuse components of the XRD

pattern, which are ignored by Rietveld analysis, appear as additional peaks in the PDF and yield information about the local structure. As with Rietveld refinements, the actual refinement of a structural model against PDF data is typically based on least-squares optimization.[41,70]

The PDF technique has already proven useful in the study of both the boehmite[58] and γ-Al_2O_3 phases,[44] so here we have applied the PDF method to our suite of evolving Al_2O_3 samples calcined between 300-1200°C. PDF data throughout the full range of calcination temperatures are shown in Figure 5.8a. The data reveal visual evidence for only two transitions. First, between 1000-1100°C, a rapid and drastic transformation occurs in the PDF which we know from our preliminary XRD analyses (Figure 5.7c) to be the transition to the α-Al_2O_3 phase. The second, less obvious transition is highlighted in the insert of Figure 5.8b; between 300-1000°C the change in the second ($r \approx 2.8$ Å) and third ($r \approx 3.4$ Å) peak ratios provides some evidence for a transition from boehmite to one of the metastable Al_2O_3 phases. Other than this low-*r* evolution, however, no significant visual changes occur in the PDF between 300-950°C except that the peaks at high-*r* became more distinct (see Figure 5.8b), indicating a slight increase in crystallinity and/or crystallite size as the calcination temperature increases. The raw PDF data thereby suggest the presence of only three phases: boehmite, a single transitional Al_2O_3 phase, and α-Al_2O_3.

As Figure 5.8c shows, the PDF data of this transitional Al_2O_3 phase match the PDF data of commercial γ-Al_2O_3 samples essentially exactly. The high-*r* data in particular resemble γ-Al_2O_3 more strongly than the γ-, δ-, θ-Al_2O_3 mixture, as the difference curves at the bottom of Figure 5.8c illustrate. Thus, the alumina synthesized via the solvent deficient method appears to follow the simplified boehmite→γ→α pathway reported in other studies of small Al_2O_3 particles.[18,57]

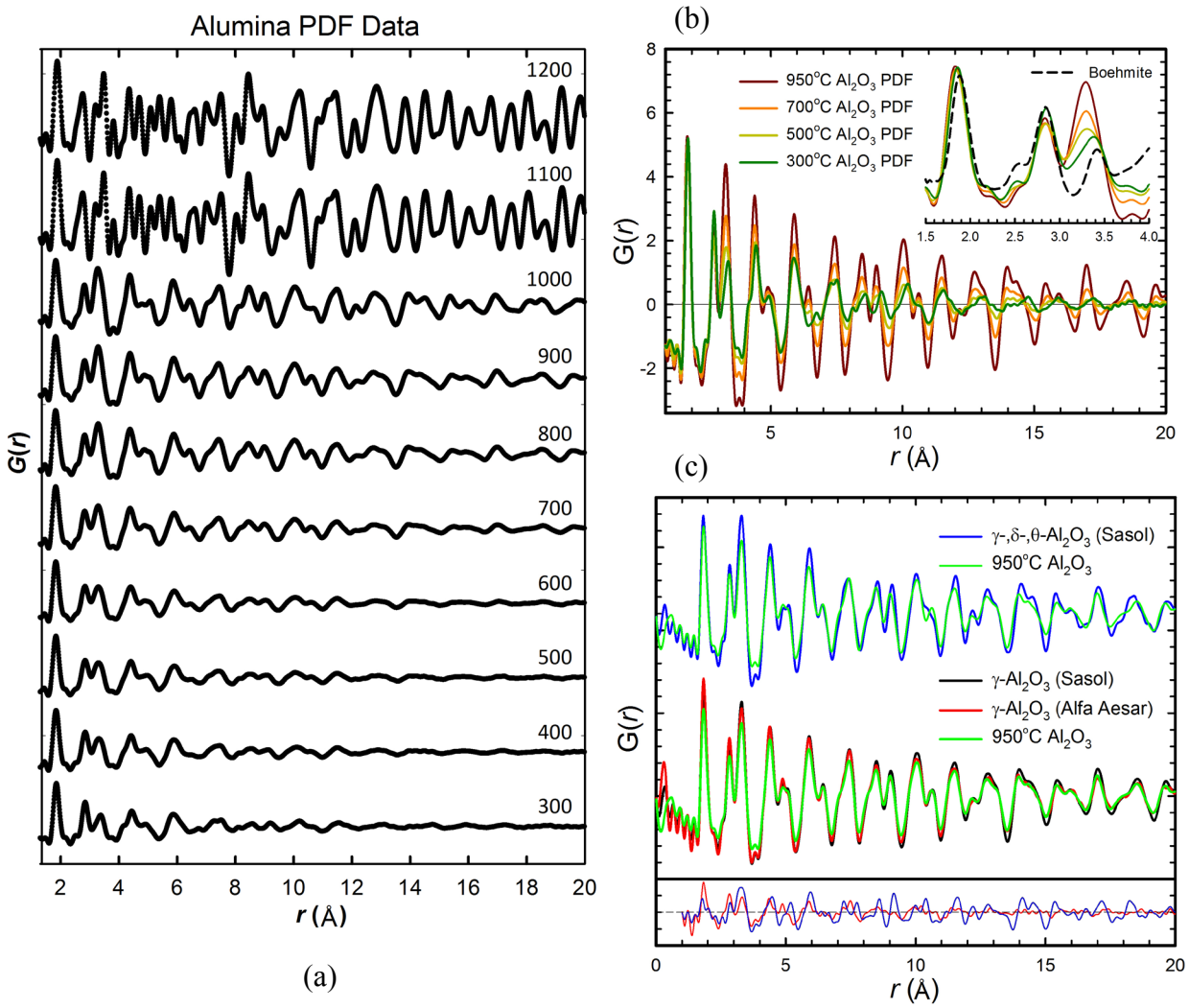

Figure 5.8 (a) PDF data throughout the full range of calcination temperatures (300-1200°C). Two phase transitions are visible: (1) a drastic transition between 1000-1100°C to the α-phase, and (2) a subtle transition between 300-1000°C. (b) The subtle transition manifested in the change in the 2nd and 3rd peak ratios at low-*r* between 300-1000°C provides some evidence for a transition from boehmite to one of the metastable Al_2O_3 phases. (c) The PDF data of this metastable phase (950°C sample, green) match the commercial γ-Al_2O_3 samples from Sasol (black) and Alfa Aesar (red) significantly better than the γ, δ, θ-Al_2O_3 mixture (blue), as the difference curves at the bottom of the graph indicate (blue curve = [γ, δ, θ-Al_2O_3 mix] – [950°C sample], red curve = [γ-Al_2O_3 (Alfa Aesar)] – [950°C sample]). Alumina synthesized via the solvent deficient method thus appears to follow a boehmite→γ→α pathway.

5.3.3 γ-Al_2O_3 Local Structure

To be certain that only one transitional Al_2O_3 phase is present and that it is indeed γ-Al_2O_3, though, we fit the PDF data of our 700, 800, and 950°C samples with the eta (η),[4] gamma (γ),[11] theta (θ),[4] and kappa (κ)[8] Al_2O_3 phases (the unsolved δ- and χ-Al_2O_3 phases could not be

tested).[xviii] The fact that the fit quality for each phase remains virtually constant at each temperature confirms to us that no phase transitions are occurring. Somewhat surprisingly, however, the η and θ phases model the data essentially as well as the γ phase (see Figure 5.9a-c), and there are curious trends in the fit qualities of the various phases. As highlighted in the difference curves in Figure 5.9a-d, both the γ- and η-Al_2O_3 phases model the data significantly better at high-*r* (above 8 Å) than at low-*r*. Conversely, the θ- and κ-Al_2O_3 structures fit very well at low-*r* but noticeably worse than γ- and η-Al_2O_3 at higher *r*. These same trends appeared in fits of the commercial γ-Al_2O_3 samples with the same γ-, η-, θ-, and κ-phases (see Appendix B.1). The PDF study of γ-Al_2O_3 by Paglia *et al.*[44] also

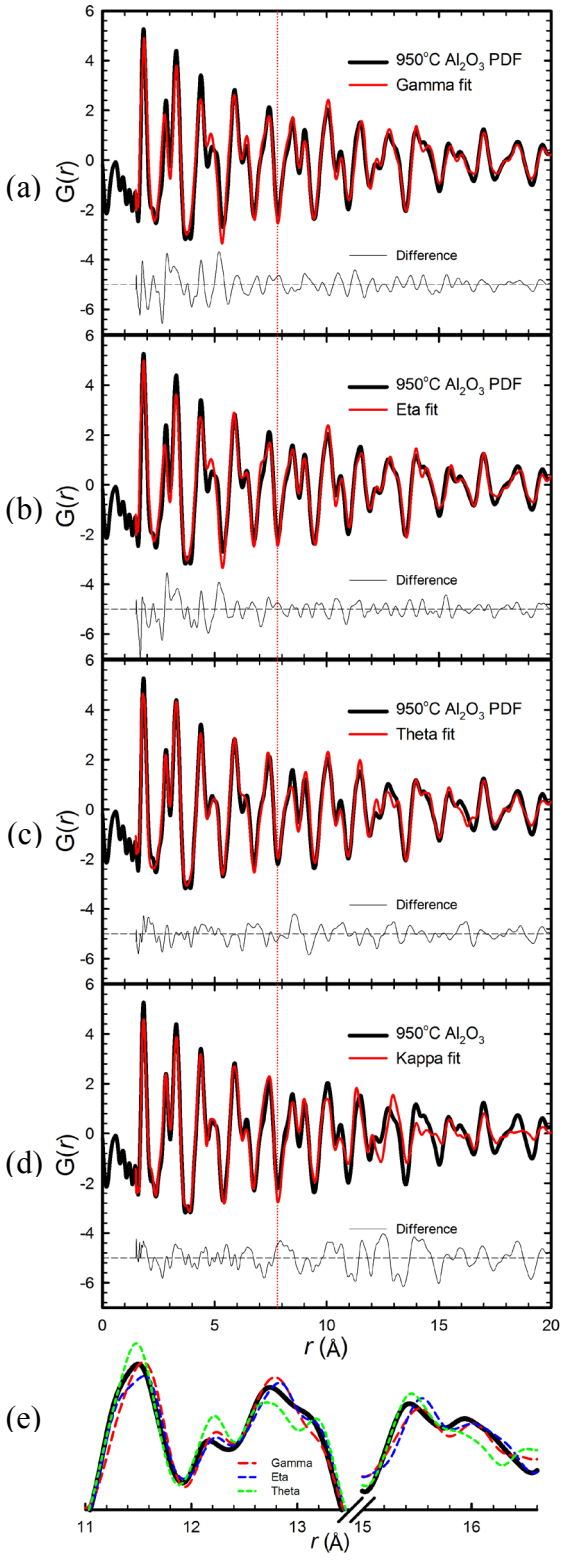

Figure 5.9 PDF refinements of the 950°C data using the (a) γ-Al_2O_3, (b) η-Al_2O_3, (c) θ-Al_2O_3, and (d) κ-Al_2O_3 structures. The vertical red line in each graph divides the low-*r* region ($r \leq 7.8$ Å) where the θ- and κ-phases fit better from the high-*r* region ($r \geq 7.8$ Å) where the γ-and η-phases fit better, as is clearly visible from the difference curves shown at the bottom of each graph. As part (e) illustrates, the high-*r* data actually appears to contain a mixture of features from the γ, η, and θ phases.

[xviii] Because there is not perfect agreement on whether the structure of γ-Al_2O_3 is cubic or tetragonal, we modeled our 700°C alumina and also the data for the 3 standard samples of γ-Al_2O_3 (obtained from Sasol and Alfa Aesar) using two different cubic γ-Al_2O_3 structures (Zhou, 1991) and a tetragonal γ-Al_2O_3 structure (Paglia, 2003). The tetragonal structure resulted in a slightly better fit, so it was the structure used in our analyses.

noted the decrease in fit quality of the gamma phase at $r < 8$ Å.

To make sense of these trends, we analyzed the similarities and differences between the four phases using some innovative symmetry mode analysis techniques. To summarize these results which are reported in greater detail in the next chapter, all four phases share roughly the same face-centered cubic (fcc) lattice of oxygen anions, but the lattice is distorted to varying extents, and the placement of the Al cations within the oxygen lattice varies between the phases (though all contain a mixture of both tetrahedrally and octahedrally coordinated Al). The γ- and η-phases are actually nearly identical, differing only in that the body-centered tetragonal cell of γ-Al_2O_3 exhibits a simple [001] lattice strain compared to the truly fcc cell of η-Al_2O_3 and that one-third of the Al positions display slightly more displacive disorder in η-Al_2O_3 than in γ-Al_2O_3. The θ-phase likewise shares roughly ½ of its Al sites with γ-Al_2O_3,[25] but its monoclinic symmetry (in which there are three separate O and two separate Al sites that each have two degrees of positional freedom) allows for much more displacive disorder in the fcc oxygen lattice and in the Al positions than in the γ- and η-phases. Like the monoclinic θ-phase, the orthorhombic symmetry of the κ-phase (in which there are six separate O and four separate Al that each have three degrees of freedom because they reside on general symmetry positions) allows more displacive disorder in the oxygen lattice and Al positions than in the γ- and η-phases.

Armed with these similarities and differences between the phases, we rationalize that displacive disorder must exist in the oxygen lattice and Al positions of the γ-Al_2O_3 phase that allow the AlO_6 octahedra and AlO_4 tetrahedra to relax/distort into substantially non-cubic configurations. This is why the monoclinic θ-Al_2O_3 and orthorhombic κ-Al_2O_3 phases, which provide the lattice with much more freedom to relax than the cubic η-Al_2O_3 and tetragonal γ-

Al_2O_3 structures, fit extremely well at low-*r*. These distortions must be randomized, however, such that when longer interatomic distances are averaged together at higher *r* the lattice appears roughly cubic, explaining why the γ- and η-phases fit better at high-*r*.

The γ-Al_2O_3 phase provides the best fit at high-*r* both for our Al_2O_3 and the commercial γAl_2O_3, but it does not definitively outperform the η and θ phases as might be expected based on the differences in Al positions between the three phases. In fact, as Figure 5.9e illustrates, the high-*r* data actually appear to contain a mixture of features from each phase, and a multiphase fit returns contributions from all three phases. This may be evidence that the Al sites themselves (and not just the displacive disorder for each site) can vary throughout γ-Al_2O_3, producing regions of local structure such as those proposed by Paglia *et al*.[71] In that study, 40% of the Al atoms within γ-Al_2O_3 were found to reside in non-spinel positions that varied from region to region (or supercell to supercell). Of these 40%, two-thirds were in c-symmetry based positions (supporting the use of a tetragonal structural model for γ-Al_2O_3) and the remainder were in a variety of non-a,-c, or –d symmetry positions which minimized the local lattice distortions. These calculations showed it to be more important to have cations in the correct Miller planes than in particular symmetry positions, thus a variety of symmetry positions were observed.

We thereby propose that while our transitional Al_2O_3 phase is as rightly labeled as γ-Al_2O_3 as commercial γ-Al_2O_3 samples, γ-Al_2O_3 itself (irrespective of synthetic method) contains randomized local structure variations both in the AlO_6/AlO_4 units and in the Al positions occupied throughout the structure which cause deviations between the average, tetragonal γ-Al_2O_3 structure and the observed PDF data, particularly at low-*r*. Both ours and Paglia *et al*.'s studies thus show that a single unit cell cannot perfectly model the γ-Al_2O_3 phase, (nor perhaps the other transitional Al_2O_3 phases, which seem likely to harbor similar local structure

distortions), and a more accurate approach to modeling γ-Al_2O_3 would be to use a collection of locally-distorted supercells as Paglia *et al.* did in their calculations.

5.3.4 Phase Transition Analyses

To quantify the boehmite→γ and γ→α transition temperatures for the alumina synthesized using the solvent deficient method, the convenience and simplicity of using a single unit cell to model the γ-Al_2O_3 phase outweighed the disadvantage of its physical inaccuracy. We thus initially modeled the PDF data of our suite of samples using only the boehmite,[72] tetragonal γ-Al_2O_3,[11] and α-Al_2O_3[73] phases of alumina (Figure 5.10).

These initial PDF fits indicated that the γ-Al_2O_3 transforms to α-Al_2O_3 between 1000-1100°C with the transition nearly complete by 1050°C, consistent with the results from previous studies of small nanoparticles.[18,57] A direct γ-to-α transition and a corresponding reduction in the alpha phase transition temperature to roughly 1050°C thus seems to be a general result for small particle sizes.

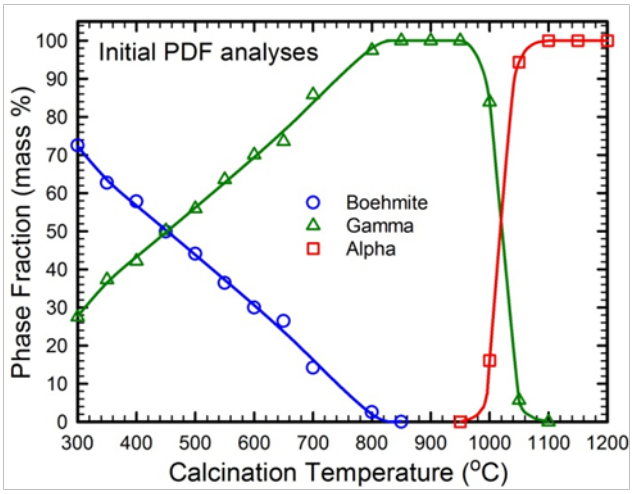

Figure 5.10 Boehmite, γ, and α phase fractions obtained from the initial PDF analyses.

Two unusual features were produced by these initial fits, however: (1) significant fractions (~30%) of the γ-Al_2O_3 phase were present in the atypically low temperature range of 300-400°C and (2) the boehmite phase did not disappear until roughly 800°C, which is an unusually high temperature for an oxyhydroxide phase. To determine the validity of the second feature, we collected TG/DTA data in tandem with MS data to see if the water loss required by the transition from the boehmite phase (AlOOH) to the γ-Al_2O_3 phase persists up to 800°C. As

Figure 5.11 shows, water loss indeed continues through 800°C, but the amount of H_2O evolved cannot justify the rather large boehmite phase fractions (~30%) still present above 600°C in the initial PDF analyses.

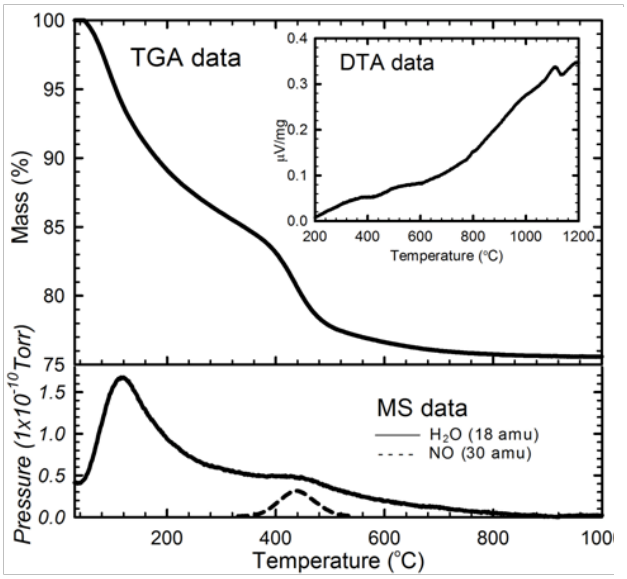

Figure 5.11 TG/DTA-MS analysis of the 300°C sample heated at 5°C/min from 25°C to 1200°C. H_2O evolved below 300°C is attributed to adsorbed water loss. The small fraction of H_2O evolved between 300-800°C is attributed to the decomposition of boehmite or boehmite-like features in the alumina.The evolution of NO (375-500°C) is likely the decomposition of residual, adsorbed nitrate species from the synthesis. In the inset, positive DTA values represent exothermic events, thus there is a steady exothermic signal which increases above 700°C and culminates in a small exothermic peak corresponding to the γ→α transition. The steady exothermic signal below the transition may correspond to the slow healing of boehmite-like features/defects in the alumina with increasing temperature.

In re-evaluating our initial PDF fits, we found that the boehmite phase does not model the data well even at the lowest calcination temperature of 300°C (Figure 5.12a) except for the first two peaks at r = 1.8 and r = 2.8 Å (a insert). In contrast, the γ-Al_2O_3 phase alone models the data surprisingly well at 300°C (Figure 5.12b) and throughout the entire temperature range, particularly at high-r when r-series fits are performed (Figure 5.12d). There are significant deviations from the tetragonal γ-Al_2O_3 structure in the low-r fits (Figure 5.12c) as may be expected based on the γ-Al_2O_3 local structure already discussed, but the data still resemble γ-Al_2O_3 much more than boehmite at all calcination temperatures between 300-950°C.

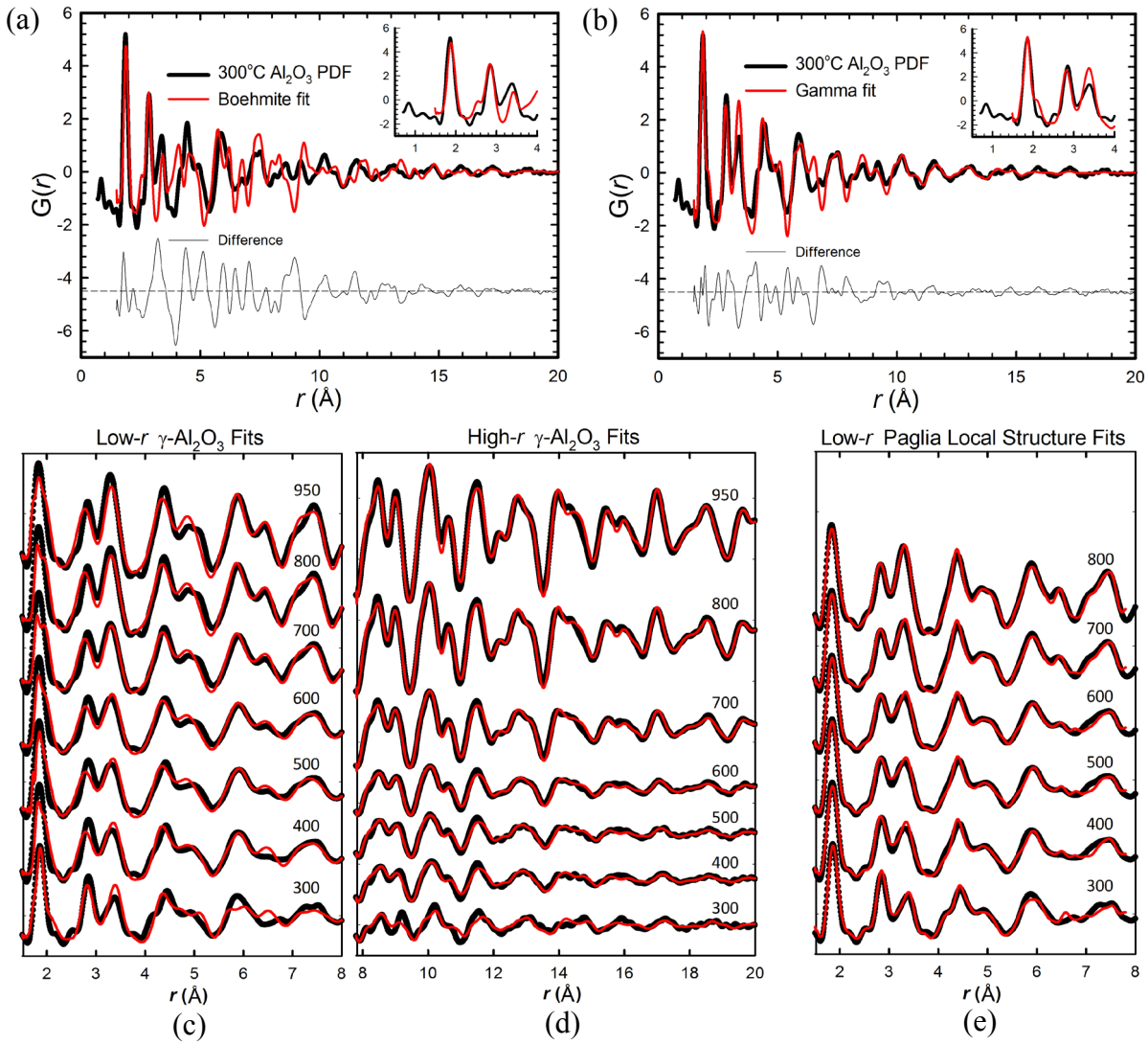

Figure 5.12(a,b) PDF data (black) for the 300°C sample modeled (red) using the (a) boehmite and (b) γ-Al_2O_3 structures. The insets highlight the only peaks (the first two PDF peaks) that the boehmite structure successfully models. (c,d,e) PDF refinements at (c) low-*r* values ($r \leq 7.8$ Å) and (d) high-*r* values ($r \geq 7.8$ Å) using only the average γ-Al_2O_3 structure for samples calcined between 300-950°C. (c) PDF refinements at low-*r* using the local γ-Al_2O_3 structure proposed by Paglia *et al*.

300°C is an atypically low temperature to observe the γ-Al_2O_3 phase, however, and it is even more unusual for it to be the primary phase present; most studies do not report the γ-Al_2O_3 phase until roughly 450-650°C (Figure 5.3b).[4,10,22,74] So, to confirm the presence and dominance of the γ-Al_2O_3 phase between 300-1000°C, we performed ^{27}Al MAS-NMR analyses for several of the samples (Figure 5.13). ^{27}Al MAS-NMR is an effective tool for distinguishing the γ-Al_2O_3 phase from the boehmite and α-Al_2O_3 phases because Al coordination is exclusively octahedral

in both the α-Al_2O_3 and boehmite phases[75] whereas it is roughly 70% (±2%) octahedral and ~30% tetrahedral in the γ-Al_2O_3 phase.[11,54] As Table 5.2 shows (see Appendix B.2 for the fits used to generate these estimates), even though a slight conversion of octahedral to tetrahedral coordination is still occurring between 300-700°C, the Al coordination is already predominantly γ-like at 350°C and remains so through 1000°C, thereby supporting the PDF finding that γ-Al_2O_3 is the primary phase present from 300-1000°C.

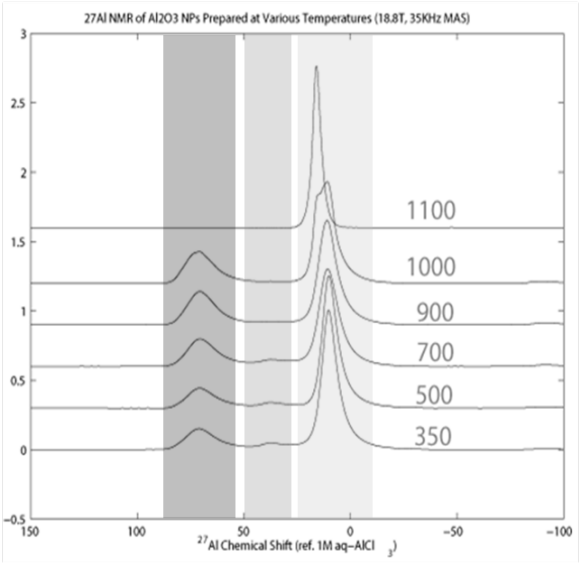

Figure 5.13 ^{27}Al MAS NMR data for the 350, 500, 700, 900, 1000, and 1100°C samples showing the tetrahedral ( ), pentahedral ( ), and octahedral ( ) Al.

Table 5.2 Quantification of the 4-, 5-, and 6-coordianted Al sites in the alumina samples calcined at 350, 500, 700, 900, 1000, and 1100°C from the ^{27}Al MAS-NMR data.

	4-coord. Al	5-coord. Al	6-coord. Al
boehmite	**0**	**0**	**100 %**
γ-Al_2O_3	**30 %**	**0**	**70 (±2)%**
α-Al_2O_3	**0**	**0**	**100 %**
350°C	19 %	5.4 %	75 %
500°C	20 %	5.2 %	75 %
700°C	27 %	6.4 %	67 %
900°C	31 %	2.7 %	66 %
1000°C	30 %	2.0 %	68 %
1100°C	0	0	100 %

Interestingly, our data in Figure 5.13 also reveal a significant amount (> 5%) of 5-coordinated Al sites in the γ-Al_2O_3 (see Appendix B.2 for a more clear representation), which is in agreement with several other high resolution ^{27}Al MAS-NMR studies of γ-Al_2O_3.[53,76-82] The fraction of these sites increases slightly from 300-700°C and then decreases substantially between 900-1000°C (Table 5.2), as was observed in at least one of these studies.[81] Several groups have suggested that these are surface sites,[53,76-77] though others have reasoned that they may exist in within the crystal.[83]

The formation of the γ-Al_2O_3 phase at the relatively low temperatures of 300-400°C could be a unique result of the solvent-deficient environment of our synthetic method.[35,84] The limited supply of water during the boehmite precursor's formation likely endows it with minimal water content, as we have found with other oxyhydroxide materials formed via this method.[85] This low water content may allow our boehmite precursor to dehydrate and decompose to Al_2O_3 more readily than boehmite produced using aqueous solution methods. Alternatively, the lowered transition temperature could be attributed to the small size of the boehmite crystallites; previous studies have shown that a small particle size in the boehmite precursor results in lower transformation temperatures throughout the subsequent sequence of calcination products,[15,17,52,86] with particles smaller than 20 nm displaying transition temperatures up to 30% lower than those observed for micron-sized particles.[87] An additional alternative is discussed in the next section.

5.3.4.1 Evolution of a boehmite-like local structure within γ-Al_2O_3

Both the ^{27}Al MAS-NMR and PDF fits thus indicate that γ-Al_2O_3 is the dominant phase between 300-1000°C. Yet even though the γ-Al_2O_3 phase models the high-*r* data extremely well at all temperatures (Figure 5.122d), the low-*r* fit quality steadily decreases with decreasing temperature (Figure 5.12c) to an extent which cannot be explained solely by the randomized local structure variations in γ-Al_2O_3 discussed earlier; in particular, no matter how much displacive freedom is allowed, none of the transitional alumina structures can reproduce the steady change in the $2^{nd}/3^{rd}$ peak ratios illustrated in Figure 5.8b.

Figure 5.14 quantifies the change in the $2^{nd}/3^{rd}$ peak ratios, which undeniably shifts from a more boehmite-like to a γ-like ratio, forming a 'pure' γ-Al_2O_3 ratio around 800°C. Because the existence of a separate, extended boehmite structure is refuted by the high-*r* PDF analyses in

Figure 5.14 and the NMR data in Table 5.2, we hypothesize that a boehmite-like local structure exists within the γ-Al_2O_3 formed at 300°C which slowly evolves/disappears between 300-800°C.

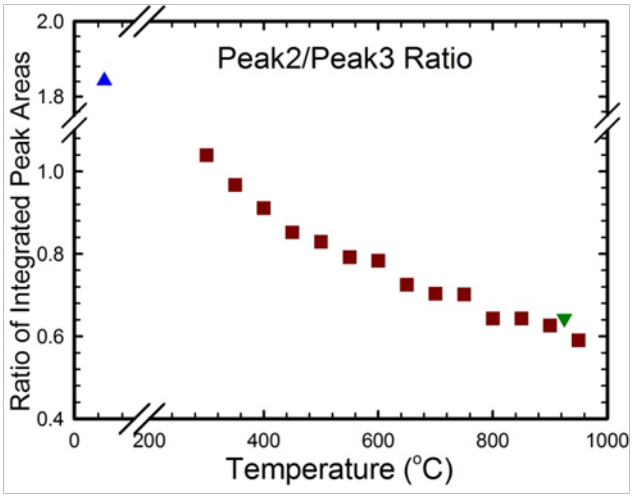

Figure 5.14 Ratios of the 2nd/3rd PDF peaks (■) between 300-1000°C change from a boehmite-like ratio (▼) to a γ-like ratio (▲), providing some evidence for a boehmite-like local structure in γ-Al_2O_3.

To determine the nature of such a boehmite-like local structure, we analyzed the interatomic distances in each phase that could contribute to the evolving low-*r* peaks. We found that for both the boehmite and γ-Al_2O_3 phases, the first peak in the PDF ($r \approx 1.8$ Å) represents the nearest-neighbor Al-O distances and the second peak ($r \approx 2.8$ Å) represents multiple O-O and Al-Al distances. In the layered boehmite (AlOOH) phase shown in Figure 5.15a, however, additional O-O distances between the oxygen atoms in the adjacent layers of the structure cause the second peak to be slightly higher for boehmite (Figure 5.8b). Similarly, the third peak ($r \approx 3.4$ Å) is primarily Al-O distances for both phases, but in the γ-Al_2O_3 phase there are a few Al-Al distances as well, causing the area of the 3rd peak to be significantly larger for the γ-Al_2O_3 phase. We therefore reason that the evolving low-*r* features in our PDF data between 300-800°C is related to the way in which O and Al atoms bridge the original boehmite layers to form the γ-Al_2O_3 structure.

Conveniently, Paglia *et al*. suggested just such a local structure model to account for the low-*r* misfits observed in their PDF study of γ-Al_2O_3.[44] In the boehmite-to-γ-Al_2O_3 transition, the boehmite structure (Figure 5.15a) must (1) lose the OH groups from between the layers, (2) shift 30% of the Al into tetrahedral positions, and (3) shift adjacent layers of boehmite in two

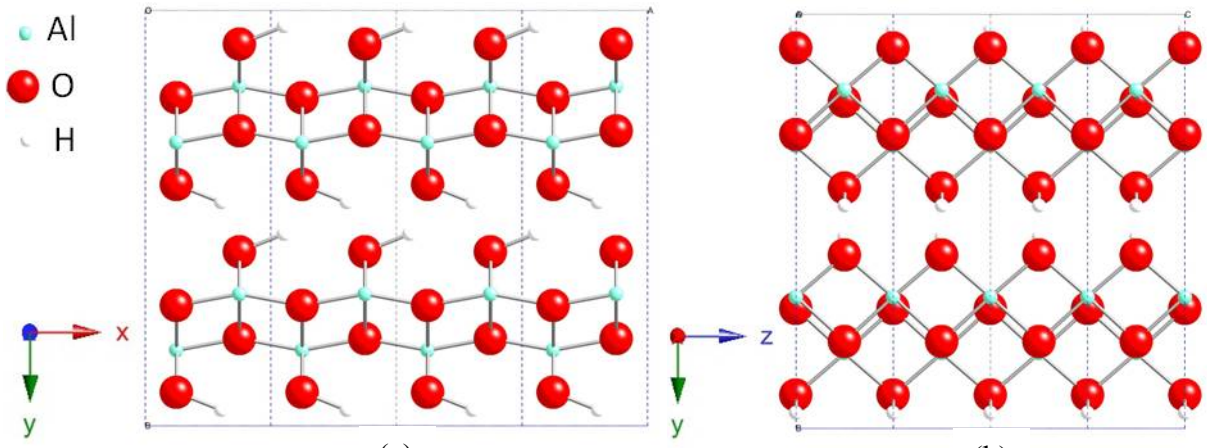

Figure 5.15 Views of the boehmite structure highlighting (a) the OH groups between the layers and (b) the mismatch between the rows of oxygen in adjacent layers. If the adjacent boehmite layers do not translate during the boehmite-to-γ transition, stacking faults will result in the oxygen sublattice, with residual OH groups and awkwardly coordinated Al bridging the fault, as shown in (c).

directions (the *z*- and *y*-directions in Figure 5.15b) in order to align the layers of oxygen to form the roughly cubic oxygen lattice of γ-Al_2O_3. Paglia *et al*.'s model is one in which this translation does not occur, leaving stacking faults in the oxygen lattice which are bridged by awkwardly coordinated Al atoms that move into the gap.

Using the local structure model proposed by Paglia *et al*., we modeled the low-*r* data (1.5 Å ≤ *r* ≤ 7.8 Å) between 300-800°C. The local structure models the data very well, including the change in the $2^{nd}/3^{rd}$ peak ratios, as Figure 5.12e shows. However, the P1 symmetry of the defect model allows it to accomplish these fits simply by shifting the atom positions very slightly within the defect structure, where the Al-O coordination is already highly distorted.[xix] We suspect that the distortions in that model are already too great to be physically realistic. Additionally, the model assumes a static defect concentration and provides no means of refining the concentration of the defect with respect to the average structure . We attempted a simple two-phase refinement using the local and average structures. But again, the P1 symmetry of the local

[xix] Paglia *et al*. proposed a version of their defect model with Pmma symmetry, but this higher symmetry structure did not model the data better than the average γ-Al_2O_3 structure.

structure allows it to dominate the refinement simply by adjusting atom positions instead of the phase fraction.

Thus, even though Paglia *et al.*'s local structure model may be conceptually viable, determining a refinable boehmite-like local structure model that evolves realistically with temperature will likely require big-box modeling approaches in which multiple versions of boehmite-like planar defects are incorporated into the average γ-Al_2O_3 structure and minimized against both energy and experimental PDF data as a function of temperature. We have left such studies for future endeavors. To roughly quantify the boehmite-like defects, however, we used the average boehmite structure as the model for the boehmite-like defects and again performed two-phase refinements with the boehmite and γ-Al_2O_3 structures, but this time using only the low-*r* data. The resulting fits and relative fractions of the boehmite-like defects, γ-Al_2O_3, and α-

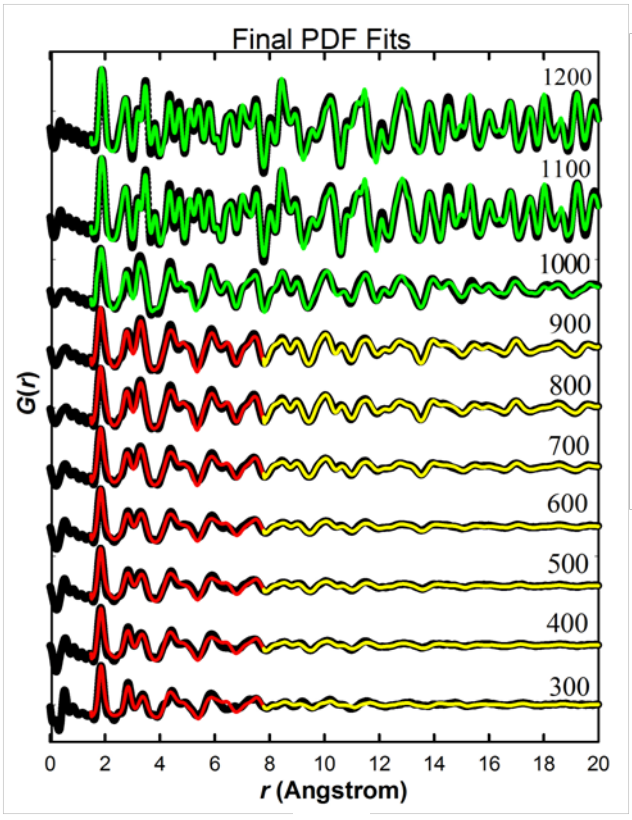

(a)

(b)

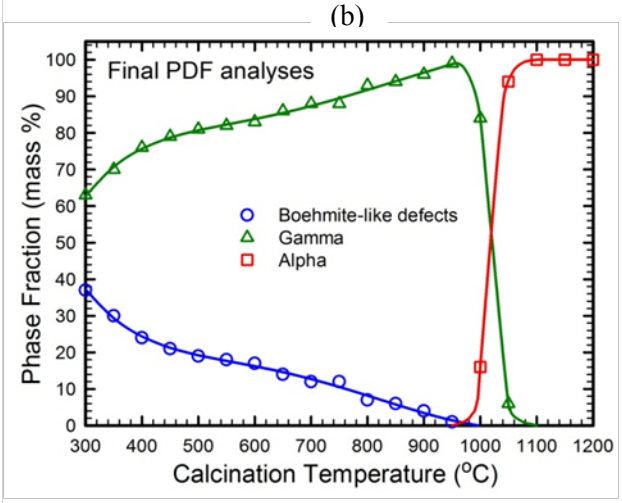

Figure 5.16 (a) Final PDF fis. Data between 300-950°C at $r \geq 7.8$ Å were fit using the γ-Al_2O_3 structure (yellow fits); the data at $r \leq 7.8$ Å were fit using a 2-phase fit including the boehmite and γ-Al_2O_3 structures (red fits) to model the evolving boehmite-like defects present in γ-Al_2O_3. Data between 1000-1100°C were fit using a 2-phase fit including the γ-Al_2O_3 and α-Al_2O_3 structures (green fits). (b) Relative phase fractions of boehmite-like defects, γ-Al_2O_3, and α-Al_2O_3 as a function of calcination temperature.

Al_2O_3 phases throughout the entire range of calcination temperatures are shown in Figure 5.16 (for the refined fit parameters see Appendix B.3).

Further modeling/calculations may provide an exact picture of the evolving, boehmite-like planar defects we have suggested, but to describe the essence of our hypothesis, we envision that the crystal structure within the layers of boehmite converts rapidly to a γ-Al_2O_3-like configuration (as low as 300-400°C), which explains why the high-*r* PDF data at 300°C has already begun to resemble γ-Al_2O_3 (Figure 5.12). As the OH between the layers are driven off, however, the requisite lattice shift does not occur for many of the layers as suggested by Paglia *et al*., resulting in extremely small coherence lengths for the γ-Al_2O_3 phase. Such small coherence lengths would cause the XRD pattern to initially appear amorphous, explaining the large delay often reported between the disappearance of boehmite and the appearance of γ-Al_2O_3 between 300-500°C (Figure 5.3) as well as the tendency of the γ-Al_2O_3 phase to be 'fine-grained' no matter the original boehmite crystal size.

Instead of having a distinct threshold temperature at which the lattice translation occurs and the layers collapse, these boehmite-like gaps heal slowly over a wide range of temperature from 300°C to 800°C. We conjecture that residual OH groups (or absorbed/adsorbed H_2O) as well as Al atoms that diffuse into the gaps stabilize them, delaying the translation/healing process and smearing it over a range in temperature due to the wide variation in gap configuration/stabilization. This would explain the impressive H_2O sorbent abilities of γ-Al_2O_3 as well as the high-temperature H retention often reported for γ-Al_2O_3[88-90] and seen in our own TG/DTA-MS analyses in Figure 5.11. Additionally, the undoubtedly awkward configurations of Al atoms inside the gaps could explain the significant fraction of pentacoordinated Al sites observed solely in γ-Al_2O_3; indeed, some of the bridging Al in Paglia *et al*.'s local structure will

be pentacoordinated. The healing of these defect planes would then explain the observed decrease in pentacoordinated sites with increasing temperature (Table 5.2) and would also account for the substantial increase in crystallinity apparent in the PDF data between 300-1000°C (Figure 5.8) despite no such substantial increase in average crystallite size observed in the TEM.

Because several ^{27}Al NMR studies report the pentacoordinated Al to be on the surface,[53,77] it seems possible that similar boehmite-like defect planes (adsorbed H_2O, pentacoordinated Al) could be located at particle surfaces or at the interface between two particles in the agglomerates. The healing of surface defects, resulting in mild sintering, would then account for the steady decrease in BET surface area with increasing temperature (Figure 5.5g) that is ubiquitously observed for γ-Al_2O_3. The resulting relaxation of the structure as the stacking faults and/or surface defects heal could also explain the steady exothermic signal in the DTA measurements in the range between 300-1000°C (inset of Figure 5.11) where no phase transition is occurring. In short, an evolving, boehmite-like defect structure within γ-Al_2O_3 could account for many of the phases most intriguing and useful properties of this system.

5.4 Conclusions

We thereby conclude that the solvent-deficient synthetic method produces a γ-Al_2O_3 material that is a promising candidate for catalyst support and adsorption applications due to the high surface area and mesoporous nature of the agglomerates consisting of the 3-5 nm crystallites. The phase progression of the alumina determined by X-ray PDF, ^{27}Al MAS-NMR, and TG/DTA analyses proceeds as shown in Figure 5.16 and as diagramed in Figure 5.17. The boehmite precursor transforms to γ-Al_2O_3 particles upon calcination at 300-400°C, a much lower temperature than previously considered possible. These γ-Al_2O_3 particles are initially riddled

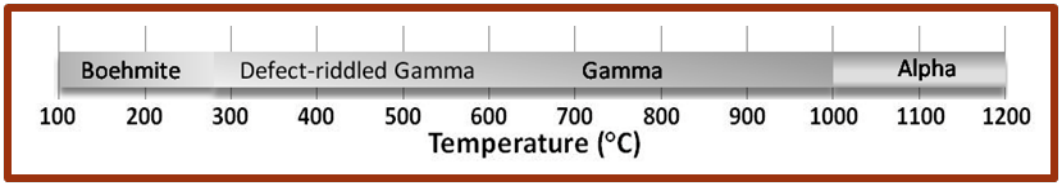

Figure 5.17 Phase progression of the Al_2O_3 nanoparticles synthesized via the solvent-deficient method.

with boehmite-like defect planes either within the particles or at particle surfaces/interfaces, but these defects heal as temperature increases through 800°C, as manifested by the change in the low-*r* ($2^{nd}/3^{rd}$ peaks) PDF peak ratios from a boehmite-like to a γ-like ratio and also by the increase in the crystallinity and/or crystallite-size of the γ-Al_2O_3 phase seen in the PDF data.

The evolution of such a boehmite-like defect/local structure in γ-Al_2O_3 provides the simplest and most cohesive explanation of several of the phase's most interesting and useful properties including its tendency to be fine-grained, to absorb and/or retain H_2O, to have 5-coordinated Al sites, and to display a continuous albeit gradual loss of surface area with temperature. Because these properties are ubiquitously reported for γ-Al_2O_3, the evolving boehmite-like local structure that we have suggested may also be ubiquitously present in γ-Al_2O_3 regardless of particle size or synthetic method.

Though essentially pure γ-Al_2O_3 is obtained at calcination temperatures between 700-950°C, even this '*pure*' γ-Al_2O_3 deviates from the average γ-Al_2O_3 structure at short interatomic distances (low-*r*) in the PDF data, as do all samples of commercial γ-Al_2O_3 as well as the γ-Al_2O_3 in other PDF studies. We propose that these local structure deviations can be explained by small, randomized, non-cubic local distortions in the AlO_6 and AlO_4 units of γ-Al_2O_3 which average together at higher *r* to produce a roughly cubic oxygen lattice. The distribution of Al cations within this locally-distorted oxygen lattice (*i.e.*, the type of Al sites, their occupancy, and their displacive disorder) may also vary throughout the γ-Al_2O_3, as suggested by previous

studies. Thus, a more physically accurate approach to modeling γ-Al_2O_3 would be to use a collection of locally-distorted supercells instead of a single unit cell.

Between 1000-1100°C, our γ-Al_2O_3 transforms directly to α-Al_2O_3 with the transition essentially complete by 1050°C. Other studies of small alumina particles have likewise observed both the lowering of the α-phase transition to 1050°C (from the typical 1100-1200°C transition temperature) and the simplification of the phase transition pathway to boehmite→γ→α from the boehmite→γ→δ→θ→α pathway commonly observed for larger particles. This result therefore appears to be generally true for alumina small nanoparticles. Thus, even though these structural analyses were performed for alumina synthesized using a unique method, we anticipate that the results (particularly the local structures discussed) are generally applicable to γ-Al_2O_3 irrespective of the synthetic method.

References

1. Saalfeld, H., Corundum structure. *Naturwissenschaften* **1961,** *48*, 24.
2. Bezjak, A.; Jelenic, I., The crystal structures of boehmite and bayerite. *Symp. Bauxites, Oxydes Hydroxydes Alum., [C. R.]* **1964,** (1), 105-12.
3. Ewing, F. J., Crystal structure of diaspore. *J. Chem. Phys.* **1935,** *3*, 203-7.
4. Zhou, R. S.; Snyder, R. L., Structures and transformation mechanisms of the η, γ, and θ transition aluminas. *Acta Crystallogr., Sect. B: Struct. Sci.* **1991,** *B47* (5), 617-30.
5. Rooksby, H. P.; Rooymans, C. J. M., The formation and structure of delta -alumina. *Clay Miner. Bull.* **1961,** *4*, 234-8.
6. Mekasuwandumrong, O.; Kominami, H.; Praserthdam, P.; Inoue, M., Synthesis of thermally stable chi-alumina by thermal decomposition of aluminum isopropoxide in toluene. *J. Am. Ceram. Soc.* **2004,** *87* (8), 1543-1549.
7. Saalfeld, H.; Wedde, M., Refinement of the crystal structure of gibbsite [Al(OH)3]. **1974,** *139* (1-2), 129-35.
8. Ollivier, B.; Retoux, R.; Lacorre, P.; Massiot, D.; Ferey, G., Crystal structure of κ-alumina: an x-ray powder diffraction, TEM and NMR study. *J. Mater. Chem.* **1997,** *7* (6), 1049-1056.
9. Yamaguchi, G.; Yanagida, H.; Ono, S., Crystal structure of tohdite. *Bull. Chem. Soc. Jpn.* **1964,** *37* (10), 1555-7.
10. Wefers, K. M., Chanakya, "Oxides and Hydroxides of Aluminum". *Tech. Pap. - Alcoa Res. Lab.* **1987,** *19*.

11. Paglia, G.; Buckley, C. E.; Rohl, A. L.; Hunter, B. A.; Hart, R. D.; Hanna, J. V.; Byrne, L. T., Tetragonal structure model for boehmite-derived gamma -alumina. *Phys. Rev. B: Condens. Matter Mater. Phys.* **2003,** *68* (14), 144110/1-144110/11.
12. Yamaguchi, G.; Yanagida, H.; Ono, S., New alumina hydrate, "tohdite" (5Al2O3.H2O). *Bull. Chem. Soc. Jpn.* **1964,** *37* (5), 752-4.
13. Du, X.; Wang, Y.; Su, X.; Li, J., Influences of pH value on the microstructure and phase transformation of aluminum hydroxide. *Powder Technol.* **2009,** *192* (1), 40-46.
14. Levin, I.; Brandon, D., Metastable alumina polymorphs: crystal structures and transition sequences. *J. Am. Ceram. Soc.* **1998,** *81* (8), 1995-2012.
15. Tsukada, T.; Segawa, H.; Yasumori, A.; Okada, K., Crystallinity of boehmite and its effect on the phase transition temperature of alumina. *J. Mater. Chem.* **1999,** *9* (2), 549-553.
16. Sato, T.; Sue, K.; Akiyama, Y.; Shibata, K.; Kawasaki, S.-i.; Tanaka, S.; Saitoh, K.; Kawai-Nakamura, A.; Aida, K.; Hiaki, T., Effect of pH on hydrothermal synthesis of gamma -Al2O3 nanoparticles at 673 K. *Chemistry Letters* **2008,** *37* (3), 242-243.
17. Bokhimi, X.; Toledo-Antonio, J. A.; Guzman-Castillo, M. L.; Hernandez-Beltran, F., Relationship between Crystallite Size and Bond Lengths in Boehmite. *J. Solid State Chem.* **2001,** *159* (1), 32-40.
18. Cava, S.; Tebcherani, S. M.; Souza, I. A.; Pianaro, S. A.; Paskocimas, C. A.; Longo, E.; Varela, J. A., Structural characterization of phase transition of Al_2O_3 nanopowders obtained by polymeric precursor method. *Mater. Chem. Phys.* **2007,** *103* (2-3), 394-399.
19. Brindley, I. G. W.; Choe, J. O., The reaction series, gibbsite→χ-alumina→κK-alumina→ corundum. *Am. Mineral.* **1961,** *46*, 771-85.
20. Kim, Y. M.; Lee, S.; Kim, Y. S.; Oh, S. H.; Kim, Y. J.; Lee, J. Y., Electron-beam-induced transition aluminas from aluminum trihydroxide. *Scr. Mater.* **2008,** *59* (9), 1022-1025.
21. Lippens, B. C.; de Boer, J. H., Study of phase transformations during calcination of aluminum hydroxides by selected area electron diffraction. *Acta Crystallogr.* **1964,** *17* (10), 1312-21.
22. Digne, M.; Sautet, P.; Raybaud, P.; Toulhoat, H.; Artacho, E., Structure and Stability of Aluminum Hydroxides: A Theoretical Study. *J. Phys. Chem. B* **2002,** *106* (20), 5155-5162.
23. Galbraith, A. B., S; Manias, E.; Hunt, B.; & Richards, A., *Fundamentals of pharmacology: a text for nurses and health professionals*. Harlow: Pearson: 1999.
24. Petrovsky, N. A., J. C., Vaccine adjuvants: current state and future trends. *Immunol. Cell Biol.* **2004,** *82* (5), 488-96.
25. Cai, S.-H.; Rashkeev, S. N.; Pantelides, S. T.; Sohlberg, K., Phase transformation mechanism between γ- and θ-alumina. *Phys. Rev. B: Condens. Matter Mater. Phys.* **2003,** *67* (22), 224104/1-224104/10.
26. Ivey, M. M.; Allen, H. C.; Avoyan, A.; Martin, K. A.; Hemminger, J. C., Dimerization of 1,3-Butadiene on Highly Characterized Hydroxylated Surfaces of Ultrathin Films of γ-Al2O3. *Journal of the American Chemical Society* **1998,** *120* (42), 10980-10981.
27. Trombetta, M.; Busca, G.; Rossini, S.; Piccoli, V.; Cornaro, U.; Guercio, A.; Catani, R.; Willey, R. J., FT-IR studies on light olefin skeletal isomerization catalysis, III. Surface acidity and activity of amorphous and crystalline catalysts belonging to the SiO2-Al2O3 system. *J. Catal.* **1998,** *179* (2), 581-596.

28. Cai, S.; Sohlberg, K., Adsorption of alcohols on γ-alumina (1 1 0 C). *Journal of Molecular Catalysis A: Chemical* **2003,** *193* (1-2), 157-164.
29. Shi, B.; Davis, B. H., Alcohol dehydration: mechanism of ether formation using an alumina catalyst. *J. Catal.* **1995,** *157* (2), 359-67.
30. Taylor, K. C., Nitric oxide catalysis in automotive exhaust systems. *Catalysis Reviews - Science and Engineering* **1993,** *35* (4), 457-81.
31. McCabe, R. W.; Usmen, R. K.; Ober, K.; Gandhi, H. S., The effect of alumina phase structure on the dispersion of rhodium/alumina catalysts. *J. Catal.* **1995,** *151* (2), 385-93.
32. Chu, W.; Chernavskii, P. A.; Gengembre, L.; Pankina, G. A.; Fongarland, P.; Khodakov, A. Y., Cobalt species in promoted cobalt alumina-supported Fischer-Tropsch catalysts. *J. Catal.* **2007,** *252* (2), 215-230.
33. Itkulova, S. S.; Zakumbaeva, G. D.; Arzumanova, R. S.; Ovchinnikov, V. A., Production of hard hydrocarbons from synthesis-gas over Co-containing supported catalysts. *Studies in Surface Science and Catalysis* **2007,** *163* (Fischer-Tropsch Synthesis, Catalysts and Catalysis), 75-85.
34. van Steen, E.; Viljoen, E. L.; van de Loosdrecht, J.; Claeys, M., Evaluation of molybdenum-modified alumina support materials for Co-based Fischer-Tropsch catalysts. *Applied Catalysis, A: General* **2008,** *335* (1), 56-63.
35. Smith, S. J.; Liu, S.; Liu, Q.; Olsen, R. E.; Rytting, M.; Selck, D. A.; Simmons, C. L.; Boerio-Goates, J.; Woodfield, B. F., Synthesis of metal oxide nanoparticles via a robust "solvent-deficient" method. *Chem. Mater.* **2012**, Submitted.
36. Woodfield, B. F.; Liu, S.; Boerio-Goates, J.; Liu, Q.; Smith, S. J. Preparation of uniform nanoparticles of ultra-high purity metal oxides, mixed metal oxides, metals, and metal alloys. 2007-US4279, 2007098111, 20070216., 2007.
37. Rutt, U.; Beno, M. A.; Strempfer, J.; Jennings, G.; Kurtz, C.; Montano, P. A., Diffractometer for high energy X-rays at the APS. *Nuclear Instruments & Methods in Physics Research, Section A: Accelerators, Spectrometers, Detectors, and Associated Equipment* **2001,** *467-468* (Pt. 2), 1026-1029.
38. "Fit2D" V. 9.129 Reference Manual V. 3.1.
39. Qiu, X.; Thompson, J. W.; Billinge, S. J. L., PDFgetX2: a GUI-driven program to obtain the pair distribution function from X-ray powder diffraction data. *J. Appl. Crystallogr.* **2004,** *37* (4), 678.
40. Egami, T. B., S. J. L., *Underneath the Bragg Peaks: Structural Analysis of Complex Materials*. First ed.; Pergamon: Kidlington, Oxford, UK, 2003; Vol. 7, p 404.
41. Farrow, C. L.; Juhas, P.; Liu, J. W.; Bryndin, D.; Bozin, E. S.; Bloch, J.; Proffen, T.; Billinge, S. J. L., PDFfit2 and PDFgui: computer programs for studying nanostructure in crystals. *J. Phys.: Condens. Matter* **2007,** *19* (33), 335219/1-335219/7.
42. Selck, D. A.; Woodfield, B. F.; Boerio-Goates, J.; Austin, D. E., Simple, inexpensive mass spectrometric analyzer for thermogravimetry. *Rev. Sci. Instrum.* **2011**, Accepted for publication.
43. Massiot, D.; Bessada, C.; Coutures, J. P.; Taulelle, F., A quantitative study of ^{27}Al MAS NMR in crystalline YAG. *Journal of Magnetic Resonance* **1990,** *90*, 231-242.
44. Paglia, G.; Bozin, E. S.; Billinge, S. J. L., Fine-Scale Nanostructure in gamma -Al2O3. *Chem. Mater.* **2006,** *18* (14), 3242-3248.

45. Balint, I.; Miyazaki, A., Novel preparation method of well-defined mesostructured nanoaluminas via carbon-alumina composites. *Microporous and Mesoporous Materials* **2009,** *122* (1-3), 216-222.
46. Kim, Y.; Kim, H. S.; Martin, S. W., Synthesis and electrochemical characteristics of Al2O3-coated LiNi1/3Co1/3Mn1/3O2 cathode materials for lithium ion batteries. *Electrochimica Acta* **2006,** *52* (3), 1316-1322.
47. Ram, S. R., S., Phase transformations in porous Al2O3 ceramic nanoclusters. *Indian J. Phys.* **2001,** *75A* (4), 437-441.
48. Azar, M.; Palmero, P.; Lombardi, M.; Garnier, V.; Montanaro, L.; Fantozzi, G.; Chevalier, J., Effect of initial particle packing on the sintering of nanostructured transition alumina. *J. Eur. Ceram. Soc.* **2008,** *28* (6), 1121-1128.
49. Mekasuwandumrong, O.; Praserthdam, P.; Inoue, M.; Pavarajarn, V.; Tanakulrungsank, W., Phase transformation behavior of nanocrystalline c-alumina powder obtained by thermal decomposition of AIP in inert organic solvent. *J. Mater. Sci.* **2004,** *39* (7), 2417-2421.
50. Tartaj, P.; Tartaj, J., Microstructural Evolution of Iron-Oxide-Doped Alumina Nanoparticles Synthesized from Microemulsions. *Chem. Mater.* **2002,** *14* (2), 536-541.
51. Roman, R.; Hernandez, T.; Gonzalez, M., Nano or micro grained alumina powder? A choice before sintering. *Boletin de la Sociedad Espanola de Ceramica y Vidrio* **2008,** *47* (6), 311-318.
52. Kim, H. J.; Kim, T. G.; Kim, J. J.; Park, S. S.; Hong, S. S.; Lee, G. D., Influences of precursor and additive on the morphology of nanocrystalline alpha -alumina. *Journal of Physics and Chemistry of Solids* **2007,** *69* (5-6), 1521-1524.
53. Kwak, J. H.; Hu, J.; Lukaski, A.; Kim, D. H.; Szanyi, J.; Peden, C. H. F., Role of Pentacoordinated Al^{3+} Ions in the High Temperature Phase Transformation of γ-Al_2O_3. *J. Phys. Chem. C* **2008,** *112* (25), 9486-9492.
54. Lee, M. H.; Cheng, C.-F.; Heine, V.; Klinowski, J., Distribution of tetrahedral and octahedral Al sites in gamma alumina. *Chemical Physics Letters* **1997,** *265* (6), 673-676.
55. Jayaram, V.; Levi, C. G., The structure of δ-alumina evolved from the melt and the $\gamma \rightarrow \delta$ transformation. *Acta Metall.* **1989,** *37* (2), 569-78.
56. Meephoka, C.; Chaisuk, C.; Samparnpiboon, P.; Praserthdam, P., Effect of phase composition between nano gamma - and c-Al2O3 on Pt/Al2O3 catalyst in CO oxidation. *Catal. Commun.* **2007,** *9* (4), 546-550.
57. Macedo, M. I. F.; Bertran, C. A.; Osawa, C. C., Kinetics of the γ to α alumina phase transformation by quantitative X-ray diffraction. *J. Mater. Sci.* **2007,** *42* (8), 2830-2836.
58. Bruehne, S.; Gottlieb, S.; Assmus, W.; Alig, E.; Schmidt, M. U., Atomic Structure Analysis of Nanocrystalline Boehmite AlO(OH). *Cryst. Growth Des.* **2008,** *8* (2), 489-493.
59. Billinge, S., Local structure from total scattering and atomic pair distribution function (PDF) analysis. *Powder Diffr.* **2008**, 464-493.
60. Billinge, S. J. L., The atomic pair distribution function: Past and present. *Z. Kristallogr.* **2004,** *219* (3), 117-121.
61. Michel, F. M. E., L.; Antao, S. M.; Lee, P. L.; Chupas, P. J.; Liu, G.; Strongin, D. R.; Schoonen, M. A. A.; Phillips, B. L.; Parise, J. B., The Structure of Ferrihydrite, a Nanocrystalline Material. *Science (Washington, DC, U. S.)* **2007,** *316*, 1726-1729.

62. Chupas, P. J.; Chapman, K. W.; Jennings, G.; Lee, P. L.; Grey, C. P., Watching nanoparticles grow: the mechanism and kinetics for the formation of TiO2-supported platinum nanoparticles. *J. Am. Chem. Soc.* **2007,** *129* (45), 13822-13824.
63. Gateshki, M.; Chen, Q.; Peng, L.-M.; Chupas, P.; Petkov, V., Structure of nanosized materials by high-energy X-ray diffraction: study of titanate nanotubes. *Z. Kristallogr.* **2007,** *222* (11), 612-616.
64. Juhas, P.; Cherba, D. M.; Duxbury, P. M.; Punch, W. F.; Billinge, S. J. L., Ab initio determination of solid-state nanostructure. *Nature (London, U. K.)* **2006,** *440* (7084), 655-658.
65. Page, K.; Proffen, T.; Terrones, H.; Terrones, M.; Lee, L.; Yang, Y.; Stemmer, S.; Seshadri, R.; Cheetham, A. K., Direct observation of the structure of gold nanoparticles by total scattering powder neutron diffraction. *Chem. Phys. Lett.* **2004,** *393* (4-6), 385-388.
66. Petkov, V., Structure of nanocrystalline materials by the atomic pair distribution function technique. *Adv. X-Ray Anal.* **2003,** *46*, 31-36.
67. Billinge, S. J. L., The structure of real materials using x-ray and neutron scattering. *Curr. Opin. Solid State Mater. Sci.* **1996,** *1* (4), 477-484.
68. Egami, T., Determining medium range order by powder diffraction. *J. Phys. Chem. Solids* **1995,** *56* (10), 1407-13.
69. Proffen, T.; Page, K. L., Obtaining structural information from the atomic pair distribution function. *Z. Kristallogr.* **2004,** *219* (3), 130-135.
70. Billinge, S. J. L., Real-space Rietveld: full profile structural refinement of the atomic pair distribution function. *Local Struct. Diffr., [Proc. Conf.]* **1998**, 137-156.
71. Paglia, G.; Rohl, A. L.; Buckley, C. E.; Gale, J. D., Determination of the structure of γ-alumina from interatomic potential and first-principles calculations: The requirement of significant numbers of nonspinel positions to achieve an accurate structural model. *Phys. Rev. B: Condens. Matter Mater. Phys.* **2005,** *71* (22), 224115/1-224115/16.
72. Christoph, G. G.; Corbato, C. E.; Hofmann, D. A.; Tettenhorst, R. T., The crystal structure of boehmite. *Clays Clay Miner.* **1979,** *27* (2), 81-6.
73. Finger, L. W.; Hazen, R. M., Crystal structure and compression of ruby to 46 kbar. *Journal of Applied Physics* **1978,** *49* (12), 5823-5826.
74. Zhang, X.; Honkanen, M.; Levaenen, E.; Maentylae, T., Transition alumina nanoparticles and nanorods from boehmite nanoflakes. *J. Cryst. Growth* **2008,** *310* (15), 3674-3679.
75. John, C. S.; Alma, N. C. M.; Hays, G. R., Characterization of transitional alumina by solid-state magic angle spinning aluminum NMR. *Applied Catalysis* **1983,** *6* (3), 341-6.
76. Duevel, A.; Romanova, E.; Sharifi, M.; Freude, D.; Wark, M.; Heitjans, P.; Wilkening, M., Mechanically Induced Phase Transformation of γ-Al2O3 into α-Al2O3. Access to Structurally Disordered γ-Al2O3 with a Controllable Amount of Pentacoordinated Al Sites. *J. Phys. Chem. C* **2011,** *115* (46), 22770-22780.
77. Kwak, J. H.; Hu, J. Z.; Kim, D. H.; Szanyi, J.; Peden, C. H. F., Penta-coordinated Al^{3+} ions as preferential nucleation sites for BaO on γ-Al_2O_3: an ultra-high-magnetic field ^{27}Al MAS NMR study. *J. Catal.* **2007,** *251* (1), 189-194.
78. Sabarinathan, V. R., S.; Ganapathy, S., Perturbations to ^{27}Al Electric Field Gradients in Nanocrystalline α-Al_2O_3 Studied by High-Resolution Solid-State NMR. *J. Phys. Chem. B* **2010,** *114*, 1775-1781.

79. Slade, R. C. T.; Southern, J. C.; Thompson, I. M., Aluminum-27 nuclear magnetic resonance spectroscopy investigation of thermal transformation sequences of alumina hydrates. I. Gibbsite, gamma -Al(OH)3. *J. Mater. Chem.* **1991,** *1* (4), 563-8.
80. Chen, F. R.; Davis, J. G.; Fripiat, J. J., Aluminum coordination and Lewis acidity in transition aluminas. *J. Catal.* **1992,** *133* (2), 263-278.
81. Pecharroman, C.; Sobrados, I.; Iglesias, J. E.; Gonzalez-Carreno, T.; Sanz, J., Thermal Evolution of Transitional Aluminas Followed by NMR and IR Spectroscopies. *J. Phys. Chem. B* **1999,** *103* (30), 6160-6170.
82. Wang, J. A.; Bokhimi, X.; Morales, A.; Novaro, O.; Lopez, T.; Gomez, R., Aluminum Local Environment and Defects in the Crystalline Structure of Sol-Gel Alumina Catalyst. *J. Phys. Chem. B* **1999,** *103* (2), 299-303.
83. Perander, L. M.; Zujovic, Z. D.; Groutso, T.; Hyland, M. M.; Smith, M. E.; O'Dell, L. A.; Metson, J. B., Characterization of metallurgical-grade aluminas and their precursors by 27Al NMR and XRD. *Can. J. Chem.* **2007,** *85* (10), 889-897.
84. Smith, S. J.; Liu, S.; Liu, Q.; Olsen, R. E.; Boerio-Goates, J.; Woodfield, B. F., Mechanism behind the "solvent-deficient" synthetic method. *Chem. Mater.* **2012**, Submitted.
85. Smith, S. J.; Page, K.; Kim, H.; Campbell, B. J.; Boerio-Goates, J.; Woodfield, B. F., Novel synthesis and structural analysis of ferrihydrite. *Inorganic Chemistry* **2012**, Accepted for publication.
86. Tsuchida, T.; Horigome, K., The effect of grinding on the thermal decomposition of alumina monohydrates, alpha - and beta -Al2O3.H2O. *Thermochim. Acta* **1995,** *254*, 359-70.
87. Lindackers, D.; Janzen, C.; Rellinghaus, B.; Wassermann, E. F.; Roth, P., Synthesis of Al_2O_3 and SnO_2 particles by oxidation of metal-organic precursors in premixed H_2/O_2/Ar low-pressure flames. *Nanostructured Materials* **1999,** *10* (8), 1247-1270.
88. Sohlberg, K.; Pennycook, S. J.; Pantelides, S. T., Hydrogen and the Structure of the Transition Aluminas. *Journal of the American Chemical Society* **1999,** *121* (33), 7493-7499.
89. Sohlberg, K.; Pennycook, S. J.; Pantelides, S. T., The bulk and surface structure of γ-alumina. *Chemical Engineering Communications* **2000,** *181*, 107-135.
90. Wolverton, C.; Hass, K. C., Phase stability and structure of spinel-based transition aluminas. *Phys. Rev. B: Condens. Matter Mater. Phys.* **2001,** *63* (2), 024102/1-024102/16.

Chapter 6

Symmetry-Mode Analyses of the Alumina Phases and Phase Transitions

6.1 Introduction

The PDF analyses in the previous chapter provide valuable insight, but they also raise several questions. First, despite their different symmetries (see Table 6.1 and Figure 6.1), all four of the well-characterized transitional alumina phases (γ, η, θ, and κ) fit the γ-Al_2O_3 PDF data remarkably well, particularly the γ, η, and θ phases. How can the local structures of the different phases be so similar?

Second, as the difference curves in Figure 6.1 highlight, both the γ- and η-Al_2O_3 phases model the high-*r* data ($r > 8$ Å) significantly better than the low-*r* data ($r < 8$ Å). Conversely, the θ- and κ-Al_2O_3 structures fit the low-*r* data very well (better than the γ and η phases) but fit the high-*r* data noticeably worse than γ- and η-Al_2O_3. These same trends appear in the fits of commercial γ-Al_2O_3 samples (see Appendix B.1), thus the local structure of γ-Al_2O_3 is consistent regardless of particle size or synthetic method. Why do the θ and κ phases fit the low-*r* region of the γ-Al_2O_3 PDF data better than the γ structure? What is the nature of the local structure in γ-Al_2O_3?

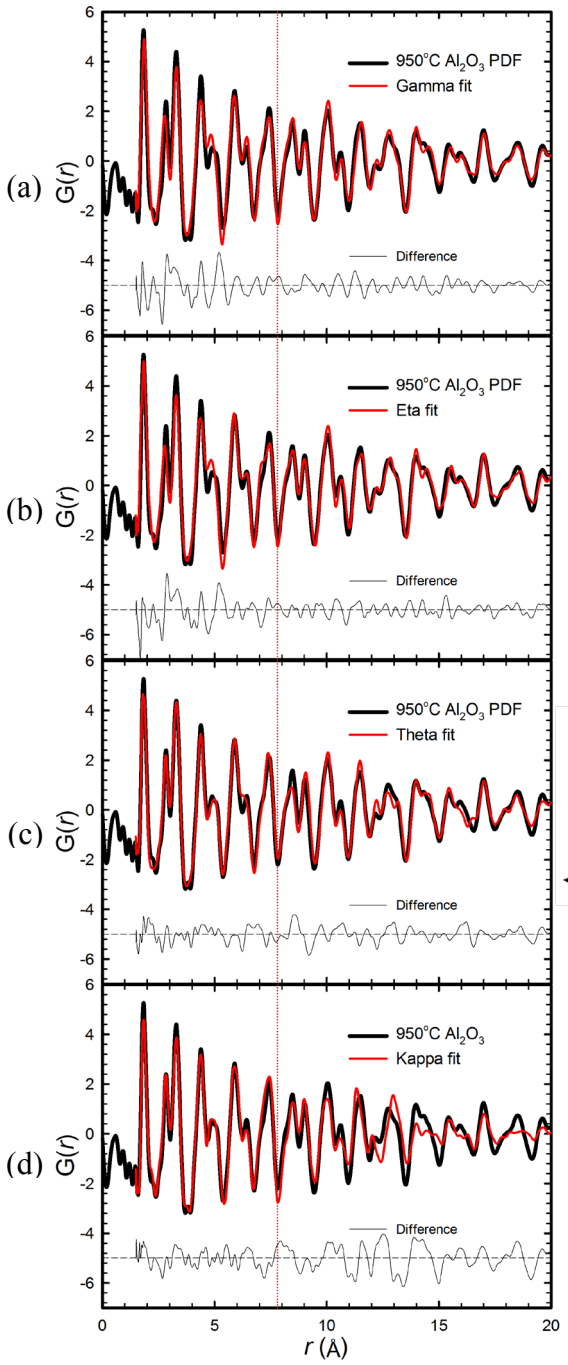

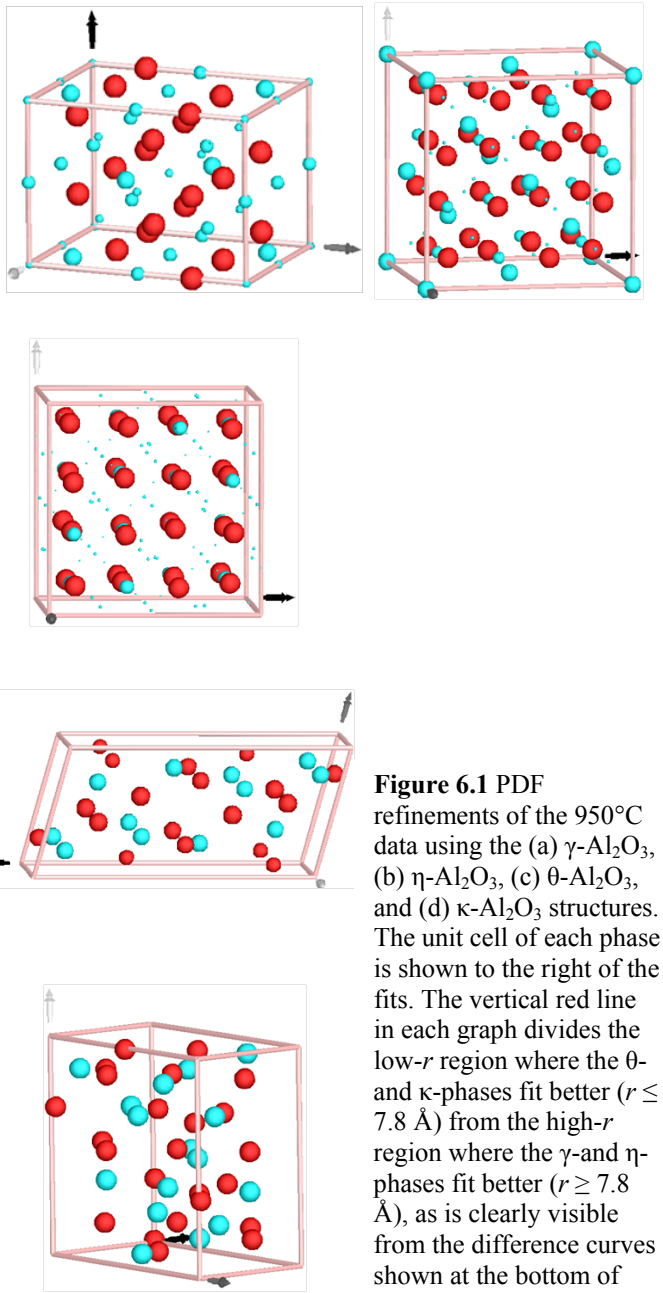

Figure 6.1 PDF refinements of the 950°C data using the (a) γ-Al_2O_3, (b) η-Al_2O_3, (c) θ-Al_2O_3, and (d) κ-Al_2O_3 structures. The unit cell of each phase is shown to the right of the fits. The vertical red line in each graph divides the low-*r* region where the θ- and κ-phases fit better ($r \leq 7.8$ Å) from the high-*r* region where the γ-and η-phases fit better ($r \geq 7.8$ Å), as is clearly visible from the difference curves shown at the bottom of each graph.

Table 6.1 Symmetries and unit cell parameters of the γ, η, θ, and κ transitional alumina phases.

	symmetry (space group)	**a** (Å)	**b** (Å)	**c** (Å)	**α**	**β**	**γ**
γ	tetragonal (141: $I4_1/amd$)	5.6521	5.65210	7.8715	90°	90°	90°
	or cubic (227: Fd-3m)	7.911	7.911	7.911	90°	90°	90°
η	cubic (227: Fd-3m)	7.914	7.914	7.914	90°	90°	90°
θ	monoclinic (12: C2/m)	11.854	2.904	5.622	90°	103.83°	90°
κ	orthorhombic (33: $Pna2_1$)	4.8340	8.3096	8.93530	90°	90°	90°

Third, the phase transition pathway is abridged in γ-Al_2O_3 nanoparticles relative to the bulk. As Figure 6.2 illustrates, the pathway is simplified from the 5 phases typically observed in bulk-sized particles (boehmite→γ→δ→θ→α) to 3 phases (boehmite→γ→α), resulting in a direct γ→α phase transition that occurs at significantly lower temperatures (1000-1050°C) than the θ→α phase transition (1100-1200°C) observed in bulk Al_2O_3. Based on similar results from other nanoparticle studies,[1-2] the abridgement appears to be a general result for γ-Al_2O_3 nanoparticles regardless of synthetic method. Why do γ-Al_2O_3 nanoparticles prefer a direct γ→α transition over the γ→θ transition?

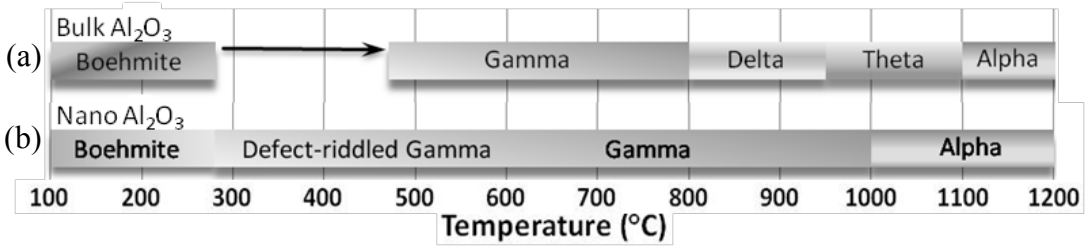

Figure 6.2 The γ-Al_2O_3 phase transition pathway (a) that is commonly reported for large Al_2O_3 particles and (b) that we and a few others have reported for γ-Al_2O_3 nanoparticles.

To find answers to these questions, we began studying the relationships between the γ, η, θ, and κ phases and the differences in the γ→θ and γ→α transitions. Of the previous work on these subjects,[3-12] the studies by Zhou *et al.*,[13] Levin *et al.*,[14-15] and Cai *et al.*[16-18] are of particular interest here. Zhou *et al.*[13] refined the γ, η, and θ structures from a combination of neutron and X-ray diffraction data, and the striking structural similarities led them to propose that the γ→θ and η→θ transitions should be topotactic (i.e. consisting of smooth and organized displacements that preserve some sublattice of the structure in a possibly modified form, see Figure 6.3).

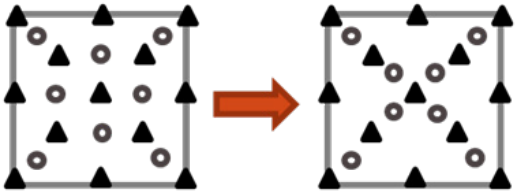

Figure 6.3 Example of a topotactic transformation.

In a subsequent insightful review, Levin *et al.*[14-15] used Zhou's and others' structural solutions to qualitatively compare the symmetry

relationships between the γ, δ, θ, η, χ and κ transitional alumina phases, noting that they are all simply different arrays of Al cations within the interstitial sites of a close-packed oxygen lattice that is either fcc (η, γ, δ, θ) or hcp (χ, κ). They likewise asserted that transitions between the fcc phases should be merely rearrangements of the cations. Levin *et al*. thus proposed that the phases could transform smoothly by passing through a hypothetical supergroup. They enumerated the space group sequence connecting the cubic γ and monoclinic θ phases, suggesting that the elusive δ phase (and any other γ-like or θ-like variant) is simply one of the superstructure intermediates.

With these theoretical underpinnings, Cai *et al.*[17] was able to propose a detailed atomic transition mechanism for the γ→θ transition. By visually comparing the γ and θ lattices, Cai *et al.* defined new unit cells in P1 symmetry for both structures in which the oxygen lattices were visually identical and the transition could proceed continuously by moving Al atoms between different interstitial sites within the fixed oxygen lattice. Total energy calculations along the various migration paths were used to map out possible transition pathways.

The work of Levin *et al*. thus established a qualitative relationship between the γ, η, θ, and κ phases, and the work of Cai *et al*. elucidated the γ→θ transition. In this chapter, we build on these studies. We have found that not only the fcc transitional alumina phases but *all* of the alumina phases can be derived from a single hypothetical parent structure, and we have used symmetry-mode analysis to determine the space group sequences which relate each phase to the parent structure. Using these relationships, we have determined a common subgroup relationship between the γ and α phases which has allowed us to propose a detailed atomic mechanism for the γ→α transition.

In the following sections, a brief introduction to crystallographic group theory and symmetry mode analysis is given. This is then followed by symmetry analyses of the γ, η, θ, and κ phase relationships and of the γ→θ and γ→α transitions, which analyses are then used to provide answers for the questions raised by Chapter 5.

6.2 Introduction to Symmetry-Mode Analysis

As discussed in the introduction, the atomic structure of a crystal is described in terms of a repeating motif called the *unit cell* and the space-group symmetries that it possesses. If the point-group of the space-group of the crystal has *n* symmetry operators, then the unit cell can be divided into *n* equivalent regions, so that one need only describe the atoms in the first region (the *asymmetric unit*). The symmetries of the space-group (e.g. rotations, reflections, inversions, roto-reflections and roto-inversions, translations, glides and screws) then copy the contents of the asymmetric unit throughout the rest of the unit cell and the rest of the crystal. To describe the entire crystal, one need only describe the free parameters of the asymmetric unit, which include the positions, occupancies and thermal parameters of each of the atoms therein, and atoms that lie directly on symmetry operators have fewer free parameters than atoms that lie on general positions. Compared to listing every parameter associated with every atom in the crystal, the crystallographic description provides a profound simplification.

Crystallographers describe the positions of the atoms in the unit cell in the lattice coordinate system, which runs from 0 to 1 along each lattice basis vector, rather than in Cartesian coordinates and Å units. Thus, regardless of the actual shape of the unit cell, an atom at the center will have coordinates (x = ½, y = ½, z = ½). This approach is useful because it is both general and absolute.

However, listing the free parameters of each atom of the unit cell individually is not the most concise way of describing the structural changes that occur during a phase transition. Phase transitions often lower the space-group symmetry of a crystal in a very simple and specific way which is best described as the distortion of a higher-symmetry parent to a phase of lower-symmetry.[19-21] By distortion, we mean the formation of any physical order parameter that lowers the symmetry of the crystal, which might include atomic displacements, site occupancy changes, magnetic moments or lattice strains, etc. When this happens, the lattice basis of the primitive unit cell of the distorted structure (i.e. the supercell) will be related to the lattice basis of the primitive parent cell by an integer matrix transform, and the symmetry of the distorted structure will be a subgroup of the parent symmetry group.

The most useful parameter set for describing a phase transition is thus one that defines the structural parameters of the distorted phase according to how they break the symmetry of the parent. Such *symmetry modes* are more precisely referred to as basis functions of the irreducible representations (irreps) of the parent space group and are computed using group matrix-representation theory.[22-23] Because of the orthogonality of irrep basis functions, symmetry modes can always be defined as unique linear combinations of the traditional crystallographic parameters. Structural degrees of freedom are not created or lost, but are merely subjected to a linear change of basis. One mode can affect many symmetry-unique atoms and one atom can be affected by many modes. Furthermore, a single symmetry modes will often yield a rather complex but familiar distortion such as a polyhedral rotation pattern.

The most important practical reason for using the symmetry-mode basis is to achieve a simpler description of the distorted phase. Symmetry-lowering phase transitions greatly increase the number of structural parameters relative to the parent structure. When superlattice peaks are

weak or suffer from high-*Q* overlap, the change often outpaces the increase of information content of the low-symmetry diffraction data, leading to an underdetermined structural problem. Using the traditional lattice coordinate basis, one expects most of the new structural parameters to deviate significantly from their parent-structure values. When working with the symmetry-mode basis, however, it is often possible to capture the essential features of a distorted structure with a relatively small number of symmetry-mode amplitudes, with the majority of the other symmetry modes being inactive. In this sense, the symmetry-mode basis is nature's basis, or the parameter set that most economically describes the onset of physical order parameters at a phase transition.

In recent years, several software packages such as ISODISTORT (formerly ISODISPLACE),[22] AMPLIMODES,[24] BasIreps,[25-26] SARAh,[27] and MODY[28] have been developed to perform symmetry mode parameterizations. ISODISTORT is the most flexible of these packages, and has been interfaced to multiple Rietveld-refinement packages. Given specific parent and distorted structures as input, it identifies the relationship between the parent and distorted cells, verifies the group-subgroup relationship, matches the atoms of the undistorted and distorted supercells, computes the symmetry modes of the parent that persist in the distortion, and calculates the actual mode amplitudes that yield the distorted structure. This last step is called symmetry-mode *decomposition*. Symmetry mode details can then be interactively visualized, or output in a variety of formats.Methods

6.2.1 Aristoalumina: A Common Parent Structure

None of the alumina phases have direct group-subgroup relationships. This means that none of the alumina phase transitions can be described simply in terms of the formation of an order parameter. However, as Levin *et al*. noted, the transitional Al_2O_3 phases (γ, δ, θ, η,χ, κ) are

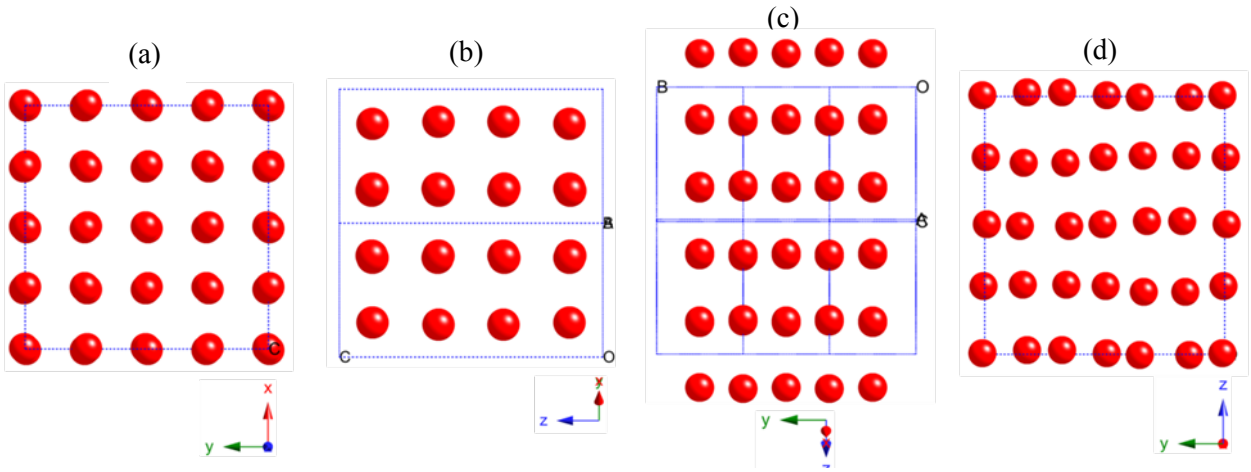

Figure 6.4 Oxygen lattices of the (a) eta, (b) tetragonal gamma, (c) theta, and (d) kappa structures.

merely rearrangements of octahedral and tetrahedral Al cations within a close-packed oxygen lattice (Figure 6.4). In fact, as Figure 6.5 illustrates, the oxygen lattices of all of the alumina phases are close-packed, though the differing symmetries of the phases endow the lattices with slightly different distortions. Thus even though the hydroxide, oxyhydroxide, and α phases only have octahedrally coordinated Al, *all* of the alumina phases can be viewed as different arrangements of Al cations within similar (close-packed) O sublattices.

We therefore hypothesize that *all* of the alumina phases can be derived from a single, hypothetical parent structure (referred to here as *aristoalumina*) containing all possible octahedral and tetrahedral sites within a close-packed oxygen lattice; occupancy modes can

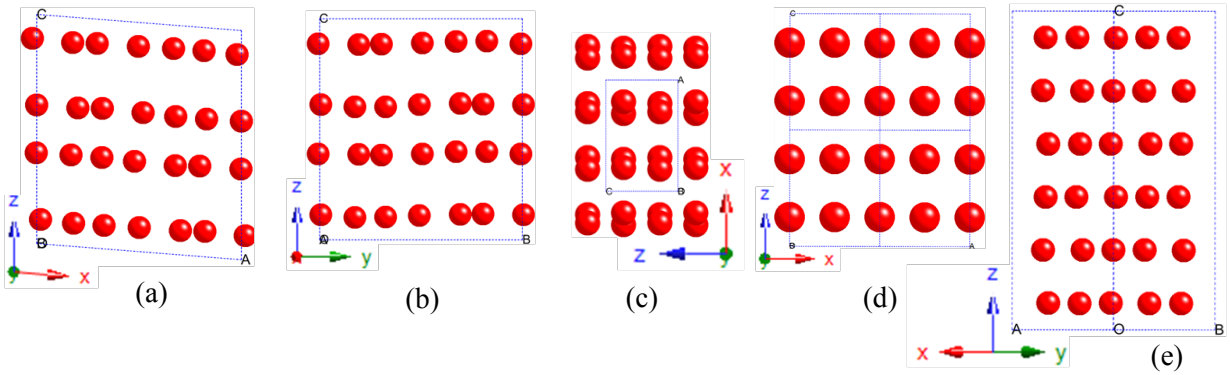

Figure 6.5 Oxygen lattices of the (a) gibbsite $Al(OH)_3$, (b) bayerite $Al(OH)_3$, (c) diaspore AlOOH, (d) boehmite AlOOH, and (e) α-Al_2O_3 structures.

induce the necessary vacancies required by the Al_2O_3, AlOOH, and $Al(OH)_3$ stoichiometries, and a combination of lattice strain and displacive modes can induce the Al migrations necessary for each phase. This aristoalumina phase (Figure 6.6) is essentially a superposition of the rocksalt (AlO) and anti-fluorite (Al_2O) structures, which fills all of the octahedrally and tetrahedrally-coordinated interstitial sites of an fcc oxygen sublattice with aluminum atoms. Using symmetry modes of this common parent structure to explore the entire alumina phase diagram has provided novel insights into the relationships between its various phases.

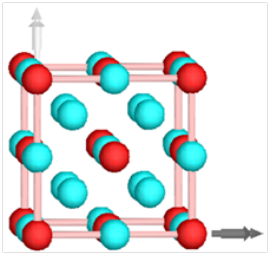

Figure 6.6 'Aristoalumina' parent structure. Red = Oxygen, blue = Al.

Table 6.2 Wyckoff sites for the aristoalumina parent structure. Space group #225: *Fm-3m* with cubic lattice parameter 3.9691 Å.

Site	Pos.	x	y	z	Occ.
O1	4a	0	0	0	1
Al1(oct)	4b	0.5	0.5	0.5	1
Al2 (tet)	8c	0.25	0.25	0.25	1

6.2.2 Ghost Atoms

As Table 6.2 indicates, the aristoalumina parent structure has an unrealistic Al_3O stoichiometry. Because there must exist a one-to-one matching of the atoms of the parent and distorted structures as Section 6.2 mentioned, extra atoms had to be inserted into the various alumina phases to match with the aristoalumina atoms. But because the actual stoichiometries of the structures need not be equal, these unwanted atoms could be assigned zero site occupancies, effectively eliminating them while still enabling the distortion to be properly defined. The positions of these 'ghost' atoms were chosen so that each Al_2O_3 phase contained Al atoms within each octahedral and tetrahedral interstice of the aristoalumina structure, thereby maximizing each phases' resemblance to the aristoalumina parent. This facilitated atom-matching and minimized

the distortion mode amplitudes necessary to remove the superfluous atoms. See Appendix C.1 for tables of the ghost-atom-containing structures for each phase.

Using these ghost-atom-containing alumina structures, the ISODISTORT program[22] was used to perform the symmetry mode decompositions of the distortions relating aristoalumina to the various alumina phases. Some additional strategies besides adding ghost atoms were required, though. First, instead of distorting aristoalumina directly into the γ and η structures, it was necessary (in order to satisfy Wyckoff site matching) to first distort aristoalumina to an idealized γ-Al_2O_3 structure in which the Al atoms occupy only the ideal spinel positions 8a and 16d. This ideal γ structure could then be distorted into the real γ and η structures, whose Al partially occupy the 8a (in γ), 16d, 32e, and 48f (in η) positions. Second, even though a direct group/subgroup relationship does not exist between aristoalumina and κ-Al_2O_3, the κ structure could be redefined in terms of *P*1 symmetry to provide a common subgroup (see the following section) through which aristoalumina and κ-Al_2O_3 could be related. Because the *P*1 subgroup structure was identical to the κ-Al_2O_3 structure, this essentially provided a direct relationship between aristoalumina and κ-Al_2O_3. Table 6.3 summarizes the distortion strategies for the various Al_2O_3 phases. The actual distortion parameters are given in the Results section (see Appendix C.2 for the AlOOH and $Al(OH)_3$ distortion information).

Table 6.3 Distortion strategies for the Al_2O_3 phases.

Aristo → Idealized γ → γ (cubic)
Aristo → Idealized γ → η
Aristo → θ
Aristo → κ (P_1)
Aristo → α

6.2.3 Common Subgroups

Once we determined the symmetry modes responsible for the distortions of aristoalumina to the various alumina phases, an additional use for them became apparent. We found that if the primary modes from two different distortions are combined, the space group of the resulting distorted structure is a subgroup of both the original distorted structures, as Figure 6.7 illustrates.

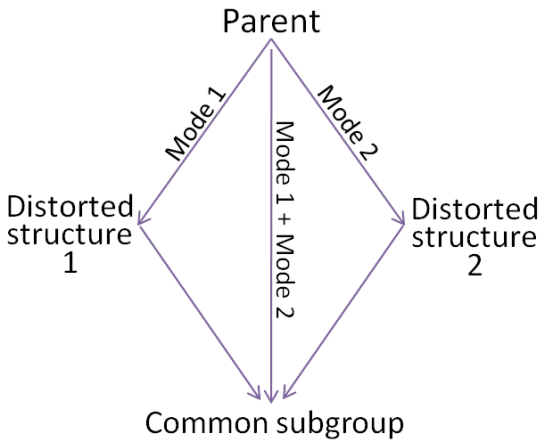

Figure 6.7 Method of finding a common subgroup between two seemingly unrelated phases.

Though the development of an order parameter violates some of the symmetry operations of the parent symmetry group, some of the symmetry operations of the parent persist in the distorted phase. The subgroup of residual symmetries comprise the space-group symmetry of the distorted structure. Two distinct order parameters will break different parent symmetries, resulting in two different subgroups. And when multiple order parameters are invoked simultaneously, the resulting symmetry is a maximal common subgroup of the individual subgroups associated with each order parameter. Common subgroups provide a mechanistic pathway through which one phase can be smoothly distorted into another, even in the absence of a group-subgroup relationship. This process was used to perform direct $\gamma \rightarrow \theta$ and $\gamma \rightarrow \alpha$ distortions. The specific symmetry mode combinations used are discussed in the Results section.

6.3 Results and Discussion

6.3.1 Vacancy Ordered Superstructures

Table 6.4 – Table 6.9 summarize the group-subgroup information, the basis and origin relationships, and the significant symmetry modes (amplitudes > 0.1) involved in distorting aristoalumina to each Al_2O_3 phase. The associated figures illustrate the distortions, highlighting the relationships between the aristo parent cell (pink) and each distorted supercell (blue).

Table 6.4 Aristo→γ distortion parameters.

Aristo → ideal γ-Al_2O_3
Space Group: 225 *Fm*-3*m* Subgroup: 227 *Fd*-3*m* basis=[(2,0,0),(0,2,0),(0,0,2)] origin=(1/4,1/4,1/4)
Occupancy Modes $\mathbf{\Gamma_1^+}$, $\mathbf{L_2^-}$, $\mathbf{X_4^+}$

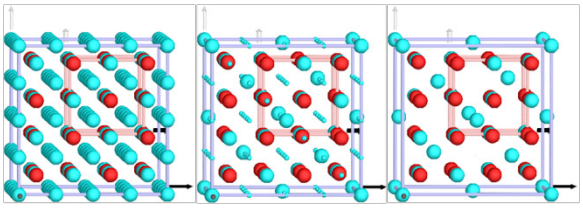

Figure 6.8 Aristo → Ideal γ distortion (O atoms = red, Al atoms = blue).

ideal γ-Al_2O_3 → cubic γ-Al_2O_3
Space Group: 225 *Fm*-3*m* Subgroup: 227 *Fd*-3*m* basis=[(1,0,0),(0,1,0),(0,0,1)] origin=(0,0,0)
Occupancy Modes $\mathbf{\Gamma_1^+}$

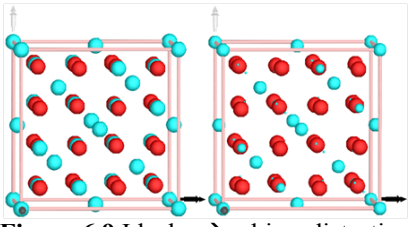

Figure 6.9 Ideal γ →cubic γ distortion (O atoms = red, Al atoms = blue).

Table 6.5 Aristo→η distortion parameters.

Aristo → ideal γ-Al_2O_3
Space Group: 225 *Fm*-3*m* Subgroup: 227 *Fd*-3*m* basis=[(2,0,0),(0,2,0),(0,0,2)] origin=(1/4,1/4,1/4)
Occupancy Modes $\mathbf{\Gamma_1^+}$, $\mathbf{L_2^-}$, $\mathbf{X_4^+}$

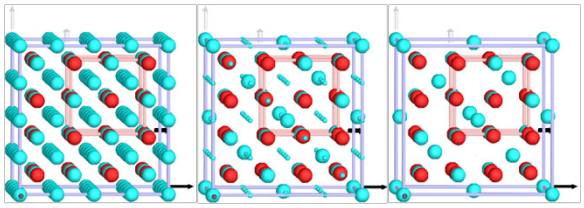

Figure 6.10 Aristo → Ideal γ distortion (O atoms = red, Al atoms = blue).

ideal γ-Al_2O_3 → η-Al_2O_3
Space Group: 227 *Fd*-3*m* Subgroup: 227 *Fd*-3*m* basis=[(1,0,0),(0,1,0),(0,0,1)] origin=(0,0,0)
Occupancy Modes $\mathbf{\Gamma_1^+}$

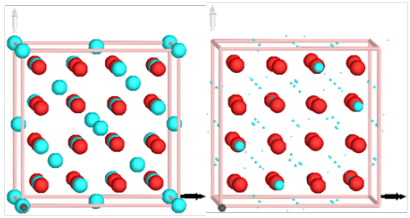

Figure 6.11 Ideal γ →η distortion (O atoms = red, Al atoms = blue).

From these tables and figures, it is plain to see that the aristo→γ and aristo→η transitions are remarkably similar, and it is useful in preparing for the subsequent discussion to explore their similarities and differences here. For both structures, the same idealized γ structure (a spinel structure) can be used as an intermediate because the η and cubic γ structures proposed by Zhou *et al*.[13] are both defect spinel structures. Table 6.6 highlights the distortions that are then necessary to form the real γ and η structures. First, the oxygen lattice shifts slightly off of the ideal 3/8 position for both phases. Second, the occupancy of each Al site is reduced to the partial occupancies listed in Table 6.6 to obtain the proper Al_2O_3 stoichiometry. Third, roughly ¼ of the Al in γ and ½ of the Al in η shift into more general (and disordered) positions. Specifically, ¼ of the Al atoms in γ and 13% of the Al in η move into the 32e position, and another ⅓ of the total Al in the η structure (the tetrahedral Al) shift off of the ideal 8a position onto the more general 48f position while the tetrahedral Al in the γ structure remain on the 8a position. Roughly ⅔ of the Al positions are therefore identical between γ and η, with the remaining ⅓ (the tetrahedral Al) being slightly more disordered in the η phase than in the γ phase.[xx]

Table 6.6 Comparison of Wyckoff sites (with their occupancies and the % of the total Al represented) in the idealized γ, the γ-Al_2O_3, and the η-Al_2O_3 structures, highlighting the atoms that must move in the idealized structure to form the real structures.

	idealized γ		**γ-Al_2O_3**			**η-Al_2O_3**		
	site	Occ.	site	Occ.	Al%	site	Occ.	Al%
O	32e (⅜,⅜,⅜)	(1.0)	32e (x,x,x) x = 0.3797	(1.0)		32e (x,x,x) x = 0.3799	(1.0)	
$Al_{tetrahedral}$	8a (0,0,0)	(1.0)	8a (0,0,0)	(0.84)	31%	48f (0.7739,0,0)	(0.16)	36%
$Al_{octahedral}$	16d (⅝,⅝,⅝)	(1.0)	16d (⅝,⅝,⅝)	(0.58)	43%	16d (⅝,⅝,⅝)	(0.68)	51%
			32e (x,x,x) x = 0.1522	(0.17)	25%	32e (x,x,x) x = 0.1949	(0.09)	13%
			+ [001] lattice strain			no strain		

[xx] The γ phase may undergo an additional lattice strain in the [001] direction to give it tetragonal symmetry, but there is still some debate on whether γ is better modeled as a cubic defect spinel or a tetragonally distorted spinel. For the sake of simplicity, the cubic structure was assumed in these studies.

Table 6.7 Aristo→θ distortion parameters.

Aristo → θ-Al_2O_3	
Space Group: 225 *Fm*-3*m* Subgroup: 12 *C*2/*m* basis=[(3,1/2,-1/2),(0,1/2,1/2),(0,-1,1)] origin=(1/2,1/2,1/2)	
Displacive Modes	$\mathbf{C_1}$, $\mathbf{L_2^-}$, $\mathbf{\Delta_1}$, $\mathbf{\Delta_3}$
Lattice Strain Mo.	$\mathbf{\Gamma_3^+}$, $\mathbf{\Gamma_5^+}$
Occupancy Modes	$\mathbf{\Gamma_1^+}$, $\mathbf{\Delta_1}$, $\mathbf{\Delta_3}$, $\mathbf{L_2^-}$, $\mathbf{C_1}$

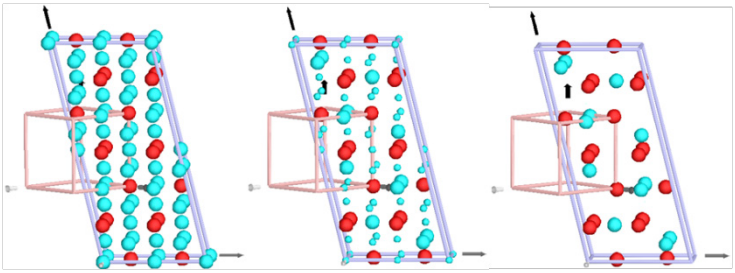

Figure 6.12 Aristo→θ distortion. (O atoms = red, Al atoms = blue).

Table 6.8 Aristo→κ distortion parameters.

Aristo → κ-Al_2O_3	
Space Group: 225 *Fm*-3*m* Subgroup: 1 *P*1 basis=[(1/2,1/2,-1),(-3/2,3/2,0),(1,3/2,3/2)] origin=(0.02206,0.53227,-0.47266)	
Displacive	$\mathbf{\Lambda_1}$, $\mathbf{\Lambda_3}$, $\mathbf{L_1^+}$, $\mathbf{L_3^+}$, $\mathbf{L_3^-}$, $\mathbf{\Gamma_4^-}$, $\mathbf{\Gamma_5^+}$, $\mathbf{GP_1}$, C_2, SM_1, Q_2
Lattice Strain	$\mathbf{\Gamma_5^+}$, $\mathbf{\Gamma_3^+}$
Occupancy	$\mathbf{\Gamma_1^+}$, $\mathbf{\Gamma_2^-}$, $\mathbf{\Lambda_1}$, $\mathbf{SM_1}$, $\mathbf{L_2^-}$, $\mathbf{Q_1}$, $\mathbf{Q_2}$, $\mathbf{GP_1}$

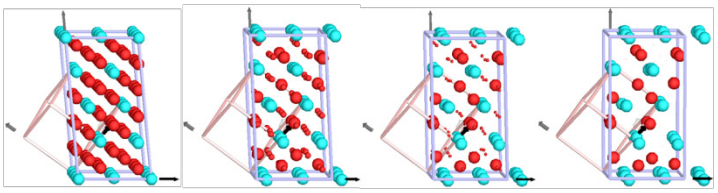

Figure 6.13 Aristo→κ distortion. (O = blue, Al = red).

Table 6.9 Aristo→α distortion parameters.

Aristo → α-Al_2O_3	
Space Group: 225 *Fm*-3*m* Subgroup: 167 *R*-3*c* basis=[(1,0,-1),(-1,1,0),(2,2,2)] origin=(1/2,1/2,1/2)	
Displacive Modes	$\mathbf{L_3^-}$, $\mathbf{X_5^+}$, $\mathbf{X_1^+}$, $\mathbf{\Gamma_5^+}$
Lattice Strain Modes	$\mathbf{\Gamma_5^+}$
Occupancy Modes	$\mathbf{\Gamma_1^+}$, $\mathbf{X_1^+}$, $\mathbf{X_4^+}$

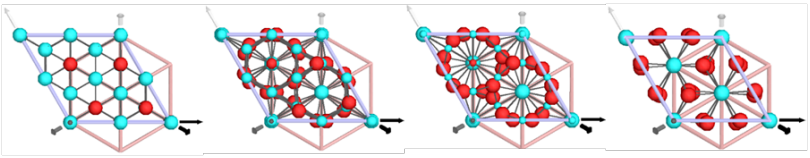

Figure 6.14 Aristo→α distortion. (O atoms = red, Al atoms = blue).

As Figure 6.8 –Figure 6.12 illustrate, minimal atomic displacements were necessary to derive the γ, η, and θ phases from aristoalumina; these structures were produced mainly by inducing the vacancies required for the proper stoichiometry via occupancy modes. The κ and α phases in Figure 6.13 – Figure 6.14 were also primarily generated via vacancy-inducing

occupancy modes, though these structures required somewhat more significant atomic displacements because the oxygen sublattice had to be converted from the fcc configuration of aristoalumina to an hcp configuration. But these distortions show that a smooth transition from an fcc to an hcp-ordered alumina structure is possible, contrary to previous suppositions that such a transition must be purely diffusive. And because of the primary role of occupancy modes in all of the distortions, phases of the Al_2O_3 phase-diagram can be thought of as distinct vacancy-ordered superstructures[xxi] of the aristoalumina parent.

Viewed in terms of vacancy ordering, the idealized γ-Al_2O_3 structure is generated from aristoalumina when the L_2^- (a,ā,ā,ā) mode (the primary order parameter) creates layers of edge-sharing octahedra in a honeycomb pattern (Figure 6.15a). Between each honeycomb layer is a network of isolated octahedra that resemble pillars (Figure 6.15b), and corner-sharing tetrahedra are dispersed between the pillars. Corner-sharing tetrahedra are dispersed between the pillars (Figure 6.15c). To then make the real γ and η structures, a small number of the Al are relocated to the octahedral holes of the honeycomb/pillar lattice in Figure 6.15a-b (the 32e position discussed previously). The more general nature of this Wyckoff position introduces a degree of

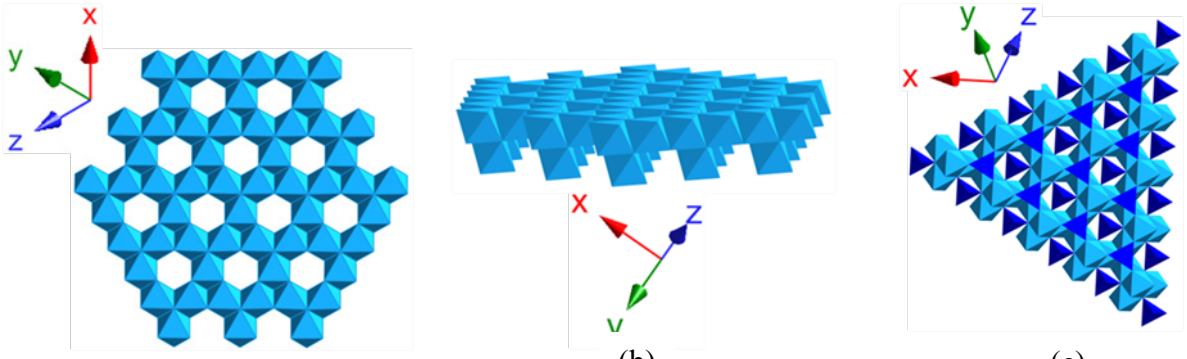

(a) (b) (c)

Figure 6.15 Idealized γ-Al_2O_3 structure resulting from the action of the L_2^- (a,ā,ā,ā) mode on aristoalumina. AlO_6 octahedra and AlO_4 tetrahedra are rendered in light blue and dark blue, respectively.

[xxi] Distorted structures are often called 'superstructures' because the volume of the distorted structure's primitive unit cell is always greater than or equal to the volume of the original structure's primitive unit cell.

displacive disorder into the γ and η structures, and the partial Al occupancies introduce occupational disorder. In η, the tetrahedral Al are also shifted slightly off of the ideal 8a position to the 48f position, adding another degree of displacive disorder. These shifts cause slight distortions in the AlO_6 (in γ and η) and AlO_4 (in η) polyhedra.

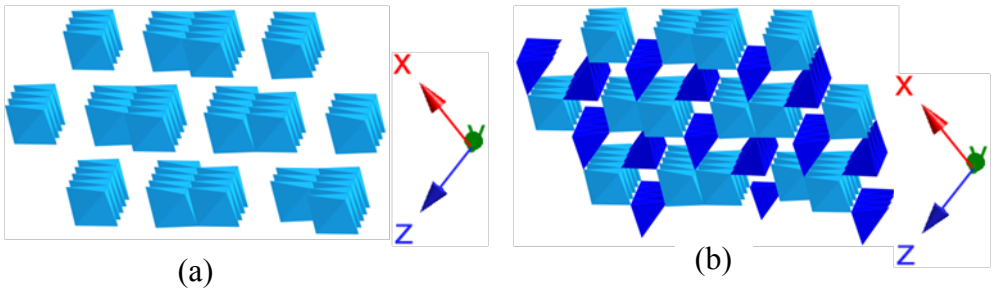

Figure 6.16 θ-Al_2O_3 structure resulting from the action of the C_1 and L_2^- (0,a,0,0) mode on aristoalumina. AlO_6 octahedra and AlO_4 tetrahedra are rendered in light blue and dark blue, respectively.

Similarly, the θ phase is derived from aristoalumina through the C_1 and L_2^- (0,a,0,0) occupancy modes (along with several others) which create layers containing double rows of edge-sharing octahedra (Figure 6.16a) , which rows are translated by ½ x + ½ z. Rows of corner-sharing tetrahedra separate the layer (Figure 6.16b).

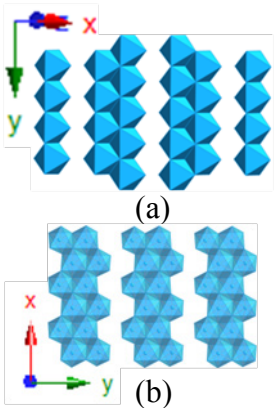

Figure 6.17 Double rows of edge-sharing AlO_6 octahedra in θ (a) and κ (b).

Much like the θ phase, the Λ_3, L_3^+, and L_3^- modes that form the κ phase create layers containing double rows of edge-sharing octahedra (Figure 6.18a), though the rows are more zipper-like in κ (see Figure 6.17), and every other layer is not only translated by ½*y* but also rotated

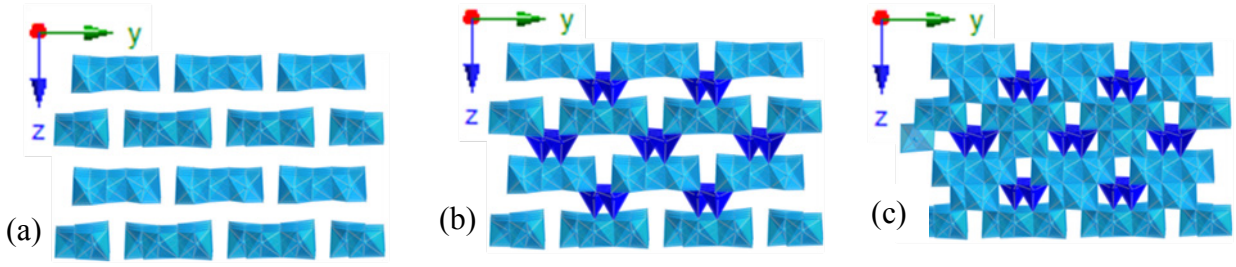

Figure 6.18 κ-Al_2O_3 structure resulting from the action of the Ld_3, L_3^+, and L_3^- modes on aristoalumina. AlO_6 octahedra and AlO_4 tetrahedra are rendered in light blue and dark blue, respectively.

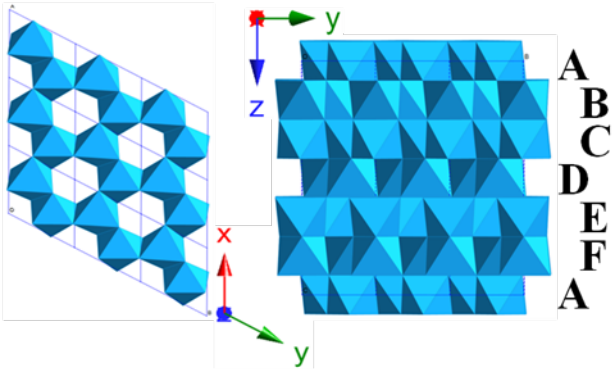

Figure 6.19 **α**-Al_2O_3 structure resulting from the action of theL_3^- mode on aristoalumina. Only AlO_6 octahedra exist in this alumina structure.

by 180°. Like θ, rows of corner-sharing tetrahedra separate these layers (Figure 6.18b); but unlike θ, single rows of edge sharing octahedra are also dispersed between the rows of tetrahedra in κ (Figure 6.18c).

To generate α-Al_2O_3, the L_3^- mode creates layers of edge-sharing octahedra with a honeycomb pattern that is similar to but different from that in γ-Al_2O_3, as Figure 6.19 illustrates. Adjacent layers are rotated 180° from each other and are shifted by $1/3y \pm 1/3x$, resulting in a unit cell consisting of 6 unique layers, ABCDEF.

Viewed as vacancy-ordered superstructures, the similarities between the γ, η, θ, and κ transitional Al_2O_3 phases becomes more clear, and an explanation for the low-*r* local structure of γ-Al_2O_3 presents itself. As Figure 6.15 - Figure 6.18 illustrate, all of the transitional Al_2O_3 phases consist of AlO_6 and AlO_4 units in roughly the same ratios, with each structure consisting of layers of AlO_6 with AlO_4 dispersed between every other layer. The first few bond distances of the AlO_6 and AlO_4 units in each of the transitional phases must therefore be quite similar. This is why the low-*r* region in the PDF data for γ-Al_2O_3 is modeled fairly well by any of the transitional alumina phases; the low-*r* local structures are truly very similar.

However, the differing symmetries of the phases cause different distortions in the AlO_6 and AlO_4 units, which distortions came to our attention while trying to center the ghost atoms in the octahedral and tetrahedral holes. As Figure 6.20 illustrates, the distortions in the AlO_6 and AlO_4 are substantially smaller in the cubic η and tetragonal γ phases (a-b) than in the monoclinic θ and the orthorhombic κ phases (c-d).

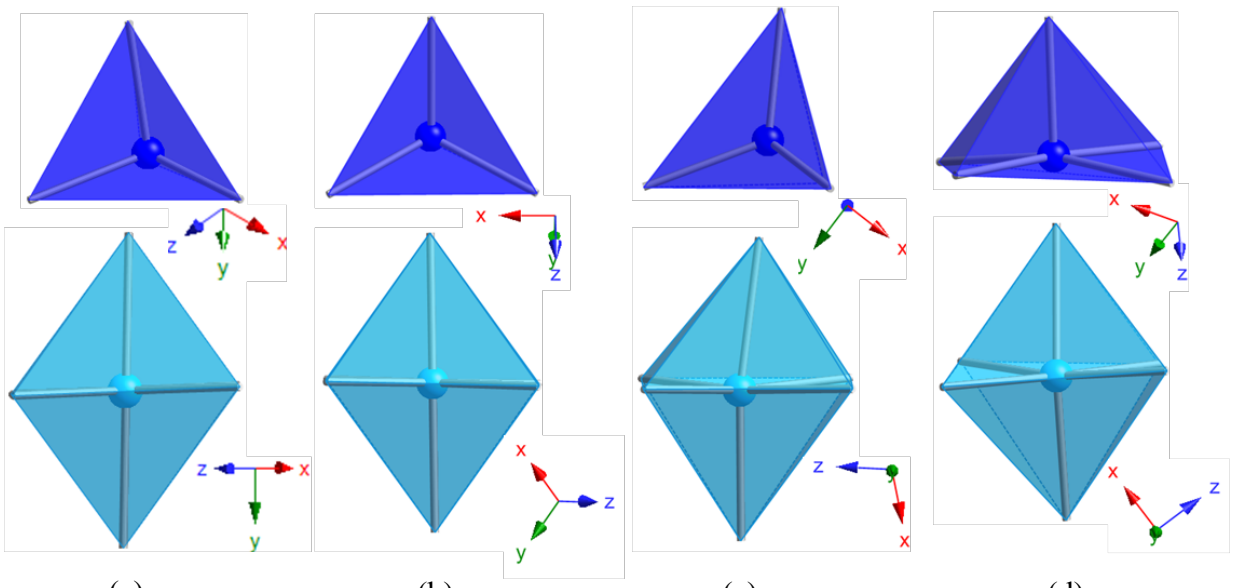

Figure 6.20 AlO_6 octahedra (light blue) and AlO_4 tetrahedra (dark blue) from the η, γ, θ, and κ (a, b, c, and d, respectively) transitional Al_2O_3 phases.

Based on these observations, we hypothesize that the AlO_6 and AlO_4 units are distorted in the γ-Al_2O_3 lattice in ways similar to (c) and (d) in Figure 6.20, causing the θ and κ structures to model the low-*r* γ-Al_2O_3 PDF data more effectively than the more rigid γ and η phases which do not allow for such extensive distortions. However, the γ and η phases begin to outperform the θ and κ structures as *r* increases, so the distortions in the AlO_6 and AlO_4 units must be randomized from one unit cell to another (at $r > 8$ Å) so that the average structure is still roughly cubic, enabling the γ and η phases to model the high-*r* γ-Al_2O_3 PDF data more effectively than the θ and κ phases, as observed.

6.3.2 The γ→θ Distortion

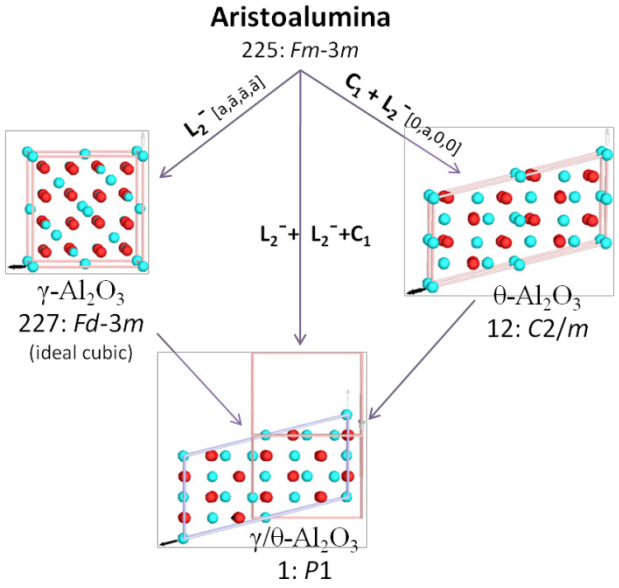

Figure 6.21 Common subgroup relationship between γ and θ derived using distortion modes from the aristoalumina parent structure.

Table 6.10 γ→γ/θ distortion parameters.

γ-Al_2O_3 → γ/θ-Al_2O_3	
Space Group: 227 *Fd*-3*m* Subgroup: 1 *P*1 basis=[(3/2,0,-1/2),(0,1/2,1/2),(0,-1/2,1/2)] origin=(1.37520,-0.12600,-0.62400)	
Displacive Modes	$\mathbf{\Gamma_5^+}$, $\mathbf{\Delta_1}$, $\mathbf{\Delta_3}$, $\mathbf{\Delta_5}$
Lattice Strain Modes	$\mathbf{\Gamma_5^+}$, $\mathbf{\Gamma_3^+}$
Al Occupancy Modes	$\mathbf{\Gamma_5^+}$, $\mathbf{\Gamma_1^+}$, $\mathbf{\Delta_1}$, $\mathbf{\Delta_3}$, $\mathbf{\Delta_5}$

As Figure 6.21 illustrates, space group #1 *P*1 was identified as a common subgroup between the γ (ideal) and θ phases by combining the L_2^- (a,ā,ā,ā) mode with the C_1 and L_2^- (0,a,0,0) modes from the aristo→γ and aristo→θ distortions (respectively). *P*1 was also the subgroup identified and used by Cai *et al.*[17] in their study of the γ→θ transition. By moving the θ structure into the *P*1 setting prescribed by that study (and adding the appropriate ghost atoms to allow Wyckoff site matching—see Appendix C.1), the idealized γ-Al_2O_3 structure could be distorted smoothly into the γ/θ-Al_2O_3 subgroup structure (see Figure 6.22) using a range of modes including Γ_1^+, Γ_3^+, Γ_5^+, Δ_1, Δ_3, and Δ_5 (Table 6.10).[xxii] Because the γ/θ subgroup structure is identical to the θ structure, the distortion is essentially a direct γ→θ distortion. Unfortunately, occupancy modes were used to change the atom positions instead of displacive modes (see

[xxii] A different basis relationship from that suggested by Cai *et al*. was used.

Figure 6.22), so the distortion does not represent a physical mechanism so much as a set of endpoints. However, the distortion identifies the atoms which *must* move during the real transition, enabling speculation on how they *might* move.

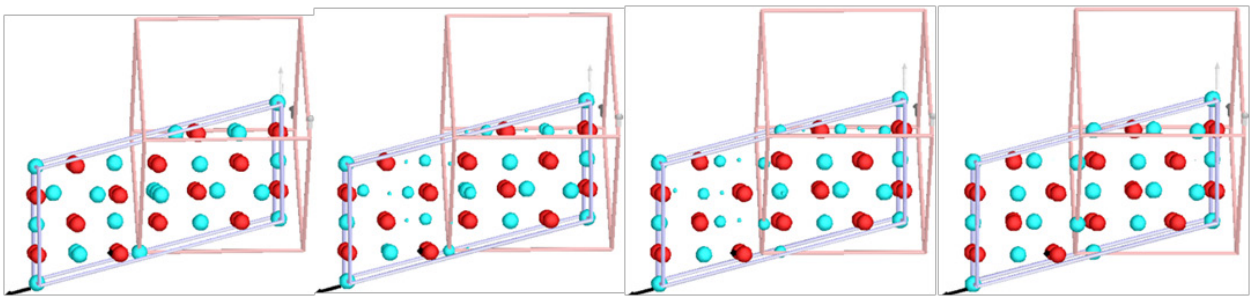

Figure 6.22 Illustration of the direct γ→θ distortion.

The γ→θ distortion has some noteworthy features. First, there is no substantial change in the oxygen lattice except for the small monoclinic distortion of the entire structure though the Γ_3^+ (in the *a* and *b* directions) and the Γ_5^+ (in the *b* direction) strain modes. Second, only ½ of the Al atoms (from both tetrahedral and octahedral positions) must diffuse a short distance to new positions. The θ structure thus essentially shares both its oxygen sublattice and roughly ½ of its Al sites with the γ phase. Since the η structure similarly shares ⅔ of its Al sites with γ (with the remaining ⅓ simply displaying more displacive disorder than in γ), the γ, η, and θ phases are all quite closely related, with the primary differences between them being relatively simple displacements of fractions of the Al positions.

Even these slight displacements, however, should allow the γ phase to model the PDF data of theoretically pure γ-Al_2O_3 noticeably better than the γ and η phases, particularly as *r* increases. The fact that the γ, η, and θ phases model the PDF data of our 'pure' γ-Al_2O_3 comparably well even at higher-*r* values suggests that real Al_2O_3 may not be as easily classified into one of these phases as one might wish. Numerous studies have reported variability in the Al sublattice.[13,29-30] Even Zhou *et al.*[13] observed different coherent domain sizes associated with the Al and O sublattices in their combined X-ray and neutron refinements which indicated a greater

degree of disorder in the Al sublattice. They attributed it to the random variation in the occupancy of the three partially occupied Al spinel sites, but an even greater degree of site occupancy disorder has since been proposed; in first principles calculations by Paglia *et al*.,[30] nearly every possible Al site (even the sites that should be holes) displayed at least a small partial occupancy, and other computational studies have also observed this.[29] It has even been recently proposed that γ-Al_2O_3 could be better described as a somewhat amorphous network-like structure than as a crystalline defect structure.[31] Thus, site disorder may allow the γ, η, and θ phases to appear even more similar, thereby explaining why these phases can all fit the γ-Al_2O_3 local structure data, even at higher *r* values.

Site disorder may also explain the mysterious δ phase sometimes reported between the γ and θ phases which can never be isolated and whose symmetry is still not agreed upon. In terms of the distortions in the current study, it is feasible to imagine a γ-like structure in which only some of the modes have been activated or, in other words, in which some of the Al atoms have begun shifting but all have not yet reached the true positions in the θ phase. Variation in the hydrothermal conditions may induce different combinations of modes as well, so that the transition proceeds in different ways under different circumstances, explaining the observed variation in δ phase symmetry.

In essence, slow kinetics of Al ion diffusion through the oxygen sublattice may be responsible for the wide variety of transitional alumina phases that have been reported. Perhaps none of the transitional Al_2O_3 phases should be viewed as distinct crystallographic phases but simply as regions along the continual redistribution of Al cations inside either an fcc or hcp oxygen lattice, which redistribution continues until all of the H_2O from the AlOOH and $Al(OH)_3$

phases is gone and the temperature is high enough to allow the oxygen lattice to reconstruct into the α phase arrangement, as the next section discusses.

6.3.3 The γ→α Distortion

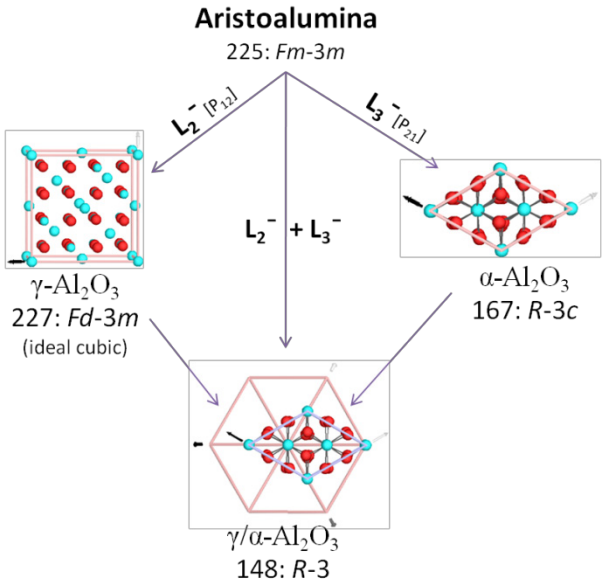

Figure 6.23 Common subgroup relationship between γ and α derived using distortion modes from the aristoalumina parent.

Table 6.11 γ→ γ/α distortion parameters.

γ-Al_2O_3 → γ/α-Al_2O_3	
Space Group: 227 *Fd*-3*m* Subgroup:148 *R*-3 basis=[(1/2,0,-1/2),(-1/2,1/2,0),(1,1,1)] origin=(1/8,1/8,1/8)	
Displacive Modes	Γ_4^+, Γ_5^+
Lattice Strain Modes	Γ_1^+, Γ_5^+
Occupancy Modes	Γ_1^+, Γ_5^+

As Figure 6.23 illustrates, space group 148 *R*-3 was identified as a common subgroup between the γ (ideal) and α phases by combining the L_2^- and L_3^- primary order parameters from the aristo→ γ and aristo→α distortions, respectively. By moving the α structure into an *R*-3 setting (and adding the appropriate ghost atoms to allow Wyckoff site matching—see Appendix C.1), the idealized γ-Al_2O_3 structure could be distorted smoothly into the γ/α-Al_2O_3 subgroup structure (Figure 6.24) using the Γ_4^+ (a,a,a) primary order parameter along with Γ_5^+ and Γ_1^+ parameters (Table 6.11). Because the γ/α subgroup structure is identical to the α structure, the distortion is essentially a direct γ→α distortion. And because the distortion uses primarily displacive modes, it also suggests a physical mechanism for the γ→α transition and not just a set of endpoints.

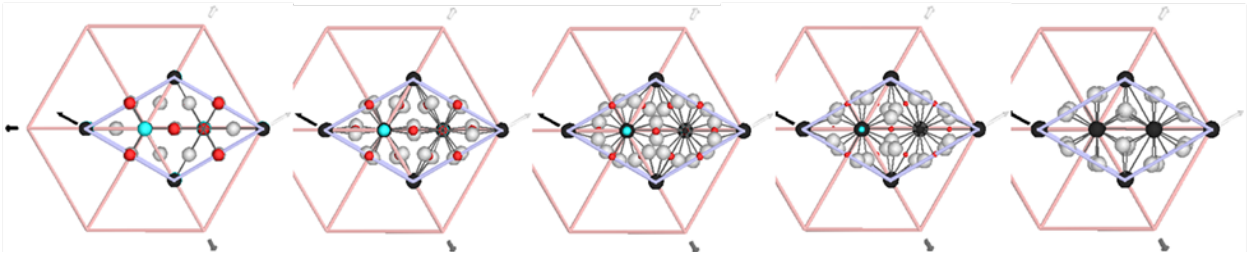

Figure 6.24 Illustration of the direct γ→α distortion. White atoms = O, black atoms = tetrahedral Al that remain stationary, red and blue = O and Al atoms, respectively, that disappear during the distortion.

There are three noteworthy features of this mechanism. First, the fcc oxygen sublattice in γ-Al_2O_3 undergoes substantial restructuring; as Figure 6.24 illustrates, oxygen atoms rotate ±30° around axes centered at either (⅓, ⅔) or (⅔, ⅓) inside the new unit cell[xxiii] in order to form the hcp sublattice of α-Al_2O_3. Second, the tetrahedral Al in γ-Al_2O_3 remain essentially stationary during the distortion and *become* octahedrally coordinated in the α-Al_2O_3 structure as a result of the O sublattice restructuring. Third, 3/5 of the octahedral Al shift positions within the unit cell (to remain octahedrally coordinated as the oxygen lattice rotates), and the other 2/5 of the octahedral Al disappear via the occupancy modes.

Because ¼ of the total Al disappear during the γ→α distortion, ¼ of the O atoms also disappear in order to retain the proper Al_2O_3 stoichiometry. In reality, these atoms would have to be diffusing the short distance to the nanoparticular grain boundaries. This diffusion of ¼ of the atoms from the unit cell is accompanied by a substantial contraction of the rhombohedral *c*-axis lattice parameter. This suggests two modes of density increase: internal volume densification and inter-grain cavity filling. Such high levels of atomic mobility are not unreasonable at the high temperatures (>1000°C) of the transition, and it would be consistent with the numerous reports identifying short-range diffusion as a primary mechanism for the transition.[3,9,32-36]

[xxiii] The direction of the rotation varies between each quadrant of the new α phase unit cell, with adjacent quadrants rotating in opposite directions.

The smooth rotational restructuring of the oxygen sublattice and the stationary nature of portions of the tetrahedral aluminum sublattice reveal a topotactic relationship between the γ and α phases. Thus, contrary to the prevailing hypothesis that the α phase transition is entirely diffusive (as Chapter 9 discusses more thoroughly), the γ→α transition could be topotactic, and this distortion provides a mechanism for smoothly transforming γ-Al_2O_3 to α-Al_2O_3.

To check the validity of this mechanism, high-temperature, in situ TEM experiments need to be performed in which a single γ-Al_2O_3 particle is viewed and the orientational relationships tracked as it transforms to α-Al_2O_3. Unfortunately, such experiments are not currently possible due to the need for a novel ultra-high temperature TEM stage, though the capability may not be far distant.

If the mechanism suggested by this distortion model is accurate, an explanation for the direct γ→α transition in nanoparticles is illuminated by comparing the γ→θ and γ→α distortions. The γ→α distortion requires the entire O sublattice to restructure and ¼ of the atoms to diffuse to the surface whereas the γ→θ distortion merely requires ½ of the Al atom to diffuse slightly within the lattice. The γ→α transition should thus require more energy than the γ→θ transition. But in nanoparticles, the O lattice is not very extended, and the surface is only a short distance from any location inside the particle as Figure 6.25 illustrates. This could lower the energy required for both the O-lattice rotations and the volume diffusion required by the γ→α transition for Al_2O_3, enabling nanoparticles to undergo a direct γ→α transition instead of pausing in the intermediate θ phase.

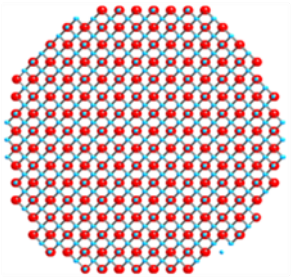

Figure 6.25 Image (so scale) of a 3nm nanoparticle of γ-Al_2O_3, illustrating the small distance of any atom in the structure to the surface.

6.4 Conclusions

To investigate the nature of the γ-Al_2O_3 local structure and the direct γ-to-α phase transition observed in our alumina nanoparticles, we analyzed the symmetry relationships between the well-defined alumina phases. We found that each of the alumina phases (whether fcc or hcp) can be derived as a distortion of a single hypothetical parent structure, which we refer to as aristoalumina, using occupancy modes and relatively small displacive modes. The alumina phases can thus be viewed as vacancy ordered superstructures of the aristoalumina parent structure.

Comparing the vacancy ordering, we noticed that the γ, η, θ, and κ transitional alumina phases all consist of roughly the same ratio of the AlO_4 and AlO_6 units, which are organized into layers of edge sharing AlO_6 with layers of corner sharing AlO_4 in between. The first few bond distances (the low-*r* local structure) of the phases are thus very similar, explaining why all four of these phases can model the low-*r* γ-Al_2O_3 PDF data reasonably well. We hypothesize, though, that non-cubic local-structure distortions in the AlO_4 and AlO_6 units allow the monoclinic θ and orthorhombic κ phases to model the low-*r* data better but that these distortions must be randomized from one unit cell to another so that the average structure appears cubic (or slightly tetragonally distorted), allowing the γ and η phases to model the higher-*r* PDF data better.

By combining the primary order parameters obtained from the aristo→γ distortions with those obtained from the aristo→θ and aristo→α distortions, we identified common-subgroup pathways for topotactic γ→θ and γ→α transitions. The γ→θ distortion revealed that only ½ of the Al sites in γ-Al_2O_3 must diffuse a short distance to form the θ-Al_2O_3 structure, making the θ phase nearly as similar to the γ phase as η-Al_2O_3, which shares ⅔ of its Al positions with γ. Considering the Al site occupancy disorder reported for γ-Al_2O_3, the γ, η, and θ phases may not

be as distinct as previously supposed; in fact, all of the transitional alumina phases may be better described as regions along the continual redistribution of Al within an fcc or hcp oxygen lattice as the AlOOH and $Al(OH)_3$ phases transform to α-Al_2O_3. This site disorder (essentially slow Al diffusion kinetics) could explain reports of δ-Al_2O_3 and all other γ-like intermediate phases.

The γ→α distortion revealed a potential topotactic relationship between the γ and α phases, providing a mechanism for the γ→α transition in which the oxygen atoms of the polyhedra in each unit cell undergo substantial rotations (±30°) to restructure the oxygen lattice from fcc to hcp, and ¼ of the atoms (both Al and O) diffuse to the surface. We hypothesize that the small size of alumina nanoparticles reduces the energy necessary for both of these processes, thereby enabling a direct γ→α transition in alumina nanoparticles.

References

1. Cava, S.; Tebcherani, S. M.; Souza, I. A.; Pianaro, S. A.; Paskocimas, C. A.; Longo, E.; Varela, J. A., Structural characterization of phase transition of Al_2O_3 nanopowders obtained by polymeric precursor method. *Mater. Chem. Phys.* **2007,** *103* (2-3), 394-399.
2. Macedo, M. I. F.; Bertran, C. A.; Osawa, C. C., Kinetics of the γ to α alumina phase transformation by quantitative X-ray diffraction. *J. Mater. Sci.* **2007,** *42* (8), 2830-2836.
3. Badkar, P. A.; Bailey, J. E., The mechanism of simultaneous sintering and phase transformation in alumina. *J. Mater. Sci.* **1976,** *11* (10), 1794-806.
4. Belonoshko, A. B.; Ahuja, R.; Johansson, B., Mechanism for the κ-Al_2O_3 to the α-Al_2O_3 transition and the stability of κ-Al_2O_3 under volume expansion. *Phys. Rev. B: Condens. Matter Mater. Phys.* **2000,** *61* (5), 3131-3134.
5. Bye, G. C.; Simpkin, G. T., Influence of chromium and iron on formation of α-alumina from γ-alumina. *J. Am. Ceram. Soc.* **1974,** *57* (8), 367-71.
6. Digne, M.; Sautet, P.; Raybaud, P.; Toulhoat, H.; Artacho, E., Structure and Stability of Aluminum Hydroxides: A Theoretical Study. *J. Phys. Chem. B* **2002,** *106* (20), 5155-5162.
7. Loffler, L.; Mader, W., Transformation mechanism of the dehydration of diaspore. *J. Am. Ceram. Soc.* **2003,** *86* (4), 534-540.
8. Ruberto, C.; Yourdshahyan, Y.; Lundqvist, B. I., Surface properties of metastable alumina: A comparative study of k- and alpha -Al2O3. *Phys. Rev. B: Condens. Matter Mater. Phys.* **2003,** *67* (19), 195412/1-195412/18.
9. Saalfeld, H., The structures of gibbsite and of the intermediate products of its dehydration. *Neues Jahrbuch fuer Mineralogie, Abhandlungen* **1960,** *95*, 1-87.

10. Stumpf, H. C.; Russell, A. S.; Newsome, J. W.; Tucker, C. M., Thermal transformations of aluminas and alumina hydrates. *J. Ind. Eng. Chem. (Washington, D. C.)* **1950,** *42*, 1398-1403.
11. Tsukada, T.; Segawa, H.; Yasumori, A.; Okada, K., Crystallinity of boehmite and its effect on the phase transition temperature of alumina. *J. Mater. Chem.* **1999,** *9* (2), 549-553.
12. Wefers, K. M., Chanakya, "Oxides and Hydroxides of Aluminum". *Tech. Pap. - Alcoa Res. Lab.* **1987,** *19*.
13. Zhou, R. S.; Snyder, R. L., Structures and transformation mechanisms of the η, γ, and θ transition aluminas. *Acta Crystallogr., Sect. B: Struct. Sci.* **1991,** *B47* (5), 617-30.
14. Levin, I.; Bendersky, L. A.; Brandon, D. G.; Ruhle, M., Cubic to monoclinic phase transformations in alumina. *Acta Materialia* **1997,** *45* (9), 3659-3669.
15. Levin, I.; Brandon, D., Metastable alumina polymorphs: crystal structures and transition sequences. *J. Am. Ceram. Soc.* **1998,** *81* (8), 1995-2012.
16. Cai, S.-H.; Rashkeev, S. N.; Pantelides, S. T.; Sohlberg, K., Atomic Scale Mechanism of the Transformation of γ-Alumina to θ-Alumina. *Phys. Rev. Lett.* **2002,** *89* (23), 235501/1-235501/4.
17. Cai, S.-H.; Rashkeev, S. N.; Pantelides, S. T.; Sohlberg, K., Phase transformation mechanism between γ- and θ-alumina. *Phys. Rev. B: Condens. Matter Mater. Phys.* **2003,** *67* (22), 224104/1-224104/10.
18. Cai, S.-H. S., Karl, Theory of transition alumina transformations. The many steps that transform boehmite to corundum. *Recent Res. Dev. Chem. Phys.* **2002,** *3* (Pt. 1), 85-98.
19. Landau, L. D.; Lifshits, E. M., *Statistical Physics*. Pergamon Press: 1969.
20. Toledano, J. C.; Toledano, P., *The Landau Theory of Phase Transitions*. World Scientific: Singapore, 1987.
21. Dove, M. T., Theory of displacive phase transitions in minerals. *Am. Mineral.* **1997,** *82* (3-4), 213-244.
22. Campbell, B. J.; Stokes, H. T.; Tanner, D. E.; Hatch, D. M., ISODISPLACE. A web-based tool for exploring structural distortions. *J. Appl. Crystallogr.* **2006,** *39* (4), 607-614.
23. Perez-Mato, J. M.; Orobengoa, D.; Aroyo, M. I., Mode crystallography of distorted structures. *Acta Crystallographica, Section A: Foundations of Crystallography* **2010,** *A66* (5), 558-590.
24. Orobengoa, D.; Capillas, C.; Aroyo, M. I.; Perez-Mato, J. M., AMPLIMODES: symmetry-mode analysis on the Bilbao Crystallographic Server. *J. Appl. Crystallogr.* **2009,** *42* (5), 820-833.
25. Hovestreydt, E.; Aroyo, M.; Sattler, S.; Wondratschek, H., KAREP - a program for calculating irreducible space-group representations. *J. Appl. Crystallogr.* **1992,** *25* (4), 544.
26. Rodríguez-Carvajal, J.; Roisnel, T. FullProf and accompanying programs at http://www-llb.cea.fr/fullweb/powder.htm.
27. Wills, A. S., A new protocol for the determination of magnetic structures using simulated annealing and representational analysis (SARAh). *Physica B: Condensed Matter (Amsterdam)* **2000,** *276-278*, 680-681.
28. Sikora, W.; Bialas, F.; Pytlik, L., MODY: a program for calculation of symmetry-adapted functions for ordered structures in crystals. *J. Appl. Crystallogr.* **2004,** *37* (6), 1015-1019.

29. Lee, M. H.; Cheng, C.-F.; Heine, V.; Klinowski, J., Distribution of tetrahedral and octahedral Al sites in gamma alumina. *Chemical Physics Letters* **1997,** *265* (6), 673-676.
30. Paglia, G.; Rohl, A. L.; Buckley, C. E.; Gale, J. D., Determination of the structure of γ-alumina from interatomic potential and first-principles calculations: The requirement of significant numbers of nonspinel positions to achieve an accurate structural model. *Phys. Rev. B: Condens. Matter Mater. Phys.* **2005,** *71* (22), 224115/1-224115/16.
31. Ching, W. Y.; Ouyang, L.; Rulis, P.; Yao, H., Ab initio study of the physical properties of gamma -Al2O3: Lattice dynamics, bulk properties, electronic structure, bonding, optical properties, and ELNES/XANES spectra. *Phys. Rev. B: Condens. Matter Mater. Phys.* **2008,** *78* (1), 014106/1-014106/13.
32. Tucker, D. S.; Hren, J. J., The γ → α phase transformation in alumina. *Materials Research Society Symposium Proceedings* **1984,** *31* (Electron Microsc. Mater.), 337-44.
33. Loong, C. K.; Richardson, J. W., Jr.; Ozawa, M., Structural phase transformations of rare-earth modified transition alumina to corundum. *Journal of Alloys and Compounds* **1997,** *250* (1-2), 356-359.
34. Nortier, P.; Soustelle, M., Alumina carriers for automotive pollution control. *Stud. Surf. Sci. Catal.* **1987,** *30* (Catal. Automot. Pollut. Control), 275-300.
35. Schaper, H.; Doesburg, E. B. M.; De Korte, P. H. M.; Van Reijen, L. L., Thermal stabilization of high surface area alumina. *Solid State Ionics* **1985,** *16*, 261-5.
36. Schaper, H.; Doesburg, E. B. M.; Van Reijen, L. L., The influence of lanthanum oxide on the thermal stability of gamma alumina catalyst supports. *Appl. Catal.* **1983,** *7* (2), 211-20.

Chapter 7

Novel, 1-pot Synthesis of La-doped γ-Al_2O_3 Nanoparticle Catalyst Supports

7.1 Introduction

The γ-Al_2O_3 nanoparticles produced using the solvent deficient method have potential as catalyst support materials due to the intrinsically high surface area and mesoporous nature of their agglomerates as well as the catalytic activity of the γ-Al_2O_3 structure itself. However, the catalytically useful gamma phase is metastable and will transform to α-Al_2O_3 phase (corundum) at sufficiently high temperatures; as shown in previous chapters and studies, the γ→α transition occurs above 1100°C for bulk γ-Al_2O_3 but is even lower (between 1000-1100°C) in γ-Al_2O_3 nanoparticles.[1] This phase transition has two ill effects for catalytic applications; first, it is accompanied by a large decrease in surface area (Figure 7.1) which results in a large drop in catalytic activity, and second, there is also a substantial decrease in volume which creates voids in the catalytic bed and leads to attrition of

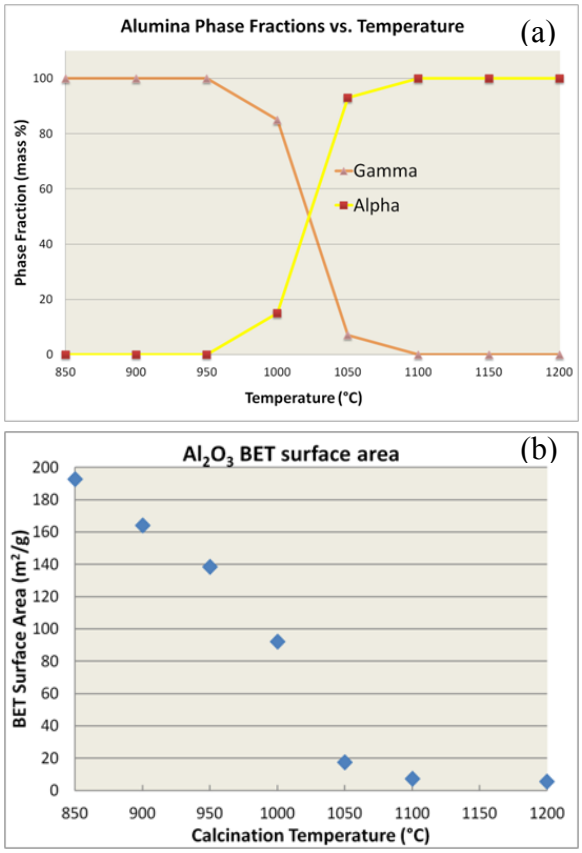

Figure 7.1 BET surface area (b) as the 3 nm γ-Al_2O_3 transforms to 60 nm α-Al_2O_3 (a).

the catalyst.[2] This transformation is thus problematic for applications that involve high temperatures (>1000°C) such as automotive exhaust gas processing and the combustion of hydrocarbons.[3]

To prevent these unfortunate effects in the catalyst, γ-Al_2O_3 can be doped with a few weight percent of one of several elements including zirconium, titanium, thorium, boron, silicon, alkaline earth, and rare earth elements.[2-12] These 'structural promoters' delay the onset of the transition to α-Al_2O_3 typically by about 100°C, thereby stabilizing the gamma phase in the range of the catalytic applications. Of these promoters, La^{3+} is the most commonly used in industry.[3] Numerous studies have shown that La^{3+} dopant percentages of 3-5% (by weight) are sufficient to achieve the stabilizing effect,[3,13-17] though several studies have indicated that loadings as low as ~0.5 wt% may be sufficient.[18-19] There is evidence that increasing the La percentage beyond 5% diminishes the surface area[14] and pore structure of the Al_2O_3 support[17] and may have negative effects on the activity of some catalysts.[5,15] Thus, a La dopant level of about 3 wt% is generally considered to be optimal and is employed in the industrial production of La-doped Al_2O_3.[14-17]

La-doping is typically accomplished either by adding the La during the preparation of the support via the sol-gel method or by modifying the surface of commercially available alumina via impregnation.[3] In the sol-gel method, $La(NO_3)_3 \cdot 9H_2O$ is added to the alumina sol at a carefully controlled acidic pH prior to the typical drying and calcination steps.[4,10,20] Of the several variations of the impregnation method,[21] incipient wetness and soaking are perhaps the most widely used.[3,22-23] With impregnation by soaking, the commercially produced Al_2O_3 is soaked in a $La(NO_3)_3 \cdot 6H_2O$ solution over a period of days to allow the alumina to adsorb/absorb the lanthanum nitrate. With incipient wetness, a volume of La solution roughly equal to that of the Al_2O_3 pore volume is added to the dry alumina slowly until the pores can absorb no more and

the alumina begins to appear wet. With either method, the impregnated alumina is dried and then calcined to remove the nitrate ions. Both the impregnation and sol-gel processes often require 2-3 days to complete.

Rather than the somewhat time-consuming impregnation method, we used the solvent deficient method to attempt a 1-pot approach similar to that used in the sol-gel process. This chapter describes the resulting method in which the La^{3+} is added during the solvent-deficient Al_2O_3 synthetic reaction rather than after the Al_2O_3 formation. The structure and morphology of the La-doped Al_2O_3 product were characterized using TEM, X-ray PDF, and BET analyses. These characterizations and the variation of the La-doped Al_2O_3 properties as a function of calcination temperature are discussed.

7.2 Experimental Methods

7.2.1 Synthesis

A 1-pot procedure for La-doping is easily accomplished using the solvent-deficient method by simply adding $La(NO_3)_3 \cdot 6H_2O$ (3-5% by weight) to the typical 1:3 mole ratio of $Al(NO_3)_3 \cdot 9H_2O$ and NH_4HCO_3 reagents used to synthesize Al_2O_3. The method then proceeds as described in Chapter 2;[24-25] the reagents are ground together until the bubbling/popping subsides (roughly 10 minutes), and the resulting wet precursor is calcined for 2 hours at the desired temperature (roughly 700-800°C for γ-Al_2O_3).

To study how the physical properties of these La-doped Al_2O_3 nanomaterials change as a function of calcination temperature, a suite of La-doped Al_2O_3 nanomaterials were produced. As with the pure Al_2O_3 samples described in Chapter 5, one large batch of the La-doped precursor material was prepared by using a mortar and pestle to grind 267.66g of $Al(NO_3)_3 \cdot 9H_2O$, 2.993 g

of $La(NO_3)_3 \cdot 6H_2O$ (both of reagent grade purity, VWR) with 170.85g NH_4HCO_3 (reagent grade purity, VWR) for 15-20 minutes until bubbling ceased and a precipitate (the precursor) had formed. The slurry containing the precursor was then dried for 12 hours in air at 100°C using a Thermo Scientific Lindberg Blue M oven. The dried precursor was split into 23 portions, roughly 8.1 g each. Using the Thermo Scientific oven, one sample was calcined at each 50°C increment between 100°C and 1200°C by heating it in air at a rate of 5°C/min to its set temperature and then holding this temperature for 2 hours before being allowed to cool to room temperature.

7.2.2 Characterization

The presence of the La dopant in the calcined samples was verified by XEDS (X-ray energy-dispersive spectrometry) analysis using a FEI Philips Technai F20 Analytical STEM operating at 200 kV. For the analysis, a small amount of the La-doped Al_2O_3 calcined at 700°C was suspended in ethanol, and a drop of the dilute solution was placed on a formvar/carbon film supported by a 200 mesh Cu grid (Ted-Pella Inc.). The solvent was allowed to evaporate, and images were recorded in standard high resolution TEM mode before switching to STEM (scanning transmission electron microscopy) mode to perform the XEDS analysis. A HAADF (high-angle annular dark-field) detector was used in the XEDS analysis.

The structural evolution of the La-doped Al_2O_3 synthesized using the 1-pot method was studied using X-ray PDF to determine the phase transition temperatures and thereby reveal the extent to which the La-doped γ-Al_2O_3 was stabilized relative to the pure, un-doped Al_2O_3. X-ray data for the PDF analyses were collected at the 11 ID-B beamline[26] at the Advanced Photon Source (APS) at Argonne National Laboratory using synchrotron radiation of energy 60 keV (λ = 0.2128 Å). For each sample, ~10 mg of powder were loaded into a 0.0395 inch inner-diameter Kapton capillary, and 2-D images of the diffraction data were collected out to a maximum value

of $Q = 29.5$ Å^{-1} in reciprocal space under ambient conditions using a Perkin Elmer area detector. The Fit2D software package[27] was used to integrate the 2D ring patterns into 1D powder diffraction patterns. The PDFgetX2 software package[28] was used to extract $G(r)$, the experimental PDF,[29] using a maximum momentum transfer of $Q = 24.5$ Å^{-1} in the Fourier transform. PDF refinements were performed using the PDFgui program.[30]

Brunauer-Emmett-Teller (BET) specific surface areas and pore sizes for each of the La-Al_2O_3 portions were determined from N_2 adsorption at 77 K using a Micromeritics TriStar II instrument. For these measurements, between 200 and 300 mg of each sample were degassed at 200°C for 12-24 hours to remove superfluous moisture. The samples were allowed to cool in air to room temperature prior to data collection.

7.3 Results and Discussion

The XRD pattern and TEM image of the La-doped γ-Al_2O_3 produced using the 1-pot, solvent-deficient method are shown in Figure 7.2. The XRD pattern verifies the γ-Al_2O_3 structure, and the TEM image reveals the same agglomerated morphology present in the pure Al_2O_3 samples produced by the solvent-deficient method (see Chapter 5). Likewise, the BET surface area and pore size estimates given in Table 7.1 for the pure and La-doped alumina are essentially identical. Thus, the addition of the 3% La^{3+} dopant during the Al_2O_3 synthetic reaction neither impedes the formation of the Al_2O_3 lattice nor alters the morphology of the Al_2O_3 produced by the solvent-deficient method.

Table 7.1 BET surface area and BJH pore size estimates for both pure Al_2O_3 and La-doped Al_2O_3 produced by the solvent-deficient method and calcined at 700°C.

	surface area	pore diameter
700°C γ-Al_2O_3	231 m^2/g	3.7 nm
700°C La-doped γ-Al_2O_3	242 m^2/g	3.5 nm

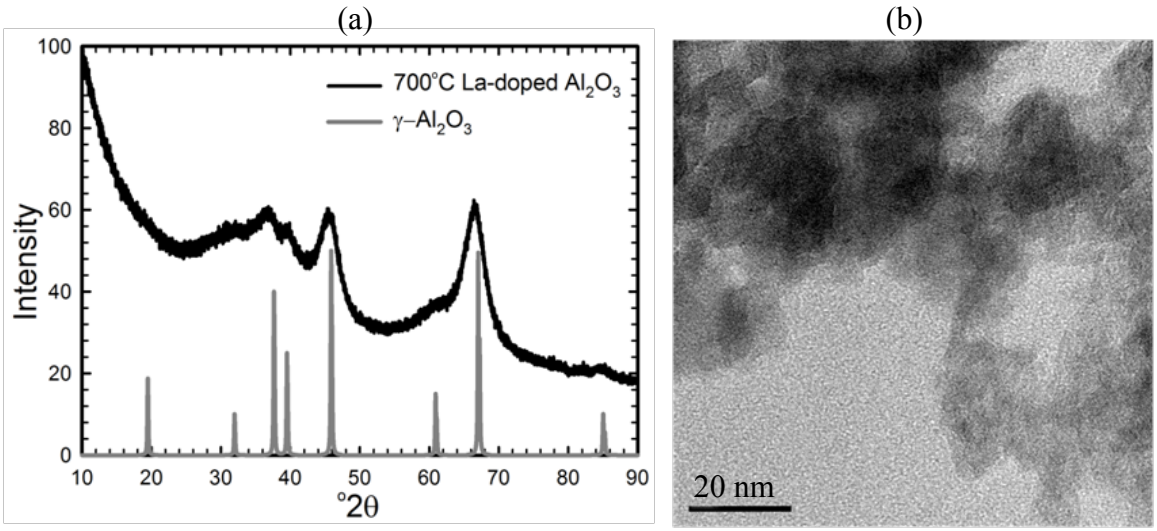

Figure 7.2 XRD pattern (a) and TEM image (b) of La-doped γ-Al_2O_3 produced by the 1-pot, solvent-deficient method. In (a), the La-doped Al_2O_3 XRD pattern (black) is compared with a γ-Al_2O_3 pattern (gray) from the ICDD database (reference number 00-010-0425).

To evaluate the success of the new 1-pot doping method, we used XEDS to detect the elemental composition of the alumina and verify the presence of the La dopant. The result of the XEDS investigation shown in Figure 7.3 confirms the presence of La^{3+} in the samples.

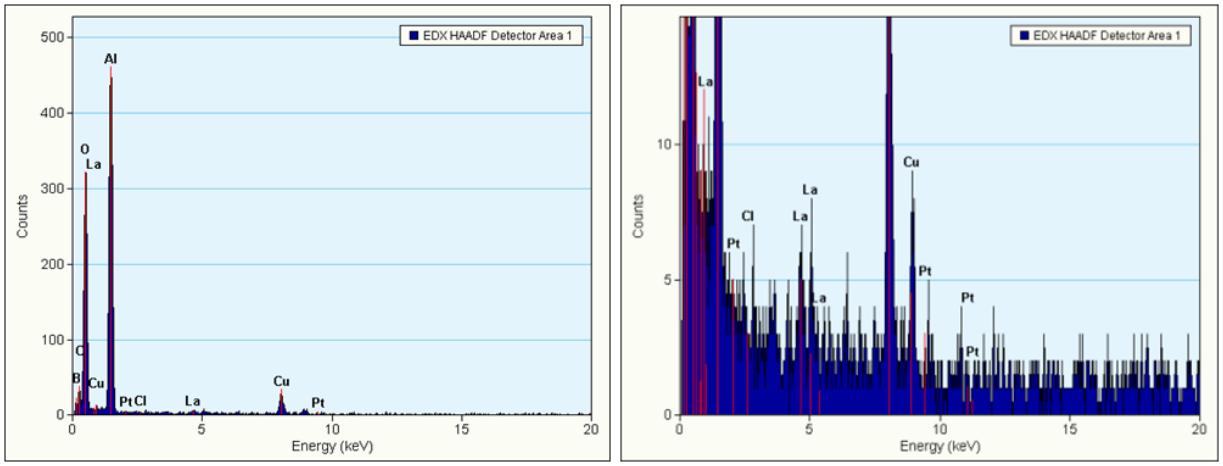

Figure 7.3 XEDS results confirming the presence of La^{3+} in La-doped Al_2O_3 produced by the 1-pot, solvent-deficient synthetic method. (Pt and Cl peaks confirm the presence of the Pt catalyst deposited on the sample.)

We also used PDF analysis to study the structural evolution of the La-doped Al_2O_3 and to determine how effectively the La dopant stabilizes the γ-Al_2O_3 phase. The PDF analyses given in

Figure 7.4 reveal that the γ→α transition occurs between ~1100-1200°C for the La-doped Al_2O_3 (the final fit parameters are given in Appendix D). Comparing this result to the 1000-1100°C phase transformation temperature of the pure Al_2O_3 (see Figure 7.5(a)) determined in Chapter 5, the La dopant appears to stabilize the γ-Al_2O_3 by roughly 100°C. The BET analyses of these same samples given in Figure 7.5(b) reveals that the decrease in surface area accompanying the γ→α transition is likewise delayed by ~100°C for the La-doped Al_2O_3 sample. These are the same margins of stabilization observed for La-doped γ-Al_2O_3 produced by other methods of doping, thus the 1-pot method developed here appears to be a viable way to synthesize La-doped γ-Al_2O_3.

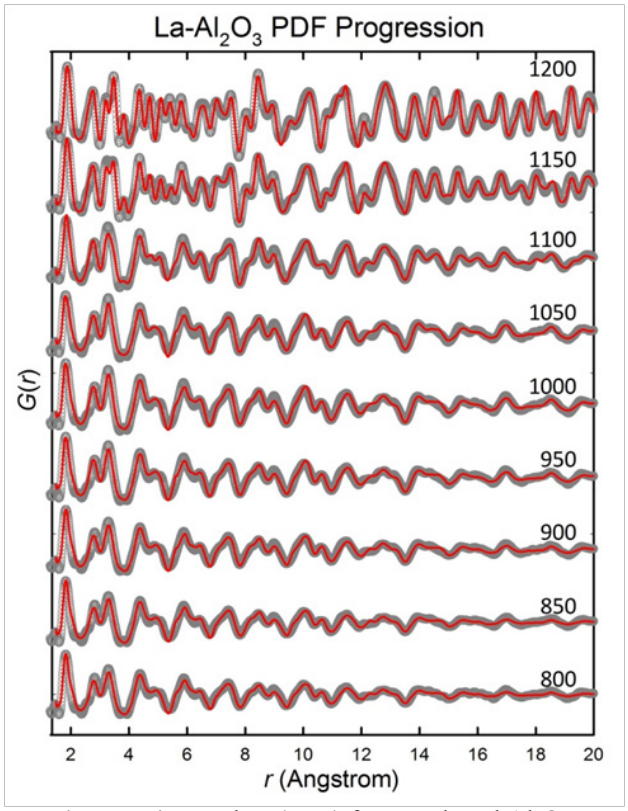

Figure 7.4 PDF data (gray) for La –doped Al_2O_3 synthesized via the 1-pot, solvent-deficient method and calcined at the given temperatures. Fits using the pure γ-Al_2O_3 structure are shown in red.

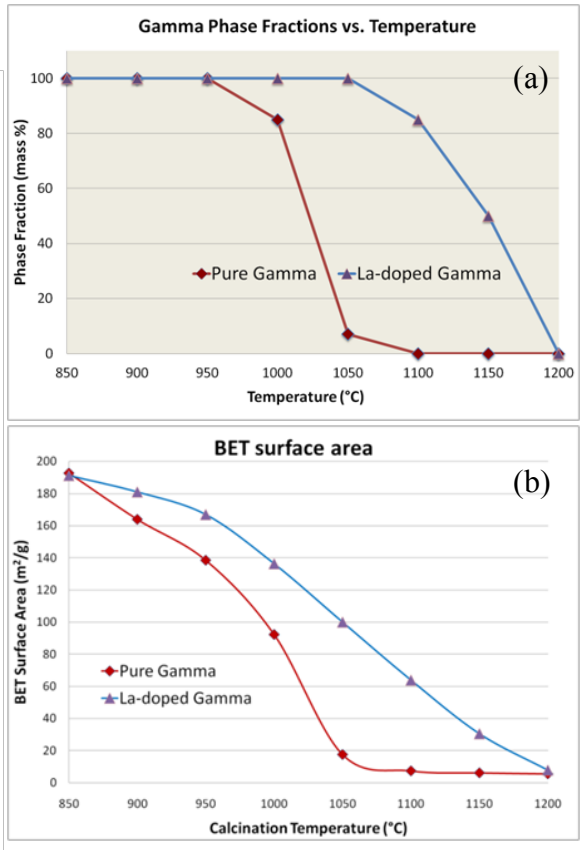

Figure 7.5 γ-Al_2O_3 phase fractions (a) and BET surface area analyses (b) during the γ→α transition for pure γ-Al_2O_3 (red) and La-doped γ-Al_2O_3 (blue).

Our 1-pot approach has several advantages over other doping methods. First, it is much faster than impregnation methods, requiring only 3 hours instead of 3 days to produce the La-doped γ-Al_2O_3 nanomaterials. Second, the synthetic procedure is much easier than either the sol-gel or impregnation methods which require careful monitoring of pH, concentration levels, solution temperatures, and soaking times. Third, it provides a more accurate means of controlling the amount of La added than impregnation methods; all the La added to the reaction mixture is utilized, so less La is used because none is discarded in the excess solution required by soaking impregnation methods. This also means that less aqueous waste is generated, so the method is more environmentally benign than soaking impregnation methods. The 1-pot, solvent deficient method thus provides a new and favorable alternative method for producing La-doped γ-Al_2O_3 nanomaterials.

References

1. Cava, S.; Tebcherani, S. M.; Souza, I. A.; Pianaro, S. A.; Paskocimas, C. A.; Longo, E.; Varela, J. A., Structural characterization of phase transition of Al_2O_3 nanopowders obtained by polymeric precursor method. *Mater. Chem. Phys.* **2007,** *103* (2-3), 394-399.
2. Nortier, P.; Soustelle, M., Alumina carriers for automotive pollution control. *Stud. Surf. Sci. Catal.* **1987,** *30* (Catal. Automot. Pollut. Control), 275-300.
3. Beguin, B.; Garbowski, E.; Primet, M., Stabilization of alumina by addition of lanthanum. *Appl. Catal.* **1991,** *75* (1), 119-32.
4. Kumar, K. N. P.; Tranto, J.; Kumar, J.; Engell, J. E., Pore-structure stability and phase transformation in pure and M-doped (M = La, Ce, Nd, Gd, Cu, Fe) alumina membranes and catalyst supports. *Journal of Materials Science Letters* **1996,** *15* (3), 266-70.
5. Fraga, M. A.; Soares de Souza, E.; Villain, F.; Appel, L. G., Addition of La and Sn to alumina-supported Pd catalysts for methane combustion. *Appl. Catal., A* **2004,** *259* (1), 57-63.
6. Cho, J.; Harmer, M. P.; Chan, H. M.; Rickman, J. M.; Thompson, A. M., Effect of yttrium and lanthanum on the tensile creep behavior of aluminum oxide. *J. Am. Ceram. Soc.* **1997,** *80* (4), 1013-1017.
7. Church, J. S.; Cant, N. W.; Trimm, D. L., Stabilization of aluminas by rare earth and alkaline earth ions. *Appl. Catal., A* **1993,** *101* (1), 105-16.
8. Ozawa, M., Thermal stabilization of catalytic compositions for automobile exhaust treatment through rare earth modification of alumina nanoparticle support. *Journal of Alloys and Compounds* **2006,** *408-412*, 1090-1095.

9. Ozawa, Y.; Tochihara, Y.; Watanabe, A.; Nagai, M.; Omi, S., Stabilizing effect of Nd_2O_3, La_2O_3 and ZrO_2 on $Pt.PdO/Al_2O_3$ during catalytic combustion of methane. *Appl. Catal., A* **2004,** *258* (2), 261-267.
10. Rossignol, S.; Kappenstein, C., Effect of doping elements on the thermal stability of transition alumina. *International Journal of Inorganic Materials* **2001,** *3* (1), 51-58.
11. Vu, B. K.; Song, M. B.; Ahn, I. Y.; Suh, Y.-W.; Suh, D. J.; Kim, W.-I.; Koh, H.-L.; Choi, Y. G.; Shin, E. W., Propane dehydrogenation over Pt-Sn/Rare-earth-doped Al2O3: Influence of La, Ce, or Y on the formation and stability of Pt-Sn alloys. *Catal. Today* **2011,** *164* (1), 214-220.
12. Wei, Q.; Chen, Z.-X.; Wang, Z.-H.; Hao, Y.-L.; Zou, J.-X.; Nie, Z.-R., Effect of La, Ce, Y and B addition on thermal stability of unsupported alumina membranes. *Journal of Alloys and Compounds* **2005,** *387* (1-2), 292-296.
13. Nishio, Y.; Ozawa, M., Thermal stability and microstructural change of lanthanum modified alumina catalytic support. *J. Ceram. Soc. Jpn.* **2007,** *115* (Oct.), 633-636.
14. Nishio, Y.; Ozawa, M., Preparation and properties of porous lanthanum doped alumina ceramic composites with self-organization. *J. Ceram. Soc. Jpn.* **2009,** *117* (Apr.), 499-502.
15. Thevenin, P. O.; Alcalde, A.; Pettersson, L. J.; Jaras, S. G.; Fierro, J. L. G., Catalytic combustion of methane over cerium-doped palladium catalysts. *J. Catal.* **2003,** *215* (1), 78-86.
16. Thevenin, P. O.; Pocoroba, E.; Pettersson, L. J.; Karhu, H.; Vaeyrynen, I. J.; Jaeras, S. G., Characterization and Activity of Supported Palladium Combustion Catalysts. *J. Catal.* **2002,** *207* (1), 139-149.
17. He, X.; Liu, Q.; Qin, Q.; Guo, L., Influence of La/Ba doping content on of alumina. *Wujiyan Gongye* **2011,** *43* (4), 18-20, 35.
18. Tijburg, I. I. M.; Geus, J. W.; Zandbergen, H. W., Application of lanthanum to pseudo-boehmite and γ-alumina. *Journal of Materials Science* **1991,** *26* (23), 6479-86.
19. Wang, S.; Borisevich, A. Y.; Rashkeev, S. N.; Glazoff, M. V.; Sohlberg, K.; Pennycook, S. J.; Pantelides, S. T., Dopants adsorbed as single atoms prevent degradation of catalysts. *Nature Materials* **2004,** *3* (3), 143-146.
20. Lin, Y. S.; De Vries, K. J.; Burggraaf, A. J., Thermal stability and its improvement of the alumina membrane top-layers prepared by sol-gel methods. *Journal of Materials Science* **1991,** *26* (3), 715-20.
21. Manual of methods and procedures for catalyst characterization. *Pure and Applied Chemistry* **1995,** *67* (8/9), 1257-306.
22. Van Dillen, A. J.; Terorde, R. J. A. M.; Lensveld, D. J.; Geus, J. W.; De Jong, K. P., Synthesis of supported catalysts by impregnation and drying using aqueous chelated metal complexes. *J. Catal.* **2003,** *216* (1-2), 257-264.
23. Boukha, Z.; Fitian, L.; Lopez-Haro, M.; Mora, M.; Ruiz, J. R.; Jimenez-Sanchidrian, C.; Blanco, G.; Calvino, J. J.; Cifredo, G. A.; Trasobares, S.; Bernal, S., Influence of the calcination temperature on the nano-structural properties, surface basicity, and catalytic behavior of alumina-supported lanthana samples. *J. Catal.* **2010,** *272* (1), 121-130.
24. Woodfield, B. F.; Liu, S.; Boerio-Goates, J.; Liu, Q.; Smith, S. J. Preparation of uniform nanoparticles of ultra-high purity metal oxides, mixed metal oxides, metals, and metal alloys. 2007-US4279, 2007098111, 20070216., 2007.

25. Smith, S. J.; Liu, S.; Liu, Q.; Boerio-Goates, R. E. O. J.; Woodfield, B. F., Synthesis of metal oxide nanoparticles via a robust "solvent-deficient" method. *Chem. Mater.* **2011**, Submitted.
26. Rutt, U.; Beno, M. A.; Strempfer, J.; Jennings, G.; Kurtz, C.; Montano, P. A., Diffractometer for high energy X-rays at the APS. *Nuclear Instruments & Methods in Physics Research, Section A: Accelerators, Spectrometers, Detectors, and Associated Equipment* **2001,** *467-468* (Pt. 2), 1026-1029.
27. "Fit2D" V. 9.129 Reference Manual V. 3.1.
28. Qiu, X.; Thompson, J. W.; Billinge, S. J. L., PDFgetX2: a GUI-driven program to obtain the pair distribution function from X-ray powder diffraction data. *J. Appl. Crystallogr.* **2004,** *37* (4), 678.
29. Egami, T. B., S. J. L., *Underneath the Bragg Peaks: Structural Analysis of Complex Materials*. First ed.; Pergamon: Kidlington, Oxford, UK, 2003; Vol. 7, p 404.
30. Farrow, C. L.; Juhas, P.; Liu, J. W.; Bryndin, D.; Bozin, E. S.; Bloch, J.; Proffen, T.; Billinge, S. J. L., PDFfit2 and PDFgui: computer programs for studying nanostructure in crystals. *J. Phys.: Condens. Matter* **2007,** *19* (33), 335219/1-335219/7.

Chapter 8

Structural Characterization of La-doped γ-Al_2O_3 Nanoparticles

8.1 Introduction

As the previous chapter revealed, the catalytically useful but metastable γ-Al_2O_3 can be stabilized by the addition of a few weight percent of a lanthanide cation such as La^{3+}. It is generally agreed that this dopant stabilizes the γ-Al_2O_3 by delaying the onset of the undesirable transition to the α-phase by roughly 100°C,[1] but it has been a matter of debate whether the La atoms enter the bulk, adsorb as isolated atoms on the surface, or form surface compounds/layers.[2-7]

The reported dopant location/environment has varied both within each doping method and between the methods. In the most widely used method of La-doping (impregnation by soaking), in which the commercially produced Al_2O_3 is soaked in a $La(NO_3)_3 \cdot 6H_2O$ solution over a period of days, dried, and then calcined to remove the nitrate ions, it is generally agreed that the La^{3+} is deposited on or near the surface of the alumina.[2,8-9] Many have suggested that the La dopant forms a La_2O_3 or $LaAlO_3$ layer on the Al_2O_3 surface.[1-2] However, most recent results have suggested that the La dopant remains dispersed as isolated atoms on the Al_2O_3 surface,[5,10] particularly at the low dopant levels (< 5%) typically employed.[11-12] In contrast, when the La dopant is added during the alumina synthesis via the sol-gel method, the dopant has been

reported to incorporate into the alumina structure,[7,13] though isolated, surface-bound dopant sites have also been reported.

Chapter 7 reported a new 1-pot procedure for synthesizing La-doped γ-Al_2O_3 nanoparticles to be used as catalyst support materials. In this process (the solvent-deficient method), the La dopant is added during the Al_2O_3 synthetic reaction instead of after the Al_2O_3 is formed, thereby making it more similar to the sol-gel rather than the impregnation method of doping. But considering the variation in the reported La dopant locations and the unique solvent-deficient synthetic environment of the new method, we thought it necessary to determine the location of the La dopant atoms in our La-doped Al_2O_3 rather than infer it from previous studies of other methods. Additionally, we wished to determine if and how the La dopant location varies as a function of calcination temperature. This chapter reports PDF and EXAFS analyses performed to accomplish these aims.

8.2 Experimental Methods

The suite of La-doped Al_2O_3 nanomaterials studied in the previous chapter also served as the subject of the present analyses. To review, one large batch of the La-doped precursor material was prepared by using a mortar and pestle to 267.66g of $Al(NO_3)_3$•$9H_2O$, 2.993 g of $La(NO_3)_3$•$6H_2O$ (both of reagent grade purity, VWR) with 170.85g NH_4HCO_3 (reagent grade purity, VWR) for 15-20 minutes, forming a solid precursor in slurry form. The precursor slurry was then dried for 12 hours in air at 100°C using a Thermo Scientific Lindberg Blue M oven. The dried precursor was split into 23 portions, roughly 8.1 g each. Using the Thermo Scientific oven, one sample was calcined at each 50°C increment between 100°C and 1200°C by heating it in air at a rate of 5°C/min to its set temperature and then holding this temperature for 2 hours before being allowed to cool to room temperature.

The PDF data discussed in the previous chapter were re-analyzed here as well. Again, X-ray data for the PDF analyses were collected at the 11 ID-B beamline[14] at the Advanced Photon Source (APS) at Argonne National Laboratory using synchrotron radiation of energy 60 keV (λ = 0.2128 Å). For each sample, ~10 mg of powder were loaded into a 0.0395 inch inner-diameter Kapton capillary, and 2-D images of the diffraction data were collected out to a maximum value of $Q = 29.5$ Å^{-1} in reciprocal space under ambient conditions using a Perkin Elmer area detector. The Fit2D software package[15] was used to integrate the 2D ring patterns and obtain 1D powder diffraction patterns. The PDFgetX2 software package[16] was used to extract $G(r)$, the experimental PDF,[17] using a maximum momentum transfer of $Q = 24.5$ Å^{-1} in the Fourier transform. PDF refinements were performed using the PDFgui program.[18]

La L_{III}-edge EXAFS (extended x-ray absorption fine structure) spectra were collected for the La-doped Al_2O_3 samples calcined every 100°C from 300-1200°C. For the sake of comparison, data were also collected for samples of La_2O_3 (Alpha Aesar, reagent grade), $LaAlO_3$ (Alpha Aesar, reagent grade), and La-doped Al_2O_3 in which the La dopant was adding using the impregnation method. Data for all samples were collected at room temperature using the 10 BM beamline[14] at the Advanced Photon Source (APS) at Argonne National Laboratory using the La L_{III}-edge (5.4827 keV). The low concentration of La^{3+} (~3% by weight) proved to be too low for transmission measurements to provide acceptable statistics, so a 16-element Ge detector was used to collect the fluorescence signal. The samples were pressed into pellets prior to data collection to increase the fluorescence signal.

Three scans of each sample were collected using an energy range of 5.2827 keV to 5.88579 keV with 3 different step sizes (0.005 keV for the pre-edge between 5.2827- 5.4527 keV, 0.0025 for the edge between 5.4527-5.5127 keV, and 0.009 keV for the post edge between

5.5127-5.88579 keV). The Athena program was used to average the three scans of each sample, fit pre- and post-edge backgrounds, and obtain the normalized EXAFS signal as a function of the wavevector *k*. Fourier transforms into direct space were performed using the range $2.0 \leq k \leq 8.2$ with no window and with a *k*-weight of 2. Linear combination fits using the spectra of the La_2O_3, $LaAlO_3$, and La-doped Al_2O_3 standards were generated in the Athena program using the EXAFS (chi) signal in *k*-space in the range $2.03 \leq k \leq 6.665$ with a *k*-weight of 2. Weights in the linear combinations were constrained to sum to 1.

8.3 Results and Discussion

Based on previous reports of the La dopant location, at least four possible scenarios (illustrated in Figure 8.1) can be envisioned for the location of the La dopant in our La-doped Al_2O_3: the La could be (1) intercalating into the alumina lattice by substituting for some of the octahedrally-coordinated Al atoms, (2) forming La_2O_3 or $LaAlO_3$ nanoparticles completely separate from the γ-Al_2O_3 nanoparticles, (3) forming a protective shell of La_2O_3 or $LaAlO_3$ around the γ-Al_2O_3 nanoparticles, or (4) residing as singly-adsorbed atoms on the γ-Al_2O_3 surface.

To test these scenarios, we attempted to model them against the experimental PDF data

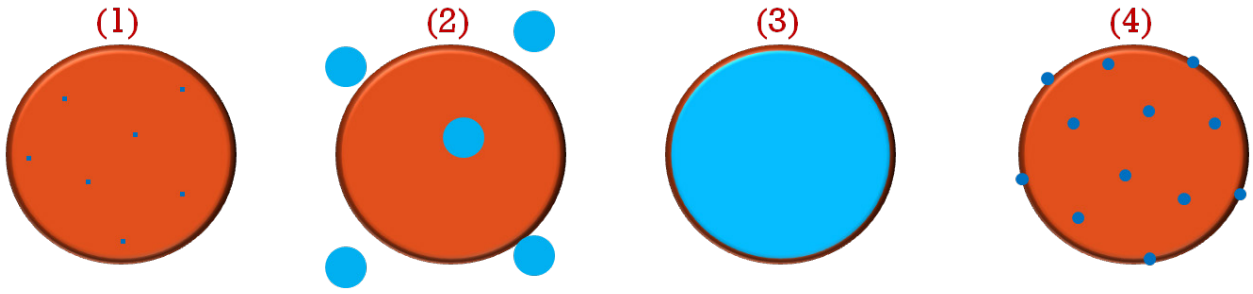

Figure 8.1 Four possible La dopant locations: (1) substitutionally doped inside the Al_2O_3 lattice, (2) separate particles of La_2O_3 or $LaAlO_3$, (3) layers of La_2O_3 or $LaAlO_3$ on the Al_2O_3 surface, or (4) singly adsorbed atoms on the Al_2O_3 surface.

for the 950°C sample. To model the second and third scenarios, separate La_2O_3 and $LaAlO_3$ phases[19-20] were combined with the γ-Al_2O_3 phase in multiphase refinements. The La_2O_3 phase fraction refined to a negative and therefore unphysical value. The $LaAlO_3$ phase fraction remained positive, but was very close to zero (0.2%) and did not visually improve the fit over the pure γ-Al_2O_3 phase. Additionally, rough calculations indicate that 3% dopant levels do not provide enough La to cover the available surface area (measured by BET analysis) with even a single layer, one unit cell thick, of either La_2O_3 or $LaAlO_3$. Indeed, previous studies have found that La atoms do not even cluster until the dopant level is increased past 3 wt%,[12] with a separate $LaAlO_3$ phase not observed until dopant levels of at least 5%.[11] Thus, it seems unlikely that separate particles or surface layers of La_2O_3 or $LaAlO_3$ are forming.

To model the first scenario, partial occupancies of La atoms were substituted into the 8c and 8d octahedrally-coordinated Al sites. Like the La_2O_3 phase fraction, the La atom occupancies in the 8c and 8d sites refined to negative and therefore unphysicalvalues. Additionally, the larger atomic radius of La should require longer La-O bond distances than the lattice positions in the γ-Al_2O_3 structure provide, as judged by the 2.37-2.82 Å La-O bond distances in the $LaAlO_3$ and La_2O_3 structures compared to the 1.8 Å Al-O bond distances in Al_2O_3. Thus, a lattice substitution would require significant distortions in the γ-Al_2O_3 lattice near the La dopant atoms, and such distortions are not reflected in the PDF data, which is modeled well by the pure γ-Al_2O_3 phase (Figure 8.2(a)). Thus, it seems unlikely that the La atoms substitute for Al atoms inside the alumina lattice.

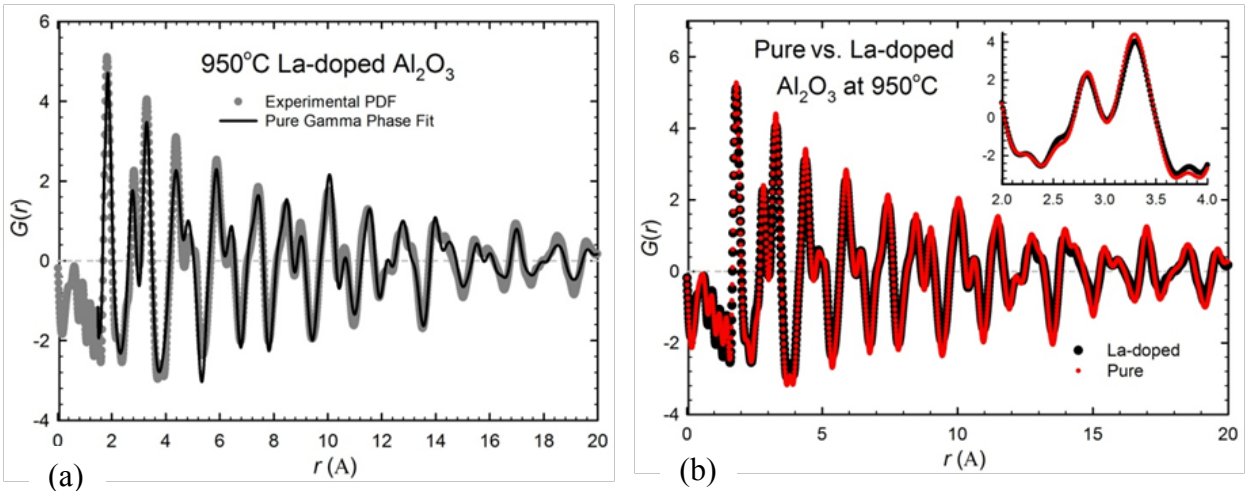

Figure 8.2 (a) PDF data for the La-doped Al_2O_3 sample calcined at 950°C fit using the pure γ-Al_2O_3 structrue and (b) comparison of the pure and La-doped Al_2O_3 at 950°C. The inset of (b) highlights the region where La-O bond distances should theoretically be.

For the remaining scenario in which the La atoms exist as singly adsorbed atoms on the γ-Al_2O_3 surface, the La-O bond distances should theoretically be represented in the PDF. Based on the $LaAlO_3$ and La_2O_3 structures, the La-O bond distance could range from 2.37-2.82 Å. Unfortunately, most of this range overlaps with the large Al_2O_3 peak at 2.8 Å, and even though the La-doped data display a slightly larger pre-edge shoulder at about 2.6 Å than the pure Al_2O_3 PDF (as shown in the inset of Figure 8.2(b)), the difference is not large enough to be conclusive; the PDFs of the La-doped Al_2O_3 and the pure Al_2O_3 are essentially identical within experimental uncertainty. Thus, despite the increased scattering strength of La over Al, the 3% La dopant concentration may be too small to be detectable by the PDF method, casting some uncertainty in the elimination of the other scenarios.

As the PDF results could not be definitive, we turned to EXAFS analysis to determine the La dopant location. The first noteworthy observation from the EXAFS analyses can be seen in Figure 8.3; all samples display a very large and sharp absorption peak that is characteristic of oxide materials. Hence, as we had anticipated in the PDF analyses, the La is bonded directly to oxygen atoms whatever its location may be.

The EXAFS data (Fourier transformed to direct-space) for all the La-doped Al_2O_3 samples are shown in Figure 8.4 where they are compared with the spectra of the La_2O_3, $LaAlO_3$, and impregnated La-doped Al_2O_3 samples. These data not only allow a closer examination of the scenarios given in Figure 8.1, they also provide insight into how the La environment changes as a function of temperature. Hence, the data is discussed below in order of increasing temperature.

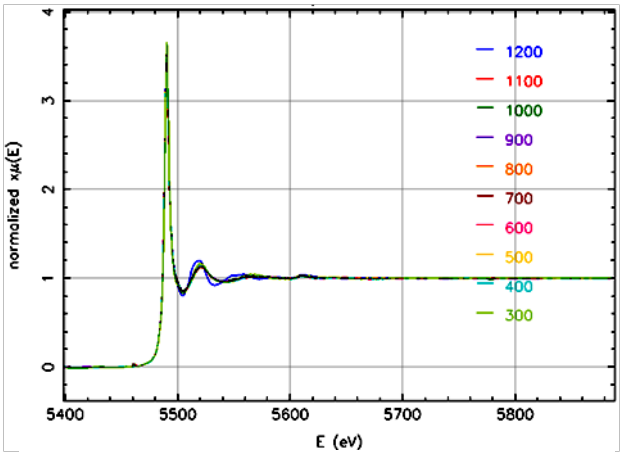

Figure 8.3 Normalized absorption data at the La L_{III}-edge for the La-doped Al_2O_3 samples.

As the first row of Figure 8.4 illustrates, the La environment of the 300°C La-doped Al_2O_3 sample matches neither La_2O_3 nor $LaAlO_3$ very closely but matches that of the impregnated La-Al_2O_3 sample (which was also calcined around 300°C) very well. Because the La dopant in the impregnated sample resides on the alumina surface (as our own XPS, or X-ray photoelectron spectroscopy, measurements have indicated), we can infer that our 3-hour, 1-pot doping method places the La on the Al_2O_3 surface in the same environment as the 3-day impregnation method. Thus, even though the La dopant is present while the alumina particles form, the La atoms do not substitute inside the Al_2O_3 lattice, and the first scenario in Figure 8.1 can be eliminated with more confidence.

At calcination temperatures between 400-1100°C (illustrated in the second row of Figure 8.4), the La environment remains fairly constant. The coordination shells of the La dopant beyond $R = 3$ Å still closely resemble those of the impregnated La-Al_2O_3 sample, but the first coordination shell ($1.5 < R < 3$) has changed shape slightly and gained a small shoulder around

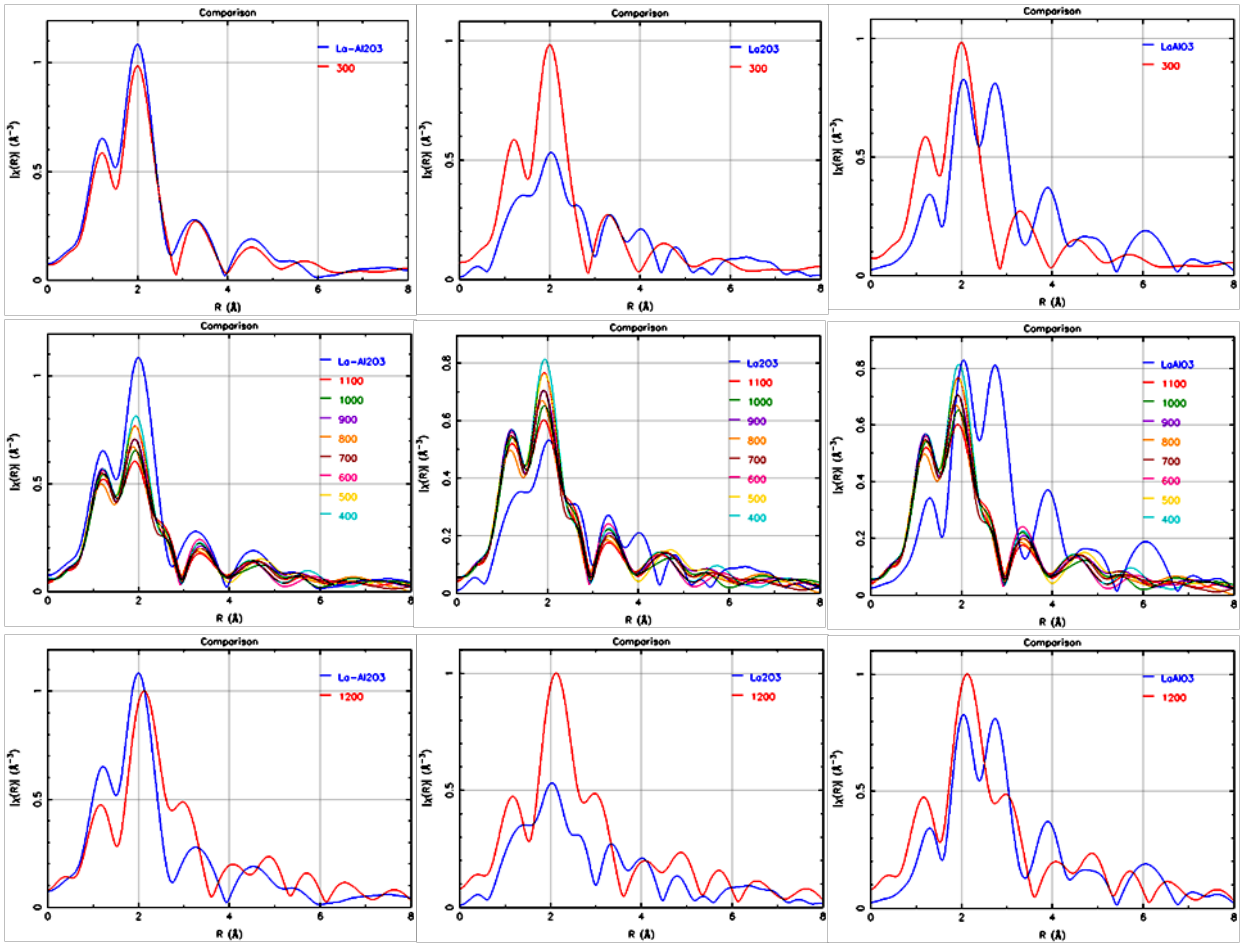

Figure 8.4 EXAFS data for the La-doped Al_2O_3 compared with the EXAFS data for La_2O_3, $LaAlO_3$, and impregnation-method La-Al_2O_3. The first, second, and third rows show, respectively, the 300°C sample (red), the 400-1100°C samples (multiple colors), and the 1200°C sample (red). The first, second, and third columns compare these samples to La_2O_3, $LaAlO_3$, and the impregnated La-doped Al_2O_3 samples in blue, respectively.

R = 2.5 Å, causing it to somewhat resemble La_2O_3. In fact, as Figure 8.5 illustrates, the first coordination shell increasingly becomes more like La_2O_3 as the calcination temperature increases, thereby lending some credence to the reports of La_2O_3 on γ-Al_2O_3.[21] A full La_2O_3 phase or layer is not formed, however, because the coordination beyond the first shell (R > 3 Å) does not resemble La_2O_3. Thus, at calcination temperatures between 300-1100°C, none of the doped samples (including the impregnation method sample) form an extended structure of La_2O_3 or $LaAlO_3$. Therefore, not only can we eliminate the second scenario in Figure 8.1 involving separate particles of these phases, we can also discount the prevalent hypothesis in the third

scenario in which surface layers of these phases form. We can hence deduce with reasonable confidence that the La dopant in our La-doped Al_2O_3 samples is adsorbed as single, isolated atoms on the Al_2O_3 surface in accordance with scenario #4 in Figure 8.1.

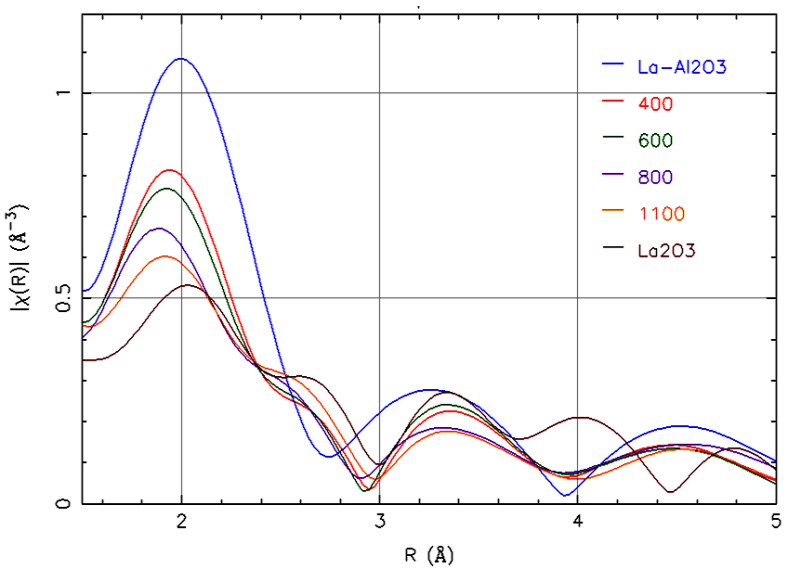

Figure 8.5 Comparison of the La_2O_3 and impregnated La-Al_2O_3 samples with our La-doped Al_2O_3 calcined at increasing temperatures between 400-1100°C, highlighting the increasing similarity between the first coordination shells ($1.5 < R < 3$) of La_2O_3 and our La-doped Al_2O_3 but also revealing that the shells beyond this still resemble the impregnated La-Al_2O_3 sample.

A drastic change in the La environment occurs at a calcination temperature of 1200°C, as shown in the third row of Figure 8.4. Here, the La environment no longer closely resembles any of the La_2O_3, $LaAlO_3$, or impregnated La-doped Al_2O_3 samples. This is the temperature at which the γ-Al_2O_3 has transformed to α-Al_2O_3. Thus, it seems that during the γ-to-α transition, the La environment changes to become unlike any stable lanthanum oxide compound.

To gain some insight into the nature of this new environment, we fit the data at 1200°C with linear combinations of the data from the La_2O_3, $LaAlO_3$, and impregnated La-doped Al_2O_3 samples. The best fit was obtained with a linear combination of the $LaAlO_3$ and impregnated La-Al_2O_3 samples. With the increasing similarity between La_2O_3 and the first coordination shell of the samples from 400-1100°C (Figure 8.5), the inclusion of $LaAlO_3$ and lack of La_2O_3 in the fit

at 1200°C was surprising, though it agrees with some previous reports in which the $LaAlO_3$ phase appeared at high temperatures.[22]

Table 8.1 Results of fits using La-Al_2O_3 alone or a linear combination of La-Al_2O_3, La_2O_3, and La-Al_2O_3.

		Linear Combinations				*La-Al_2O_3 alone*
	Phases	La-Al_2O_3 weight	La_2O_3 weight	$LaAlO_3$ weight	R-factor	R-factor
300	La-Al_2O_3	0.88	0.00	0.00	0.027	0.027
400	La-Al_2O_3 + La_2O_3	0.61	0.39	0.00	0.056	0.063
600	La-Al_2O_3 + La_2O_3	0.59	0.41	0.00	0.071	0.070
800	La-Al_2O_3 + La_2O_3 + $LaAlO_3$	0.51	0.48	0.01	0.121	0.089
1100	La-Al_2O_3 + La_2O_3 + $LaAlO_3$	0.45	0.50	0.05	0.123	0.116
1200	La-Al_2O_3 + $LaAlO_3$	0.54	0.00	0.46	0.385	0.463

Due to this surprising result, we also fit the data below 1200°C to linear combinations of the La_2O_3, $LaAlO_3$, and impregnated La-Al_2O_3 samples in order to better quantify the similarities of these phases to our La-Al_2O_3 samples. The results of some of these fits are given in Table 8.1 and are shown in Figure 8.6. Although the data from samples below 1200°C were generally fit best by the La-Al_2O_3 impregnated model alone, a fit nearly as good could be achieved by including an increasing amount of La_2O_3 between 400-1100°C, as may be expected from Figure 8.5. At temperatures above 800°C, a very small amount of $LaAlO_3$ was present in the best linear combination fits, and this amount increased with temperature. Close examination of the data suggests that $LaAlO_3$ is included at these temperatures because it best models the peak at $k = 5$ $Å^{-1}$ seen in the 1200°C data, which is only just beginning to appear above 800°C. Thus, as the alpha phase transition is approached and occurs, the La nearest-neighbor environment changes to become more like $LaAlO_3$ rather than La_2O_3. This suggests that the La is being enveloped inside the alumina lattice as the particles sinter.

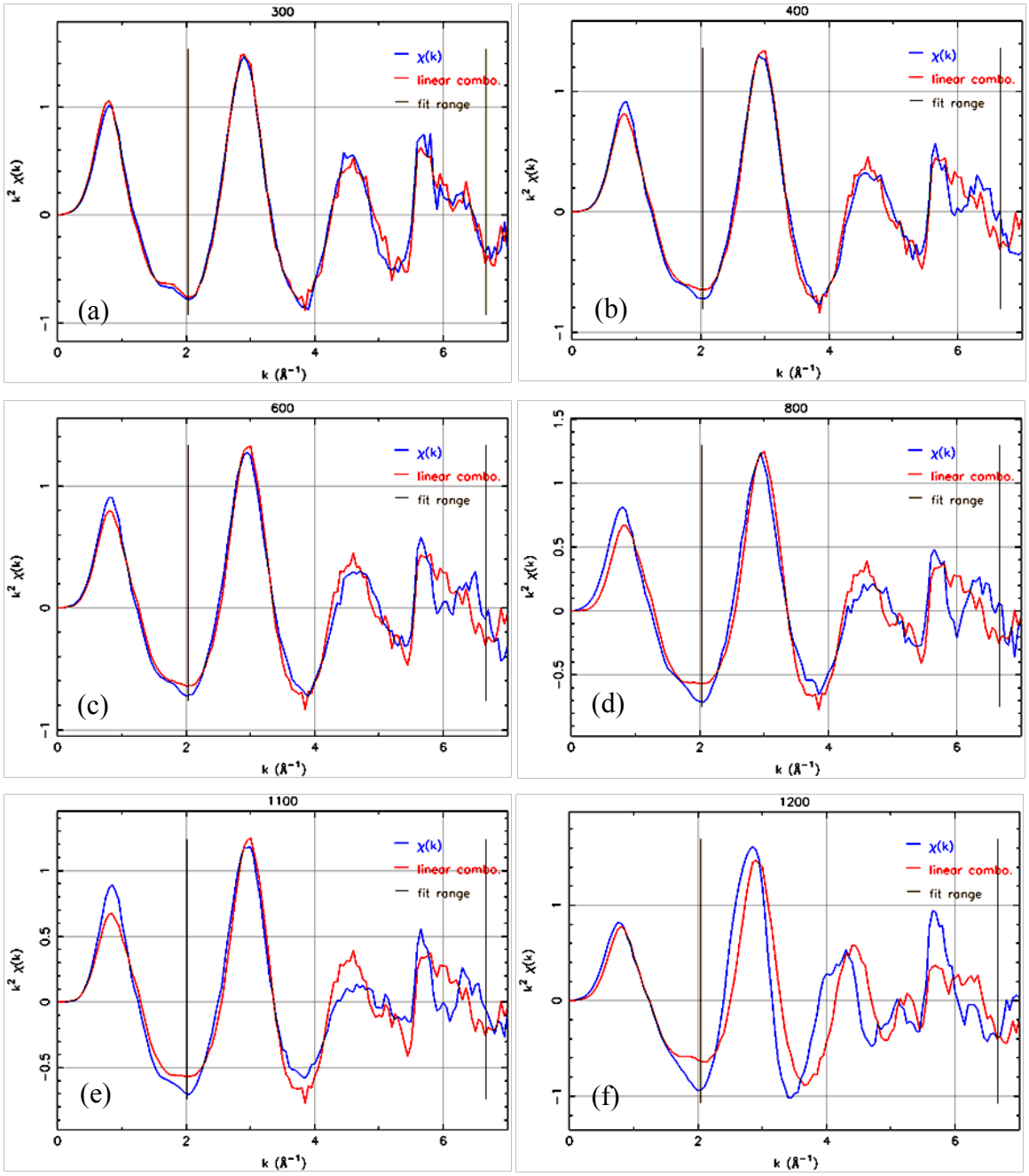

Figure 8.6 The best linear combination fits for the 300 (a), 400 (b), 600 (c), 800 (d), 1100 (e), and 1200 (f) samples whose specifications are given in Table 8.1. Note that a slight shift to lower *k* values would enable a combination of $LaAlO_3$ and La-Al_2O_3 to match the 1200°C data quite well, as opposed to lower temperatures at which a combination of La_2O_3 and La-Al_2O_3 match the data best.

8.4 Conclusions

In La-doped γ-Al_2O_3 samples produced by both the impregnation and 1-pot methods, the La dopant appears to adsorb as single, isolated atoms on the Al_2O_3 surface. The immediate oxygen coordination shell of the La is somewhat similar to that of La_2O_3 and becomes increasingly like La_2O_3 as calcination temperature increases from 300-1100°C, though an extended La_2O_3 lattice is not formed presumably due to the sparse (3%) concentration of La atoms. During the γ-to-α transition, the La environment undergoes a drastic change and becomes more like $LaAlO_3$ than La_2O_3, suggesting that the La is enveloped by the alumina lattice during the alpha phase transition even though an extended $LaAlO_3$ lattice is not formed. Hopefully this understanding of the location of the La will lead to a better understanding of its role in the stabilization of the γ-Al_2O_3.

References

1. Schaper, H.; Doesburg, E. B. M.; Van Reijen, L. L., The influence of lanthanum oxide on the thermal stability of gamma alumina catalyst supports. *Appl. Catal.* **1983,** *7* (2), 211-20.
2. Beguin, B.; Garbowski, E.; Primet, M., Stabilization of alumina by addition of lanthanum. *Appl. Catal.* **1991,** *75* (1), 119-32.
3. Kumar, K. N. P.; Tranto, J.; Kumar, J.; Engell, J. E., Pore-structure stability and phase transformation in pure and M-doped (M = La, Ce, Nd, Gd, Cu, Fe) alumina membranes and catalyst supports. *Journal of Materials Science Letters* **1996,** *15* (3), 266-70.
4. Oudet, F.; Courtine, P.; Vejux, A., Thermal stabilization of transition alumina by structural coherence with lanthanide aluminum oxide (LnAlO3, Ln = lanthanum, praseodymium, neodymium). *J. Catal.* **1988,** *114* (1), 112-20.
5. Wang, S.; Borisevich, A. Y.; Rashkeev, S. N.; Glazoff, M. V.; Sohlberg, K.; Pennycook, S. J.; Pantelides, S. T., Dopants adsorbed as single atoms prevent degradation of catalysts. *Nature Materials* **2004,** *3* (3), 143-146.
6. Yamamoto, T.; Tanaka, T.; Matsuyama, T.; Funabiki, T.; Yoshida, S., Structural analysis of La/Al2O3 catalysts by La K-edge XAFS. *J. Synchrotron Radiat.* **2001,** *8* (2), 634-636.
7. Vazquez, A.; Lopez, T.; Gomez, R.; Bokhimi; Morales, A.; Novaro, O., X-ray diffraction, FTIR, and NMR characterization of sol-gel alumina doped with lanthanum and cerium. *Journal of Solid State Chemistry* **1997,** *128* (2), 161-168.

8. Van Dillen, A. J.; Terorde, R. J. A. M.; Lensveld, D. J.; Geus, J. W.; De Jong, K. P., Synthesis of supported catalysts by impregnation and drying using aqueous chelated metal complexes. *J. Catal.* **2003,** *216* (1-2), 257-264.
9. Boukha, Z.; Fitian, L.; Lopez-Haro, M.; Mora, M.; Ruiz, J. R.; Jimenez-Sanchidrian, C.; Blanco, G.; Calvino, J. J.; Cifredo, G. A.; Trasobares, S.; Bernal, S., Influence of the calcination temperature on the nano-structural properties, surface basicity, and catalytic behavior of alumina-supported lanthana samples. *J. Catal.* **2010,** *272* (1), 121-130.
10. Borisevich, A. Y.; Pennycook, S. J.; Rashkeev, S. N.; Pantelides, S. T., Studies of Single Dopant Atoms on Nanocrystalline gamma-Alumina Supports by Aberration-Corrected Z-contrast STEM and First Principles Calculations *Microsc. Microanal.* **2003,** *9* (2), 398-399.
11. Nishio, Y.; Ozawa, M., Formation of featured nano-structure in thermal stable La-doped alumina composite catalyst. *Journal of Alloys and Compounds* **2009,** *488* (2), 546-549.
12. Yamamoto, T.; Hatsui, T.; Matsuyama, T.; Tanaka, T.; Funabiki, T., Structures and Acid-Base Properties of La/Al2O3 - Role of La Addition to Enhance Thermal Stability of gamma -Al2O3. *Chem. Mater.* **2003,** *15* (25), 4830-4840.
13. Cho, J.; Wang, C. M.; Chan, H. M.; Rickman, J. M.; Harmer, M. P., Improved tensile creep properties of yttrium- and lanthanum-doped alumina: a solid solution effect. *J. Mater. Res.* **2001,** *16* (2), 425-429.
14. Rutt, U.; Beno, M. A.; Strempfer, J.; Jennings, G.; Kurtz, C.; Montano, P. A., Diffractometer for high energy X-rays at the APS. *Nuclear Instruments & Methods in Physics Research, Section A: Accelerators, Spectrometers, Detectors, and Associated Equipment* **2001,** *467-468* (Pt. 2), 1026-1029.
15. "Fit2D" V. 9.129 Reference Manual V. 3.1.
16. Qiu, X.; Thompson, J. W.; Billinge, S. J. L., PDFgetX2: a GUI-driven program to obtain the pair distribution function from X-ray powder diffraction data. *J. Appl. Crystallogr.* **2004,** *37* (4), 678.
17. Egami, T. B., S. J. L., *Underneath the Bragg Peaks: Structural Analysis of Complex Materials*. First ed.; Pergamon: Kidlington, Oxford, UK, 2003; Vol. 7, p 404.
18. Farrow, C. L.; Juhas, P.; Liu, J. W.; Bryndin, D.; Bozin, E. S.; Bloch, J.; Proffen, T.; Billinge, S. J. L., PDFfit2 and PDFgui: computer programs for studying nanostructure in crystals. *J. Phys.: Condens. Matter* **2007,** *19* (33), 335219/1-335219/7.
19. Aldebert, P.; Traverse, J. P., Neutron diffraction study of the high temperature structures of lanthanum oxide and neodymium oxide. *Materials Research Bulletin* **1979,** *14* (3), 303-23.
20. Howard, C. J.; Kennedy, B. J.; Chakoumakos, B. C., Neutron powder diffraction study of rhombohedral rare-earth aluminates and the rhombohedral to cubic phase transition. *Journal of Physics: Condensed Matter* **2000,** *12* (4), 349-365.
21. Lin, Y. S.; De Vries, K. J.; Burggraaf, A. J., Thermal stability and its improvement of the alumina membrane top-layers prepared by sol-gel methods. *Journal of Materials Science* **1991,** *26* (3), 715-20.
22. Church, J. S.; Cant, N. W.; Trimm, D. L., Stabilization of aluminas by rare earth and alkaline earth ions. *Appl. Catal., A* **1993,** *101* (1), 105-16.

Chapter 9

New Insights into the Stabilizing Effect of the La in La- doped γ-Al_2O_3

9.1 Introduction

As Chapter 8 demonstrated, doping Al_2O_3 with a few weight percent La^{3+} stabilizes the γ-Al_2O_3 phase, delaying the transition to the alpha phase and the accompanying loss of surface area by ≥100°C. Yet despite its widespread use, a consensus on the mechanism by which the La dopant accomplishes this stabilization remains elusive.

Part of the uncertainty is in the γ→α phase transformation mechanism itself. During this transformation, the cubic (fcc) lattice of O^{2-} in γ-Al_2O_3 must transform to the hexagonal (hcp) lattice of α-Al_2O_3 with the simultaneous rearrangement of the Al^{3+} sites. Several mechanisms for this process have been suggested over the years,[xxiv] and a few, albeit outdated, summaries are available.[1-3] In early studies based on the analogous γ→α transition in Fe_2O_3, a diffusionless cooperative movement of atoms was suggested (termed synchro-shear) consisting of a shearing motion of the close-packed oxygen layers with a synchronized short-range movement of cations.[4] A combination of this synchro-shear process with diffusion and sintering was then suggested[2] before the synchro-shear mechanism was abandoned in favor of diffusion-based nucleation and growth mechanisms. Both volume diffusion[5] and surface diffusion have been

[xxiv] Most of these studies have been in relation to the θ→α transition, but as Chapter 6 revealed, the γ and θ phases are similar enough that the mechanisms of their transitions to the α phase should be quite similar.

suggested, but the prevailing hypothesis today seems to be that surface diffusion occurring at the high temperatures (≥1000°C) of the transformation leads to sintering of the crystallites, enabling the alpha phase to nucleate in the neck formations between crystallites.[1,3,6-10] Most theories regarding La stabilization are thus centered on how the La prevents or inhibits surface diffusion.

To specify how the La dopant inhibits surface diffusion, the location and form of the dopant must be identified. Herein lies the primary source of the differing theories, for while it is generally agreed that the La dopant resides on the alumina surface,[10-17] the form of the La dopant on the surface has been much debated. Some suggest that the ionic diffusion is hindered by the presence of La_2O_3 on the Al_2O_3 surface,[18] whereas others attribute the stabilization to surface layers or microdomains of $LaAlO_3$.[9,13,16,19] However, as Chapter 8 indicated, at the relatively low La dopant concentrations typically employed, most recent studies including our own have found that the La atoms on the γ-Al_2O_3 surface are highly dispersed and follow no apparent pattern of distribution, suggesting that the dopant atoms are effectively isolated from one another.[14-15,17,20-21] Indeed, several studies have shown that clustering of the La atoms on the surface is energetically unfavorable.[14-15]

Understanding how a few isolated, adsorbed atoms can prevent sintering and the phase transformation of an entire nanocrystal has been the subject of several recent studies.[14-17,20-22] In one of the emerging theories, the addition of La converts strong Lewis acid sites on the γ-Al_2O_3 surface (which are suspected to be the source of nucleation) to medium-strength Lewis acid sites which are less reactive and thus enhance thermal stability.[17] Recent ^{27}Al-NMR studies have suggested that these reactive Lewis acid sites may be pentacoordinated aluminum atoms present on the surface of γ-Al_2O_3 and that the role of the La dopant is to convert these 5-coordinated aluminum ions into 6-coordinated ones.[20,23-24] Support for this theory has come from another

recent NMR study in which the alpha transition occurred after mechanical stress induced the formation of an unusually high number of pentacoordinated surface sites.[24] Somewhat also in agreement, first principle calculations performed by Wang *et al.* showed that a pentacoordinated Al atom adjacent to a La atom on the γ-Al_2O_3 surface will be displaced into sub-surface tetrahedral vacancies, thereby relaxing the alumina structure into a lower energy and therefore stabilized state.[15]

To investigate the role of pentacoordinated Al sites in the stabilization mechanism of the La dopant, we have conducted our own ^{27}Al -NMR studies on both pure and La-doped Al_2O_3 synthesized via the solvent deficient method. With these analyses, we have combined BET analyses and the results from several of our previous studies including the PDF studies in Chapters 5 and 7, the symmetry analyses in Chapter 6, and the EXAFS analyses in Chapter 8 to provide some new insight into the mechanism by which the La dopant may stabilize γ-Al_2O_3.

9.2 Experimental Methods

The same Al_2O_3 and La-doped Al_2O_3 samples studied in Chapter 5 and Chapter 7, respectively, were used in these studies. Al^{27} MAS NMR data were collected for a La-doped Al_2O_3 calcined at 700°C and for pure Al_2O_3 samples calcined at 500, 700, 900, 1000, and 1100°C (the same data presented in Chapter 5). The data were collected on a 800 MHz (18.8 T) Varian dual solids/liquids NMR spectrometer operating at a ^{27}Al frequency of 104.16 MHz. The samples were spun in 1.6mm zirconia rotors at 35 kHz MAS to avoid overlap between the central transition and the first order spinning sidebands. 2048 scans were collected using a 310 ns (pi/12) pulse for non-selective excitation along with a 1s recycle delay.[25] All spectra were collected under identical conditions and externally referenced to a 1M aluminum chloride

solution. The ratios of the various Al coordination environments were quantified by fitting under their respective resonances.

Brunauer-Emmett-Teller (BET) specific surface areas for all Al_2O_3 and La-doped Al_2O_3 samples studied in Chapter 5 and Chapter 7 were determined from N_2 adsorption at 77 K using a Micromeritics TriStar II instrument. Approximately 300 mg of each sample were degassed at 200°C for 12-24 hours and then allowed to cool to room temperature prior to data collection.

9.3 Results and Discussion

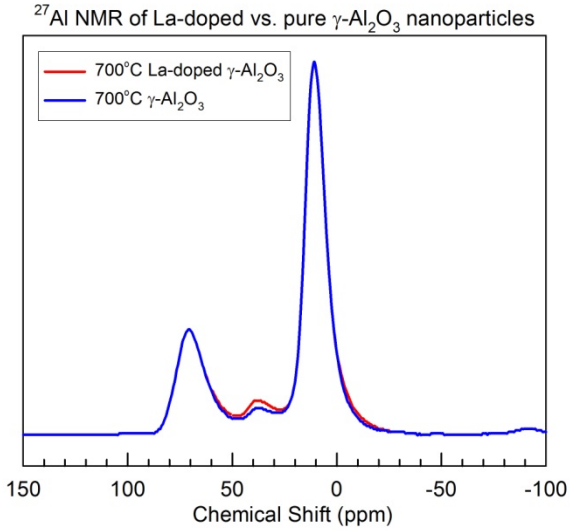

Figure 9.1 ^{27}Al-NMR data for both pure (blue) and La-doped (red) γ-Al_2O_3 synthesized via the solvent deficient method.

Table 9.1 Estimated fractions of 4-, 5-, and 6-coordinatd Al sites calculated from the ^{27}Al-NMR data of both pure and La-doped γ-Al_2O_3 synthesized via the solvent efficient method and calcined at the given temperature.

	4-coord. Al	5-coord. Al	6-coord. Al
500°C Al_2O_3	20 %	5.2 %	75 %
700°C Al_2O_3	**27 %**	**6.4 %**	**67 %**
700°C La-doped Al_2O_3	**26 %**	**8.1 %**	**66 %**
900°C Al_2O_3	31 %	2.7 %	66 %
1000°C Al_2O_3	30 %	2.0 %	68 %
1100°C Al_2O_3	0	0	100 %

NMR data for our pure and La-doped γ-Al_2O_3 samples are shown in Figure 9.1. Typical ^{27}Al MAS NMR chemical-shift ranges for oxygen-bound Al^{3+} atoms are –10 to 20 ppm for octahedrally coordinated aluminum, 30 to 40 ppm for pentahedrally coordinated aluminum, and 50 to 80 ppm for tetrahedrally coordinated aluminum.[26-28] Based on these shifts, we can assign the peak at 10 ppm to 6-coordinated Al, the peak at 40 ppm to 5-coordinated Al, and the peak at 70 ppm to 4-coordianted Al. Using the integrated areas for each of these peaks, we have

estimated the relative numbers of 4-, 5-, and 6-coordinated Al sites for both pure γ-Al_2O_3 and La-doped γ-Al_2O_3 to be those given in Table 9.1. As the table reveals, the La-doped sample displays a slight *increase* in pentacoordinated sites relative to the pure γ-Al_2O_3 sample.

This result contrasts the study by Kwak *et al.* in which the La-doped sample displayed 50% fewer pentacoordinated sites than the pure γ-Al_2O_3 sample,[20] with a Ba-doped sample displaying an even lower pentacoordinated ratio.[23] One possible reason for the discrepancy is that the solvent deficient synthetic process may not allow sufficient time or mobility for the La to preferentially seek out and bind to the pentacoordinated sites. Perhaps at higher temperatures than 700°C the La may gain enough mobility to migrate to the pentacoordinated sites and convert these sites to 4- or 6-coordinated sites as previously suggested. To know for certain, we will need to perform ^{27}Al-NMR experiments on our La-doped γ-Al_2O_3 samples calcined at temperatures approaching the alpha phase transition.

However, our EXAFS data do not reveal any drastic changes in the La environment between 400-1100°C to suggest such a rearrangement (Figure 8.4). Additionally, the number of pentacoordinated sites in the ^{27}Al-NMR data for our pure γ-Al_2O_3 begins decreasing long before the transition to the alpha phase (Table 9.1), casting more uncertainty on the role of 5-coordinated Al in alpha phase nucleation. Our current data thus prompts us to consider alternate stabilization mechanisms.

Based on the observation that cations which are larger than Al^{3+} tend to exhibit a stabilizing effect on γ-Al_2O_3, some have suggested that it is simply the large ionic size of La that hinders ionic diffusion at the surface.[1,8] Wang *et al*. put forth an attractive theory in line with this reasoning .[15] They performed first principles calculations which showed it is energetically unfavorable for a La atom to be trapped inside the γ-Al_2O_3 structure. Indeed, if placed within the

first few layers near the surface, the La atom will relax up to the γ-Al_2O_3 surface (a result that is perhaps not surprising considering the large ionic size difference between Al^{3+} and La^{3+}). An additional component of their calculations showed that the La binding energy is much stronger on the γ-Al_2O_3 surface than on the α-Al_2O_3 surface, which they conjectured would increase the enthalpy of α-Al_2O_3 relative to γ-Al_2O_3. Combining these calculations with the results of their EXAFS and TEM analyses, Wang *et al*. asserted that the La dopant eschews the bulk and resides as isolated, strongly adsorbed atoms on the γ-Al_2O_3 surface, pinning the γ-Al_2O_3 surface in place and impeding sintering (and thus alpha phase nucleation) in order to avoid being trapped inside the γ-Al_2O_3 structure or on the α-Al_2O_3 surface.

Our EXAFS analyses support and perhaps explain these observations. As Figure 8.4 shows, the first two coordination shells involving La-O bonds are quite similar to those of La_2O_3 as long as the alumina remains in the γ-Al_2O_3 phase (between 400-1100°C for our particles); but after the alpha phase transition (1200°C), the La bonding environment does not closely resemble any other stable compound. Thus, the stronger binding energy of La on the γ-Al_2O_3 surface is likely due to the more favorable and familiar La_2O_3-like bonding environment provided by the γ-Al_2O_3 surface.[xxv]

Similarly, the resistance of the La to being enveloped inside the alumina lattice is evidenced in our analyses. As Table 8.1 shows, the best linear combination fit to our EXAFS data prior to the alpha phase transition (T < 1200°C) was by the La-Al_2O_3 impregnated sample alone, wherein the La resides on the surface (though with increasingly La_2O_3-like oxygen coordination). But after the transition, the La environment is fit best by a combination of the

[xxv] Corroborating this interpretation, the study by Bye and Simpkin on the effects of Cr doping broached a similar theory that the preference of the Cr for the tetrahedral binding provided by the γ-Al_2O_3 lattice delayed the transition to the alpha phase.[2]

impregnated sample's surface environment and a $LaAlO_3$ environment (see Table 8.1 and Figure 8.6). The $LaAlO_3$ contribution suggests that part of the La is enveloped inside the alumina lattice—an energetically unfavorable position if the results obtained by Wang *et al*. apply to α as well as γ alumina.[xxvi]

However, if resistance of the La to being caught insight the γ-Al_2O_3 lattice is the only factor at play, the La dopant should presumably suppress diffusion and sintering at all temperatures to avoid being caught inside the γ-Al_2O_3 lattice. BET data do not show this. As seen in Figure 9.2, both pure and La-doped γ-Al_2O_3 experience the same roughly linear reduction in surface area at temperatures below ~950°C, as many others have also noted.[1-2,9-10,20] Thus, some other essential piece of understanding is still missing.

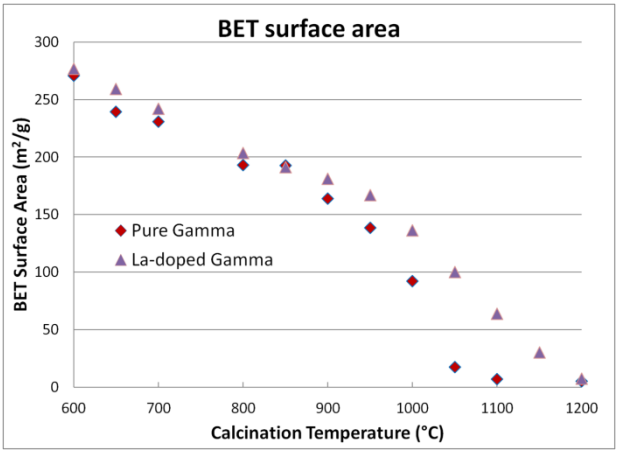

Figure 9.2 BET surface area of both pure and La-doped Al_2O_3 synthesized via the solvent deficient method and calcined at the given temperatures for 2 hours.

A closer look at Figure 9.2 reveals some interesting trends. Even though the La dopant does not inhibit the decrease in surface area before the transition (T ≤ 950°C), the La dopant does slow the drop in surface area *during* the γ→α phase transition; as Figure 9.2 highlights, at T ≥

[xxvi] If ionic size is the reason that La atoms avoid being caught inside the γ-Al_2O_3 structure, the denser α-Al_2O_3 structure should likewise provide an energetically unfavorable environment.

950°C the decrease is delayed first by 50°C and then by 100°C at T ≥ 1050°C. Additionally, there is actually a noticeable inflection or change in the slope of the surface area curve (in both pure and La-doped Al_2O_3) as the alpha phase transition begins at T ~ 950°C, indicating a change in the sintering phenomenon.

The missing piece of information seems to be this: the sintering prior to the alpha phase transition must be fundamentally different from the sintering during the transition. Understanding how they differ may be the key to fully elucidating the La stabilization mechanism.

Some have cited the formation of the δ and/or θ phases as the cause of the drop in surface area prior to the transition,[2] but these phases are not always observed (as in our Al_2O_3 samples).[xxvii] The continual decrease in surface area prior to the alpha transition is perhaps better explained using the defect model developed in Chapter 5. In this model, the oxygen sublattice of γ-Al_2O_3 is riddled with boehmite-like defects (both within the nanoparticles and possibly at their interfaces) remaining from the boehmite→γ phase transition. The defects heal as temperatures increase through 900°C (see the PDF results in Figure 5.17), causing the crystallites to sinter internally, the coherent domain size apparent in PDF data to increase (Figure 5.8a), and the area accessible to gaseous adsorbents to decrease (Figure 9.2). We thus hypothesize that sintering *prior to* the alpha phase transition is related to the healing of boehmite-like defects within the nanoparticles, which would occur for both pure and La-doped γ-Al_2O_3, as observed.

During the alpha phase transition, the loss of surface area is more likely related to the sintering between crystallites since the particle size is much larger in α-Al_2O_3 than γ-Al_2O_3 (see

[xxvii] Additionally, such phase changes merely require the redistribution of a few Al cations within the same oxygen lattice (as Chapter 6 revealed), which small amount of diffusion does not seem likely to be the cause of the substantial sintering observed.

Table 2.2). Because of this, many studies have hypothesized that the alpha phase nucleates in neck formations between particles and that the La dopant inhibits the phase transition by inhibiting sintering. However, the La dopant does not completely stop the sintering—it simply slows it, as shown by both Figure 9.2 and by our linear combination EXAFS fits which show an increasing amount of a $LaAlO_3$ environment as the alpha phase transition is approached (see the discussion in Chapter 8). The alpha phase should still be able to nucleate if sintering is its source, albeit at a slower rate. Yet, the La dopant completely inhibits the alpha phase from nucleating for a full 100°C, even though it does not completely inhibit the accelerated sintering above 950°C. There must be another factor at play besides the impedance of sintering.

We speculate that the transition mechanism suggested by our $\gamma \rightarrow \alpha$ symmetry mode distortion in Chapter 6 is realistic and that it reveals this other factor in addition to illuminating the true nature of the sintering *during* the alpha phase transition. In this mechanism, illustrated in Figure 6.24, the cubic (fcc) oxygen lattice within each γ-Al_2O_3 unit cell undergoes a substantial restructuring; oxygen atoms rotate ±30° around multiple axes internal to the unit cell, effectively rearranging each AlO_x polyhedron in order to form the hexagonal (hcp) oxygen lattice of α-Al_2O_3. This localized polyhedra restructuring is accompanied by the diffusion of ¼ of the atoms (both O and Al) to the surface of the nanoparticles as well as by a substantial contraction of what will become the rhombohedral *c*-axis lattice parameter. This suggests two modes of density increase: internal volume densification and inter-grain cavity filling. The sintering that would be induced by this pore-filling is likely the source of the extreme particle size increase and loss of surface area during the alpha phase transition. But according to this mechanism, sintering is only a secondary effect to the real source of alpha phase nucleation—the restructuring of the oxygen lattice.

We propose that the primary role of the La dopant is to obstruct the restructuring of the oxygen lattice. The strong La-O binding energy observed by Wang *et al*. on the γ-Al_2O_3 surface, which we attribute to the favorable La_2O_3-like environment it provides, pins the γ-Al_2O_3 oxygen lattice in place, increasing the energy required for its restructuring and thereby delaying the alpha phase transition by ~100°C. We concur with other studies that the La also causes a slight suppression or delay of the sintering associated with the transition, and our EXAFS analyses support the idea by Wang *et al*. that the resistance of the La to be caught inside the alumina lattice could be the responsible factor. But because sintering is not completely prevented in the manner that the phase transition is, the suppression of sintering cannot be the primary mechanism of γ-phase stabilization.

9.4 Conclusions

Combining our PDF, EXAFS, BET, and NMR analyses, we have provided new insight into the γ→α transition and the role of isolated, adsorbed La dopant atoms in inhibiting it. Our ^{27}Al MAS NMR analyses contradict the theory that the La dopant's primary role is to delay sintering by converting pentacoordinated Al on the surface (the supposed alpha nucleation sites) to lower energy sites. Our BET data confirm that sintering is slowed during the alpha phase transition, and our EXAFS analyses support the theory of Wang *et al*. that the La dopant resists sintering to avoid being caught inside the alumina structure and to maintain the energetically favorable La_2O_3-like environment provided by the γ-Al_2O_3 surface. However, the fact that the La dopant does not at all inhibit the loss of surface area prior to the alpha phase transition and that it only slows (not stops) the sintering above the normal transition temperature (even though the alpha phase nucleation is completely delayed by 100°C) casts doubt on the inhibition of sintering as the La dopant's primary mechanism of stabilization.

A closer examination of the BET data suggest that the loss of surface area *prior to* the alpha phase transition must be fundamentally different from the loss of surface area *during* the transition. According to our PDF analyses, the steady loss of surface area prior to the alpha phase transition ($T \leq 950°C$) could be related to the healing/sintering of boehmite-like defects within the nanoparticles. Then, if the topotactic $\gamma \rightarrow \alpha$ transition mechanism proposed by our symmetry-mode analyses is realistic, the alpha phase transition actually consists of a combination of volume diffusion and a local restructuring of the oxygen lattice, and the loss of surface area at $T \geq 950°C$ is a result of the sintering induced by the volume diffusion component.

This view of the $\gamma \rightarrow \alpha$ transition combined with the strong La-O binding energy on the γ-Al_2O_3 surface suggests that the primary role of the La dopant is to inhibit the restructuring of the oxygen lattice, which restructuring may be the real source of alpha phase 'nucleation.' If the inhibition of sintering is only a secondary mechanism or effect, this would explain why nucleation is completely delayed by 100°C while sintering is only slowed. Thus, we propose that the isolated, adsorbed La atoms stabilize the γ-Al_2O_3 phase primarily by pinning the oxygen lattice—and thus the entire γ-Al_2O_3 structure—in place.

References

1. Nortier, P.; Soustelle, M., Alumina carriers for automotive pollution control. *Stud. Surf. Sci. Catal.* **1987,** *30* (Catal. Automot. Pollut. Control), 275-300.
2. Bye, G. C.; Simpkin, G. T., Influence of chromium and iron on formation of α-alumina from γ-alumina. *J. Am. Ceram. Soc.* **1974,** *57* (8), 367-71.
3. Tucker, D. S.; Hren, J. J., The γ → α phase transformation in alumina. *Materials Research Society Symposium Proceedings* **1984,** *31* (Electron Microsc. Mater.), 337-44.
4. Kronberg, M. L., Plastic deformation of single crystals of sapphire: basal slip and twinning. *Acta Metall.* **1957,** *5*, 507-24.
5. Ridge, M. J.; Molony, B.; Boell, G. R., Transformation of finely divided cubic to trigonal iron(III) oxide. *Journal of the Chemical Society [Section] A: Inorganic, Physical, Theoretical* **1967,** (4), 594-7.
6. Badkar, P. A.; Bailey, J. E., The mechanism of simultaneous sintering and phase transformation in alumina. *J. Mater. Sci.* **1976,** *11* (10), 1794-806.

7. Saalfeld, H., The structures of gibbsite and of the intermediate products of its dehydration. *Neues Jahrbuch fuer Mineralogie, Abhandlungen* **1960,** *95*, 1-87.
8. Loong, C. K.; Richardson, J. W., Jr.; Ozawa, M., Structural phase transformations of rare-earth modified transition alumina to corundum. *Journal of Alloys and Compounds* **1997,** *250* (1-2), 356-359.
9. Schaper, H.; Doesburg, E. B. M.; De Korte, P. H. M.; Van Reijen, L. L., Thermal stabilization of high surface area alumina. *Solid State Ionics* **1985,** *16*, 261-5.
10. Schaper, H.; Doesburg, E. B. M.; Van Reijen, L. L., The influence of lanthanum oxide on the thermal stability of gamma alumina catalyst supports. *Appl. Catal.* **1983,** *7* (2), 211-20.
11. Van Dillen, A. J.; Terorde, R. J. A. M.; Lensveld, D. J.; Geus, J. W.; De Jong, K. P., Synthesis of supported catalysts by impregnation and drying using aqueous chelated metal complexes. *J. Catal.* **2003,** *216* (1-2), 257-264.
12. Boukha, Z.; Fitian, L.; Lopez-Haro, M.; Mora, M.; Ruiz, J. R.; Jimenez-Sanchidrian, C.; Blanco, G.; Calvino, J. J.; Cifredo, G. A.; Trasobares, S.; Bernal, S., Influence of the calcination temperature on the nano-structural properties, surface basicity, and catalytic behavior of alumina-supported lanthana samples. *J. Catal.* **2010,** *272* (1), 121-130.
13. Beguin, B.; Garbowski, E.; Primet, M., Stabilization of alumina by addition of lanthanum. *Appl. Catal.* **1991,** *75* (1), 119-32.
14. Borisevich, A. Y.; Pennycook, S. J.; Rashkeev, S. N.; Pantelides, S. T., Studies of Single Dopant Atoms on Nanocrystalline gamma-Alumina Supports by Aberration-Corrected Z-contrast STEM and First Principles Calculations *Microsc. Microanal.* **2003,** *9* (2), 398-399.
15. Wang, S.; Borisevich, A. Y.; Rashkeev, S. N.; Glazoff, M. V.; Sohlberg, K.; Pennycook, S. J.; Pantelides, S. T., Dopants adsorbed as single atoms prevent degradation of catalysts. *Nature Materials* **2004,** *3* (3), 143-146.
16. Nishio, Y.; Ozawa, M., Formation of featured nano-structure in thermal stable La-doped alumina composite catalyst. *Journal of Alloys and Compounds* **2009,** *488* (2), 546-549.
17. Yamamoto, T.; Hatsui, T.; Matsuyama, T.; Tanaka, T.; Funabiki, T., Structures and Acid-Base Properties of La/Al2O3 - Role of La Addition to Enhance Thermal Stability of gamma -Al2O3. *Chem. Mater.* **2003,** *15* (25), 4830-4840.
18. Lin, Y. S.; De Vries, K. J.; Burggraaf, A. J., Thermal stability and its improvement of the alumina membrane top-layers prepared by sol-gel methods. *Journal of Materials Science* **1991,** *26* (3), 715-20.
19. Oudet, F.; Courtine, P.; Vejux, A., Thermal stabilization of transition alumina by structural coherence with lanthanide aluminum oxide (LnAlO3, Ln = lanthanum, praseodymium, neodymium). *J. Catal.* **1988,** *114* (1), 112-20.
20. Kwak, J. H.; Hu, J.; Lukaski, A.; Kim, D. H.; Szanyi, J.; Peden, C. H. F., Role of Pentacoordinated Al3+ Ions in the High Temperature Phase Transformation of gamma -Al2O3. *Journal of Physical Chemistry C* **2008,** *112* (25), 9486-9492.
21. Cho, J.; Wang, C. M.; Chan, H. M.; Rickman, J. M.; Harmer, M. P., Improved tensile creep properties of yttrium- and lanthanum-doped alumina: a solid solution effect. *J. Mater. Res.* **2001,** *16* (2), 425-429.
22. Ozawa, Y.; Tochihara, Y.; Watanabe, A.; Nagai, M.; Omi, S., Stabilizing effect of Nd_2O_3, La_2O_3 and ZrO_2 on Pt.PdO/Al_2O_3 during catalytic combustion of methane. *Appl. Catal., A* **2004,** *258* (2), 261-267.

23. Kwak, J. H.; Hu, J. Z.; Kim, D. H.; Szanyi, J.; Peden, C. H. F., Penta-coordinated Al^{3+} ions as preferential nucleation sites for BaO on γ-Al_2O_3: an ultra-high-magnetic field ^{27}Al MAS NMR study. *J. Catal.* **2007,** *251* (1), 189-194.
24. Duevel, A.; Romanova, E.; Sharifi, M.; Freude, D.; Wark, M.; Heitjans, P.; Wilkening, M., Mechanically Induced Phase Transformation of γ-Al2O3 into α-Al2O3. Access to Structurally Disordered γ-Al2O3 with a Controllable Amount of Pentacoordinated Al Sites. *J. Phys. Chem. C* **2011,** *115* (46), 22770-22780.
25. Massiot, D.; Bessada, C.; Coutures, J. P.; Taulelle, F., A quantitative study of ^{27}Al MAS NMR in crystalline YAG. *Journal of Magnetic Resonance* **1990,** *90*, 231-242.
26. Perander, L. M.; Zujovic, Z. D.; Groutso, T.; Hyland, M. M.; Smith, M. E.; O'Dell, L. A.; Metson, J. B., Characterization of metallurgical-grade aluminas and their precursors by 27Al NMR and XRD. *Can. J. Chem.* **2007,** *85* (10), 889-897.
27. Slade, R. C. T.; Southern, J. C.; Thompson, I. M., Aluminum-27 nuclear magnetic resonance spectroscopy investigation of thermal transformation sequences of alumina hydrates. I. Gibbsite, gamma -Al(OH)3. *J. Mater. Chem.* **1991,** *1* (4), 563-8.
28. Smith, M. E., Application of aluminum-27 NMR techniques to structure determination in solids. *Applied Magnetic Resonance* **1993,** *4* (1-2), 1-64.

Appendices

Appendix A

Chapter 3 Supplemental Material

This section provides the experimental XRD data summarized in Table 3.1 along with the TG/DTA-MS data discussed in Section 3.3.2.

A.1 XRD Analyses of the Precursors

Figure A.1.1 XRD patterns/analyses of the dried (D), dried-rinsed-dried (DRD), and rinsed-dried (RD) precursors (where applicable) plotted with the ICDD standard patterns of the materials they contain. The identities and PDF reference numbers of the standard patterns are given in the legend of each graph.

	D precursors	DRD precursors	RD precursors
	Transition metal oxides		
Group 3: Y_2O_3	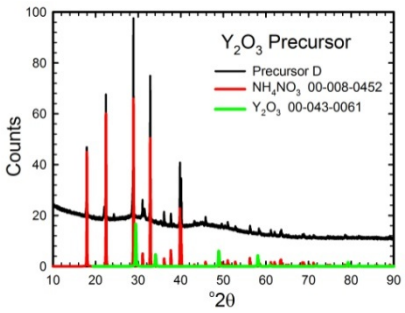	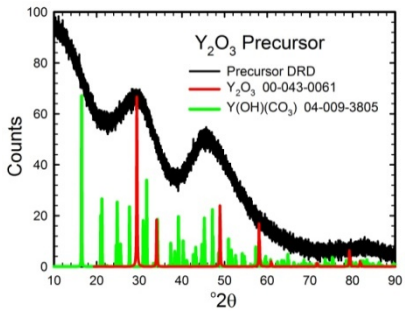	

Group 4: TiO_2

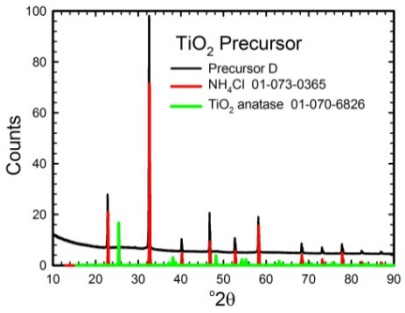

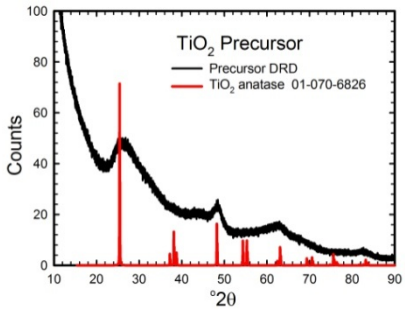

Group 4: ZrO_2

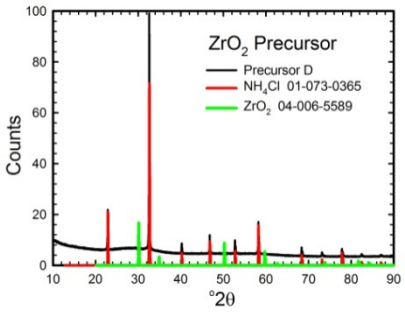

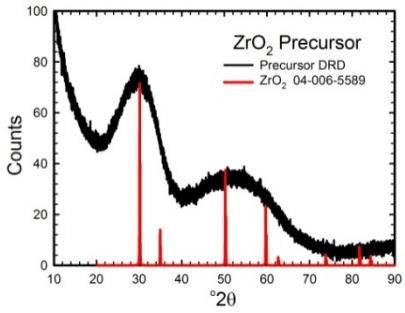

Group 6: MoO_3

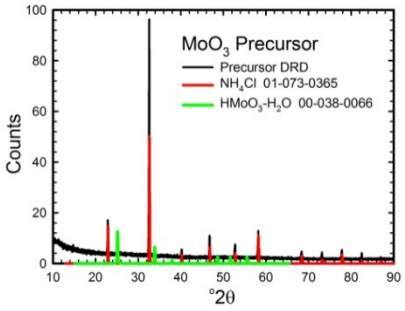

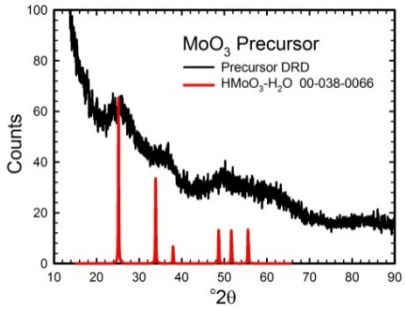

Group 7: Mn_2O_3

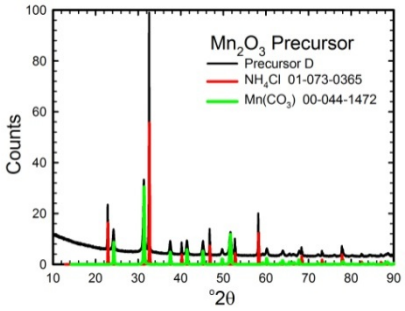

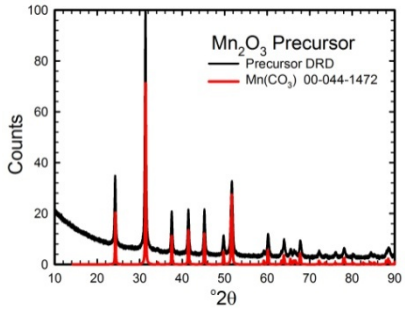

Group 8: Fe_2O_3

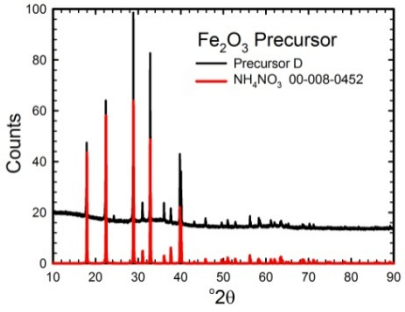

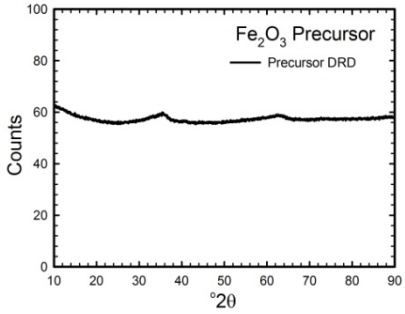

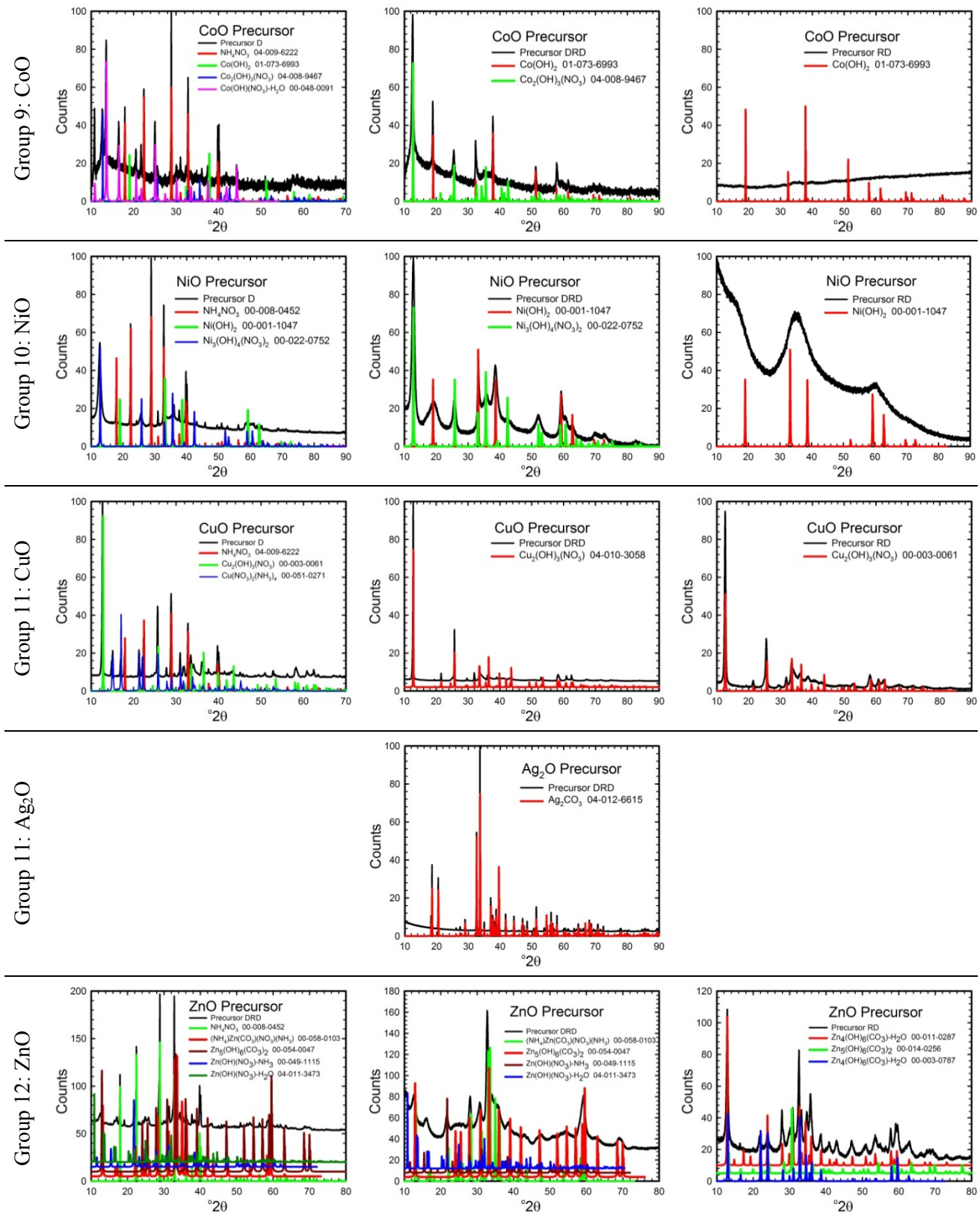

Semi-metal oxides

Group 13: Al_2O_3

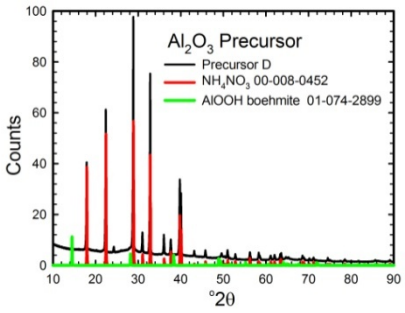

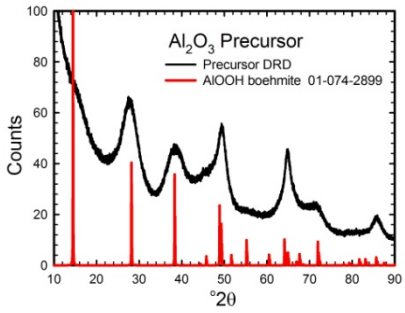

Group 13: In_2O_3

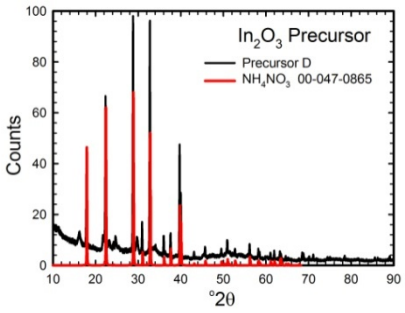

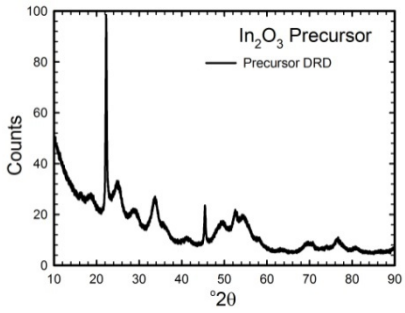

Group 14: SnO_2

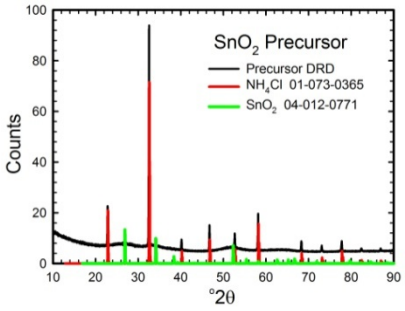

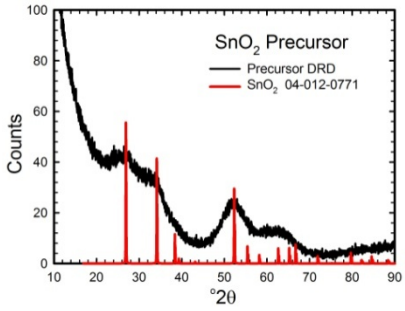

Group 15: Bi_2O_3

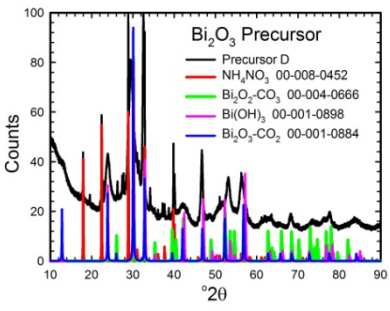

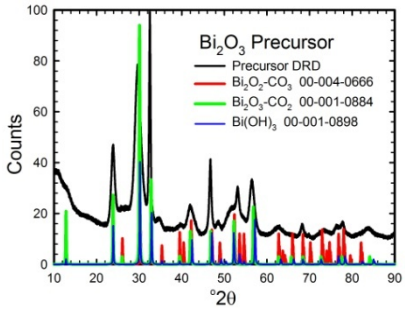

Lanthanide metal oxides

CeO_2

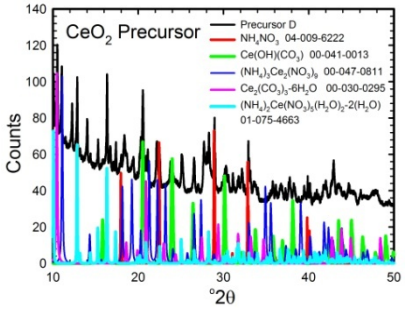

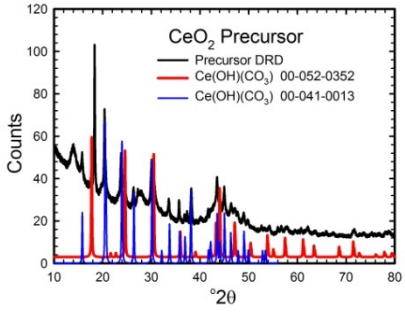

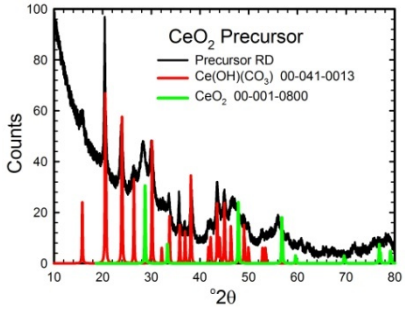

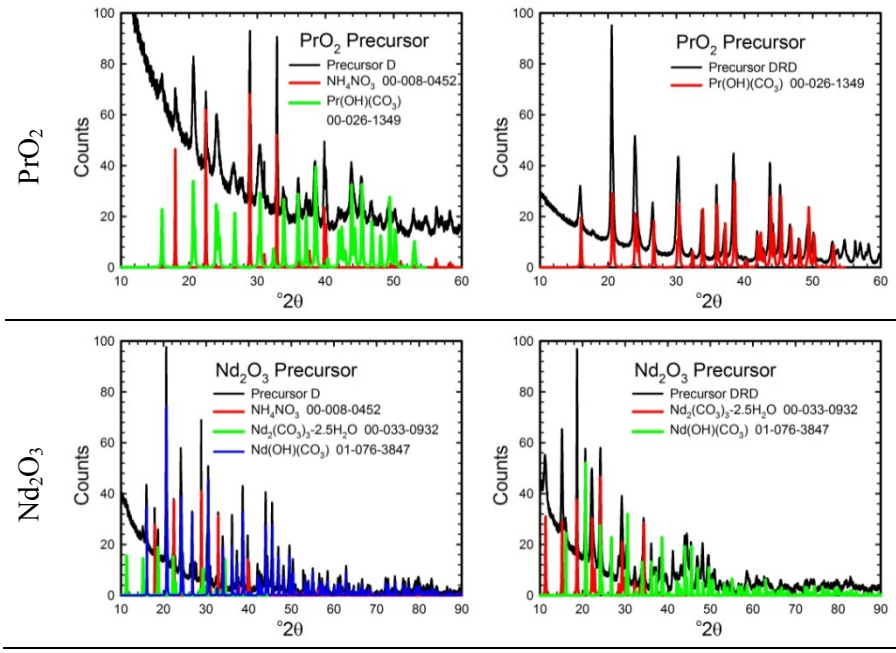

A.2 TG/DTA-MS Analyses of the Precursors

Figure A.2.1 TG/DTA-MS data for the dried (un-rinsed) precursors. Positive and negative DTA values correspond to exothermic and endothermic events, respectively.

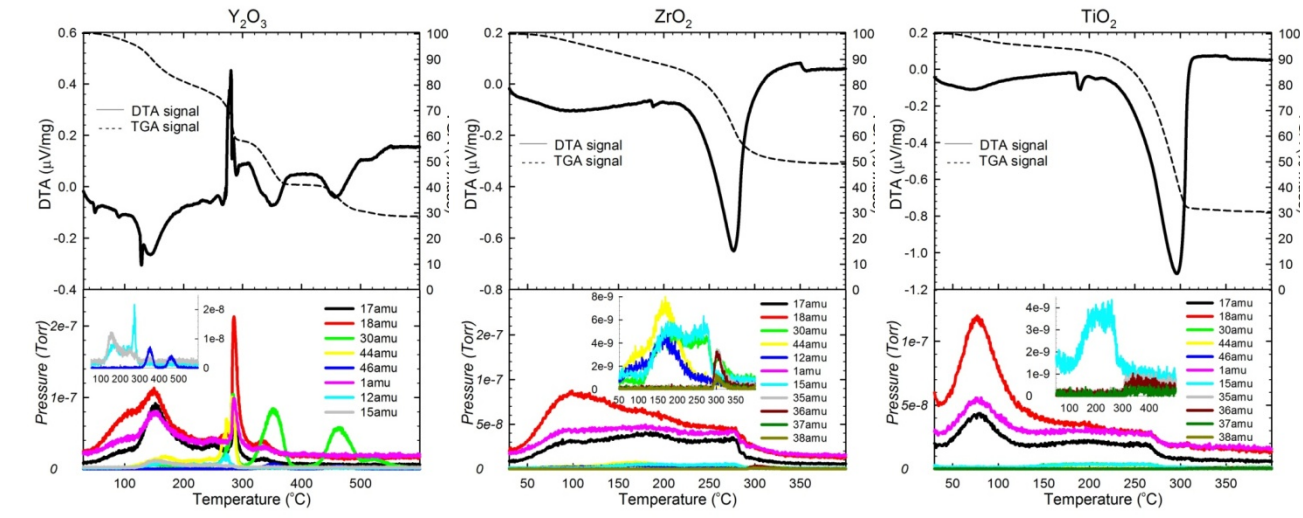

Group 6: MoO_3	Group 7: Mn_2O_3	Group 8: Fe_2O_3
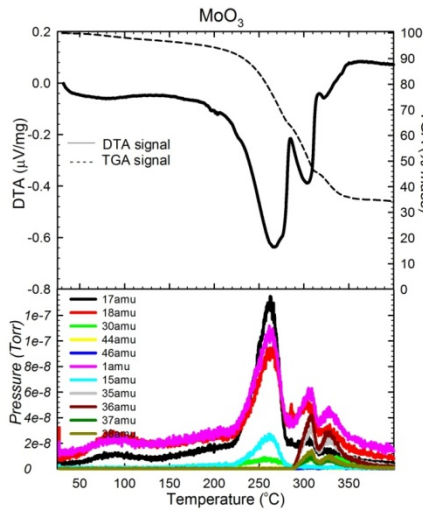	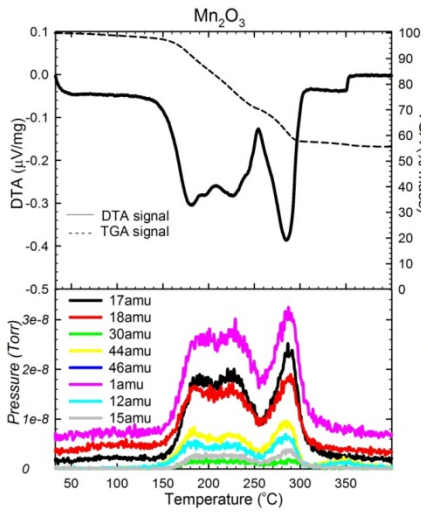	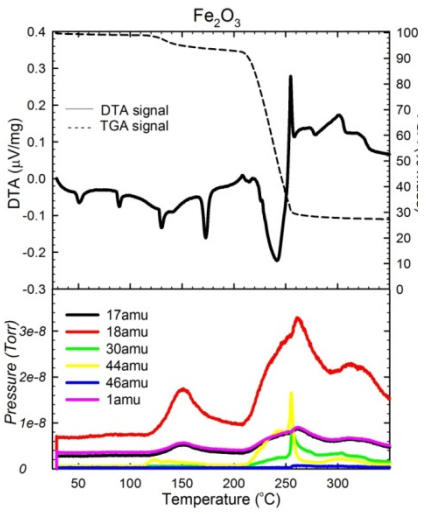
Group 9: CoO	Group 10: NiO	Group 11: CuO
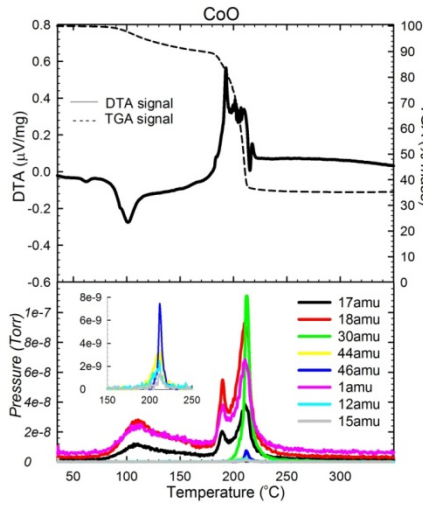	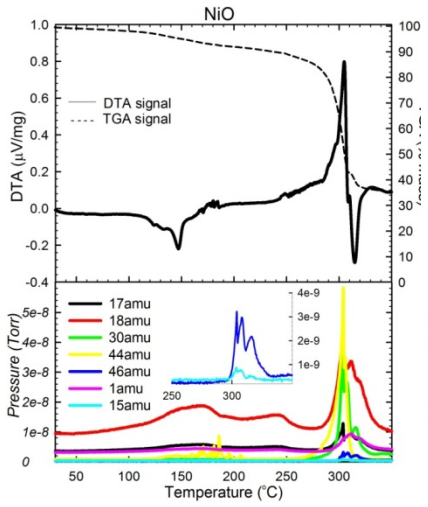	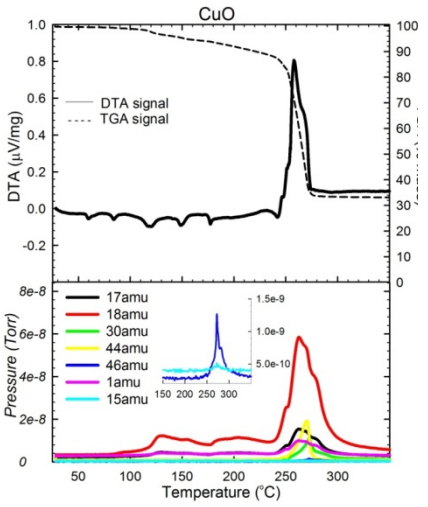
Group 11: Ag_2O	Group 12: ZnO	Group 13: Al_2O_3
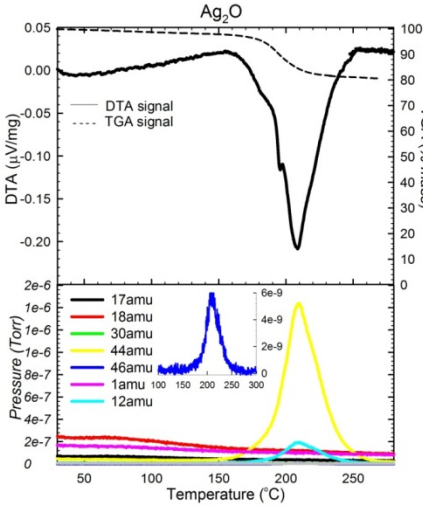	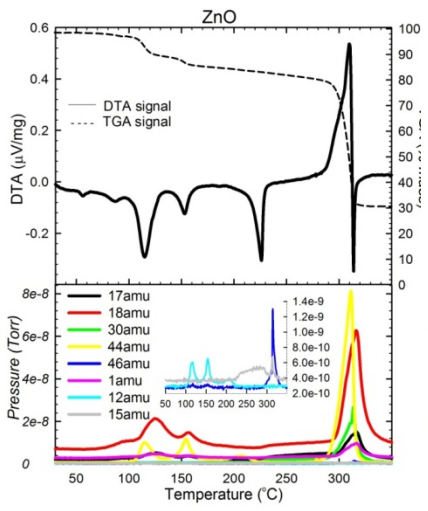	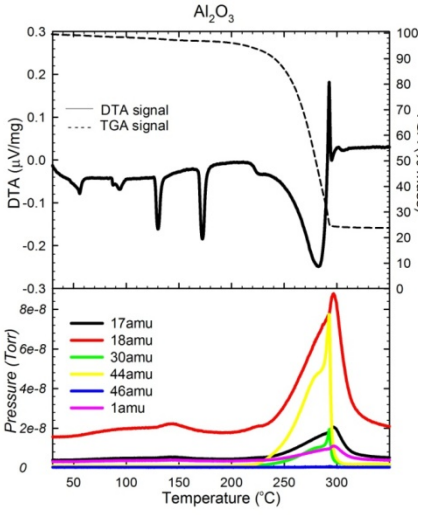

Group 13: In_2O_3	Group 14: SnO_2	Group 15: Bi_2O_3
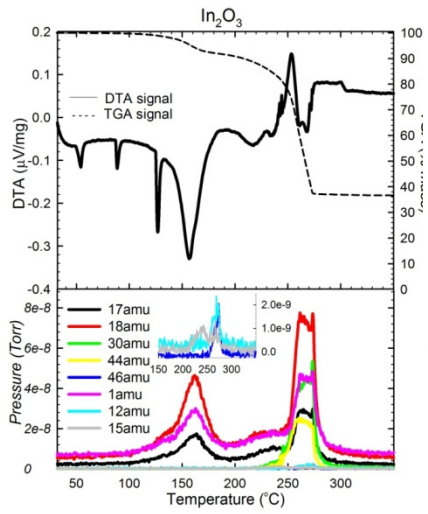	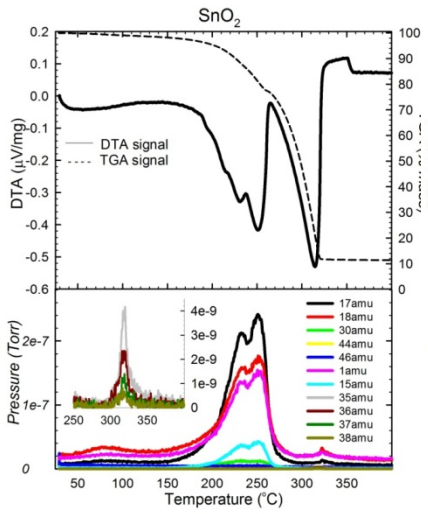	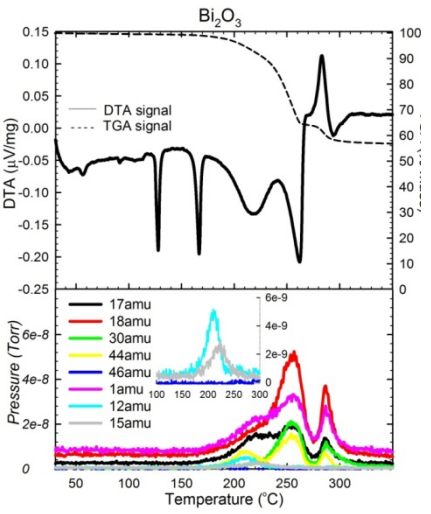
CeO_2	Nd_2O_3	PrO_2
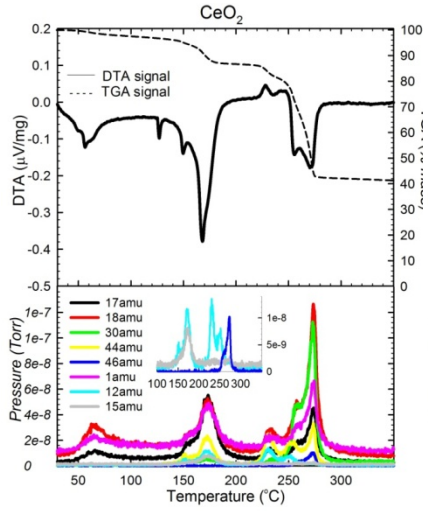	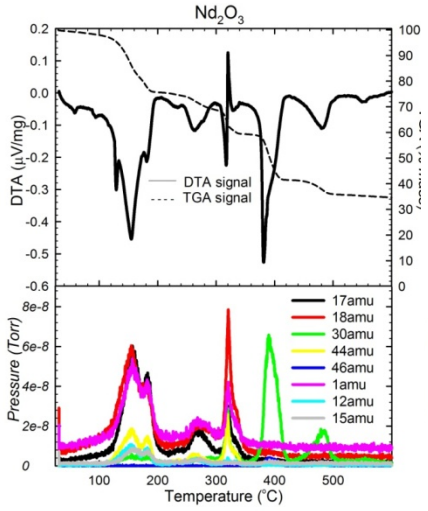	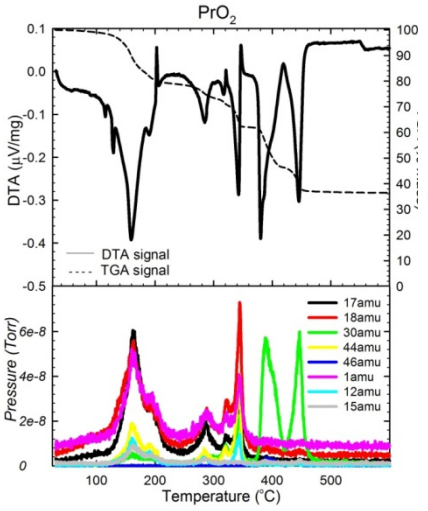

Figure A.2.2 TG/DTA-MS data of the calcination of rinsed precursors. DTA values correspond to exothermic and endothermic events, respectively.

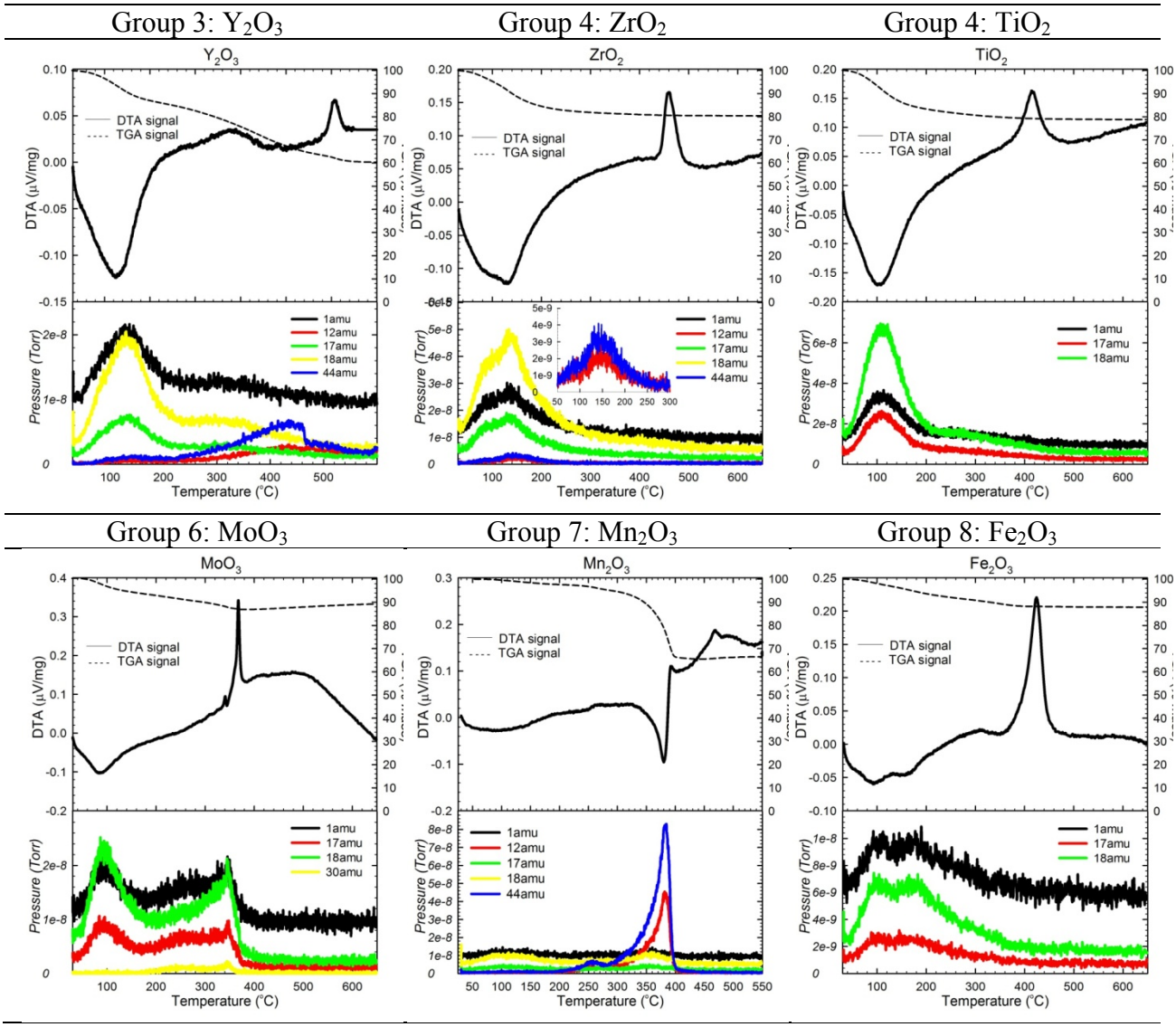

Group 9: CoO	Group 10: NiO	Group 11: CuO
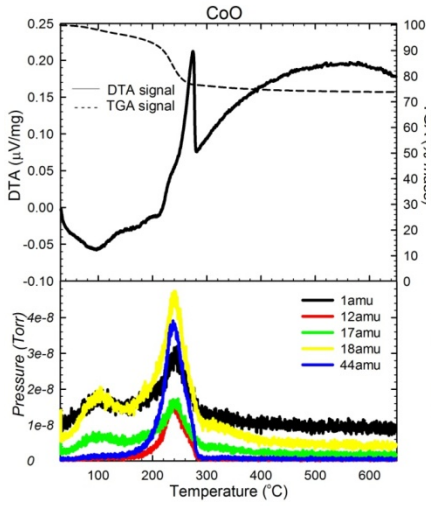	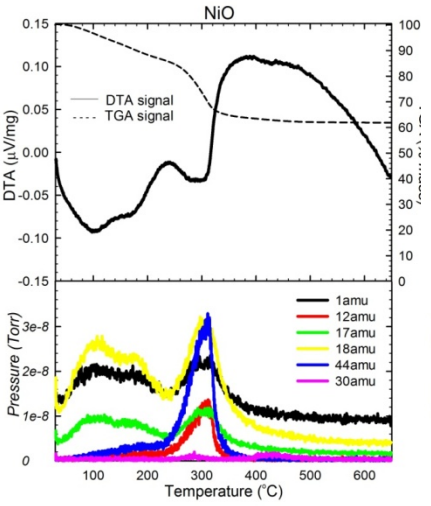	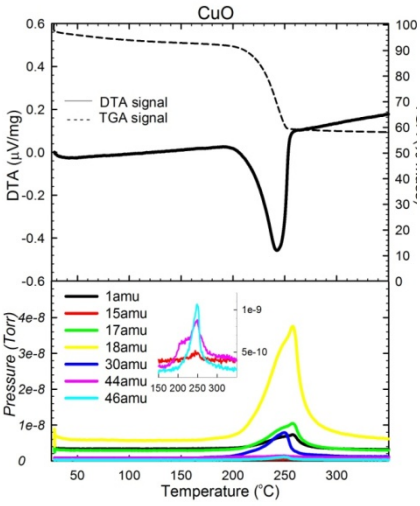
Group 12: ZnO	Group 14: SnO_2	Group 15: Bi_2O_3
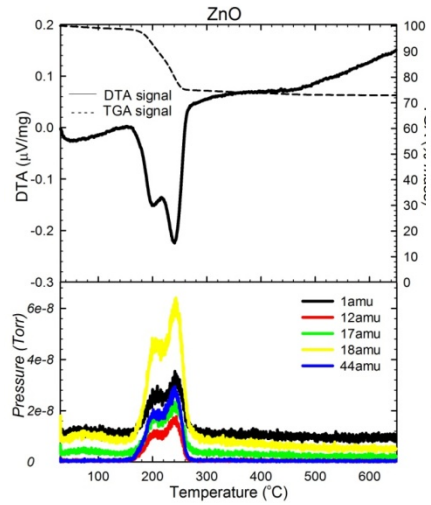	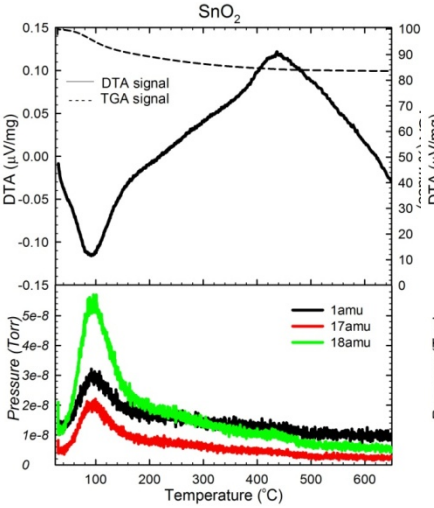	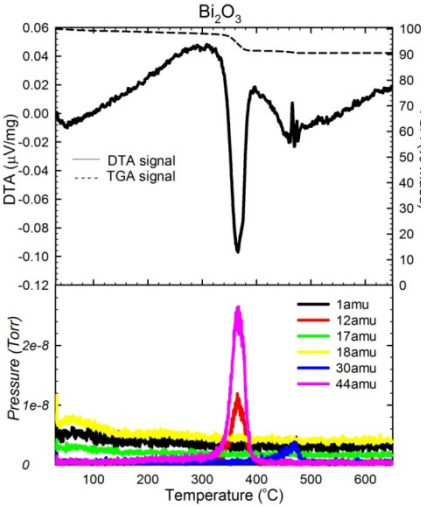

Appendix B

Chapter 5 Supplemental Material

B.1 PDF Fits of Commercial γ-Al_2O_3

Figure B.1.1 Shown below are the PDF refinements of commercial γ-Al_2O_3 samples obtained from Sasol (a-d) and Alfa Aesar (e-h) using the (a,e) gamma,[1] (b,f) eta,[2] (c,g) theta,[2] and (d,h) kappa[3] Al_2O_3 structures. The vertical red line in each graph divides the low-*r* region ($r \leq 7.8$ Å) where the θ- and κ-phases fit better from the high-*r* region ($r \geq 7.8$ Å) where the γ-and η-phases fit better, as is clearly visible from the difference curves shown at the bottom of each graph.

References

1. Paglia, G.; Buckley, C. E.; Rohl, A. L.; Hunter, B. A.; Hart, R. D.; Hanna, J. V.; Byrne, L. T., Tetragonal structure model for boehmite-derived gamma -alumina. *Phys. Rev. B: Condens. Matter Mater. Phys.* **2003**, 68 (14), 144110/1-144110/11.
2. Zhou, R. S.; Snyder, R. L., Structures and transformation mechanisms of the eta, gamma and theta transition aluminas. *Acta Crystallogr., Sect. B: Struct. Sci.* **1991**, B47 (5), 617-30.
3. Ollivier, B.; Retoux, R.; Lacorre, P.; Massiot, D.; Ferey, G., Crystal structure of κ-alumina: an x-ray powder diffraction, TEM and NMR study. *J. Mater. Chem.* **1997**, 7 (6), 1049-1056.

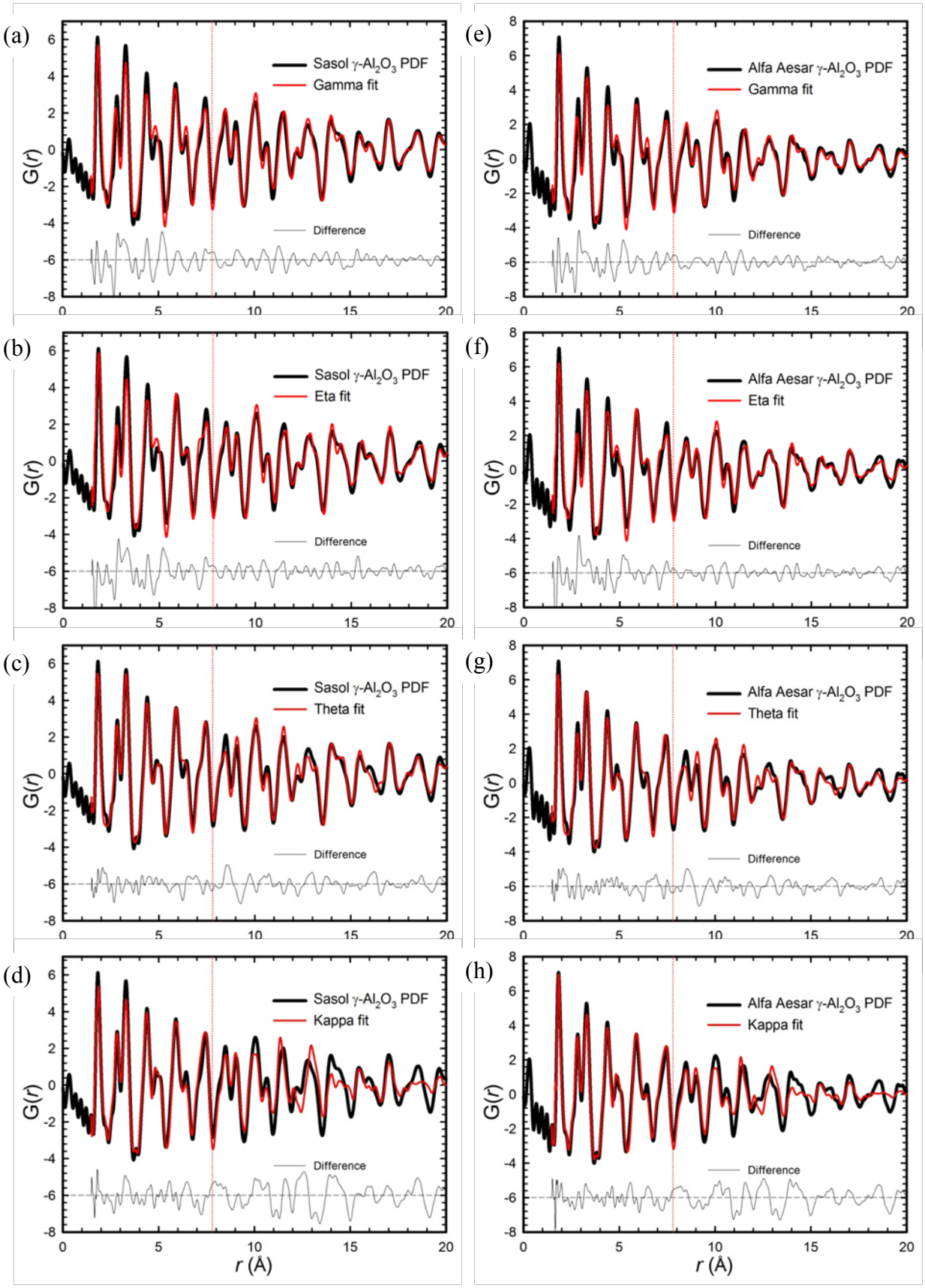

B.2 ^{27}Al MAS NMR fits

To quantify the three Al coordination environments (4-, 5-, and 6-coordinated Al) in γ-Al_2O_3, Lorentzian functions were fit to the resonance peaks corresponding to each coordination environment. The area under each peak was then integrated to quantify the percentage of Al in each coordination environment.

Figure B.2.1 ^{27}Al MAS-NMR data (top line) for the 350 (a), 500 (b), 700 (c), 900 (d), and 1000°C (e) samples along with the individual Lorentzian fits for the 4-, 5-, and 6-coordinated Al (bottom lines) and the combination of the three fits into a single fit (middle line) for comparison with the original data**.**

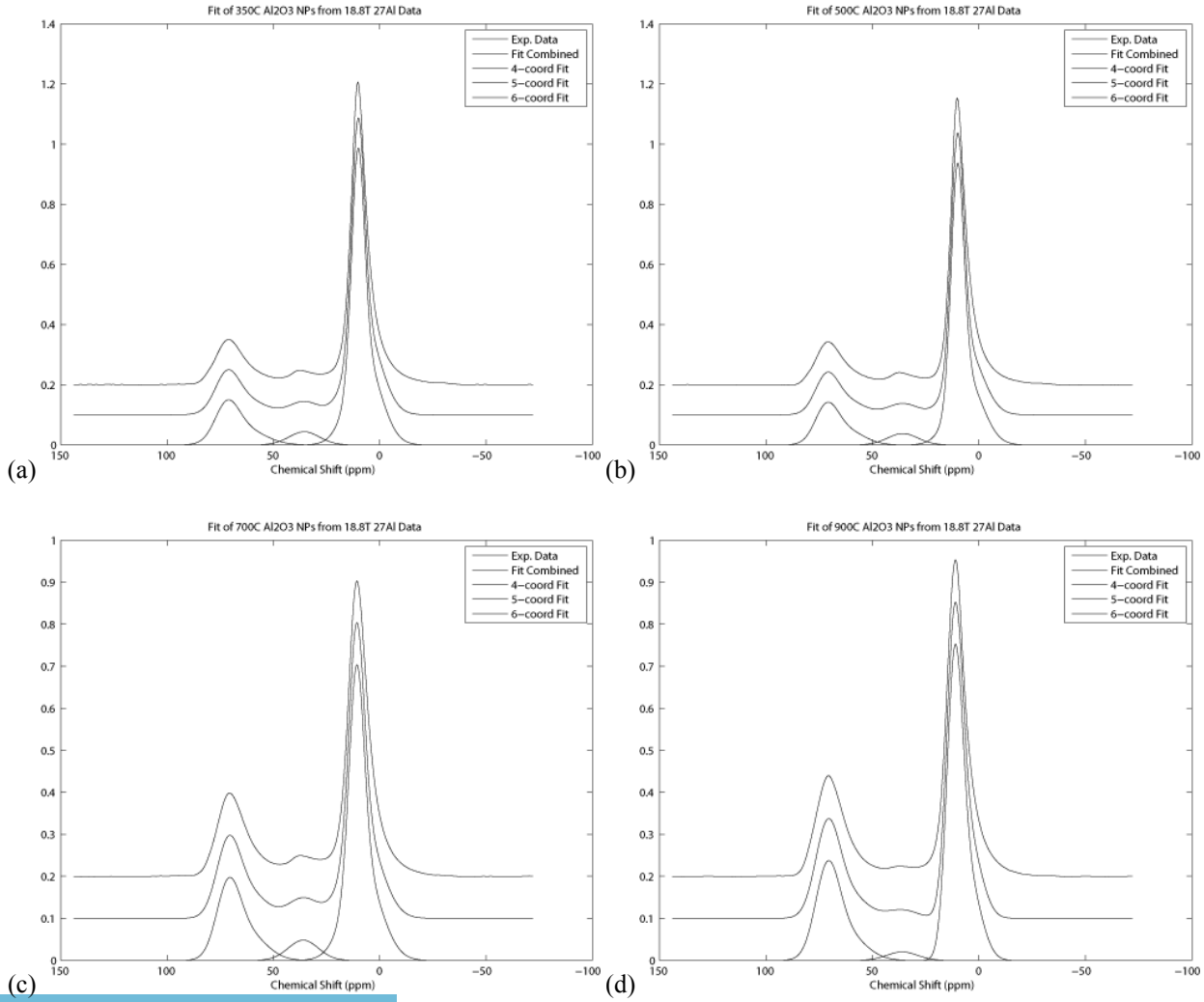

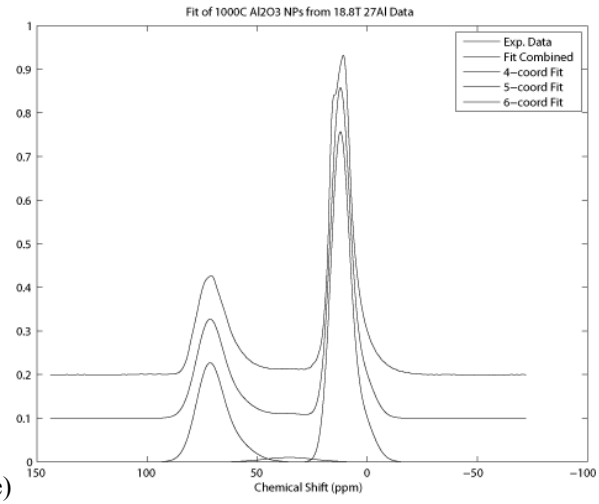

(e)

B.3 Final PDF Fit Parameters

Table B.3.1 PDF fit parameters for the γ-Al_2O_3 phase and the boehmite-like defect (modeled using the boehmite structure) used in the low-*r* (1.5 Å ≤ *r* ≤ 7.8 Å) refinements between 300-950°C.

Boehmite-like defect fit parameters

Sample	*a*	*b*	*c*	y_{Al}	y_{O1}	y_{O2}	R_w	mass%
300°C	2.85	12.63	3.87	0.689	0.281	0.096	0.30	37

Qdamp (0.141), delta2 (2.70), and all the boehmite phase parameters were refined at 300°C then fixed at every temperature.

Low-r Gamma fit parameters

Sample	*a,b*	*c*	y_O	z_O	R_w	γ-Al_2O_3 mass%	defect mass%
300°C	5.73	7.75	0.788	0.359	0.30	63	37
350°C	5.71	7.76	0.786	0.360	0.28	70	30
400°C	5.69	7.77	0.788	0.361	0.27	76	24
450°C	5.66	7.81	0.788	0.361	0.27	79	21
500°C	5.64	7.84	0.784	0.361	0.27	81	19
550°C	5.63	7.86	0.786	0.363	0.27	82	18
600°C	5.63	7.85	0.783	0.363	0.26	83	17
650°C	5.61	7.88	0.781	0.365	0.25	86	14
700°C	5.60	7.89	0.778	0.366	0.25	88	12
750°C	5.60	7.90	0.779	0.366	0.25	88	12
800°C	5.58	7.93	0.775	0.369	0.24	93	7
850°C	5.58	7.93	0.775	0.369	0.24	94	6
900°C	5.57	7.94	0.774	0.370	0.25	96	4
950°C	5.56	7.95	0.774	0.370	0.26	99	1

Qdamp (0.141), delta2 (2.70), and occupancies (O = 1.0, Al_{4a} = 0.88, Al_{8c} = 0.31, Al_{8d} = 0.58) were refined at 800°C then fixed at every temperature.

Table B.3.2 PDF fit parameters for γ-Al_2O_3 phase in the high-*r* ($r \geq 7.8$ Å) refinements between 300-950°C.

High-r Gamma fit parameters

Sample	*a,b*	*c*	y_O	z_O	Qdamp	R_w
300°C	5.69	7.86	0.784	0.364	0.113	0.56
350°C	5.67	7.84	0.783	0.361	0.118	0.40
400°C	5.66	7.77	0.771	0.372	0.120	0.30
450°C	5.66	7.77	0.768	0.380	0.123	0.27
500°C	5.65	7.77	0.767	0.381	0.120	0.25
550°C	5.64	7.78	0.765	0.381	0.117	0.23
600°C	5.63	7.78	0.763	0.382	0.114	0.22
650°C	5.62	7.79	0.760	0.383	0.106	0.19
700°C	5.61	7.79	0.758	0.385	0.100	0.18
750°C	5.60	7.79	0.759	0.384	0.101	0.18
800°C	5.60	7.79	0.759	0.385	0.092	0.17
850°C	5.60	7.79	0.760	0.385	0.092	0.17
900°C	5.60	7.78	0.759	0.386	0.088	0.17
950°C	5.60	7.76	0.761	0.387	0.084	0.18

Occupancies (O = 1.0, Al_{4a} = 0.88, Al_{8c} = 0.31, Al_{8d} = 0.58) were refined at 800°C then fixed at all temperatures.

Table B.3.3 PDF fit parameters for the γ and α-phase refinements between 1000-1200°C.

Gamma fit parameters

Sample	*a,b*	*c*	y_O	z_O	*delta2*	*Qdamp*	R_w	mass%
1000°C	5.60	7.76	0.759	0.391	2.74	0.091	0.27	84
1050°C	5.64	7.68	0.750	0.386	2.78	0.091	0.21	6

Alpha fit parameters

Sample	*a,b*	*c*	z_{Al}	x_O	*delta2*	*Qdamp*	R_w	mass%
1000°C	4.75	12.89	0.351	0.299	1.92	0.091	0.27	16
1050°C	4.73	12.92	0.352	0.307	1.91	0.091	0.21	94
1100°C	4.73	12.93	0.352	0.307	1.91	0.055	0.21	100
1150°C	4.73	12.92	0.352	0.307	1.91	0.055	0.21	100
1200°C	4.73	12.92	0.352	0.307	1.91	0.054	0.21	100

Appendix C

Chapter 6 Supplemental Material

C.1 Ghost atom structures

Table C.1.1 Aristoalumina structure used in all of the aristo distortions. Space group 225: Fm-3m with lattice parameters $a = b = c = 3.9691$ Å, $\alpha = \beta = \gamma = 90°$.

Site	Pos.	x	y	z	Occ.
O1	4a	0	0	0	1
Al1(oct)	4b	0.5	0.5	0.5	1
Al2 (tet)	8c	0.25	0.25	0.25	1

Table C.1.2 Ideal γ structure (with ghost atoms in gray) used in the aristo→ideal γ distortion. Space group 227: Fd-3m, origin choice 1, lattice parameters $a = b = c = 7.9382$ Å, $\alpha = \beta = \gamma = 90°$.

Site	Pos.	x	y	z	Occ.
O1	32e	0.375	0.375	0.375	1
Al1	8a	0	0	0	1
Al2	16d	0.625	0.625	0.625	1
*Al3	8b	0.5	0.5	0.5	0
*Al4	48f	0.25	0	0	0
*Al5	16c	0.125	0.125	0.125	0

Table C.1.3 Ideal γ structure (with ghost atoms in gray) used in the ideal γ→ cubic γ distortion. Space group 227: Fd-3m, origin choice 1, lattice parameters $a = b = c = 7.9382$ Å, $\alpha = \beta = \gamma = 90°$.

Site	Pos.	x	y	z	Occ.
O1	32e	0.375	0.375	0.375	1
Al1	8a	0	0	0	1
Al2	16d	0.625	0.625	0.625	1
*Al3	32e	0.1949	0.1949	0.1949	0

Table C.1.4 Cubic γ-Al_2O_3 structure (with ghost atoms in gray) used in the ideal γ→cubic γ distortion: Space group 227: Fd-3m. Origin choice 1, lattice parameters $a = b = c = 7.911$ Å, $\alpha = \beta = \gamma = 90°$.

Site	Pos.	x	y	z	Occ.
O1	32e	0.3797	0.3797	0.3797	1
Al1	8a	0	0	0	0.84
Al2	16d	0.625	0.625	0.625	0.58
Al3	32e	0.1522	0.1522	0.1522	0.17

Table C.1.5 Ideal γ structure (with ghost atoms in gray) used in the aristo→ideal γ distortion. Space group 227: Fd-3m, origin choice 1, lattice parameters $a = b = c = 7.9382$ Å. $\alpha = \beta = \gamma = 90°$.

Site	Pos.	x	y	z	Occ.
O1	32e	0.375	0.375	0.375	1
Al1	8a	0	0	0	1
Al2	16d	0.625	0.625	0.625	1
*Al3	8b	0.5	0.5	0.5	0
*Al4	48f	0.25	0	0	0
*Al5	16c	0.125	0.125	0.125	0

Table C.1.6 Ideal γ structure (with ghost atoms in gray) used in the ideal γ→η distortion. Space group 227: Fd-3m, origin choice 1, lattice parameters $a = b = c = 7.9382$ Å. $\alpha = \beta = \gamma = 90°$.

Site	Pos.	x	y	z	Occ.
O1	32e	0.375	0.375	0.375	1
Al1	8a	0	0	0	1
Al2	16d	0.625	0.625	0.625	1
*Al3	48f	0.25	0	0	0
*Al4	32e	0.375	0. 375	0. 375	0

Table C.1.7 η-Al_2O_3 structure (with ghost atoms in gray) used in the ideal γ→η distortion. Space group 227: Fd-3m, origin choice 1, lattice parameters $a = b = c = 7.914$ Å. $\alpha = \beta = \gamma = 90°$.

Site	Pos.	x	y	z	Occ.
O1	32e	0.3799	0.3799	0.3799	1
Al1	16d	0.625	0.625	0.625	0.68
Al2	48f	0.7739	0	0	0.16
Al3	32e	0.1949	0.1949	0.1949	0.09
*Al4	8a	0	0	0	0

Table C.1.8 θ-Al_2O_3 structure (with ghost atoms in gray) used in the aristo→θ distortion. Space group 12: C2/m, monoclinic cell choice 1, lattice parameters $a = 11.854$ Å, $b = 2.904$ Å, $c = 5.622$ Å, $\alpha = \gamma = 90°$, $\beta = 103.83$.

Site	Pos.	x	y	z	Occ.
O1	4i	0.8272	0	0.4273	1.00
O2	4i	0.4950	0	0.2526	0.93
O3	4i	0.1611	0	0.0984	0.80
Al1	4i	0.6595	0	0.3165	0.90
Al2	4i	-0.0834	0	0.2073	0.92
*Al3	2a	0	0	0	0
*Al4	2c	0	0	0.5	0
*Al5	4i	0.84	0.5	0.15	0
*Al6	4i	0.08	0.5	0.05	0
*Al7	4i	-0.0834	0.5	0.5	0
*Al8	4i	0.77	0	0.12	0
*Al9	4i	0.77	0	0.66666	0
*Al10	4i	0.0834	0	0.3165	0

Table C.1.9 κ-Al_2O_3 structure (with ghost atoms in gray) used in the aristo→κ distortion. Space group 33: $Pna2_1$, lattice parameters a = 4.834 Å, b = 8.3096 Å, c = 8.9353 Å, $\alpha = \beta = \gamma = 90°$. In the distortion, the structure was written in the P1 setting, meaning the position of each atom in the unit cell was explicitly listed.

Site	Pos.	x	y	z	Occ.
O1	4a	0.4796	0.8529	0.4977	1
O2	4a	0.5085	0.5089	0.505	1
O3	4a	0.1627	0.1632	0.2429	1
O4	4a	0.1544	0.4953	0.2656	1
O5	4a	-0.0202	0.3231	0.5166	1
O6	4a	0.1638	0.841	0.2708	1
Al1	4a	0.1778	0.8383	0.6466	1
Al2	4a	0.3307	0.0245	0.3775	1
Al3	4a	0.3138	0.3502	0.5713	1
Al4	4a	0.3156	0.6576	0.3734	1
*Al5	4a	0.3156	0.33	0.375	0
*Al6	4a	0.341	0	0.5713	0
*Al7	4a	0.81	0.835	0.5685	0
*Al8	4a	0.17	0.5	0.65	0
*Al9	4a	0.165	0.17	0.64	0
*Al10	4a	0.165	0.5	0.44	0
*Al11	4a	0.17	0.17	0.45	0
*Al12	4a	0.175	0.8383	0.45	0
*Al13	4a	0.995	0.33	0.71	0
*Al14	4a	0.02	0.345	0.83	0
*Al15	4a	0.995	0.65	0.685	0
*Al16	4a	0.02	0.675	0.815	0
*Al17	4a	0	0	0.69	0
*Al18	4a	0.995	0.005	0.83	0

Table C.1.10 α-Al_2O_3 structure (with ghost atoms in gray) used in the aristo→α distortion. Space group 167: R-3c, hexagonal setting, lattice parameters $a = b$ = 4.7617 Å, c = 12.9947 Å, $\alpha = \beta = 90°$, $\gamma = 120°$.

Site	Pos.	x	y	z	Occ.
O1	18e	0.3065	0	0.25	1
*O2	6a	0	0	0.25	0
Al1	12c	0	0	0.3521	1
*Al2	18d	0.5	0	0	0
*Al3	6b	0	0	0	0
*Al4	36f	0.83333	0.16667	0.04167	0

Table C.1.11 Ideal γ structure (with ghost atoms in gray) used in the γ→θ and the γ→α distortions. Space group 227: Fd-3m, origin choice 1, lattice parameters $a = b = c = 7.9382$ Å. $\alpha = \beta = \gamma = 90°$.

Site	Pos.	x	y	z	Occ.
O1	32e	0.375	0.375	0.375	1.000
Al1	8a	0	0	0	1.000
Al2	16d	0.625	0.625	0.625	0.833
*Al3	8b	0.5	0.5	0.5	0
*Al4	48f	0.25	0	0	0
*Al5	16c	0.125	0.125	0.125	0

Table C.1.12 θ-Al_2O_3 structure (with ghost atoms in gray) used in the γ→θ distortion. Space group 12: C2/m, monoclinic cell choice 1, lattice parameters $a = 11.854$ Å, $b = 2.904$ Å, $c = 5.622$ Å, $\alpha = \gamma = 90°$, $\beta = 103.83$. For the distortion, the structure was written in the P1 setting, and the origin was shifted by (0.08340, 0.04170, -0.20730) in order to match the P1 structure prescribed by Cai *et al*.

Site	Pos.	x	y	z	Occ.
O1	4i	0.8272	0	0.4273	1.00
O2	4i	0.495	0	0.2526	0.93
O3	4i	0.1611	0	0.0984	0.80
Al1	4i	0.6595	0	0.3165	0.90
Al2	4i	-0.0834	0	0.2073	0.92
*Al3	2a	0	0	0	0
*Al4	2c	0	0	0.5	0
*Al5	4i	0.84	0.5	0.15	0
*Al6	4i	0.08	0.5	0.05	0
*Al7	4i	-0.0834	0.5	0.5	0
*Al8	4i	0.77	0	0.12	0
*Al9	4i	0.77	0	0.66666	0
*Al10	4i	0.0834	0	0.3165	0

Table C.1.13 α-Al_2O_3 structure in the R-3 setting (with ghost atoms in gray) used in the γ→α distortion. Space group 148: R-3, hexagonal axes, lattice parameters $a = b = 4.7617$ Å, $c = 12.9947$ Å, $\alpha = \beta = 90°$, $\gamma = 120°$.

Site	Pos.	x	y	z	Occ.
O1	18f	0	0.3065	0.25	1
*O2	6c	0	0	0.25	0
Al1	6c	0	0	0.3521	1
Al2	6c	0	0	0.1479	1
*Al3	3a	0	0	0	0
*Al4	3b	0	0	0.5	0
*Al5	9e	0.5	0	0	0
*Al6	9d	0.5	0	0.5	0
*Al7	18f	0.83333	0.16667	0.04167	0
*Al8	18f	0.5	0	0.125	0

C.2 Hydroxide and Oxyhydroxide Distortions

As with the Al_2O_3 structures, ghost atoms were added to the AlOOH and $Al(OH)_3$ phases. However, we found that a rocksalt (AlO) intermediate was beneficial for distortions to the hydroxides and oxyhydroxides, thus only enough ghost atoms were added to the AlOOH and $Al(OH)_3$ phases to achieve a rocksalt (AlO) stoichiometry. Table C.2.1 summarizes the distortion strategies for the AlOOH and $Al(OH)_3$ phases. As the table indicates, another intermediate was necessary for the boehmite phase..

Table C.2.1 Distortion strategies for the AlOOH (boehmite and diaspore) and $Al(OH)_3$ (gibbsite and bayerite) phases.

Aristoalumina → rocksalt AlO → Single-slab boehmite → Boehmite AlOOH
Aristoalumina → rocksalt AlO → diaspore AlOOH
Aristoalumina → rocksalt AlO → gibbsite $Al(OH)_3$
Aristoalumina → rocksalt AlO → bayerite $Al(OH)_3$

C.2.1 Boehmite AlOOH

Table C.2.2- Table C.2.4 provide the structures used in the boehmite distortions. 'Single-slab' boehmite is simply ½ of the real boehmite unit cell; it was constructed by putting the boehmite unit cell in P1 symmetry, deleting the atoms with $z > 0.5$, resizing the z-axis to be ½ of its former size, and repositioning the remaining atoms so that the remaining cell resembles the bottom half of the boehmite unit cell. Using the ISOCIF program, the real symmetry of the single slab unit cell was determined to be 59 Pmmn. The appropriate ghost atoms were then added to the structure.

Table C.2.2 Structural parameters for the rocksalt intermediate.
The ghost atom (gray) was removed for the distortion to single-slab boehmite.

Rocksalt: space group 225 Fm-3m
a = b = c = 3.9691 Å
α = β = γ = 90°

Site	Pos.	x	y	z	Occ.
O1	4a	0	0	0	1
Al1(oct)	4b	0.5	0.5	0.5	1
*Al2 (tet)	8c	0.25	0.25	0.25	1

Table C.2.3 Structrual parameters for the intermediate structure, 'single-slab' boehmite.

Single-Slab boehmite: space group 59 Pmmn
a = 3.69 Å, b = 2.86 Å, c = 6.12 Å
α = β = γ = 90°

Site	Pos.	x	y	z	Occ.
Al1	2b	0.25	0.75	0.366	1
*Al2	2b	0.25	0.75	0.778	0
O1	2a	0.25	0.25	0.572	1
O2	2a	0.25	0.25	0.160	1

Table C.2.4 Boehmite structrual parameters.

Boehmite: space group 63 Cmcm
a = 2.86 Å, b = 12.22 Å, c = 3.69 Å
α = β = γ = 90°

Site	Pos.	x	y	z	Occ.
Al1	4c	0	0.683	0.25	1
O1	4c	0	0.286	0.25	1
O2	4c	0	0.080	0.25	1

The parameters for the distortions in the Aristoalumina → rocksalt AlO → Single-slab boehmite → Boehmite AlOOH sequence are summarized in Table C.2.5.

Table C.2.5 Aristo→boehmite distortion parameters.

Rocksalt → single-slab boehmite

Space Group: 225 Fm-3m
Subgroup: 59 Pmmn
basis=[(1,0,0),(0,1/2,1/2),(0,-1,1)]
origin=(1/4,0,1/4)

Displacive Modes	$\mathbf{X_5^-}$, $\mathbf{Sm_1}$
Lattice Strain Modes	$\mathbf{G_3^+}$, $\mathbf{G_5^+}$
Occupancy Modes	$\mathbf{G_1^+}$, $\mathbf{Sm_1}$

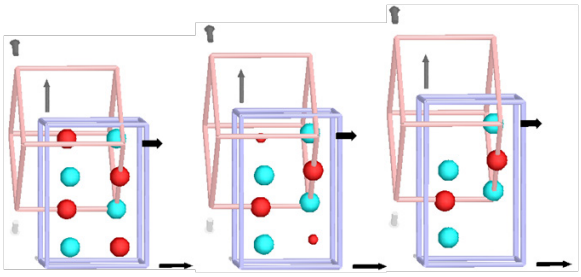

Aristo → single-slab boehmite distortion.

single-slab → real boehmite

Stack 2 unit cells in the z-direction
Shift the top cell by –½y
Shift the bottom cell by +½y
Merge the cells, re-define the axes:
x→z, y→x, 2z→y

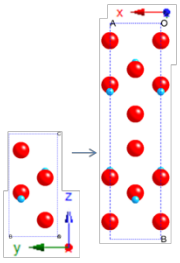

Ideal γ →η distortion.

To form boehmite (AlOOH) from aristoalumina, the tetrahedrally coordinated atoms must first be removed from the aristoalumina parent via the G_1^+ mode, making a rocksalt (AlO) parent structure in the same Fm-3m group (#225). The X_5^-, SM_1, and G_1^+ modes then remove ½ of the Al atoms to reach the appropriate AlOOH stoichiometry, creating sheets of tilted, edge-sharing octahedra in the x-z plane (or *a*-*c* plane).

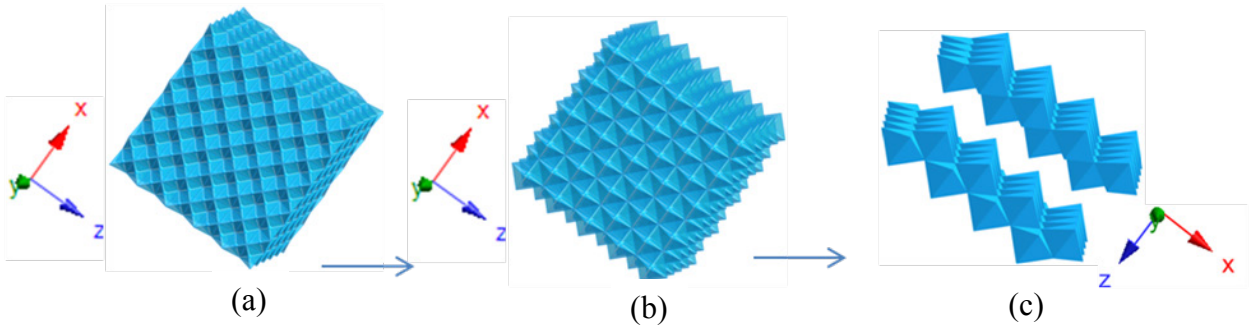

Figure C.2.1 In the distortion to boehmite, aristoalumina (Al_3O in (a)) is converted to rocksalt (AlO in (b)) which is then converted to a boehmite-like precursor (AlOOH in (c)) that consists of sheets of edge-sharing octahedra.

To reach the real boehmite structure, two unit cells must be stacked in the z-direction and then shifted by ±¼y relative to one another as the figure below directs. Along with a small lattice distortion, the unit cell vectors are then redefined so that x becomes z, y becomes x, and the two z-lengths become y.

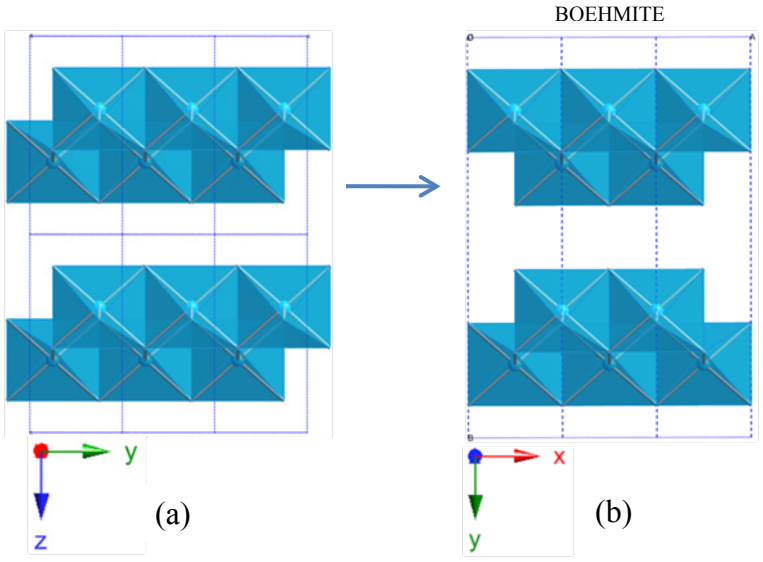

Figure C.2.2 To distort the boehmite-like precursor to the real boehmite structure, (1) two unit cells of the boehmite-like precursor are stacked in the z-direction, (2) the top cell is shifted by –¼y and the bottom by –¼y, and (3) the unit cell directions are redefined so that the previous y-axis is now the x-axis, x is now z, and 2z is now y.

C.2.2 Gibbsite $Al(OH)_3$, Bayerite $Al(OH)_3$, and Diaspore AlOOH

Ghost atoms were added to gibbsite $Al(OH)_3$, bayerite $Al(OH)_3$, and diaspore AlOOH to achieve a rocksalt AlO stoichiometry.

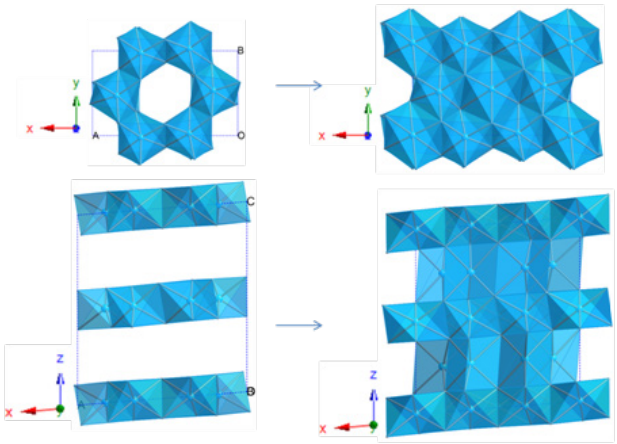

Figure C.2.3 Illustration of the vacancies in gibbsite and the ghost atoms used to fill them.

Table C.2.6 Wyckoff sites for the gibbsite structure (space group 14: $P2_1/n$) including the ghost atoms (*).

	site	x	y	z	Occ.
Al1	4e	0.1679	0.5295	-0.0023	1.00
Al2	4e	0.3344	0.0236	-0.0024	1.00
*Al3	4e	0.6644	0.0236	0.7475	0
*Al4	4e	0.3344	0.0236	0.7476	0
*Al5	4e	0.5000	0.5000	-0.0023	0
*Al6	4e	0.0000	0.0000	-0.0023	0
O1	4e	0.1779	0.2183	0.8885	1.00
O2	4e	0.6692	0.6558	0.8977	1.00
O3	4e	0.4984	0.1315	0.8956	1.00
O4	4e	-0.0205	0.6293	0.8932	1.00
O5	4e	0.2971	0.7178	0.8948	1.00
O6	4e	0.8194	0.1491	0.8985	1.00
H1	*4e*	*0.101*	*0.152*	*-0.124*	*1.00*
H2	*4e*	*0.595*	*0.573*	*-0.098*	*1.00*
H3	*4e*	*0.503*	*0.137*	*-0.190*	*1.00*
H4	*4e*	*-0.029*	*0.801*	*-0.107*	*1.00*
H5	*4e*	*0.293*	*0.724*	*-0.196*	*1.00*
H6	*4e*	*0.815*	*0.160*	*-0.190*	*1.00*

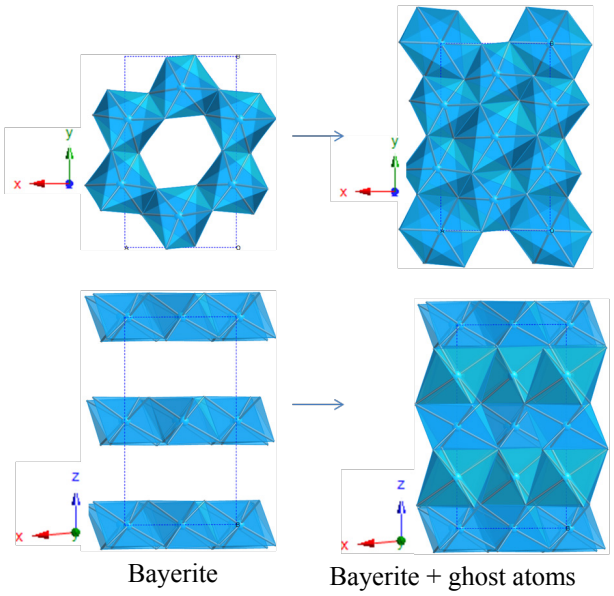

Figure C.2.4 Illustration of the vacancies in bayerite and the ghost atoms used to fill them.

Table C.2.7 Wyckoff sites for the bayerite structure (space group 14: $P2_1/n$) including the ghost atoms (*).

Site	Pos.	x	y	z	Occ.
Al1	4e	0.5114	0.1642	0.0004	1.00
Al2	4e	0.0326	0.3315	0.0015	1.00
*Al3	4e	0.5114	0.1642	0.2500	0
*Al4	4e	0.0326	0.3315	0.2500	0
*Al5	4e	0.5000	0.5000	0.0009	0
*Al6	4e	0.5000	0.5000	0.2500	0
O1	4e	0.1299	0.5072	0.3875	1.00
O2	4e	0.3573	0.3254	0.1020	1.00
O3	4e	0.7122	0.3057	0.3829	1.00
O4	4e	0.8819	0.4928	0.1111	1.00
O5	4e	0.6578	0.6747	0.3988	1.00
O6	4e	0.2829	0.6938	0.1142	1.00
H1	*4e*	*0.0527*	*0.5020*	*0.2940*	*1.00*
H2	*4e*	*0.3162*	*0.3034*	*0.2064*	*1.00*
H3	*4e*	*0.7458*	*0.2750*	*0.2883*	*1.00*
H4	*4e*	*0.6934*	*0.4657*	*0.1285*	*1.00*
H5	*4e*	*0.5602*	*0.5833*	*0.3883*	*1.00*
H6	*4e*	*0.3598*	*0.6006*	*0.1523*	*1.00*

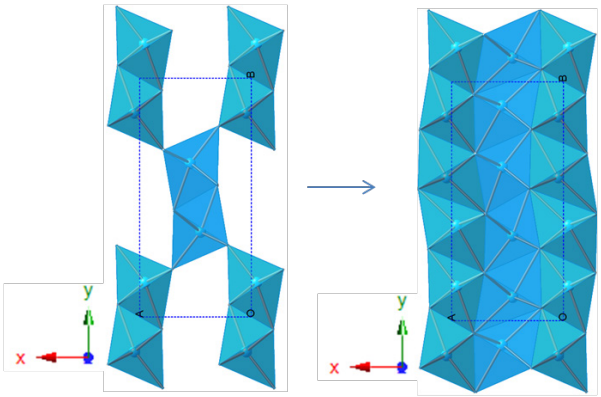

Diaspore Diaspore + ghost atoms

Figure C.2.5 Illustration of the vacancies in diaspore and the ghost atoms used to fill them.

Table C.2.8 Wyckoff sites for the diaspore structure (space group 62: Pbnm) including the ghost atoms (*).

Site	Pos.	x	y	z	Occ.
Al1	4c	0.0451	0.8554	0.2500	1.00
*Al2	4c	0.9549	0.4000	0.2500	0
O1	4c	0.712	0.1989	0.2500	1.00
O2	4c	0.197	0.0532	0.2500	1.00
H	4c	0.4095	0.0876	0.2500	1.00

ISODISTORT could not find a basis relationship between rocksalt and the bayerite, gibbsite, and diaspore phases, however, so we identified our own bases, shown in Table C.2.9.

Table C.2.9 New basis vectors for the gibbsite, bayerite, and diaspore structures in terms of the rocksalt basis vectors.

Gibbsite $Al(OH)_3$	Bayerite $Al(OH)_3$	Diaspore AlOOH
$\mathbf{a}_{new} = ½\mathbf{a} + ½\mathbf{b} - \mathbf{c}$	$\mathbf{a}_{new} = ½\mathbf{a} + ½\mathbf{b} - \mathbf{c}$	$\mathbf{a}_{new} = ⅔\mathbf{a} + ⅔\mathbf{b} - ⅔\mathbf{c}$
$\mathbf{b}_{new} = -1½\mathbf{a} + 1½\mathbf{b}$	$\mathbf{b}_{new} = -1½\mathbf{a} + 1½\mathbf{b}$	$\mathbf{b}_{new} = \mathbf{a} + \mathbf{b} + 2\mathbf{c}$
$\mathbf{c}_{new} = 1½\mathbf{a} + 1½\mathbf{b} + \mathbf{c}$	$\mathbf{c}_{new} = 1½\mathbf{a} + 1½\mathbf{b} + \mathbf{c}$	$\mathbf{c}_{new} = ½\mathbf{a} - ½\mathbf{b}$

In bayerite and gibbsite, our new bases were successful, but the atom matching process in Isodistort resulted in unrealistically large atomic motions (>2 Å). With diaspore, Isodistort would not accept the new basis vectors. For all three structures, we will most likely need to find an intermediate or precursor structure between rocksalt and the final gibbsite, bayerite, and diaspore structures (as we did with boehmite) and then manually elucidate the relationship between the precursors and the real structures. Because these structures were not critical for the analyses at hand, these decompositions were not pursued any further.

Appendix D

Chapter 7 Supplemental Material

Table 0.1 PDF fit parameters for gamma phase refinements.

	Gamma fit parameters									
Sample	***a,b***	***c***	***y*$_O$**	***z*$_O$**	***sratio***	***spdiam***	***delta2***	**mass%**	***Qdamp***	**R_w**
800°C	5.61	7.78	0.755	0.385	0.564	32.82		100	0.0939	0.246
850°C	5.61	7.78	0.755	0.385	0.564	32.75		100	0.0909	0.242
900°C	5.60	7.79	0.755	0.385	0.587	32.83		100	0.0786	0.233
950°C	5.60	7.79	0.757	0.384			2.49	100	0.1098	0.239
1000°C	5.60	7.79	0.757	0.384			2.43	100	0.1043	0.244
1050°C	5.59	7.79	0.756	0.384			2.41	100	0.1013	0.259
1100°C	5.59	7.78	0.756	0.386			2.23	79.0	0.0940	0.244
1150°C	5.51	7.97	0.766	0.379			2.46	43.7	0.0680	0.216

Table 0.2 PDF fit parameters for alpha phase refinements.

	Alpha fit parameters								
Sample	***a,b***	***c***	***z*$_{Al}$**	***x*$_O$**	***sratio***	***delta2***	**mass%**	***Qdamp***	**R_w**
1100°C	4.75	12.89	0.353	0.304	0.977	1.94	21.0	0.056	0.173
1150°C	4.73	12.91	0.352	0.306	0.877	1.02	56.3	0.056	0.175
1200°C	4.73	12.91	0.352	0.307	0.835	0.78	100	0.056	0.175